THE UNIVERSITY OF CHICAGO

ENHANCED TRANSPORT PHENOMENA IN CELLULOSE NANOCRYSTAL POLYMER COMPOSITES

A DISSERTATION SUBMITTED TO

THE FACULTY OF THE PRITZKER SCHOOL OF MOLECULAR ENGINEERING

IN CANDIDACY FOR THE DEGREE OF

DOCTOR OF PHILOSOPHY

BY

HARRISON RICHARD PAUL

CHICAGO, ILLINOIS

MARCH 2024

Table of Contents

List of Figures

List of Tables

Acknowledgements

There are many people that I have met throughout my PhD that I would like to thank for all the support and encouragement that they have given me over the years. It has been my privilege to know all of them.

Firstly, I would like to thank my PIs, Drs. Matthew Tirrell and Stuart Rowan. They have been invaluable mentors and advisors to me. They have shown me that with grit and determination I am capable of overcoming any obstacle, no matter how daunting it may seem. I am grateful for their guidance along the path of discovery, which is often winding and difficult. I am thankful for their lessons and will carry them with me throughout the rest of my life, especially how to finish what I have started. I would also like to thank my committee members, Drs. Paul Nealey and Seth Darling, whose scientific expertise is an inspiration. I would also like to thank Dr. Nealey for the opportunity to TA in his classes and grow as a mentor and teacher. I would also like to thank Seth for cheering me on in a brief foray into entrepreneurship with the Oleo Sponge technology. I learned more than I ever though I could from all of these experiences.

There are also many other members of the university, whose assistance has been integral to my success during my PhD. Thank you all for assisting me in countless ways: Briana Konnick, LaKesha Lloyd, Tracy Walker, Susan Podoba, Lisa Vonesh, Alicia Bearden-Mannie, and Maria Rubio. I would also like to thank my mentors and colleagues in the technology commercialization space, Yu Kambe, Steve Lehmann, Nora Mansfield, Jason Pariso, Emily Underwood, Cole Johnson, George Chellapa, Margaret Fleetwood, Joseph Gammie, Maya Bulkeley-Krane, Katherine Rhodes, Sean Shangguan, Zach Taylor, and Nicholas Vasdekas for showing me a path forward in my career.

I would also like to thank all of the wonderful lab members that I met along this journey. You have all been excellent colleagues, mentors, mentees, and friends: Amanda Marciel, Jeffrey Vieregg, Samanvaya Srivastava, Michael Lueckheide, Handan Acar, Michael Mellas, Lu Li, Hao Wu, Jeffrey Ting, Alex Marras, Yu Tian, John Barrett, Jelena Dinic, Whitney Fowler, Angelika Neitzel, Guilhem De Hoe, Ed Jiang, Carlos Medina Jimenez, Yan Fang, Dean Mastropietro, Siqi Meng, Mathew Schnorenberg, Kaden Stevens, Ge Zhang, Sean Mao, Qiming He, Wei Chen, Mrinal Bera, Pam Cai, Lauryn Carver, Vishnu Dharmaraj, Brian Khau, Ha Ram Kim, Shinya Wai, Siyang Wang, Brian Xi, Zhengjie Zhou, Sovan Banerjee, Hannah Morin, Sohee Park, Lily Alperstein, Nick Boynton, Chuqiao (Elise) Chen, Alex Crolais, Neil Dolinski, Simon Fawcett, Elina Ghimire, Jerry Hertzog, Samir Hossainy, Pin-Ruei (Ray) Huang, Tyler Jorgenson, Sheila Keating, Hojin Kim, Sean Lee, Cathy Li, Charlie Lindberg, Guancen Liu (Mike), Nicholas Macke, Sam Marsden, Natsumi Nitta, Jongwon Oh, Zehra Oluz Yazlak, Nanetta Pon, Adarsh Suresh, Haoyang You, Hongyi Zhang, Yunhao Zhao, Stanley Bilatto, Céline Calvino, Lifeng Chen, Elvis Cudjoe, Forrest Etheridge, Hongbo Feng, Amy Guo, Laura Hart, Katie Herbert, Xin Hu, Paul Jokinen, Isobel Jones, Ryo Kato, Bill Lenart, James Lettow, Ziyao Li, Marek Piechowicz, Erik Price, Phil Rauscher, Benjamin Rawe, Debbie Schneiderman, Arvin Sookezian, Marissa Tranquilli, Adam Weiss, Qiong Wu, Han Yang, Yefei Zhang and many others.

Finally, I would like to thank my family. To my parents, thank you for all the support you have given me over the years, and to my brother, good luck on your own PhD journey. Thank you to Jess, my wife, for all the love, support, and encouragement you provide me. I don’t know how I would have made it this far without your incredible support.

Abstract

The overall goal of my thesis work was to incorporate sustainable materials into polymer matrices to create nanocomposites with enhanced transport properties. Primarily, I focused on the study of ion structure to improve the fundamental understanding of cellulose-based sorbets, on the development of enhanced water transport materials for applications in membrane filtration and in new types of wicking materials, and on the improvement of heat transfer through thermally active materials.

In chapter 1, I introduce cellulose nanocrystals (CNCs) as a sustainable material and the qualities that make them promising nanofillers for polymer nanocomposites. I then discuss the potential applications of CNCs as sorbents and membranes for water purification, as the wicking component of rubbery wicking materials, and as the active component in thermally active materials.

In chapter 2, we used Anomalous Small Angle X-ray Scattering (ASAXS) to determine quantitatively the three-dimensional distribution of metal ions of different valencies surrounding negatively charged carboxylate functionalized CNCs. These distributions can affect water and ionic permeability in these materials. The data show that increasing the carboxylate density on the surface of the CNCs changed the nature of the structure of the adsorbed ions from a monolayer into a multilayer structure. Additionally, the data show that the CNCs can leverage multiple mechanisms, such as electrostatic attraction and the chaotropic effect, to adsorb ions of different valencies. By understanding the spatial organization of the adsorbed metal ions, the design of cellulose-based sorbents can be further optimized to improve uptake capacity and selectivity in separation applications.

In chapter 3, I present our work on the use of polymer grafted CNCs in membrane applications. The impact of the polymer grafting density and polymer conformation was investigated and showed that by increasing the grafting density of PEG such that it adopted a semi-dilute polymer brush conformation, the water flux through the membranes could be increased by up to three orders of magnitude while maintaining their rejection performances.

In chapter 4, I report our studies aimed at accessing moisture wicking rubbery films by the incorporation of CNCs into a hydrophobic latex matrix. This design is inspired by treated-wool fibers, which exhibit excellent wicking properties aided by a hydrophobic cuticle coated by a hydrophilic exterior layer. The hydrophobic cuticle mitigates water absorption while the hydrophilic protein sheath provides a wetting surface for the water to wick. Using a latex templating approach, CNC:polydimethylsiloxane (PDMS) composites were prepared with the ability to wick water through the composite film. I then used this rubbery wicking composite to develop a prototype for a sweat wicking prosthesis liner.

In chapter 5, I present our work on a thermal switching composite that changes its thermal conductivity based on applied strain. The composite is composed of CNCs incorporated into a shape-memory polymer matrix. Measurements show up to a two-fold increase in the thermal conductivity upon application of strain.

Chapter 1: Introduction

As the effects of climate change continue to worsen, there is a growing need for sustainable, petroleum-free materials to enable the transition towards a circular economy. Therefore, the study of sustainable materials for advanced material applications that leverage complex transport phenomena is critically important. In this chapter, I will introduce cellulose, specifically cellulose nanocrystals (CNCs), as a promising sustainable component for a variety of materials. I will then discuss nanocomposites and the ability of nanocellulose to enhance the properties of polymeric materials as well as how the manipulation of the architecture of such nanocomposites can enable access to a wider range of material properties. I will then discuss the application of CNCs and cellulose based nanocomposites in applications such as sorbents, water filtration membranes, wicking materials, and thermally active materials.

1.1 Cellulose Nanocrystals and Their Potential Chemical Functionalization

Natural biopolymers derived from low-cost, renewable biosources such as algae, plants, microbes, and animals represent promising sustainable alternatives to petroleum derived materials.[1,2] Cellulose is particularly promising as it is the most common biopolymer on the planet with over 100 billion tonnes produce by the natural world each year.[3,4] Cellulose can be isolated and extracted from a variety of biological sources including several marine animals,[5–10] algae,[11–18] fungi,[19,20] bacteria,[21–26] and plants.[2,27–48] Cellulose is usually extracted from the cell walls of these biosources through top-down isolation techniques that involve enzymatic, chemical, or physical methods.[2,49–51] Cellulose's great abundance and sustainable nature combined with its promising mechanical strength and ease of chemical modification have led to an increased amount of study and exploration of its possible applications in a wide range of fields such as textiles,[52,53] energy

storage,[54–56] biomedical applications,[57–59] packaging,[60,61] water purification,[1,62–68] and other composite systems.[69,70]

Cellulose is a β(1→4)-linked D-glucose polymer, where intrachain hydrogen bonding between hydroxyl groups and oxygens of the adjacent rings stabilize the β(1→4) linkages and cause the cellulose chains to adopt a linear configuration.[71–73] The hydroxyl groups and oxygen atoms within these linear cellulose chains can then engage in intermolecular hydrogen bonding, which when combined with Van der Waals forces, promote the parallel stacking of cellulose chains. The chains then form fibrils, larger microfibrils, and ultimately fibers (Figure 1.1).[71–76] These cellulose fibrils are comprised of highly crystalline domains, which are hierarchically organized within amorphous cellulose to create a rigid structure (Figure 1.1). Cellulose nanocrystals (CNCs) can then be isolated by extracting these crystalline regions.[71]

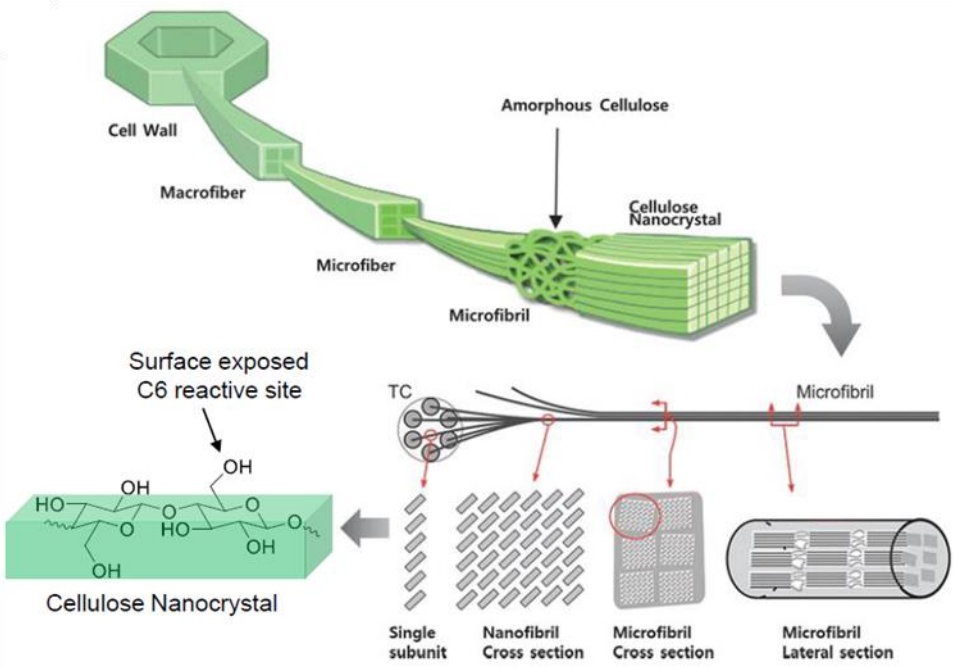

Figure 1.1. Overview of the hierarchical structure of cellulose showing the fibril packing, cellulose nanocrystals, and the cellulose chain structure. The exposed C6 hydroxyl can undergo additional reactions without significantly disrupting the crystallinity. Figure adapted from Kim *et al*.[74]

CNCs are highly crystalline, rod-like nanoparticles. The dimensions of these high aspect ratio nanoparticles are highly dependent on the biosource from which they are isolated. For example, CNCs isolated from tunicates have been shown to have aspect ratios above 75 with lengths ranging from 500 nm to 3000 nm, while CNCs from wood or cotton exhibit smaller dimensions on the order of 75 nm to 200 nm and aspect ratios of 10 to 25.[3,6,77] CNCs isolated from *Miscanthus x. Giganteus* (*MxG*) have been shown to have aspect ratios between 50 and 75 with lengths between 150 nm and 300 nm on average.[2,77]

These nanoparticles are often extracted from cellulose through acid hydrolysis, which can introduce various moieties to the surface depending on the specific acid that is used. The early instances of CNC isolation typically involved the hydrolysis of wood or cotton with sulfuric acid, which results in the formation of anionic sulfate ester groups at the C6 position of some of the

cellulose rings throughout surface of the CNCs.[78] The anionic sulfate esters on the surface of the CNCs isolated by sulfuric acid hydrolysis cause electrostatic repulsion, which improves the dispersion of these CNCs in both aqueous and organic solutions by mitigating CNC aggregation.[78,79] In addition to sulfuric acid, hydrochloric acid has commonly been used to isolate nanocellulose.[2,80–83] Unlike the CNCs that result from sulfuric acid hydrolysis, the CNCs that are isolated by hydrochloric acid hydrolysis are uncharged and exhibit hydroxyl groups along the surface, which can lead to issues with colloidal stability.[29] These hydroxyl functionalized CNCs tend to aggregate because of the high degree of hydrogen bonding between the surface hydroxyl groups.[78,79] The hydrochloric acid-treated CNCs can undergo additional modification via (2,2,6,6-tetramethylpiperidin-1-yl)oxyl (TEMPO)-mediated oxidation or ammonium persulfate oxidation to introduce negative charges in the form of carboxylate moieties to the surface of the CNCs, which will improve their colloidal stability.[51,81–83]

In addition to improving the dispersion of the CNCs in solution, the carboxylate groups introduced by TEMPO oxidation can act as reactive handles for further modification of the CNC surface. While first reported by Araki et al.,[84] the use of carbodiimide-mediated reactions to covalently attach molecules with primary amines to the CNC surface has since become a widely used method to further engineer the surface of the CNCs.[85–92] The reaction to form the amide bond that attaches these molecules to the CNC surface involves the formation of a N-hydroxysuccinimydyl ester at the C6 position of the cellulose ring to activate the carboxylic acid followed by reaction with the primary amine. Rowan and coworkers used this approach to functionalize the surface of tunicate CNCs with ethylene diamine so that the modified CNCs were able to form a pH-responsive gel.[89] Additional studies have used a similar method to attach alkylamines to the CNC surface, enabling the synthesis of hydrophobically functionalized CNCs,

which were shown to improve the ability of these CNCs to stabilize polystyrene emulsions and latexes in aqueous solutions without the need for small molecule surfactants.[91]

While this peptide coupling approach has been shown to be effective at covalently binding small molecules to the CNC surface, the same strategy has been employed to graft primary amine terminated polymers to CNCs as well.[55,84,87,88,93,94] By grafting polymers to the CNCs, the chemical and physical properties of the tethered polymer can complement the inherent properties of the nanoparticles.[95] For example, Wooley and coworkers used this peptide coupling strategy to graft poly(styrene) and poly(tert-butyl acrylate) onto carboxylate functionalized cotton CNCs, which exhibited increased the colloidal stability of the polymer-grafted nanoparticles (PGNs) in organic solvents like acetone, chloroform, and toluene after polymer grafting.[87] Similarly, Araki et al. grafted amine-terminated poly(ethylene glycol) (PEG) onto cotton CNCs with the same carbodiimide-mediated reaction to synthesize PGNs with improved colloidal stability.[84] Additionally, Jean and coworkers were able to create thermally responsive PGNs by tethering thermally responsive Jeffamines to the surface of cotton CNCs through peptide coupling.[86]

Using the amide coupling reactions to attach polymers to the CNC surface is an example of the "grafting to" approach for functionalized CNCs with polymer. The "grafting to" approach involves synthesizing polymers with a reactive end group and modifying the surface of the nanoparticle with a complementary reactive group. The preformed polymer is then reacted with the surface to form a covalent bond, thus, tethering the polymer to the surface. One of the advantages of this approach is that the polymer of interest can be thoroughly characterized and well defined before being attached to the nanoparticle. This approach does have some limitations, such as lower grafting density due to the effects of steric hindrance from the large polymer chains. However, Rowan and coworkers[94] have shown that grafting density can be improved by controlling the

solvent quality as it relates to the grafting polymer. Their results showed that when grafting PEG to CNCs in DMF, which is a poorer solvent for PEG than water, the grafting density was significantly higher than what was achieved by performing the grafting reaction in water.[94] The grafting density was improved in part due to the PEG chains having a less elongated conformation in DMF, which reduced the effect of steric hindrance on the grafting reaction.[94] In addition to the "grafting to" approach, alternative grafting strategies such as the "grafting from" method have been used to synthesize PGNs. The "grafting from" approach involves the modification of the nanoparticle surface with reactive groups that can act as initiation sites for the polymerization of a second monomer. The monomer is added to the solution and allowed to grow from the surface to from a PGN. While alternative approaches to polymer grafting on CNCs are beyond the scope of this thesis, excellent reviews and studies involving these techniques are available.[95–100]

1.2 Polymer Nanocomposites

Polymer nanocomposites are multicomponent materials generally composed of a nanofiller, defined by having at least one dimension that is 100 nm or less, imbedded within a polymer matrix. These nanocomposites often exhibit properties inherent to both the polymer matrix and the nanofiller. However, their characteristics are more than just the sum of their parts, as the filler architecture, the filler-matrix interactions, and the filler-filler interactions each play a critical role in the overall properties of the composite.[101] As such, polymer nanocomposites are utilized in a wide variety of applications,[102,103] especially where the nanocomposite nature of the material enhances the mechanical properties,[104–108] electrical properties,[109–112] or water purification capabilities[62–64,113,114] of the polymer matrix. The degree to which these properties can be improved is highly dependent upon the amount of nanofiller that can be loaded into the polymer matrix as well as how well the nanofiller is dispersed throughout the material. As such, chemically

modifying the nanofiller to improve its dispersion within the polymer matrix can mitigate phase separation and increase the maximal loading of nanofiller in the composite.[94,115,116]

The facile chemical modification of CNCs makes them an excellent candidate for nanofillers in a variety of potential polymer matrices. CNCs were first reported as a nanofiller by Favier *et al.* when they incorporated CNCs into poly(styrene-co-butyl acrylate) in order to reinforce the mechanical properties of the material.[117] Since this initial demonstration, interest in CNCs as a nanofiller has continued to grow as a result of their appealing inherent properties such as high surface area, low density, sustainability, high tensile strength, and their ability to be easily chemically modified. CNCs have been incorporated into a wide variety of polymer matrices such as polypropylene,[118] polyethylene,[119] polyurethane,[37,120–122] poly(vinyl acetate),[89] poly(styrene-co-butadiene),[123,124] poly(lactic acid),[94,97,125,126] and poly(ε-caprolactone)[98–100] among many others. In order to synthesize a functional CNC nanocomposite with enhanced properties, the CNCs must be well dispersed throughout the polymer matrix, which requires proper processing techniques and involves a thorough understanding of the surface chemistry on the CNCs, the type of polymer matrix, and the desired final properties of the nanocomposite.[3] As such, CNCs have been used to create polymeric nanocomposites with reinforced mechanical properties,[107,108,120,125,127–129] improved thermal conductivity,[130] or better ion conductivity.[55,56]

Many of these enhancements leverage the CNCs' ability to form a percolating network throughout the polymeric matrix.[128,131] To form a percolating network, the CNCs must be well dispersed in the polymer, which, as previously discussed, often necessitates chemical modification of the CNC surface. Additionally, the CNCs must reach a sufficient volume fraction to form a continuous network that can transfer load when mechanical stress is applied to the composite.[51,94,115,132] According to percolation theory, the onset of percolation occurs at a critical

volume fraction of anisotropic, rigid filler, X_c, where $X_c=0.7/A_r$ and A_r is the aspect ratio of the filler.[131,133] The percolation model relies on the nanofiller having strong nanoparticle-nanoparticle interactions to share induced stress upon the nanofiller across the percolating network. For example, the hydrogen bonding interactions between CNCs enable the nanoparticles to form a percolating network if the volume fraction of CNCs is above the percolation threshold.[133]

While this model was developed for simple polymer matrices, it has been shown that more complex polymer structures such as polymer latexes can influence the formation of a percolating network.[92,108,134–141] As demonstrated by Limousin *et al.*, the size of the latex particle relative to the dimensions of the CNCs has a critical impact on the ability of the CNCs to form a percolating network.[138] By increasing the size of the latex particles to be at least five times larger than the CNCs, they found that the anionic CNCs would adsorb onto the positively charged latex polymer surface, which when cast into a film would encourage the formation of a percolating network. However, when the size of the latex particles was reduced to be significantly smaller than the size of the CNCs, the cationic charged latex particles would adsorb onto the anionic CNCs, preventing the CNCs from interacting with each other and thus a percolating network would not form even at the same volume fractions as the previous experiments.[138]

However, when CNCs do not form a percolating network, they can still enhance the mechanical properties of the nanocomposite, according to the Haplin-Kardos theory.[93,120,133] This theory assumes a homogenously dispersed anisotropic filler within a polymer matrix, where there are no major filler-filler interactions.[120] In addition to enhancing the material properties of these latex based nanocomposites, CNCs can impart additional benefits to the latex particles by acting as stabilizers and macrosurfactants.[91,92,137] As Rowan and coworkers have shown, hydrophobically functionalized CNCs can stabilize the interface between a poly(styrene-co-2-ethylhexyl acrylate)

emulsion and the surrounding water without the need for additional surfactants, and the subsequent latex composite film exhibits significantly higher moduli and lower water uptake.[92]

In many of the applications of nanocomposites, the ratio of nanofiller to polymer is a critical factor that determines the extent to which the nanofiller is able to influence the overall properties of the material. As previously discussed, chemically modifying the surface chemistry of the nanofiller to enhance its dispersibility in the polymer matrix is one strategy to increase nanofiller loading. However, this method has its limitations as the nanocomposites may still be prone to phase separation at particularly high nanofiller loadings or if there is inherent incompatibility between the nanofiller and the matrix.[142] An approach that can address some of these limitations and potentially access nanocomposites with significantly higher nanofiller volume fractions is to covalently bind the polymer matrix to the nanoparticle filler to make PGNs. These PGNs can then be processed into polymeric films, which are one-component nanocomposites (OCNs).[93,142,143] The covalently linked nature of these materials prevents phase separation between the nanofiller and the polymer. The lack of de-mixing in these OCNs also allows them to achieve a wider range of polymer to nanofiller ratios than traditional two-component composites.[93,144–147]

While the homogeneous nature of OCNs provides many potentially desirable material properties, such as high nanofiller loadings, the initial step of grafting polymers onto nanoparticles is also inherently beneficial. Polymer grafting enhances interactions between the nanoparticles and the polymer, thereby mitigating phase separation. Additionally, the structure property relationships of spherical PGN that have been reported indicate that the grafted polymer conformation plays a critical role in the overall properties of the PGNs and the OCNs fabricated from these PGNS.[145–148]

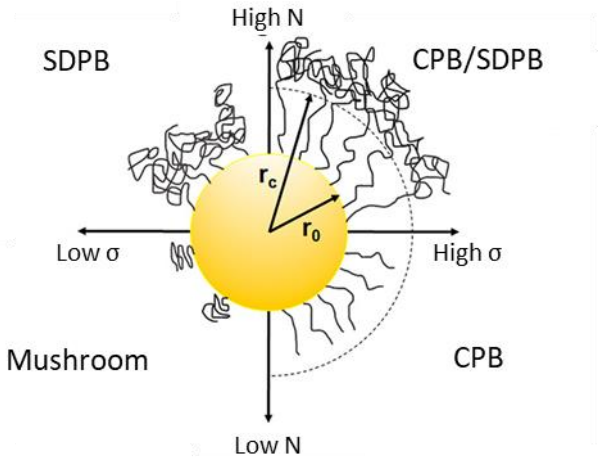

Figure 1.2. Chain conformation of polymer-grafted nanoparticles (PGN) as a function of chain grafting density, σ, and degree of polymerization, N, at a given particle radius, r_0. The polymer conformations include mushroom (bottom left), concentrated polymer brush (CPB) (bottom right), semi-dilute polymer brush (SDPB) (top left), and mixed CPB/SDPB (top right) with a transition at a critical radius, r_c. Adapted from Jiao *et al*.[147]

Similar to results seen in traditional brush literature on planar surfaces, the tethered polymer conformations can be divided into three regimes, namely the mushroom regime, the concentrated brush regime (CPB), and the semi-dilute brush regime (SDPB) (Figure 1.2).[93,147,149–151] The radius of gyration (R_g) and the grafting density of the tethered polymer largely influence which conformation will be adopted by the grafted polymer.[142] The mushroom regime is defined by the phase space in which the tethered polymers are spread across the surface such that adjacent chains do no interact with each other.[93,94] As such, the boundary of mushroom regime is the point at which each polymer chain's conformation would be influenced by its neighbors for a given molecular weight. This critical grafting density is defined as $1/(\pi R_g^2)$, which is the projection of a sphere, whose size is equivalent to the loose coil conformation of the tethered polymer, onto the grafted surface. As grafting density is increased above this critical threshold to the point that neighboring chains start to overlap, the polymers adopt a SDPB conformation.[152] In this regime, the polymers

extend away from the nanoparticle surface and deviate from the loose coil shape seen in the mushroom regime. As chains are packed more densely on the nanoparticle surface, the polymers enter the CPB regime, where they elongate to form a stiffer polymer layer. For PGNs that exhibit a CPB, the polymer chains may transition to a CPB/SDPB conformation at high molecular weights due to the innate curvature of the nanoparticle.[153] At some distance away from the rounded surface, there is a transition from a CPB to a SDPB conformation as the volume increases, following predictions by Daoud−Cotton models applied to nanoparticles.[93,153–155]

Daoud and Cotton initially developed their model to describe the behavior of star shaped polymers.[156] The Daoud-Cotton model predicted that star polymers would exhibit two characteristic lengths based on the radial monomer density of the polymer. The first characteristic length was defined as a radius in which other star polymers could not penetrate due to the steric hindrance cause by a high monomer density, while the second length was an outer radius with a lower monomer density that could be interpenetrated by other star polymers. This model has since been applied to PGNs to describe their polymer conformations such that the Daoud-Cotton model predicts that at a critical polymer length, the tethered polymer conformation would transition from a CPB to SDPB because the monomer density decreases as the distance from the center of the particle increases. This transition results in a CPB inner layer surrounded by a SDPB outer corona defined as the CPB/SDPB regime (Figure 1.2).[142,147,156]

By controlling the grafted polymer conformation, beneficial interactions between the polymers and the nanoparticle can be enhanced, leading to improvements in properties such as increased ion conduction for brush conformation polyelectrolyte grafted CNC films.[56] The polymer conformation has also been shown to be critical to the mechanical properties of PGN films and nanocomposites. Polymers in the SDPB regime enable increased penetration by neighboring

polymer brushes, allowing increased interaction between particles, which leads to significant improvements in mechanical strength and toughness.[94,145,146]

1.3 Water Purification Applications of Nanocellulose and Cellulose Based Nanocomposites

As the need for water in industrial processes, agriculture, and personal consumption continues to increase and natural reservoirs are strained, more regions are becoming water-stressed such that the demand for water in these regions has (or soon will) exceed the available water.[157,158] Increased urbanization in these water-stressed regions, coupled with industrial expansion, increases the demand for limited water sources.[157,158] Additionally, pollution from dyes[159], heavy metals,[68,160–162] and pesticides[163] is a growing problem that threatens the supply of fresh water.[1,164] Dye effluents have been identified as the largest class of pollutants from industrial sources and are especially problematic as they pose health risks to humans, flora, and fauna.[1,159,165,166] In addition to dye contamination, heavy metal pollution is a growing ecological and public health concern.[167,168] Heavy metals can have deleterious effects even at extremely low concentrations, so effective removal methods are essential to producing safe, potable water.

This demand, coupled with the declining supply, heightens the need for potable water to be produced from underutilized resources, like contaminated fresh water and wastewater. For example, according to the US Environmental Protection Agency (EPA), only 7 to 8% of the thirty-two billion gallons of waste effluent produced each day are recycled.[169] To help address these issues, several technologies like membrane filtration,[170–176] flocculation,[160,177,178] and sorbents[1,179,180] are used to generate potable water.

1.3.1 Mass Transfer to Sorbent Surfaces

Sorbents are commonly used to remove contaminants that are not easily degraded, as they sequester chemicals from the water through adsorption and absorption processes, thereby enabling the elimination of the contaminants when the sorbents are removed from solution. Activated carbons are commonly used as sorbents. Activated carbon has been established as one of the most effective traditional adsorbents with a high sorption capacity because of the high porosity and resulting high surface area.[180–182] However, activated carbon has some drawbacks for its use in industrial settings; one of the most limiting disadvantages is that activated carbon can be expensive both from financial and energy standpoints.[180] To address the expensive nature of activated carbon, studies have been conducted to attempt to find alternative sources for activated carbon as well as regenerate spent carbon sorbents.[183,184] In addition to the cost, activated carbon has limited selectivity. As shown in Radovic et al.,[185] the primary mechanism for adsorption onto activated carbons is physisorption, which means that activated carbons are not selective.[185,186] As such, attempts have been made to identify alternative sorbent materials.[1,159,180,187]

Natural biopolymers derived from low-cost, renewable bio-sources such as algae, plants, microbes, and animals represent promising foundations for sustainable sorbent materials.[1,2] In particular, polysaccharides and their derivatives have exhibited high removal efficiency for both inorganic contaminants, like heavy metals, and organic pollutants, such as dyes, via adsorption. As such, various polysaccharides, including chitosan[165,168,188] and cellulose[189,190], have been utilized in water purification applications.[1] For example, a recent study by Guibal and coworkers investigated the use of chitosan copper oxide composites for removal of arsenic from solution.[168] The sorbent exhibited two possible adsorption sites for the metal ions, one of which was associated with the copper oxide and had a strong affinity for As(V) and a second site that showed a lower

affinity for adsorption associated with the chitosan. With both of these possible adsorption sites, the composite adsorbents exhibited pH dependent Langmuir adsorption of As(V) with a maximum adsorption capacity seen at pH 4.[168] These chitosan-based purification materials are not limited to removing ionic species from solution, for as seen in Liu et al., chitosan copper composite affinity membranes can be used to remove urea from solution with a maximum adsorption capacity of 78.8 mg of urea per g of membrane.[191]

Cellulose, especially nanocellulose, is a type of polysaccharide that is particularly promising as a sorbent as it is an abundant, low-cost material with a surface that can be engineered through facile chemical modification to enhance the sorption capacity and selectivity.[62,192] Various charged moieties, such as sulfates, phosphates, carboxylates, and amines, have been introduced to the surface of CNCs. Studies have been conducted to evaluate the ability of these functionalized materials to remove inorganic contaminants such as Cr^{3+}, Pb^{2+}, and Cd^{2+}, among many others (Table 1.1).[21,62,190,192–203] For example, Liu et al. reported that CNCs obtained by sulfuric acid hydrolysis have a higher Ag(I) adsorption capacity (34 mg/g) than cellulose nanofibrils (CNF) obtained through mechanical grinding (14 mg/g), due to the presence of sulfate esters on the CNC surface. In these uptake experiments, the solution pH was found to be a critical parameter that can affect the uptake characteristics of the sorbents such that the maximum uptake capacity was measured around neutral pH and that uptake performance declines at lower pH values since the H^+ competes with Ag^+ for the sulfate groups on the cellulose surface.[195] Carboxylate functionalized nanocellulose has been used by Tinguat and coworkers to selectively recover Cu(II) from solution.[200] The adsorption capacity of Cu(II) onto the carboxylate functionalized CNFs increased with increasing pH from pH 3 to 7 and showed that Cu(II) ions could be desorbed with acid washes, thus recovering the copper and regenerating the cellulose sorbent. These cellulose based sorbents

Table 1.1. Overview of heavy metal uptake by functionalized nanocellulose materials with the pH and maximum uptake capacity (Q_{max}) highlighted. Table adapted from Voisin *et al*.[62]

Functionalization Nature and Route	Contaminant	pH	Q_{max} (mg/g)
None (CNF-OH obtained through mechanical treatment)	Cd^{2+} Ni^{+} Pb^{+}	5.5	11 11 10
CNC-SO^{3-} (sulfuric acid hydrolysis)	Ag^{+}	6.5	34
CNC-PO_4^{2-} (phosphorylation of CNC)	Ag+ Cu^{2+} Fe^{3+}	4	136 117 115
CNC-COOH (Succinic anhydride)	Pb^{2+} Cd^{2+}	5.5	458 335
CNC-COOH (sodium periodate/chlorite)	Cu^{2+}	4	185
CNF-COOH (TEMPO)	Cu^{2+} Ni^{2+} Cr(III) Zn^{2+} UO_2^{2+}	6.2–6.5	112 49 58 67 167
CNF-$(PO(OH)_2)_2$	VO_3^{-}	2	194
CNF-NH_2 (reaction with APTES)	Ni(II) Cu(II) Cd(II)	5	179 163 388
NC-$ROCS_2$—Na (reaction with C2)	Cd(II)	6	154
CNC-NH_2 (reaction with $K_2S_2O_8$ and ethylenediamine)	Cr(VI)		3
BC-NH_2 (reaction with epichlrorhydrin and diethylenetramine)	Pb^{2+} Cu^{2+}	4.5	84 63
CNC-NH_2 (grafting with PEG-NH_2)	Hg^{2+}		
CNC-$CONH_2$ (grafting of isopropylacrylamide)	Hg^{2+}		
CNC-PLA (grafting)	Cu^{2+} Ni^{2+} Cd^{2+} Pb^{2+}	4.9 5.9 5.7 4.5	
TEMPO CNF-PEI	Cu^{2+}	5	52.3
CNF-CMC (crosslinked using butanetetracarboxylic acid)	Ag^{+} Cu^{2+} Pb^{2+} Hg^{2+}		106 74.8 111.5 131.4

are not just limited to adsorption based on ionic interactions. Wang and coworkers have demonstrated that amine functionalized cellulose, synthesized by reacting the bacterial cellulose with epichlorhydrin and diethylenetramine, can adsorb cations through coordination interactions.[21] The amine functionalized materials showed maximum adsorption uptake capacities of 63 mg of Cu^{2+} per gram of cellulose and 87 mg of Pb^{2+} per gram of cellulose at a pH value of 4.5. However, the coordination interactions are disrupted at lower pHs when the amine groups are protonated.[21]

In addition to removing heavy metal, studies have also been conducted to adsorb charged organic dyes such as Methylene Blue and Crystal Violet.[62,196,199,204–206] For example, studies have been conducted by Tam and coworkers to compare the methylene blue uptake capacity of TEMPO oxidized CNCs to the methylene blue uptake capacity of sulfate functionalized CNCs.[204] The study found that at pH 9 the carboxylate functionalized CNCs exhibited significantly higher maximum uptake capacity of 769 mg of methylene blue per gram of CNC when compared 118 mg of methylene blue per gram of CNC for the sulfate functionalized CNCs.[204] In addition to targeting cationic dyes, studies have utilized cationic charged nanocellulose to adsorb anionic dyes from solution as well.[207–210] As reported in Jin et al., cationic CNCs can be prepared through sodium periodate oxidation and subsequent functionalization with ethylenediamine to introduce amine groups on the surface of the CNCs. These cationic CNCs were then shown to adsorb up to 556 mg of acid red GR per gram of CNC. The adsorption capacity of these cationic CNC sorbents exhibits a pH dependency based on the pH-dependent dissociation of the amine functional groups which results in maximum adsorption at low pH and a significant decrease in the uptake capacity at pH values of 8 or higher once the amine groups are no longer charged.[207] In addition to organic dyes, nanocellulose based sorbents have also been used to target other organic molecules like pharmaceuticals.[211–214] Rathod et al. has demonstrated that sulfate functionalized CNCs can be used to adsorb tetracycline hydrochloride, one of the most used antibiotics, from water with a maximum uptake capacity of 7 mg/g at pH 5.[211] While these studies have shown that nanocellulose holds great promise for use as a sorbent material, the structure and mechanisms driving these adsorption properties have not been thoroughly explored, limiting the ability to optimize and design a new generation of cellulose based sorbents. Chapter 2 of this thesis will focus on

investigating the fundamental structure of metal ion adsorption onto CNCs to partially fill in this gap in the literature.

1.3.2 Membrane Filtration

Another common method of water purification is membrane filtration, as it typically exhibits a sufficiently high separation efficiency to provide high quality water with low chemical sludge effluent.[170] Membrane filtration often relies on porous films to separate contaminants from water through either size exclusion, which depends on the membrane's microstructure, or adsorption, which targets specific solutes based on the surface chemistry of the membrane.[170,176,215–218] Filtration membranes are classified into different regimes based on their pore sizes, i.e. microfiltration (5 to 0.1 μm), ultrafiltration (0.1 to 0.01 μm), nanofiltration (0.01 to 0.001 μm), or reverse osmosis membranes (0.001 to 0.0001 μm or nonporous).[170,219] These pore sizes in turn determine the types of contaminants that each membrane can remove. For example, ultrafiltration membranes are suitable for the removal of bio-based contaminants such as viruses or proteins from water.[170,219,220] However, there are several challenges that must be resolved in order for membrane filtration technology to fully meet the growing demand for potable water. Some of these challenges include improved water permeability, membrane stability, environmental impact, fouling, and water solute selectivity.[65,170,221]

Typical materials used for ultrafiltration membranes include cellulose derivatives,[222–226] inorganic ceramics, and organic polymers like polyacrylonitrile (PAN),[227,228] polysulfone amides (PSA),[170] polysulfone (PSU),[229] polyether sulfone (PES),[230] and polyvinylidene fluoride (PVDF).[170,176,215,220,231,232] While membranes synthesized from these polymers typically exhibit good water permeability, high selectivity for the permeate, strong mechanical stability, and chemical resistance, they still have some significant drawbacks. Many of these membrane

materials are produced using chemicals from petroleum-based sources, often requiring a significant number of organic solvents and small molecule components to manufacture functional membranes.[233,234] Even when materials like cellulose acetate are produced from renewable feed stocks, they must be chemically modified and fabricated into membranes, an energy intensive process that still requires large amounts of organic solvents.[189,235,236]

Additionally, most of these polymers are inherently hydrophobic, which means that the membranes have a strong tendency towards fouling. Fouling is the process of unwanted substances accumulating on the membrane surface or within the membrane pores. Since many membranes are hydrophobic in nature, many foulants are hydrophobic solutes or have hydrophobic regions in the case of many biofoulants, and thus these foulants adsorb onto the hydrophobic membrane surface.[237] As foulants build up on the membrane surface, the performance of the membrane declines leading to a shortening of the membrane's lifetime. As such, many studies have been conducted to improve the water permeation flux, fouling resistance, and life span of these membranes.[237–252] One common strategy to reduce membrane fouling is to increase the hydrophilicity of the membrane surface and as a result, reduce the hydrophobic interactions that lead to membrane fouling. For example, Deng and coworkers treated commercial nanofiltration membranes with a low-pressure NH_3 plasma in order to modify the membrane's surface.[247] The treated membranes exhibited increased surface hydrophilicity and demonstrated decreased bovine serum albumin adsorption. The negatively charged membrane surface created by the plasma treatment also mitigated humic acid attachment on the membrane surface.[247] In addition to treatments that improve the hydrophilicity of the membrane surface, other studies have investigated the incorporation of hydrophilic components into the membrane structure. As reported in Sinha *et al.*, poly(ethylene glycol) methyl ether was used as a hydrophilic polymer additive to

augment the properties of asymmetric polysulfone membranes, and as the molecular weight of the additive was increased from 550 Da to 5000 Da, the membrane's hydrophilicity and the porosity of the resulting membranes also increased leading to higher water flux.[250]

An alternative to hydrophilic polymers that has been used to enhance the water transport through membranes is nanocellulose. Previous investigations incorporating nanocellulose into the barrier layers of membranes have blended the nanocellulose into a second barrier layer polymer. For example, Chu and coworkers incorporated cellulose nanofibers into poly(vinyl alcohol) barrier layers showing that the inclusion of the nanofibers increased the flux through the membrane by ten-fold based on the introduction of more directed water channels along the cellulose nanofiber network.[253] Additional studies have investigated the potential of nanocellulose as the sole component of the membrane barrier layer. Many of these membranes focused on the removal of charged contaminants like metal ions or organic dyes from solution and were able to enhance the separation efficiency of the membranes by leveraging the functionality of the nanocellulose.[62,63,65,254,255] However, Mautner *et al.* has shown that size exclusion based ultrafiltration membranes can be fabricated from nanocellulose without being blended with a polymer.[256] Membranes were fabricated from nanocellulose derived from multiple biosources such as bacteria or wood so that the dimensions of the nanocellulose would vary. The resulting membranes exhibited molecular weight cut-offs ranging from 6 kDa to 25 kDa, which correspond to average pore sizes of a few nanometers and is in the range of ultrafiltration membranes. The exact pore size was shown to be dependent on the size of the nanocellulose used in the fabrication of the membrane with larger diameter nanoparticles leading to larger pore sizes.[256] The potential of nanocellulose based membranes has been demonstrated, and the two-component CNC membranes and the CNC only membranes each exhibit promising water purification properties.

Polymer-grafted CNCs as OCN membranes has not been thoroughly investigated; in Chapter 3 of this thesis, I will investigate this design space. By using PGNs, membranes with high CNC content can be fabricated with the additional benefits provided by the tethered polymers.

1.4 Fluid Dynamics through Wicking Materials

In addition to enhancing water purification, nanocellulose holds great potential for improving moisture management in composite materials. Moisture management is defined as the ability of a garment to transport moisture away from one side of the material to the opposite surface.[257] The moisture management performance of fabrics is dictated by the mechanisms of wetting, wicking, and water vapor transmission. Wetting is the ability of a liquid to maintain contact with a solid surface and is determined by the intermolecular interactions between the liquid and the solid.[258,259] The wettability of the textile fibers also determines the initial imbibition of fluid into the woven structure. Wicking is the spontaneous transfer of liquid into a porous structure by capillary action.[260,261] Once the fibers are in contact with the solution, wicking can occur; therefore, a liquid that does not wet the fibers cannot be wicked through the material.[260]

Fibrous materials can also enable water vapor transport in addition to liquid transport. Breathability is an important characteristic for many fabrics as it is an essential component to wearer comfort. Walsh and coworkers demonstrated that vapor transport is the dominant form of moisture transport when the moisture content is low and wicking did not occur until moisture content was above 30% of regain, which the amount of water uptake upon a second wetting cycle after the garment has been dried.[262] These water transport properties of the fabric are influenced by the composition of the fibers, the structure of the fibers, and the chemical treatment of the fabric.[257,260–272] For example, Araujo and coworkers evaluated the effect of fiber cross-sectional shape as well as the fiber diameter on both the water vapor transmission and the wicking

capabilities of fabric.[269] When manipulating the size and shape of the fiber cross-section, it was found that any increase in the specific surface area of the fiber lead to an increase in wicking rates, while the increase in specific surface area decreased the water vapor permeability.[269]

As reported in Das *et al.*, the hydrophilicity of the fabric has a significant impact on the water transport properties of the material.[271] By blending polyester fibers with viscose fibers, the hydrophilicity of the fabric was varied and then the water vapor transport and wicking properties were tested. The study found that as the number of hydrophilic fibers in the fabric increased, the absorbency and water vapor permeability of the fabric also increased; however, the increase in hydrophilic character of the fabric appeared to have an adverse effect of the wicking rate through the material.[271]

Natural fibers can also have a large impact on a fabric's water management capabilities depending on the type of fiber selected. Cotton is often considered the most classic fiber in garment technology.[260] The versatility, softness, and comfort of cotton have encouraged its use in a wide variety of applications. However, cotton's high absorbency and tendency to retain water mean that cotton fibers exhibit poor wicking characeristics.[266] Wool is another natural fiber that is commonly used to make fabrics. Natural wool exhibits excellent breathability, i.e. water vapor transport properties, and water repellant qualities due to the wool fiber being composed of a hydroscopic interior surrounded by a hydrophobic exterior coating.[273] Wool can be treated through chlorination to remove the waxy coating around the wool fiber, which makes the surface hydrophilic.[274,275] Treated wool is an ideal wicking fabric, as the hydrophobic cuticle of the fiber minimizes absorption of water, while the hydrophilic protein sheath around the fiber enables rapid water transport between fibers as a result of capillary action.[274–279]

In addition to natural fibers, several synthetic polymers have been used to create fibers for fabric manufacturing. While many trademarked formulations and specifically structured fibers are employed in textile manufacturing, the most common synthetic polymers tend to be polyester, polypropylene, and nylon.[266] Polyester is commonly used in base fabrics for active-wear because of its low moisture absorption, leading to desirable wicking properties. Polypropylene is regarded as a key component in moisture management due to its hydrophobic nature. Nylon fibers also exhibit good wicking behavior but have low vapor permeability.[266] However, no one fiber exhibits all of the desired properties for a garment, so fabrics are usually composed of blends of fibers to engineer the material to meet the demands of specific applications.[260]

While fibrous moisture management fabrics that promote sweat wicking away from the skin are well-known and commercially available, these materials lack other properties needed in a number of applications. For example, prothesis liners commonly use materials like silicone and polyurethane elastomers that provide mechanical protection that moisture wicking fabrics lack.[280] However, these materials trap moisture in the socket as their low water permeability prevents moisture from evaporating.[281] Thus, while moisture management along the residual limb is an essential consideration for the comfort, performance, and health of prosthesis wearers, the current industry standards for prothesis liners provide no such accommodation.[280–285] The moisture build-up in the liner is not only uncomfortable for the patient, but can also lead to skin breakdown as the moisture softens the skin. In addition, moisture build up can result in a poor fit for the prosthesis, which can result in severe consequences such as slippage, skin irritation and skin lesions.[281,282,285,286] The resulting wounds can become especially problematic as the moist environment provides an ideal breeding ground for bacteria that can lead to infection of the patient.

Investigations into wicking through dense polymer films with robust mechanical properties are of interest in this field. Some groups have developed breathable polymeric materials for use as socket liners that allow the water vapor to escape the socket.[287,288] These methods for creating breathable liners involve introducing perforations along the liner through which moisture can escape. While these breathable perforations improve moisture management, they can compromise the mechanical properties and durability of the liner, which results in physical discomfort for the patient as the stresses from the prosthesis are inadequately dissipated.[286]

1.5 Heat Transfer in Active Thermal Materials

In addition to mass transfer and fluid mechanics, another type of transport phenomena where CNCs may be of interest is heat transfer; specifically, their use to enhance the thermal properties of composite materials. Active control of thermal transport has the potential to revolutionize thermal management in fields as diverse as electronics, building materials, and textiles. Whereas current design practice relies predominantly on passive thermal elements such as thermal resistance (e.g., insulation) or capacitance (thermal mass), active thermal elements such as thermal diodes, regulators, and switches, (Figure 1.3) would open new control approaches that could lead to increased energy efficiency and performance.[289] Thermal diodes allow heat to pass in only one direction. Thermal regulators attempt to maintain a fixed temperature by varying conductance between two states. Thermal switches permit or restrict heat flow based on the state of the switch. A thermal switch is characterized by the ratio of the thermal conductivity between the 'on' and 'off' states. Conduction-based thermal switches rely on changes in thermal conductivity to regulate heat flow through a material and utilize mechanisms such as phase transitions to accomplish this heat flow control. Representative implementations of this approach have made use of metal-insulator transitions,[290] solid-solid transitions,[291] solid-liquid transitions,[292] and miscibility limits

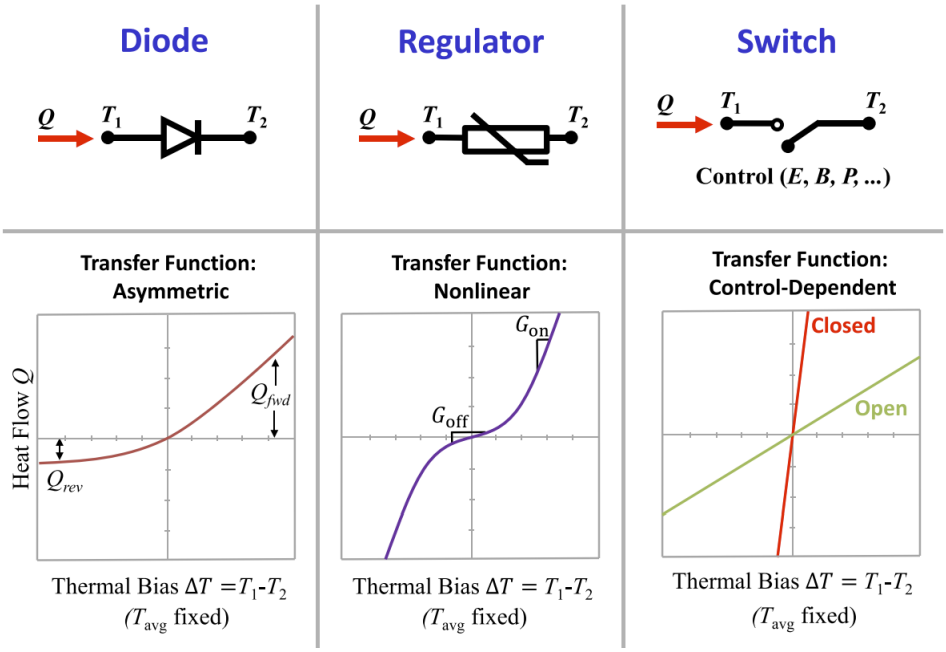

Figure 1.3. Nonlinear and switchable thermal components. Thermal devices such as diodes, regulators, and switches are defined by their transfer functions, which relate the heat flow Q to the thermal bias, analogous to current-voltage curves in the electrical domain. Thermal diodes have asymmetric heat transfer such that the magnitudes of the forward and reverse heat transfer rates Q differ. Regulators have a strongly nonlinear transfer function, which can be symmetric or asymmetric. The transfer function of a thermal switch depends on a non-thermal control parameter such as electric field (E), magnetic field (B), or pressure (P). Adapted from Wehmeyer *et al.*[289]

in aqueous polymer solutions.[293] For example, Tian and coworkers engineered a fast thermal switching material by leveraging the abrupt second-order phase transitions seen in thermoresponsive polymer aqueous solutions to create a thermal switch that exhibited a switching ratio of up to 1.15 across the transition.[293]

Studies of semicrystalline polymers have shown that the thermal conductivity is influenced by temperature, polymer chain alignment, and the degree of crystallinity in the polymer.[294,295] High thermal conductivity values have been measured for ultra-drawn polyethylene.[296] These high values have been attributed to polymer chain alignment and the elimination of material defects as

a result of stretching the polymer. These reported values of thermal conductivity approach the theoretical limit of defect-free polyethylene.[297]

In addition to manipulating the polymer to influence the thermal conductivity of the material, nanomaterials such as CNCs can be added to the polymer matrix to enhance the thermal properties of the composite. On account of their high crystallinity, CNCs have been shown to exhibit a relatively high thermal conductivity (1-6 W/mK) for an organic material.[298–300] Additionally, Youngblood and coworkers have shown that CNCs can enhance the thermal stability of composite materials when dispersed in a polymer matrix like polyurethane.[301]

1.6 References

(1) Nasrollahzadeh, M.; Sajjadi, M.; Iravani, S.; Varma, R. S. Starch, Cellulose, Pectin, Gum, Alginate, Chitin and Chitosan Derived (Nano)Materials for Sustainable Water Treatment: A Review. *Carbohydr Polym* **2021**, *251*, 116986. https://doi.org/10.1016/J.CARBPOL.2020.116986.

(2) Cudjoe, E.; Hunsen, M.; Xue, Z.; Way, A. E.; Barrios, E.; Olson, R. A.; Hore, M. J. A.; Rowan, S. J. Miscanthus Giganteus: A Commercially Viable Sustainable Source of Cellulose Nanocrystals. *Carbohydr Polym* **2017**, *155*, 230–241. https://doi.org/10.1016/J.CARBPOL.2016.08.049.

(3) Habibi, Y.; Lucia, L. A.; Rojas, O. J. Cellulose Nanocrystals: Chemistry, Self-Assembly, and Applications. *Chem Rev* **2010**, *110* (6), 3479–3500. https://doi.org/https://doi.org/10.1021/cr900339w.

(4) Klemm, D.; Heublein, B.; Fink, H. P.; Bohn, A. Cellulose: Fascinating Biopolymer and Sustainable Raw Material. *Angewandte Chemie International Edition* **2005**, *44* (22), 3358–3393. https://doi.org/10.1002/ANIE.200460587.

(5) Belton, P. S.; Tanner, S. F.; Cartier, N.; Chanzy, H. High-Resolution Solid-State 13C Nuclear Magnetic Resonance Spectroscopy of Tunicin, an Animal Cellulose. *Macromolecules* **1989**, *22* (4), 1615–1617. https://doi.org/10.1021/MA00194A019/ASSET/MA00194A019.FP.PNG_V03.

(6) Adriana Šturcová, †; Geoffrey R. Davies, ‡ and; Stephen J. Eichhorn*, †. Elastic Modulus and Stress-Transfer Properties of Tunicate Cellulose Whiskers. **2005**. https://doi.org/10.1021/BM049291K.

(7) Helbert, W.; Nishiyama, Y.; Okano, T.; Sugiyama, J. Molecular Imaging of Halocynthia Papillosa Cellulose. *J Struct Biol* **1998**, *124* (1), 42–50. https://doi.org/10.1006/JSBI.1998.4045.

(8) Iwamoto, S.; Kai, W.; Isogai, A.; Iwata, T. Elastic Modulus of Single Cellulose Microfibrils from Tunicate Measured by Atomic Force Microscopy. *Biomacromolecules* **2009**, *10* (9), 2571–2576. https://doi.org/10.1021/bm900520n.

(9) Kimura, S.; Itoh, T. New Cellulose Synthesizing Complexes (Terminal Complexes) Involved in Animal Cellulose Biosynthesis in the Tunicate Metandrocarpa Uedai. *Protoplasma* **1996**, *194* (3–4), 151–163. https://doi.org/10.1007/BF01882023/METRICS.

(10) Kimura, S.; Itoh, T. Cellulose Synthesizing Terminal Complexes in the Ascidians. *Cellulose 2004 11:3* **2004**, *11* (3), 377–383. https://doi.org/10.1023/B:CELL.0000046414.72903.33.

(11) Chen, Y. W.; Lee, H. V.; Juan, J. C.; Phang, S. M. Production of New Cellulose Nanomaterial from Red Algae Marine Biomass Gelidium Elegans. *Carbohydr Polym* **2016**, *151*, 1210–1219. https://doi.org/10.1016/J.CARBPOL.2016.06.083.

(12) Hua, K.; Carlsson, D. O.; Ålander, E.; Lindström, T.; Strømme, M.; Mihranyan, A.; Ferraz, N. Translational Study between Structure and Biological Response of Nanocellulose from Wood and Green Algae. *RSC Adv* **2013**, *4* (6), 2892–2903. https://doi.org/10.1039/C3RA45553J.

(13) Imai, T.; Sugiyama, J. Nanodomains of Iα and Iβ Cellulose in Algal Microfibrils. *Macromolecules* **1998**, *31* (18), 6275–6279. https://doi.org/10.1021/MA980664H.

(14) Hanley, S. J.; Giasson, J.; Revol, J. F.; Gray, D. G. Atomic Force Microscopy of Cellulose Microfibrils: Comparison with Transmission Electron Microscopy. *Polymer (Guildf)* **1992**, *33* (21), 4639–4642. https://doi.org/10.1016/0032-3861(92)90426-W.

(15) Sugiyama, J.; Harada, H.; Fujiyoshi, Y.; Uyeda, N. Lattice Images from Ultrathin Sections of Cellulose Microfibrils in the Cell Wall of Valonia Macrophysa Kütz. *Planta* **1985**, *166* (2), 161–168. https://doi.org/10.1007/BF00397343/METRICS.

(16) Revol, J. F. On the Cross-Sectional Shape of Cellulose Crystallites in Valonia Ventricosa. *Carbohydr Polym* **1982**, *2* (2), 123–134. https://doi.org/10.1016/0144-8617(82)90058-3.

(17) Hanley, S. J.; Revol, J. F.; Godbout, L.; Gray, D. G. Atomic Force Microscopy and Transmission Electron Microscopy of Cellulose from Micrasterias Denticulata; Evidence for a Chiral Helical Microfibril Twist. *Cellulose* **1997**, *4* (3), 209–220. https://doi.org/10.1023/A:1018483722417/METRICS.

(18) Kim, N. H.; Herth, W.; Vuong, R.; Chanzy, H. The Cellulose System in the Cell Wall OfMicrasterias. *J Struct Biol* **1996**, *117* (3), 195–203. https://doi.org/10.1006/JSBI.1996.0083.

(19) Yang, Y.; Lu, Y. T.; Zeng, K.; Heinze, T.; Groth, T.; Zhang, K. Recent Progress on Cellulose-Based Ionic Compounds for Biomaterials. *Advanced Materials* **2021**, *33* (28), 2000717. https://doi.org/10.1002/ADMA.202000717.

(20) Elsacker, E.; Vandelook, S.; Van Wylick, A.; Ruytinx, J.; De Laet, L.; Peeters, E. A Comprehensive Framework for the Production of Mycelium-Based Lignocellulosic Composites. *Science of The Total Environment* **2020**, *725*, 138431. https://doi.org/10.1016/J.SCITOTENV.2020.138431.

(21) Shen, W.; Chen, S.; Shi, S.; Li, X.; Zhang, X.; Hu, W.; Wang, H. Adsorption of Cu(II) and Pb(II) onto Diethylenetriamine-Bacterial Cellulose. *Carbohydr Polym* **2009**, *75* (1), 110–114. https://doi.org/10.1016/J.CARBPOL.2008.07.006.

(22) Cai, Z.; Kim, J. Bacterial Cellulose/Poly(Ethylene Glycol) Composite: Characterization and First Evaluation of Biocompatibility. *Cellulose* **2010**, *17* (1), 83–91. https://doi.org/10.1007/s10570-009-9362-5.

(23) Lee, K.-Y.; Buldum, G.; Mantalaris, A.; Bismarck, A. More Than Meets the Eye in Bacterial Cellulose: Biosynthesis, Bioprocessing, and Applications in Advanced Fiber Composites. *Macromol Biosci* **2014**, *14* (1), 10–32. https://doi.org/10.1002/mabi.201300298.

(24) Bacterial Cellulose: The Ultimate Nano-Scalar Cellulose Morphology for the Production of High-Strength Composites. https://doi.org/10.1007/s00339-004-2932-3.

(25) Tokoh, C.; Takabe, K.; Fujita, M.; Saiki, H. Cellulose Synthesized by Acetobacter Xylinum in the Presence of Acetyl Glucomannan. *Cellulose* **1998**, *5* (4), 249–261. https://doi.org/10.1023/A:1009211927183/METRICS.

(26) Jonas, R.; Farah, L. F. Production and Application of Microbial Cellulose. *Polym Degrad Stab* **1998**, *59* (1–3), 101–106. https://doi.org/10.1016/S0141-3910(97)00197-3.

(27) *Isolation and characterization of cellulose nanocrystals from Agave angustifolia fibre :: BioResources*. https://bioresources.cnr.ncsu.edu/resources/isolation-and-characterization-of-cellulose-nanocrystals-from-agave-angustifolia-fibre/ (accessed 2023-09-22).

(28) Mueller, S.; Weder, C.; Foster, E. J. Isolation of Cellulose Nanocrystals from Pseudostems of Banana Plants. *RSC Adv* **2013**, *4* (2), 907–915. https://doi.org/10.1039/C3RA46390G.

(29) Araki, J.; Wada, M.; Kuga, S.; Okano, T. Flow Properties of Microcrystalline Cellulose Suspension Prepared by Acid Treatment of Native Cellulose. *Colloids Surf A Physicochem Eng Asp* **1998**, *1* (142), 75–82. https://doi.org/10.1016/S0927-7757(98)00404-X.

(30) Hess-Dunning, A. E.; Tyler, D. J.; Harris, J. P.; Capadona, J. R.; Weder, C.; Rowan, S. J.; Zorman, C. A. Microscale Characterization of a Mechanically Adaptive Polymer Nanocomposite With Cotton-Derived Cellulose Nanocrystals for Implantable BioMEMS. *Journal of Microelectromechanical Systems* **2014**, *23* (4), 774–784. https://doi.org/10.1109/JMEMS.2014.2327035.

(31) Shanmuganathan, K.; Capadona, J. R.; Rowan, S. J.; Weder, C. Bio-Inspired Mechanically-Adaptive Nanocomposites Derived from Cotton Cellulose Whiskers. **2010**, *20* (1), 180–186. https://doi.org/10.1039/b916130a.

(32) Elazzouzi-Hafraoui, S.; Nishiyama, Y.; Putaux, J. L.; Heux, L.; Dubreuil, F.; Rochas, C. The Shape and Size Distribution of Crystalline Nanoparticles Prepared by Acid Hydrolysis of Native Cellulose. *Biomacromolecules* **2008**, *9* (1), 57–65. https://doi.org/10.1021/BM700769P/SUPPL_FILE/BM700769P-FILE003.PDF.

(33) Saito, T.; Nishiyama, Y.; Putaux, J. L.; Vignon, M.; Isogai, A. Homogeneous Suspensions of Individualized Microfibrils from TEMPO-Catalyzed Oxidation of Native Cellulose. *Biomacromolecules* **2006**, *7* (6), 1687–1691. https://doi.org/https://doi.org/10.1021/bm060154s.

(34) Habibi, Y.; Dufresne, A. Highly Filled Bionanocomposites from Functionalized Polysaccharide Nanocrystals. *Biomacromolecules* **2008**, *9* (7), 1974–1980. https://doi.org/10.1021/bm8001717.

(35) Garcia de Rodriguez, N. L.; Thielemans, W.; Dufresne, A. Sisal Cellulose Whiskers Reinforced Polyvinyl Acetate Nanocomposites. *Cellulose* **2006**, *13* (3), 261–270. https://doi.org/10.1007/S10570-005-9039-7/METRICS.

(36) Siaueira, G.; Bras, J.; Dufresne, A. Cellulose Whiskers versus Microfibrils: Influence of the Nature of the Nanoparticle and Its Surface Functionalization on the Thermal and Mechanical Properties of Nanocomposites. *Biomacromolecules* **2009**, *10* (2), 425–432. https://doi.org/https://doi.org/10.1021/bm801193d.

(37) Cao, X.; Dong, H.; Li, C. M. New Nanocomposite Materials Reinforced with Flax Cellulose Nanocrystals in Waterborne Polyurethane. *Biomacromolecules* **2007**, *8* (3), 899–904. https://doi.org/https://doi.org/10.1021/bm0610368.

(38) Alemdar, A.; Sain, M. Isolation and Characterization of Nanofibers from Agricultural Residues – Wheat Straw and Soy Hulls. *Bioresour Technol* **2008**, *99* (6), 1664–1671. https://doi.org/10.1016/J.BIORTECH.2007.04.029.

(39) Zimmermann, T.; Bordeanu, N.; Strub, E. Properties of Nanofibrillated Cellulose from Different Raw Materials and Its Reinforcement Potential. *Carbohydr Polym* **2010**, *79* (4), 1086–1093. https://doi.org/10.1016/J.CARBPOL.2009.10.045.

(40) Hong, Y.; Zhang, Y.; Zhu, L.; Gu, Z. Study on Physicochemical Characteristics of Waxy Potato Starch in Comparison with Other Waxy Starches. *Starch/Staerke* **2011**, *63* (12), 754–759. https://doi.org/10.1002/STAR.201100013.

(41) Leitner, J.; Hinterstoisser, B.; Wastyn, M.; Keckes, J.; Gindl, W. Sugar Beet Cellulose Nanofibril-Reinforced Composites. *Cellulose* **2007**, *14* (5), 419–425. https://doi.org/10.1007/S10570-007-9131-2/FIGURES/7.

(42) Zhang, T.; Zheng, Y.; Cosgrove, D. J. Spatial Organization of Cellulose Microfibrils and Matrix Polysaccharides in Primary Plant Cell Walls as Imaged by Multichannel Atomic Force Microscopy. *Plant Journal* **2016**, *85* (2), 179–192. https://doi.org/10.1111/TPJ.13102.

(43) Samir, M. A. S. A.; Alloin, F.; Paillet, M.; Dufresne, A. Tangling Effect in Fibrillated Cellulose Reinforced Nanocomposites. *Macromolecules* **2004**, *37* (11), 4313–4316. https://doi.org/10.1021/MA035939U/ASSET/MA035939U.FP.PNG_V03.

(44) Wang, B.; Sain, M. Isolation of Nanofibers from Soybean Source and Their Reinforcing Capability on Synthetic Polymers. *Compos Sci Technol* **2007**, *67* (11–12), 2521–2527. https://doi.org/10.1016/J.COMPSCITECH.2006.12.015.

(45) Zuluaga, R.; Putaux, J. L.; Restrepo, A.; Mondragon, I.; Gañán, P. Cellulose Microfibrils from Banana Farming Residues: Isolation and Characterization. *Cellulose* **2007**, *14* (6), 585–592. https://doi.org/10.1007/S10570-007-9118-Z/FIGURES/7.

(46) Capron, I.; Rojas, O. J.; Bordes, R. Behavior of Nanocelluloses at Interfaces. *Current Opinion in Colloid and Interface Science*. 2017. https://doi.org/10.1016/j.cocis.2017.04.001.

(47) Klemm, D.; Cranston, E. D.; Fischer, D.; Gama, M.; Kedzior, S. A.; Kralisch, D.; Kramer, F.; Kondo, T.; Lindström, T.; Nietzsche, S.; Petzold-Welcke, K.; Rauchfuß, F. Nanocellulose as a Natural Source for Groundbreaking Applications in Materials Science: Today's State. *Materials Today*. 2018. https://doi.org/10.1016/j.mattod.2018.02.001.

(48) Dufresne, A. Nanocellulose: A New Ageless Bionanomaterial. *Materials Today* **2013**, *16* (6), 220–227. https://doi.org/10.1016/J.MATTOD.2013.06.004.

(49) Yarbrough, J. M.; Zhang, R.; Mittal, A.; Vander Wall, T.; Bomble, Y. J.; Decker, S. R.; Himmel, M. E.; Ciesielski, P. N. Multifunctional Cellulolytic Enzymes Outperform Processive Fungal Cellulases for Coproduction of Nanocellulose and Biofuels. *ACS Nano* **2017**, *11* (3), 3101–3109. https://doi.org/10.1021/acsnano.7b00086.

(50) Klemm, D.; Kramer, F.; Moritz, S.; Lindström, T.; Ankerfors, M.; Gray, D.; Dorris, A. Nanocelluloses: A New Family of Nature-Based Materials. *Angewandte Chemie International Edition* **2011**, *50* (24), 5438–5466. https://doi.org/10.1002/ANIE.201001273.

(51) Yang, H.; Zhang, Y.; Kato, R.; Rowan, S. J. Preparation of Cellulose Nanofibers from Miscanthus x. Giganteus by Ammonium Persulfate Oxidation. *Carbohydr Polym* **2019**, *212*. https://doi.org/10.1016/j.carbpol.2019.02.008.

(52) Cho, S. Y.; Yu, H.; Choi, J.; Kang, H.; Park, S.; Jang, J. S.; Hong, H. J.; Kim, I. D.; Lee, S. K.; Jeong, H. S.; Jung, H. T. Continuous Meter-Scale Synthesis of Weavable Tunicate Cellulose/Carbon Nanotube Fibers for High-Performance Wearable Sensors. *ACS Nano* **2019**, *13* (8), 9332–9341. https://doi.org/10.1021/acsnano.9b03971.

(53) Jia, C.; Chen, C.; Kuang, Y.; Fu, K.; Wang, Y.; Yao, Y.; Kronthal, S.; Hitz, E.; Song, J.; Xu, F.; Liu, B.; Hu, L. From Wood to Textiles: Top-Down Assembly of Aligned Cellulose Nanofibers. *Advanced Materials* **2018**, *30* (30), 1801347. https://doi.org/10.1002/ADMA.201801347.

(54) Chen, C.; Hu, L. Nanocellulose toward Advanced Energy Storage Devices: Structure and Electrochemistry. *Acc Chem Res* **2018**, *51* (12), 3154–3165. https://doi.org/https://doi.org/10.1021/acs.accounts.8b00391.

(55) Kato, R.; Lettow, J. H.; Patel, S. N.; Rowan, S. J. Ion-Conducting Thermoresponsive Films Based on Polymer-Grafted Cellulose Nanocrystals. *ACS Appl Mater Interfaces* **2020**, *12* (48), 54083–54093. https://doi.org/10.1021/acsami.0c16059.

(56) Lettow, J. H.; Kaplan, R. Y.; Nealey, P. F.; Rowan, S. J. Enhanced Ion Conductivity through Hydrated, Polyelectrolyte-Grafted Cellulose Nanocrystal Films. *Macromolecules* **2021**, *54* (14), 6925–6936. https://doi.org/10.1021/ACS.MACROMOL.1C01155.

(57) Abdul Khalil, H. P. S.; Adnan, A. S.; Yahya, E. B.; Olaiya, N. G.; Safrida, S.; Hossain, M. S.; Balakrishnan, V.; Gopakumar, D. A.; Abdullah, C. K.; Oyekanmi, A. A.; Pasquini, D. A Review on Plant Cellulose Nanofibre-Based Aerogels for Biomedical Applications. *Polymers 2020, Vol. 12, Page 1759* **2020**, *12* (8), 1759. https://doi.org/10.3390/POLYM12081759.

(58) Sheikhi, A.; Hayashi, J.; Eichenbaum, J.; Gutin, M.; Kuntjoro, N.; Khorsandi, D.; Khademhosseini, A. Recent Advances in Nanoengineering Cellulose for Cargo Delivery. *Journal of Controlled Release* **2019**, *294*, 53–76. https://doi.org/10.1016/J.JCONREL.2018.11.024.

(59) Weiss, A. M.; MacKe, N.; Zhang, Y.; Calvino, C.; Esser-Kahn, A. P.; Rowan, S. J. In Vitro and in Vivo Analyses of the Effects of Source, Length, and Charge on the Cytotoxicity and Immunocompatibility of Cellulose Nanocrystals. *ACS Biomater Sci Eng* **2021**, *7* (4), 1450–1461. https://doi.org/10.1021/acsbiomaterials.0c01618.

(60) Khan, A.; Huq, T.; Khan, R. A.; Riedl, B.; Lacroix, M. Nanocellulose-Based Composites and Bioactive Agents for Food Packaging. *Crit Rev Food Sci Nutr* **2014**, *54* (2), 163–174. https://doi.org/10.1080/10408398.2011.578765.

(61) Sirviö, J. A.; Kolehmainen, A.; Liimatainen, H.; Niinimäki, J.; Hormi, O. E. O. Biocomposite Cellulose-Alginate Films: Promising Packaging Materials. *Food Chem* **2014**, *151*, 343–351. https://doi.org/10.1016/J.FOODCHEM.2013.11.037.

(62) Voisin, H.; Bergström, L.; Liu, P.; Mathew, A. P. Nanocellulose-Based Materials for Water Purification. *Nanomaterials (Basel)* **2017**, *7* (3). https://doi.org/10.3390/nano7030057.

(63) Ma, H.; Burger, C.; Hsiao, B. S.; Chu, B. Ultrafine Polysaccharide Nanofibrous Membranes for Water Purification. **2011**. https://doi.org/10.1021/bm1013316.

(64) Thakur, V. K.; Voicu, S. I. Recent Advances in Cellulose and Chitosan Based Membranes for Water Purification: A Concise Review. *Carbohydr Polym* **2016**, *146*, 148–165. https://doi.org/10.1016/J.CARBPOL.2016.03.030.

(65) Ma, H.; Burger, C.; Hsiao, B. S.; Chu, B. Highly Permeable Polymer Membranes Containing Directed Channels for Water Purification. *ACS Macro Lett* **2012**, *1* (6), 723–726. https://doi.org/10.1021/mz300163h.

(66) Hokkanen, S.; Bhatnagar, A.; Sillanpää, M. A Review on Modification Methods to Cellulose-Based Adsorbents to Improve Adsorption Capacity. *Water Research*. 2016. https://doi.org/10.1016/j.watres.2016.01.008.

(67) Liu, L.; Gao, Z. Y.; Su, X. P.; Chen, X.; Jiang, L.; Yao, J. M. Adsorption Removal of Dyes from Single and Binary Solutions Using a Cellulose-Based Bioadsorbent. *ACS Sustain Chem Eng* **2015**, *3* (3), 432–442. https://doi.org/10.1021/sc500848m.

(68) O'Connell, D. W.; Birkinshaw, C.; O'Dwyer, T. F. Heavy Metal Adsorbents Prepared from the Modification of Cellulose: A Review. *Bioresour Technol* **2008**, *99* (15), 6709–6724. https://doi.org/10.1016/J.BIORTECH.2008.01.036.

(69) Kangas, H. Guide to Cellulose Nanomaterials- English Summary. **2014**.

(70) Trache, D.; Hussin, M. H.; Haafiz, M. K. M.; Thakur, V. K. Recent Progress in Cellulose Nanocrystals: Sources and Production. *Nanoscale* **2017**, *9* (5), 1763–1786. https://doi.org/10.1039/C6NR09494E.

(71) Moon, R. J.; Martini, A.; Nairn, J.; Simonsen, J.; Youngblood, J. Cellulose Nanomaterials Review: Structure, Properties and Nanocomposites. *Chem Soc Rev* **2011**, *40* (7), 3941–3994. https://doi.org/10.1039/C0CS00108B.

(72) Šturcova, A.; His, I.; Apperley, D. C.; Sugiyama, J.; Jarvis, M. C. Structural Details of Crystalline Cellulose from Higher Plants. *Biomacromolecules* **2004**, *5* (4), 1333–1339. https://doi.org/10.1021/BM034517P.

(73) Klemm, D.; Philipp, B.; Heinze, T.; Heinze, U.; Wagenknecht, W. Comprehensive Cellulose Chemistry: Volume I: Fundamentals and Analytical Methods. *Methods* **1998**, *I*, 260.

(74) Kim, J. H.; Shim, B. S.; Kim, H. S.; Lee, Y. J.; Min, S. K.; Jang, D.; Abas, Z.; Kim, J. Review of Nanocellulose for Sustainable Future Materials. *International Journal of Precision Engineering and Manufacturing - Green Technology* **2015**, *2* (2), 197–213. https://doi.org/10.1007/S40684-015-0024-9/METRICS.

(75) Rowland, S. P.; Howley, P. S. Hydrogen Bonding on Accessible Surfaces of Cellulose from Various Sources and Relationship to Order within Crystalline Regions. *J Polym Sci A Polym Chem* **1988**, *26* (7), 1769–1778. https://doi.org/10.1002/POLA.1988.080260708.

(76) Rowland, S. P.; Roberts, E. J. The Nature of Accessible Surfaces in the Microstructure of Cotton Cellulose. *J Polym Sci A1* **1972**, *10* (8), 2447–2461. https://doi.org/10.1002/POL.1972.150100819.

(77) Calvino, C.; Macke, N.; Kato, R.; Rowan, S. J. Development, Processing and Applications of Bio-Sourced Cellulose Nanocrystal Composites. *Prog Polym Sci* **2020**, *103*, 101221. https://doi.org/10.1016/J.PROGPOLYMSCI.2020.101221.

(78) Rånby, B. G.; Banderet, A.; Sillén, L. G. Aqueous Colloidal Solutions of Cellulose Micelles. *Acta Chem Scand* **1949**, *3*, 649–650. https://doi.org/10.3891/ACTA.CHEM.SCAND.03-0649.

(79) Camarero Espinosa, S.; Kuhnt, T.; Foster, E. J.; Weder, C. Isolation of Thermally Stable Cellulose Nanocrystals by Phosphoric Acid Hydrolysis. *Biomacromolecules* **2013**, *14* (4), 1223–1230. https://doi.org/10.1021/BM400219U.

(80) Zhao, Y.; Moser, C.; Lindström, M. E.; Henriksson, G.; Li, J. Cellulose Nanofibers from Softwood, Hardwood, and Tunicate: Preparation-Structure-Film Performance Interrelation. *ACS Appl Mater Interfaces* **2017**, *9* (15), 13508–13519. https://doi.org/10.1021/ACSAMI.7B01738.

(81) Isogai, A.; Saito, T.; Fukuzumi, H. TEMPO-Oxidized Cellulose Nanofibers. *Nanoscale* **2011**, *3* (1), 71–85. https://doi.org/10.1039/c0nr00583e.

(82) Habibi, Y.; Chanzy, H.; Vignon, M. R. TEMPO-Mediated Surface Oxidation of Cellulose Whiskers. *Cellulose* **2006**, *13* (6), 679–687. https://doi.org/10.1007/S10570-006-9075-Y/METRICS.

(83) Fraschini, C.; Chauve, G.; Bouchard, J. TEMPO-Mediated Surface Oxidation of Cellulose Nanocrystals (CNCs). *Cellulose* **2017**, *24* (7), 2775–2790. https://doi.org/10.1007/s10570-017-1319-5.

(84) Araki, J.; Wada, M.; Kuga, S. Steric Stabilization of a Cellulose Microcrystal Suspension by Poly(Ethylene Glycol) Grafting. *Langmuir* **2001**, *17* (1), 21–27. https://doi.org/10.1021/la001070m.

(85) Fox, J. D.; Capadona, J. R.; Marasco, P. D.; Rowan, S. J. Bioinspired Water-Enhanced Mechanical Gradient Nanocomposite Films That Mimic the Architecture and Properties of the Squid Beak. *J Am Chem Soc* **2013**, *135* (13), 5167–5174. https://doi.org/10.1021/JA4002713.

(86) Azzam, F.; Heux, L.; Putaux, J. L.; Jean, B. Preparation by Grafting onto, Characterization, and Properties of Thermally Responsive Polymer-Decorated Cellulose Nanocrystals. *Biomacromolecules* **2010**, *11* (12), 3652–3659. https://doi.org/10.1021/BM101106C.

(87) Harrisson, S.; Drisko, G. L.; Malmström, E.; Hult, A.; Wooley, K. L. Hybrid Rigid/Soft and Biologic/Synthetic Materials: Polymers Grafted onto Cellulose Microcrystals. *Biomacromolecules* **2011**, *12* (4), 1214–1223. https://doi.org/10.1021/BM101506J.

(88) Cudjoe, E.; Khani, S.; Way, A. E.; Hore, M. J. A.; Maia, J.; Rowan, S. J. Biomimetic Reversible Heat-Stiffening Polymer Nanocomposites. *ACS Cent Sci* **2017**, *3* (8), 886–894. https://doi.org/10.1021/ACSCENTSCI.7B00215.

(89) Way, A. E.; Hsu, L.; Shanmuganathan, K.; Weder, C.; Rowan, S. J. PH-Responsive Cellulose Nanocrystal Gels and Nanocomposites. *ACS Macro Lett* **2012**, *1* (8), 1001–1006. https://doi.org/10.1021/mz3003006.

(90) Dagnon, K. L.; Way, A. E.; Carson, S. O.; Silva, J.; Maia, J.; Rowan, S. J. Controlling the Rate of Water-Induced Switching in Mechanically Dynamic Cellulose Nanocrystal Composites. *Macromolecules* **2013**, *46* (20), 8203–8212. https://doi.org/10.1021/ma4008187.

(91) Zhang, Y.; Karimkhani, V.; Makowski, B. T.; Samaranayake, G.; Rowan, S. J. Nanoemulsions and Nanolatexes Stabilized by Hydrophobically Functionalized Cellulose Nanocrystals. *Macromolecules* **2017**, *50* (16), 6032–6042. https://doi.org/10.1021/acs.macromol.7b00982.

(92) Zhang, Y.; Yang, H.; Naren, N.; Rowan, S. J. Surfactant-Free Latex Nanocomposites Stabilized and Reinforced by Hydrophobically Functionalized Cellulose Nanocrystals. *ACS Appl Polym Mater* **2020**, *2* (6), 2291–2302. https://doi.org/10.1021/ACSAPM.0C00263/SUPPL_FILE/AP0C00263_SI_001.PDF.

(93) Lettow, J. H.; Yang, H.; Nealey, P. F.; Rowan, S. J. Effect of Graft Molecular Weight and Density on the Mechanical Properties of Polystyrene-Grafted Cellulose Nanocrystal Films. *Macromolecules* **2021**, *54* (22), 10594–10604. https://doi.org/10.1021/ACS.MACROMOL.1C01886.

(94) Macke, N.; Hemmingsen, C. M.; Rowan, S. J. The Effect of Polymer Grafting on the Mechanical Properties of PEG-Grafted Cellulose Nanocrystals in Poly(Lactic Acid). *Journal of Polymer Science* **2022**, *60* (24), 3318–3330. https://doi.org/10.1002/POL.20220127.

(95) Roy, D.; Semsarilar, M.; Guthrie, J. T.; Perrier, S. Cellulose Modification by Polymer Grafting: A Review. *Chem Soc Rev* **2009**, *38* (7), 2046–2064. https://doi.org/10.1039/B808639G.

(96) Roy, D.; Guthrie, J. T.; Bastien Perrier, S. Graft Polymerization: Grafting Poly(Styrene) from Cellulose via Reversible Addition-Fragmentation Chain Transfer (RAFT) Polymerization. https://doi.org/10.1021/ma0515026.

(97) Lin, N.; Chen, G.; Huang, J.; Dufresne, A.; Chang, P. R. Effects of Polymer-Grafted Natural Nanocrystals on the Structure and Mechanical Properties of Poly(Lactic Acid): A Case of Cellulose Whisker-Graft-Polycaprolactone. *J Appl Polym Sci* **2009**, *113* (5), 3417–3425. https://doi.org/10.1002/APP.30308.

(98) Chen, G.; Dufresne, A.; Huang, J.; Chang, P. R. A Novel Thermoformable Bionanocomposite Based on Cellulose Nanocrystal-Graft-Poly(ε-Caprolactone). *Macromol Mater Eng* **2009**, *294* (1), 59–67. https://doi.org/10.1002/MAME.200800261.

(99) Goffin, A. L.; Raquez, J. M.; Duquesne, E.; Siqueira, G.; Habibi, Y.; Dufresne, A.; Dubois, P. From Interfacial Ring-Opening Polymerization to Melt Processing of Cellulose Nanowhisker-Filled Polylactide-Based Nanocomposites. *Biomacromolecules* **2011**, *12* (7), 2456–2465. https://doi.org/10.1021/BM200581H.

(100) Habibi, Y.; Goffin, A. L.; Schiltz, N.; Duquesne, E.; Dubois, P.; Dufresne, A. Bionanocomposites Based on Poly(ε-Caprolactone)-Grafted Cellulose Nanocrystals by Ring-Opening Polymerization. *J Mater Chem* **2008**, *18* (41), 5002–5010. https://doi.org/10.1039/B809212E.

(101) Hsu, L.; Weder, C.; Rowan, S. J. Stimuli-Responsive, Mechanically-Adaptive Polymer Nanocomposites. *J Mater Chem* **2011**, *21* (9), 2812–2822. https://doi.org/10.1039/C0JM02383C.

(102) Bet-Moushoul, E.; Mansourpanah, Y.; Farhadi, K.; Tabatabaei, M. TiO2 Nanocomposite Based Polymeric Membranes: A Review on Performance Improvement for Various Applications in Chemical Engineering Processes. *Chemical Engineering Journal* **2016**, *283*, 29–46. https://doi.org/10.1016/J.CEJ.2015.06.124.

(103) Kumar, S. K.; Benicewicz, B. C.; Vaia, R. A.; Winey, K. I. 50th Anniversary Perspective: Are Polymer Nanocomposites Practical for Applications? *Macromolecules* **2017**, *50* (3), 714–731. https://doi.org/https://doi.org/10.1021/acs.macromol.6b02330.

(104) Kumar, A.; Sharma, K.; Dixit, A. R. A Review of the Mechanical and Thermal Properties of Graphene and Its Hybrid Polymer Nanocomposites for Structural Applications. *J Mater Sci* **2019**, *54* (8), 5992–6026. https://doi.org/10.1007/S10853-018-03244-3/TABLES/4.

(105) Hsieh, J. H.; Liu, P. C.; Li, C.; Cheng, M. K.; Chang, S. Y. Mechanical Properties of TaN-Cu Nanocomposite Thin Films. *Surf Coat Technol* **2008**, *202* (22–23), 5530–5534. https://doi.org/10.1016/J.SURFCOAT.2008.06.131.

(106) Crosby, A. J.; Lee, J. Y. Polymer Nanocomposites: The “Nano” Effect on Mechanical Properties. *Polymer Reviews* **2007**, *47* (2), 217–229. https://doi.org/10.1080/15583720701271278.

(107) Coulibaly, S.; Roulin, A.; Balog, S.; Biyani, M. V.; Foster, E. J.; Rowan, S. J.; Fiore, G. L.; Weder, C. Reinforcement of Optically Healable Supramolecular Polymers with Cellulose Nanocrystals. *Macromolecules* **2014**, *47* (1), 152–160. https://doi.org/10.1021/ma402143c.

(108) Yuan, H. ; Li, P. ; Wang, X. ; Zhao, H. ; Sun, J.; Yuan, H.; Li, P.; Wang, X.; Zhao, H.; Sun, J. Rod-like Cellulose Regenerated by Bottom-Up Assembly in Natural Rubber Latex and Its Reinforcement. *International Journal of Molecular Sciences 2023, Vol. 24, Page 6457* **2023**, *24* (7), 6457. https://doi.org/10.3390/IJMS24076457.

(109) Demirocak, D. E.; Srinivasan, S. S.; Stefanakos, E. K. A Review on Nanocomposite Materials for Rechargeable Li-Ion Batteries. *Applied Sciences 2017, Vol. 7, Page 731* **2017**, *7* (7), 731. https://doi.org/10.3390/APP7070731.

(110) Wang, Q.; Liu, S.; Liu, J.; Sun, J.; Zhang, Z.; Zhu, Q. Sustainable Cellulose Nanomaterials for Environmental Remediation - Achieving Clean Air, Water, and Energy: A Review. *Carbohydr Polym* **2022**, *285*. https://doi.org/10.1016/j.carbpol.2022.119251.

(111) Gadim, T. D. O.; Vilela, C.; Loureiro, F. J. A.; Silvestre, A. J. D.; Freire, C. S. R.; Figueiredo, F. M. L. Nafion® and Nanocellulose: A Partnership for Greener Polymer Electrolyte Membranes. *Ind Crops Prod* **2016**, *93*, 212–218. https://doi.org/10.1016/J.INDCROP.2016.01.028.

(112) Kim, D. J.; Jo, M. J.; Nam, S. Y. A Review of Polymer–Nanocomposite Electrolyte Membranes for Fuel Cell Application. *Journal of Industrial and Engineering Chemistry* **2015**, *21*, 36–52. https://doi.org/10.1016/J.JIEC.2014.04.030.

(113) Bassyouni, M.; Abdel-Aziz, M. H.; Zoromba, M. S.; Abdel-Hamid, S. M. S.; Drioli, E. A Review of Polymeric Nanocomposite Membranes for Water Purification. *Journal of Industrial and Engineering Chemistry* **2019**, *73*, 19–46. https://doi.org/10.1016/J.JIEC.2019.01.045.

(114) Ashraf, S.; Siddiqa, A.; Shahida, S.; Qaisar, S. Titanium-Based Nanocomposite Materials for Arsenic Removal from Water: A Review. *Heliyon* **2019**, *5* (5). https://doi.org/10.1016/J.HELIYON.2019.E01577.

(115) Jantachum, P.; Khumpaitool, B.; Utara, S. Effect of Silane Coupling Agent and Cellulose Nanocrystals Loading on the Properties of Acrylonitrile Butadiene Rubber/Natural Rubber Nanocomposites. *Ind Crops Prod* **2023**, *195*, 116407. https://doi.org/10.1016/J.INDCROP.2023.116407.

(116) Zhu, S.; Sun, H.; Lu, Y.; Wang, S.; Yue, Y.; Xu, X.; Mei, C.; Xiao, H.; Fu, Q.; Han, J. Inherently Conductive Poly(Dimethylsiloxane) Elastomers Synergistically Mediated by Nanocellulose/Carbon Nanotube Nanohybrids toward Highly Sensitive, Stretchable, and Durable Strain Sensors. *ACS Appl Mater Interfaces* **2021**, *13* (49), 59142–59153.

(117) Favier, V.; Chanzy, H.; Cavaillé, J. Y. Polymer Nanocomposites Reinforced by Cellulose Whiskers. *Macromolecules* **1995**, *28* (18), 6365–6367. https://doi.org/10.1021/MA00122A053.

(118) Ljungberg, N.; Bonini, C.; Bortolussi, F.; Boisson, C.; Heux, L.; Cavaillé, J. Y. New Nanocomposite Materials Reinforced with Cellulose Whiskers in Atactic Polypropylene: Effect of Surface and Dispersion Characteristics. *Biomacromolecules* **2005**, *6* (5), 2732–2739. https://doi.org/10.1021/BM050222V.

(119) Azouz, K. Ben; Ramires, E. C.; Van Den Fonteyne, W.; El Kissi, N.; Dufresne, A. Simple Method for the Melt Extrusion of a Cellulose Nanocrystal Reinforced Hydrophobic Polymer. *ACS Macro Lett* **2012**, *1* (1), 236–240. https://doi.org/10.1021/MZ2001737.

(120) Mendez, J.; Annamalai, P. K.; Eichhorn, S. J.; Rusli, R.; Rowan, S. J.; Foster, E. J.; Weder, C. Bioinspired Mechanically Adaptive Polymer Nanocomposites with Water-Activated Shape-Memory Effect. *Macromolecules* **2011**, *44* (17), 6827–6835. https://doi.org/10.1021/ma201502k.

(121) Girouard, N. M.; Xu, S.; Schueneman, G. T.; Shofner, M. L.; Meredith, J. C. Site-Selective Modification of Cellulose Nanocrystals with Isophorone Diisocyanate and Formation of Polyurethane-CNC Composites. *ACS Appl Mater Interfaces* **2016**, *8* (2), 1458–1467. https://doi.org/10.1021/acsami.5b10723.

(122) Rueda, L.; Fernández d'Arlas, B.; Zhou, Q.; Berglund, L. A.; Corcuera, M. A.; Mondragon, I.; Eceiza, A. Isocyanate-Rich Cellulose Nanocrystals and Their Selective Insertion in Elastomeric Polyurethane. *Compos Sci Technol* **2011**, *71* (16), 1953–1960. https://doi.org/10.1016/J.COMPSCITECH.2011.09.014.

(123) Dagnon, K. L.; Shanmuganathan, K.; Weder, C.; Rowan, S. J. Water-Triggered Modulus Changes of Cellulose Nanofiber Nanocomposites with Hydrophobic Polymer Matrices. *Macromolecules* **2012**, *45* (11), 4707–4715. https://doi.org/10.1021/ma300463y.

(124) Annamalai, P. K.; Dagnon, K. L.; Monemian, S.; Foster, E. J.; Rowan, S. J.; Weder, C. Water-Responsive Mechanically Adaptive Nanocomposites Based on Styrene-Butadiene Rubber and Cellulose Nanocrystals - Processing Matters. *ACS Appl Mater Interfaces* **2014**, *6* (2), 967–976. https://doi.org/10.1021/am404382x.

(125) Gupta, A.; Simmons, W.; Schueneman, G. T.; Hylton, D.; Mintz, E. A. Rheological and Thermo-Mechanical Properties of Poly(Lactic Acid)/Lignin-Coated Cellulose Nanocrystal Composites. *ACS Sustain Chem Eng* **2017**, *5* (2), 1711–1720.

(126) Gwon, J.-G.; Cho, H.-J.; Chun, S.-J.; Lee, S.; Wu, Q.; Lee, S.-Y. Physiochemical, Optical and Mechanical Properties of Poly(Lactic Acid) Nanocomposites Filled with Toluene Diisocyanate Grafted Cellulose Nanocrystals. *RSC Adv* **2016**, *6* (12), 9438–9445. https://doi.org/10.1039/C5RA26337A.

(127) Zhang, Y.; Edelbrock, A. N.; Rowan, S. J. Effect of Processing Conditions on the Mechanical Properties of Bio-Inspired Mechanical Gradient Nanocomposites. *Eur Polym J* **2019**, *115*, 107–114. https://doi.org/10.1016/j.eurpolymj.2019.03.022.

(128) Favier, V.; Cavaille, J. Y.; Canova, G. R.; Shrivastava, S. C. Mechanical Percolation in Cellulose Whisker Nanocomposites. *Polym Eng Sci* **1997**, *37* (10), 1732–1739. https://doi.org/10.1002/pen.11821.

(129) Xu, X.; Liu, F.; Jiang, L.; Zhu, J. Y.; Haagenson, D.; Wiesenborn, D. P. Cellulose Nanocrystals vs. Cellulose Nanofibrils: A Comparative Study on Their Microstructures and Effects as Polymer Reinforcing Agents. *ACS Appl Mater Interfaces* **2013**, *5* (8), 2999–3009.

(130) Hostler, S. R.; Peswani, M.; Yang, H.; Paul, H.; Rowan, S. J.; Abramson, A. R. Stretching-Induced Thermal Conductivity Change in Shape-Memory Polymer Composites. *J Heat Transfer* **2020**, *142* (8). https://doi.org/10.1115/1.4046970/1082730.

(131) Cudjoe, E.; Advisor, D.; Rowan, S. J.; Rowan, S.; Korley, L. CELLULOSE NANOCRYSTALS AND RELATED POLYMER NANOCOMPOSITES. **2017**.

(132) Isogai, A.; Saito, T.; Fukuzumi, H. TEMPO-Oxidized Cellulose Nanofibers. *Nanoscale* **2011**, *3* (1), 71–85. https://doi.org/10.1039/C0NR00583E.

(133) Capadona, J. R.; Shanmuganathan, K.; Tyler, D. J.; Rowan, S. J.; Weder, C. Stimuli-Responsive Polymer Nanocomposites Inspired by the Sea Cucumber Dermis. *Science (1979)* **2008**, *319* (5868), 1370–1374. https://doi.org/10.1126/science.1153307.

(134) Gabriel, V. A.; Tousignant, M. N.; Wilson, S. M. W.; Faure, M. D. M.; Cranston, E. D.; Cunningham, M. F.; Lessard, B. H.; Dubé, M. A. Improving Latex-Based Pressure-Sensitive Adhesive Properties Using Carboxylated Cellulose Nanocrystals. *Macromol React Eng* **2022**, *16* (3), 2100051. https://doi.org/10.1002/MREN.202100051.

(135) Kiriakou, M. V.; Pakdel, A. S.; Berry, R. M.; Hoare, T.; Dubé, M. A.; Cranston, E. D. Incorporation of Polymer-Grafted Cellulose Nanocrystals into Latex-Based Pressure-Sensitive Adhesives. *ACS Materials Au* **2022**, *2* (2), 176–189.

(136) Gabriel, V. A.; Cranston, E. D.; Dubé, M. A. Pushing the Limits with Cellulose Nanocrystal Loadings in Latex-Based Pressure-Sensitive Adhesive Nanocomposites. *Macromol React Eng* **2020**, *14* (6). https://doi.org/10.1002/MREN.202000027.

(137) Kedzior, S. A.; Dubé, M. A.; Cranston, E. D. Cellulose Nanocrystals and Methyl Cellulose as Costabilizers for Nanocomposite Latexes with Double Morphology. *ACS Sustain Chem Eng* **2017**, *5* (11), 10509–10517.

(138) Limousin, E.; Rafaniello, I.; Schäfer, T.; Ballard, N.; Asua, J. M. Linking Film Structure and Mechanical Properties in Nanocomposite Films Formed from Dispersions of Cellulose Nanocrystals and Acrylic Latexes. *Langmuir* **2020**, *36* (8), 2052–2062. https://doi.org/10.1021/ACS.LANGMUIR.9B03861/SUPPL_FILE/LA9B03861_SI_001.PDF.

(139) Banjar, M. F.; Yahaya, A. N. A.; Khalil, N. A.; Al-Dulaimi, A. A.; Singh, M.; Zulkifli, M. Mechanical Properties and Conductivity of Polyaniline-Cellulose-Latex Hybrid. *Mater Today Proc* **2023**, *74*, 489–491. https://doi.org/10.1016/J.MATPR.2022.11.475.

(140) Pakdel, A. S.; Cranston, E. D.; Dubé, M. A. Incorporating Hydrophobic Cellulose Nanocrystals inside Latex Particles via Mini-Emulsion Polymerization. *Macromol React Eng* **2021**, *15* (5), 2100023. https://doi.org/10.1002/MREN.202100023.

(141) Rui, W.; Sun, Y.; Tian, Y.; Li, X.; Han, J. Poly(Dopamine)-Modified Microcrystalline Cellulose,a Green Reinforcing Filler for Natural Rubber Latex with High Performance. *https://doi.org/10.1080/09276440.2022.2116074* **2022**, *30* (4), 361–375. https://doi.org/10.1080/09276440.2022.2116074.

(142) Fernandes, N. J.; Koerner, H.; Giannelis, E. P.; Vaia, R. A. Hairy Nanoparticle Assemblies as One-Component Functional Polymer Nanocomposites: Opportunities and Challenges. *MRS Commun* **2013**, *3* (1), 13–29. https://doi.org/10.1557/MRC.2013.9/METRICS.

(143) Hore, M. J. A.; Korley, L. S. T. J.; Kumar, S. K. Polymer-Grafted Nanoparticles. *J Appl Phys* **2020**, *128* (3), 30401. https://doi.org/10.1063/5.0019326/1025564.

(144) Kato, R.; Lettow, J. H.; Patel, S. N.; Rowan, S. J. Ion-Conducting Thermoresponsive Films Based on Polymer-Grafted Cellulose Nanocrystals. *ACS Appl Mater Interfaces* **2020**, *12* (48), 54083–54093. https://doi.org/10.1021/ACSAMI.0C16059/SUPPL_FILE/AM0C16059_SI_003.MP4.

(145) Schmitt, M.; Choi, J.; Hui, C. M.; Chen, B.; Korkmaz, E.; Yan, J.; Margel, S.; Ozdoganlar, O. B.; Matyjaszewski, K.; Bockstaller, M. R. Processing Fragile Matter: Effect of Polymer Graft Modification on the Mechanical Properties and Processibility of (Nano-) Particulate Solids. *Soft Matter* **2016**, *12* (15), 3527–3537. https://doi.org/10.1039/C6SM00095A.

(146) Choi, J.; Hui, C. M.; Pietrasik, J.; Dong, H.; Matyjaszewski, K.; Bockstaller, M. R. Toughening Fragile Matter: Mechanical Properties of Particle Solids Assembled from Polymer-Grafted Hybrid Particles Synthesized by ATRP. *Soft Matter* **2012**, *8* (15), 4072–4082. https://doi.org/10.1039/C2SM06915F.

(147) Jiao, Y.; Tibbits, A.; Gillman, A.; Hsiao, M. S.; Buskohl, P.; Drummy, L. F.; Vaia, R. A. Deformation Behavior of Polystyrene-Grafted Nanoparticle Assemblies with Low Grafting Density. *Macromolecules* **2018**, *51* (18), 7257–7265. https://doi.org/https://doi.org/10.1021/acs.macromol.8b01524.

(148) Midya, J.; Cang, Y.; Egorov, S. A.; Matyjaszewski, K.; Bockstaller, M. R.; Nikoubashman, A.; Fytas, G. Disentangling the Role of Chain Conformation on the Mechanics of Polymer Tethered Particle Materials. *Nano Lett* **2019**, *19* (4), 2715–2722. https://doi.org/10.1021/ACS.NANOLETT.9B00817/ASSET/IMAGES/LARGE/NL-2019-00817D_0004.JPEG.

(149) Halperin, A.; Tirrell, M.; Lodge, T. P. Tethered Chains in Polymer Microstructures. *Advances in Polymer Science* **1991**, *100*, 30–71. https://doi.org/10.1007/BFB0051635/COVER.

(150) Dan, N.; Tirrell, M. Polymers Tethered to Curved Interfaces. A Self-Consistent-Field Analysis. *Macromolecules* **1992**, *25* (11), 2890–2895. https://doi.org/10.1021/MA00037A016/ASSET/MA00037A016.FP.PNG_V03.

(151) Lenart, W. R.; Hore, M. J. A. Structure–Property Relationships of Polymer-Grafted Nanospheres for Designing Advanced Nanocomposites. *Nano-Structures & Nano-Objects* **2018**, *16*, 428–440. https://doi.org/10.1016/J.NANOSO.2017.11.005.

(152) Fischer, S.; Salcher, A.; Kornowski, A.; Weller, H.; Förster, S. Completely Miscible Nanocomposites. *Angewandte Chemie International Edition* **2011**, *50* (34), 7811–7814. https://doi.org/10.1002/ANIE.201006746.

(153) Ohno, K.; Morinaga, T.; Koh, K.; Tsujii, Y.; Fukuda, T. Synthesis of Monodisperse Silica Particles Coated with Well-Defined, High-Density Polymer Brushes by Surface-Initiated Atom Transfer

Radical Polymerization. *Macromolecules* **2005**, *38* (6), 2137–2142. https://doi.org/10.1021/MA048011Q.

(154) Ohno, K.; Morinaga, T.; Takeno, S.; Tsujii, Y.; Fukuda, T. Suspensions of Silica Particles Grafted with Concentrated Polymer Brush: Effects of Graft Chain Length on Brush Layer Thickness and Colloidal Crystallization. *Macromolecules* **2007**, *40* (25), 9143–9150. https://doi.org/https://doi.org/10.1021/ma071770z.

(155) Morinaga, T.; Honma, S.; Ishizuka, T.; Kamijo, T.; Sato, T.; Tsujii, Y. Synthesis of Monodisperse Silica Particles Grafted with Concentrated Ionic Liquid-Type Polymer Brushes by Surface-Initiated Atom Transfer Radical Polymerization for Use as a Solid State Polymer Electrolyte. *Polymers (Basel)* **2016**, *8* (4). https://doi.org/10.3390/POLYM8040146.

(156) Daoud, M.; Cotton, J. P. Star Shaped Polymers : A Model for the Conformation and Its Concentration Dependence. *Journal de Physique* **1982**, *43* (3), 531–538. https://doi.org/10.1051/JPHYS:01982004303053100.

(157) Vörösmarty, C. J.; Green, P.; Salisbury, J.; Lammers, R. B. Global Water Resources: Vulnerability from Climate Change and Population Growth. *Science (1979)* **2000**, *289* (5477), 284–288. https://doi.org/10.1126/SCIENCE.289.5477.284/ASSET/8277DF2D-D298-4C85-88F2-B3A4F9CE0C3B/ASSETS/GRAPHIC/SE2508647003.JPEG.

(158) Vörösmarty, C. J.; McIntyre, P. B.; Gessner, M. O.; Dudgeon, D.; Prusevich, A.; Green, P.; Glidden, S.; Bunn, S. E.; Sullivan, C. A.; Liermann, C. R.; Davies, P. M. Global Threats to Human Water Security and River Biodiversity. *Nature 2010 467:7315* **2010**, *467* (7315), 555–561. https://doi.org/10.1038/nature09440.

(159) Crini, G. Non-Conventional Low-Cost Adsorbents for Dye Removal: A Review. *Bioresour Technol* **2006**, *97* (9), 1061–1085. https://doi.org/10.1016/J.BIORTECH.2005.05.001.

(160) Fu, F.; Wang, Q. Removal of Heavy Metal Ions from Wastewaters: A Review. *J Environ Manage* **2011**, *92* (3), 407–418. https://doi.org/10.1016/J.JENVMAN.2010.11.011.

(161) Li, M.; Gou, H.; Al-Ogaidi, I.; Wu, N. Nanostructured Sensors for Detection of Heavy Metals: A Review. *ACS Sustain Chem Eng* **2013**, *1* (7), 713–723. https://doi.org/10.1021/sc400019a.

(162) Güçlü, G.; Gürdağ, G.; Özgümüş, S. Competitive Removal of Heavy Metal Ions by Cellulose Graft Copolymers. *J Appl Polym Sci* **2003**, *90* (8), 2034–2039. https://doi.org/10.1002/app.12728.

(163) Sahithya, K.; Das, D.; Das, N. Effective Removal of Dichlorvos from Aqueous Solution Using Biopolymer Modified MMT–CuO Composites: Equilibrium, Kinetic and Thermodynamic Studies. *J Mol Liq* **2015**, *211*, 821–830. https://doi.org/10.1016/J.MOLLIQ.2015.08.013.

(164) Keith, L. H.; Telliard, W. A. Priority Pollutants. I. A Perspective View. *Environ Sci Technol* **1979**, *13* (4), 416–423. https://doi.org/10.1021/ES60152A601/ASSET/ES60152A601.FP.PNG_V03.

(165) Khan, S. B.; Ali, F.; Kamal, T.; Anwar, Y.; Asiri, A. M.; Seo, J. CuO Embedded Chitosan Spheres as Antibacterial Adsorbent for Dyes. *Int J Biol Macromol* **2016**, *88*, 113–119. https://doi.org/10.1016/J.IJBIOMAC.2016.03.026.

(166) Albukhari, S. M.; Ismail, M.; Akhtar, K.; Danish, E. Y. Catalytic Reduction of Nitrophenols and Dyes Using Silver Nanoparticles @ Cellulose Polymer Paper for the Resolution of Waste Water Treatment Challenges. *Colloids Surf A Physicochem Eng Asp* **2019**, *577*, 548–561. https://doi.org/10.1016/J.COLSURFA.2019.05.058.

(167) Sun, Y.; Zhou, G.; Xiong, X.; Guan, X.; Li, L.; Bao, H. Enhanced Arsenite Removal from Water by Ti(SO4)2 Coagulation. *Water Res* **2013**, *47* (13), 4340–4348. https://doi.org/10.1016/J.WATRES.2013.05.028.

(168) Elwakeel, K. Z.; Guibal, E. Arsenic(V) Sorption Using Chitosan/Cu(OH)2 and Chitosan/CuO Composite Sorbents. *Carbohydr Polym* **2015**, *134*, 190–204. https://doi.org/10.1016/J.CARBPOL.2015.07.012.

(169) Epa, U.; Supply, W.; Resources Division, W.; Smith, C. 2012 Guidelines for Water Reuse. **2004**.

(170) Lee, A.; Elam, J. W.; Darling, S. B. Membrane Materials for Water Purification: Design, Development, and Application. *Environ Sci (Camb)* **2016**, *2* (1), 17–42. https://doi.org/10.1039/C5EW00159E.

(171) Hilal, N.; Al-Zoubi, H.; Darwish, N. A.; Mohamma, A. W.; Abu Arabi, M. A Comprehensive Review of Nanofiltration Membranes:Treatment, Pretreatment, Modelling, and Atomic Force Microscopy. *Desalination* **2004**, *170* (3), 281–308. https://doi.org/10.1016/j.desal.2004.01.007.

(172) Klein, E. Affinity Membranes: A 10-Year Review. *J Memb Sci* **2000**, *179* (1–2), 1–27. https://doi.org/10.1016/S0376-7388(00)00514-7.

(173) Geise, G. M.; Lee, H.-S.; Miller, D. J.; Freeman, B. D.; McGrath, J. E.; Paul, D. R. Water Purification by Membranes: The Role of Polymer Science. *J Polym Sci B Polym Phys* **2010**, *48* (15), 1685–1718. https://doi.org/10.1002/polb.22037.

(174) Goosen, M. F. A.; Sablani, S. S.; Al-Hinai, H.; Al-Obeidani, S.; Al-Belushi, R.; Jackson, D. Fouling of Reverse Osmosis and Ultrafiltration Membranes: A Critical Review. *Sep Sci Technol* **2005**, *39* (10), 2261–2297. https://doi.org/10.1081/SS-120039343.

(175) Lau, W. J.; Gray, S.; Matsuura, T.; Emadzadeh, D.; Paul Chen, J.; Ismail, A. F. A Review on Polyamide Thin Film Nanocomposite (TFN) Membranes: History, Applications, Challenges and Approaches. *Water Res* **2015**, *80*, 306–324. https://doi.org/10.1016/J.WATRES.2015.04.037.

(176) Baker, R. W. *Membrane Technology and Applications*; John Wiley & Sons, Ltd: Chichester, UK, 2012. https://doi.org/10.1002/9781118359686.

(177) Liu, T.; Ding, E.; Xue, F. Polyacrylamide and Poly(N,N-Dimethylacrylamide) Grafted Cellulose Nanocrystals as Efficient Flocculants for Kaolin Suspension. *Int J Biol Macromol* **2017**, *103*, 1107–1112. https://doi.org/10.1016/J.IJBIOMAC.2017.05.098.

(178) Verma, A. K.; Dash, R. R.; Bhunia, P. A Review on Chemical Coagulation/Flocculation Technologies for Removal of Colour from Textile Wastewaters. *J Environ Manage* **2012**, *93* (1), 154–168. https://doi.org/10.1016/J.JENVMAN.2011.09.012.

(179) Crini, G. Non-Conventional Low-Cost Adsorbents for Dye Removal: A Review. *Bioresour Technol* **2006**, *97* (9), 1061–1085. https://doi.org/10.1016/J.BIORTECH.2005.05.001.

(180) Crini, G.; Lichtfouse, E.; Wilson, L. D.; Morin-Crini, N. Conventional and Non-Conventional Adsorbents for Wastewater Treatment. *Environ Chem Lett* **2019**, *17* (1), 195–213. https://doi.org/10.1007/S10311-018-0786-8/FIGURES/5.

(181) Dąbrowski, A.; Podkościelny, P.; Hubicki, Z.; Barczak, M. Adsorption of Phenolic Compounds by Activated Carbon—a Critical Review. *Chemosphere* **2005**, *58* (8), 1049–1070. https://doi.org/10.1016/J.CHEMOSPHERE.2004.09.067.

(182) Nouri, S.; Haghseresht, F.; Lu, M. Adsorption of Aromatic Compounds by Activated Carbon: Effects of Functional Groups and Molecular Size. *Adsorption Science and Technology* **2002**, *20* (1), 1–16. https://doi.org/10.1260/026361702760120890.

(183) Li, L.; Liu, S.; Zhu, T. Application of Activated Carbon Derived from Scrap Tires for Adsorption of Rhodamine B. *Journal of Environmental Sciences* **2010**, *22* (8), 1273–1280. https://doi.org/10.1016/S1001-0742(09)60250-3.

(184) Aktaş, Ö.; Çeçen, F. Bioregeneration of Activated Carbon: A Review. *Int Biodeterior Biodegradation* **2007**, *59* (4), 257–272. https://doi.org/10.1016/J.IBIOD.2007.01.003.

(185) Radovic, L. R.; Moreno-Castilla, C.; Rivera-Utrilla, J. Carbon Materials as Adsorbents in Aqueous Solutions. *Chemistry and Physics of Carbon* **2000**, *27*, 227–405.

(186) Ania, C. O.; Parra, J. B.; Pis, J. J. Influence of Oxygen-Containing Functional Groups on Active Carbon Adsorption of Selected Organic Compounds. *Fuel Processing Technology* **2002**, *79* (3), 265–271. https://doi.org/10.1016/S0378-3820(02)00184-4.

(187) Wang, S.; Peng, Y. Natural Zeolites as Effective Adsorbents in Water and Wastewater Treatment. *Chemical Engineering Journal* **2010**, *156* (1), 11–24. https://doi.org/10.1016/J.CEJ.2009.10.029.

(188) Mende, M.; Schwarz, D.; Steinbach, C.; Boldt, R.; Schwarz, S. The Influence of Salt Anions on Heavy Metal Ion Adsorption on the Example of Nickel. *Materials* **2018**, *11* (3). https://doi.org/10.3390/MA11030373.

(189) Mautner, A.; Lee, K. Y.; Tammelin, T.; Mathew, A. P.; Nedoma, A. J.; Li, K.; Bismarck, A. Cellulose Nanopapers as Tight Aqueous Ultra-Filtration Membranes. *React Funct Polym* **2015**, *86*, 209–214. https://doi.org/10.1016/j.reactfunctpolym.2014.09.014.

(190) Mautner, A.; Maples, H. A.; Sehaqui, H.; Zimmermann, T.; Perez de Larraya, U.; Mathew, A. P.; Lai, C. Y.; Li, K.; Bismarck, A. Nitrate Removal from Water Using a Nanopaper Ion-Exchanger. *Environ Sci (Camb)* **2016**, *2* (1), 117–124. https://doi.org/10.1039/C5EW00139K.

(191) Liu, J.; Chen, X.; Shao, Z.; Zhou, P. Preparation and Characterization of Chitosan/Cu(II) Affinity Membrane for Urea Adsorption. *J Appl Polym Sci* **2003**, *90*, 1108–1112.

(192) Yu, X.; Tong, S.; Ge, M.; Wu, L.; Zuo, J.; Cao, C.; Song, W. Adsorption of Heavy Metal Ions from Aqueous Solution by Carboxylated Cellulose Nanocrystals. *Journal of Environmental Sciences* **2013**, *25* (5), 933–943. https://doi.org/10.1016/S1001-0742(12)60145-4.

(193) Pillai, S. S.; Deepa, B.; Abraham, E.; Girija, N.; Geetha, P.; Jacob, L.; Koshy, M. Biosorption of Cd(II) from Aqueous Solution Using Xanthated Nano Banana Cellulose: Equilibrium and Kinetic Studies. *Ecotoxicol Environ Saf* **2013**, *98*, 352–360. https://doi.org/10.1016/J.ECOENV.2013.09.003.

(194) Kardam, A.; Raj, K. R.; Srivastava, S.; Srivastava, M. M. Nanocellulose Fibers for Biosorption of Cadmium, Nickel, and Lead Ions from Aqueous Solution. *Clean Technol Environ Policy* **2014**, *16* (2), 385–393. https://doi.org/10.1007/S10098-013-0634-2/TABLES/4.

(195) Liu, P.; Sehaqui, H.; Tingaut, P.; Wichser, A.; Oksman, K.; Mathew, A. P. Cellulose and Chitin Nanomaterials for Capturing Silver Ions (Ag+) from Water via Surface Adsorption. *Cellulose* **2014**, *21* (1), 449–461. https://doi.org/10.1007/s10570-013-0139-5.

(196) Sehaqui, H.; Perez de Larraya, U.; Tingaut, P.; Zimmermann, T. Humic Acid Adsorption onto Cationic Cellulose Nanofibers for Bioinspired Removal of Copper(Ii) and a Positively Charged Dye. *Soft Matter* **2015**, *11* (26), 5294–5300. https://doi.org/10.1039/C5SM00566C.

(197) Sheikhi, A.; Safari, S.; Yang, H.; Van De Ven, T. G. M. Copper Removal Using Electrosterically Stabilized Nanocrystalline Cellulose. *ACS Appl Mater Interfaces* **2015**, *7* (21), 11301–11308. https://doi.org/10.1021/ACSAMI.5B01619/SUPPL_FILE/AM5B01619_SI_001.ZIP.

(198) Mautner, A.; Maples, H. A.; Kobkeatthawin, T.; Kokol, V.; Karim, Z.; Li, K.; Bismarck, A. Phosphorylated Nanocellulose Papers for Copper Adsorption from Aqueous Solutions. *International Journal of Environmental Science and Technology* **2016**, *13* (8). https://doi.org/10.1007/s13762-016-1026-z.

(199) Saito, T.; Isogai, A. Ion-Exchange Behavior of Carboxylate Groups in Fibrous Cellulose Oxidized by the TEMPO-Mediated System. *Carbohydr Polym* **2005**, *61* (2), 183–190. https://doi.org/10.1016/J.CARBPOL.2005.04.009.

(200) Sehaqui, H.; de Larraya, U. P.; Liu, P.; Pfenninger, N.; Mathew, A. P.; Zimmermann, T.; Tingaut, P. Enhancing Adsorption of Heavy Metal Ions onto Biobased Nanofibers from Waste Pulp Residues for Application in Wastewater Treatment. *Cellulose* **2014**, *21* (4), 2831–2844. https://doi.org/10.1007/S10570-014-0310-7/FIGURES/9.

(201) Sehaqui, H.; Mautner, A.; Perez de Larraya, U.; Pfenninger, N.; Tingaut, P.; Zimmermann, T. Cationic Cellulose Nanofibers from Waste Pulp Residues and Their Nitrate, Fluoride, Sulphate and Phosphate Adsorption Properties. *Carbohydr Polym* **2016**, *135*, 334–340. https://doi.org/10.1016/J.CARBPOL.2015.08.091.

(202) Liu, P.; Borrell, P. F.; Božič, M.; Kokol, V.; Oksman, K.; Mathew, A. P. Nanocelluloses and Their Phosphorylated Derivatives for Selective Adsorption of Ag+, Cu2+ and Fe3+ from Industrial Effluents. *J Hazard Mater* **2015**, *294*, 177–185. https://doi.org/10.1016/J.JHAZMAT.2015.04.001.

(203) Ma, H.; Hsiao, B. S.; Chu, B. Ultrafine Cellulose Nanofibers as Efficient Adsorbents for Removal of UO22+ in Water. *ACS Macro Lett* **2012**, *1* (1), 213–216.

(204) Batmaz, R.; Mohammed, N.; Zaman, M.; Minhas, G.; Berry, R. M.; Tam, K. C. Cellulose Nanocrystals as Promising Adsorbents for the Removal of Cationic Dyes. *Cellulose* **2014**, *21* (3), 1655–1665. https://doi.org/10.1007/S10570-014-0168-8/FIGURES/4.

(205) Qiao, H.; Zhou, Y.; Yu, F.; Wang, E.; Min, Y.; Huang, Q.; Pang, L.; Ma, T. Effective Removal of Cationic Dyes Using Carboxylate-Functionalized Cellulose Nanocrystals. *Chemosphere* **2015**, *141*, 297–303. https://doi.org/10.1016/J.CHEMOSPHERE.2015.07.078.

(206) Timofei, S.; Schmidt, W.; Kurunczi, L.; Simon, Z. A Review of QSAR for Dye Affinity for Cellulose Fibres. *Dyes and Pigments* **2000**, *47* (1–2), 5–16. https://doi.org/10.1016/S0143-7208(00)00058-9.

(207) Jin, L.; Li, W.; Xu, Q.; Sun, Q. Amino-Functionalized Nanocrystalline Cellulose as an Adsorbent for Anionic Dyes. *Cellulose* **2015**, *22* (4), 2443–2456. https://doi.org/10.1007/S10570-015-0649-4.

(208) Pei, A.; Butchosa, N.; Berglund, L. A.; Zhou, Q. Surface Quaternized Cellulose Nanofibrils with High Water Absorbency and Adsorption Capacity for Anionic Dyes. *Soft Matter* **2013**, *9* (6), 2047–2055. https://doi.org/10.1039/C2SM27344F.

(209) Jin, L.; Sun, Q.; Xu, Q.; Xu, Y. Adsorptive Removal of Anionic Dyes from Aqueous Solutions Using Microgel Based on Nanocellulose and Polyvinylamine. *Bioresour Technol* **2015**, *197*, 348–355. https://doi.org/10.1016/J.BIORTECH.2015.08.093.

(210) Zhu, W.; Liu, L.; Liao, Q.; Chen, X.; Qian, Z.; Shen, J.; Liang, J.; Yao, J. Functionalization of Cellulose with Hyperbranched Polyethylenimine for Selective Dye Adsorption and Separation. *Cellulose* **2016**, *23* (6), 3785–3797. https://doi.org/10.1007/S10570-016-1045-4.

(211) Rathod, M.; Haldar, S.; Basha, S. Nanocrystalline Cellulose for Removal of Tetracycline Hydrochloride from Water via Biosorption: Equilibrium, Kinetic and Thermodynamic Studies. *Ecol Eng* **2015**, *84*, 240–249. https://doi.org/10.1016/J.ECOLENG.2015.09.031.

(212) Espino-Pérez, E.; Bras, J.; Ducruet, V. J.; Guinault, A.; Dufresne, A.; Domenek, S.; Ducruet, V. Influence of Chemical Surface Modification of Cellulose Nanowhiskers on Thermal, Mechanical, and Barrier Properties of Poly(Lactide) Based Influence of Chemical Surface Modification of Cellulose Nanowhiskers on Thermal, Mechanical, and Barrier Properties of Poly(Lactide) Based Bionanocomposites. *Macromolecular Nanotechnology* **2013**, No. 10, 3144–3154. https://doi.org/10.1016/j.eurpolymj.2013.07.017ï.

(213) Jackson, J. K.; Letchford, K.; Wasserman, B. Z.; Ye, L.; Hamad, W. Y.; Burt, H. M. The Use of Nanocrystalline Cellulose for the Binding and Controlled Release of Drugs. *Int J Nanomedicine* **2011**, *6*, 321–330. https://doi.org/10.2147/IJN.S16749.

(214) Le-Minh, N.; Khan, S. J.; Drewes, J. E.; Stuetz, R. M. Fate of Antibiotics during Municipal Water Recycling Treatment Processes. *Water Res* **2010**, *44* (15), 4295–4323. https://doi.org/10.1016/J.WATRES.2010.06.020.

(215) Ulbricht, M. Advanced Functional Polymer Membranes. *Polymer (Guildf)* **2006**, *47* (7), 2217–2262. https://doi.org/10.1016/J.POLYMER.2006.01.084.

(216) Carpenter, A. W.; de Lannoy, C.-F.; Wiesner, M. R. Cellulose Nanomaterials in Water Treatment Technologies. *Environ Sci Technol* **2015**, *49* (9), 5277–5287. https://doi.org/10.1021/es506351r.

(217) Van der Bruggen, B. Microfiltration, Ultrafiltration, Nanofiltration, Reverse Osmosis, and Forward Osmosis. *Fundamental Modelling of Membrane Systems* **2018**, 25–70. https://doi.org/10.1016/B978-0-12-813483-2.00002-2.

(218) Wang, J.; Zhu, J.; Zhang, Y.; Liu, J.; Van der Bruggen, B. Nanoscale Tailor-Made Membranes for Precise and Rapid Molecular Sieve Separation. *Nanoscale* **2017**, *9* (9), 2942–2957. https://doi.org/10.1039/C6NR08417F.

(219) Jonsson, G. Molecular Weight Cut-off Curves for Ultrafiltration Membranes of Varying Pore Sizes. *Desalination* **1985**, *53* (1–3), 3–10. https://doi.org/10.1016/0011-9164(85)85048-7.

(220) Pellegrin, M.-L.; Aguinaldo, J.; Arabi, S.; Sadler, M. E.; Min, K.; Liu, M.; Salamon, C.; Greiner, A. D.; Diamond, J.; McCandless, R.; Owerdieck, C.; Wert, J.; Padhye, L. P. Membrane Processes. *Water Environment Research* **2013**, *85* (10), 1092–1175. https://doi.org/10.2175/106143013X13698672321940.

(221) Werber, J. R.; Deshmukh, A.; Elimelech, M. The Critical Need for Increased Selectivity, Not Increased Water Permeability, for Desalination Membranes. *Environ Sci Technol Lett* **2016**, *3* (4), 112–120. https://doi.org/10.1021/acs.estlett.6b00050.

(222) Qin, J. J.; Li, Y.; Lee, L. S.; Lee, H. Cellulose Acetate Hollow Fiber Ultrafiltration Membranes Made from CA/PVP 360 K/NMP/Water. *J Memb Sci* **2003**, *218* (1–2), 173–183. https://doi.org/10.1016/S0376-7388(03)00170-4.

(223) Shibutani, T.; Kitaura, T.; Ohmukai, Y.; Maruyama, T.; Nakatsuka, S.; Watabe, T.; Matsuyama, H. Membrane Fouling Properties of Hollow Fiber Membranes Prepared from Cellulose Acetate Derivatives. *J Memb Sci* **2011**, *376* (1–2), 102–109. https://doi.org/10.1016/J.MEMSCI.2011.04.006.

(224) Soyekwo, F.; Zhang, Q. G.; Deng, C.; Gong, Y.; Zhu, A. M.; Liu, Q. L. Highly Permeable Cellulose Acetate Nanofibrous Composite Membranes by Freeze-Extraction. *J Memb Sci* **2014**, *454*, 339–345. https://doi.org/10.1016/J.MEMSCI.2013.12.014.

(225) Goetz, L. A.; Jalvo, B.; Rosal, R.; Mathew, A. P. Superhydrophilic Anti-Fouling Electrospun Cellulose Acetate Membranes Coated with Chitin Nanocrystals for Water Filtration. *J Memb Sci* **2016**, *510*, 238–248. https://doi.org/10.1016/J.MEMSCI.2016.02.069.

(226) Lv, J.; Zhang, G.; Zhang, H.; Yang, F. Exploration of Permeability and Antifouling Performance on Modified Cellulose Acetate Ultrafiltration Membrane with Cellulose Nanocrystals. *Carbohydr Polym* **2017**, *174*, 190–199. https://doi.org/10.1016/J.CARBPOL.2017.06.064.

(227) Lohokare, H. R.; Muthu, M. R.; Agarwal, G. P.; Kharul, U. K. Effective Arsenic Removal Using Polyacrylonitrile-Based Ultrafiltration (UF) Membrane. *J Memb Sci* **2008**, *320* (1–2), 159–166. https://doi.org/10.1016/J.MEMSCI.2008.03.068.

(228) Kim, I. C.; Yun, H. G.; Lee, K. H. Preparation of Asymmetric Polyacrylonitrile Membrane with Small Pore Size by Phase Inversion and Post-Treatment Process. *J Memb Sci* **2002**, *199* (1), 75–84. https://doi.org/10.1016/S0376-7388(01)00680-9.

(229) Saljoughi, E.; Mousavi, S. M. Preparation and Characterization of Novel Polysulfone Nanofiltration Membranes for Removal of Cadmium from Contaminated Water. *Sep Purif Technol* **2012**, *90*, 22–30. https://doi.org/10.1016/J.SEPPUR.2012.02.008.

(230) Ahmad, A. L.; Abdulkarim, A. A.; Ooi, B. S.; Ismail, S. Recent Development in Additives Modifications of Polyethersulfone Membrane for Flux Enhancement. *Chemical Engineering Journal* **2013**, *223*, 246–267. https://doi.org/10.1016/J.CEJ.2013.02.130.

(231) Yuliwati, E.; Ismail, A. F. Effect of Additives Concentration on the Surface Properties and Performance of PVDF Ultrafiltration Membranes for Refinery Produced Wastewater Treatment. *Desalination* **2011**, *273* (1), 226–234. https://doi.org/10.1016/J.DESAL.2010.11.023.

(232) Liu, F.; Hashim, N. A.; Liu, Y.; Abed, M. R. M.; Li, K. Progress in the Production and Modification of PVDF Membranes. *J Memb Sci* **2011**, *375* (1–2), 1–27. https://doi.org/10.1016/J.MEMSCI.2011.03.014.

(233) Lee, K. P.; Arnot, T. C.; Mattia, D. A Review of Reverse Osmosis Membrane Materials for Desalination—Development to Date and Future Potential. *J Memb Sci* **2011**, *370* (1–2), 1–22. https://doi.org/10.1016/J.MEMSCI.2010.12.036.

(234) Soroko, I.; Bhole, Y.; Livingston, A. G. Green Chemistry Environmentally Friendly Route for the Preparation of Solvent Resistant Polyimide Nanofiltration Membranes. **2011**. https://doi.org/10.1039/c0gc00155d.

(235) Mungray, A. A.; Murthy, Z. V. P. Comparative Performance Study of Four Nanofiltration Membranes in the Separation of Mercury and Chromium. *Ionics (Kiel)* **2012**, *18* (8), 811–816. https://doi.org/10.1007/s11581-012-0743-7.

(236) Henmi, M.; Nakatsuji, K.; Ichikawa, T.; Tomioka, H.; Sakamoto, T.; Yoshio, M.; Kato, T. Self-Organized Liquid-Crystalline Nanostructured Membranes for Water Treatment: Selective Permeation of Ions. *Advanced Materials* **2012**, *24* (17), 2238–2241. https://doi.org/10.1002/adma.201200108.

(237) Rana, D.; Matsuura, T. Surface Modifications for Antifouling Membranes. *Chem Rev* **2010**, *110* (4), 2448–2471. https://doi.org/10.1021/CR800208Y/ASSET/CR800208Y.FP.PNG_V03.

(238) Miller, D. J.; Paul, D. R.; Freeman, B. D. An Improved Method for Surface Modification of Porous Water Purification Membranes. *Polymer (Guildf)* **2014**, *55* (6), 1375–1383. https://doi.org/10.1016/J.POLYMER.2014.01.046.

(239) Zhou, R.; Ren, P. F.; Yang, H. C.; Xu, Z. K. Fabrication of Antifouling Membrane Surface by Poly(Sulfobetaine Methacrylate)/Polydopamine Co-Deposition. *J Memb Sci* **2014**, *466*, 18–25. https://doi.org/10.1016/J.MEMSCI.2014.04.032.

(240) Yang, C.; Ding, X.; Ono, R. J.; Lee, H.; Hsu, L. Y.; Tong, Y. W.; Hedrick, J.; Yang, Y. Y. Brush-Like Polycarbonates Containing Dopamine, Cations, and PEG Providing a Broad-Spectrum, Antibacterial, and Antifouling Surface via One-Step Coating. *Advanced Materials* **2014**, *26* (43), 7346–7351. https://doi.org/10.1002/ADMA.201402059.

(241) Moses Varin, K. J.; Cohen, Y. Wettability of Terminally Anchored Polymer Brush Layers on a Polyamide Surface. *J Colloid Interface Sci* **2014**, *436*, 286–295. https://doi.org/10.1016/J.JCIS.2014.08.042.

(242) Vázquez, M. I.; De Lara, R.; Galán, P.; Benavente, J. Modification of Cellulosic Membranes by γ-Radiation: Effect on Electrochemical Parameters and Protein Adsorption. *Colloids Surf A Physicochem Eng Asp* **2005**, *270–271* (1–3), 245–251. https://doi.org/10.1016/J.COLSURFA.2005.06.008.

(243) Tripathi, B. P.; Dubey, N. C.; Stamm, M. Polyethylene Glycol Cross-Linked Sulfonated Polyethersulfone Based Filtration Membranes with Improved Antifouling Tendency. *J Memb Sci* **2014**, *453*, 263–274. https://doi.org/10.1016/J.MEMSCI.2013.11.007.

(244) Tao, M.; Liu, F.; Xue, L. Persistently Hydrophilic Microporous Membranes Based on in Situ Cross-Linking. *J Memb Sci* **2015**, *474*, 224–232. https://doi.org/10.1016/J.MEMSCI.2014.09.045.

(245) Ulbricht, M.; Belfort, G. Surface Modification of Ultrafiltration Membranes by Low Temperature Plasma II. Graft Polymerization onto Polyacrylonitrile and Polysulfone. *J Memb Sci* **1996**, *111* (2), 193–215. https://doi.org/10.1016/0376-7388(95)00207-3.

(246) Ulbricht, M.; Belfort, G. Surface Modification of Ultrafiltration Membranes by Low Temperature Plasma. I. Treatment of Polyacrylonitrile. *J Appl Polym Sci* **1995**, *56* (3), 325–343. https://doi.org/10.1002/APP.1995.070560304.

(247) Kim, E. S.; Yu, Q.; Deng, B. Plasma Surface Modification of Nanofiltration (NF) Thin-Film Composite (TFC) Membranes to Improve Anti Organic Fouling. *Appl Surf Sci* **2011**, *257* (23), 9863–9871. https://doi.org/10.1016/J.APSUSC.2011.06.059.

(248) Pezeshk, N.; Rana, D.; Narbaitz, R. M.; Matsuura, T. Novel Modified PVDF Ultrafiltration Flat-Sheet Membranes. *J Memb Sci* **2012**, *389*, 280–286. https://doi.org/10.1016/J.MEMSCI.2011.10.039.

(249) Richard Bowen, W.; Doneva, T. A.; Yin, H. B. Polysulfone — Sulfonated Poly(Ether Ether) Ketone Blend Membranes: Systematic Synthesis and Characterisation. *J Memb Sci* **2001**, *181* (2), 253–263. https://doi.org/10.1016/S0376-7388(00)00541-X.

(250) Sinha, M. K.; Purkait, M. K. Increase in Hydrophilicity of Polysulfone Membrane Using Polyethylene Glycol Methyl Ether. *J Memb Sci* **2013**, *437*, 7–16. https://doi.org/10.1016/J.MEMSCI.2013.03.003.

(251) Fan, X.; Su, Y.; Zhao, X.; Li, Y.; Zhang, R.; Zhao, J.; Jiang, Z.; Zhu, J.; Ma, Y.; Liu, Y. Fabrication of Polyvinyl Chloride Ultrafiltration Membranes with Stable Antifouling Property by Exploring the Pore Formation and Surface Modification Capabilities of Polyvinyl Formal. *J Memb Sci* **2014**, *464*, 100–109. https://doi.org/10.1016/J.MEMSCI.2014.04.005.

(252) Kochkodan, V.; Johnson, D. J.; Hilal, N. Polymeric Membranes: Surface Modification for Minimizing (Bio)Colloidal Fouling. *Adv Colloid Interface Sci* **2014**, *206*, 116–140. https://doi.org/10.1016/J.CIS.2013.05.005.

(253) Ma, H.; Yoon, K.; Rong, L.; Shokralla, M.; Kopot, A.; Wang, X.; Fang, D.; Hsiao, B. S.; Chu, B. Thin-Film Nanofibrous Composite Ultrafiltration Membranes Based on Polyvinyl Alcohol Barrier Layer

Containing Directional Water Channels. *Ind Eng Chem Res* **2010**, *49* (23), 11978–11984. https://doi.org/10.1021/ie100545k.

(254) Karim, Z.; Mathew, A. P.; Grahn, M.; Mouzon, J.; Oksman, K. Nanoporous Membranes with Cellulose Nanocrystals as Functional Entity in Chitosan: Removal of Dyes from Water. *Carbohydr Polym* **2014**, *112*, 668–676. https://doi.org/10.1016/J.CARBPOL.2014.06.048.

(255) Ma, H.; Burger, C.; Hsiao, B. S.; Chu, B. Nanofibrous Microfiltration Membrane Based on Cellulose Nanowhiskers. https://doi.org/10.1021/bm201421g.

(256) Mautner, A.; Lee, K.-Y.; Tammelin, T.; Mathew, A. P.; Nedoma, A. J.; Li, K.; Bismarck, A. Cellulose Nanopapers as Tight Aqueous Ultra-Filtration Membranes. *React Funct Polym* **2015**, *86*, 209–214. https://doi.org/10.1016/j.reactfunctpolym.2014.09.014.

(257) Yilma, K. T.; Limeneh, D. Y. Review on Moisture Management Finish: Mechanism and Evaluation. *Journal of Natural Fibers* **2022**, *19* (14), 8628–8636. https://doi.org/10.1080/15440478.2021.1966566.

(258) Carroll, G. T.; Turro, N. J.; Mammana, A.; Koberstein, J. T. Photochemical Immobilization of Polymers on a Surface: Controlling Film Thickness and Wettability. *Photochem Photobiol* **2017**, *93* (5), 1165–1169. https://doi.org/10.1111/PHP.12751.

(259) El-Ghazali, S.; Khatri, M.; Kobayashi, S.; Kim, I. S. An Overview of Medical Textile Materials. *Medical Textiles from Natural Resources* **2022**, 3–42. https://doi.org/10.1016/B978-0-323-90479-7.00026-9.

(260) Mallick, P.; De, S. S.; Mallick, P.; De, S. S. Absorbency and Wicking Behaviour of Natural Fibre-Based Yarn and Fabric. *Natural Fiber* **2022**. https://doi.org/10.5772/INTECHOPEN.102584.

(261) Azeem, M.; Boughattas, A.; Wiener, J.; Havelka, A. Mechanism of Liquid Water Transport in Fabrics; A Review. *Vlakna a Textil* **2017**, *24* (4), 58–65.

(262) Adler, M. M.; Walsh, W. K. Mechanisms of Transient Moisture Transport Between Fabrics. *http://dx.doi.org/10.1177/004051758405400510* **1984**, *54* (5), 334–343. https://doi.org/10.1177/004051758405400510.

(263) Song, L. F.; Tao, Y.; Cheung, T. W.; Li, L. A Design-Driven Creation of an Innovative and Environment-Friendly Nature-Based Yarn with Moisture Wicking and Fast-Drying Effect. *https://doi.org/10.1177/00405175231163587* **2023**. https://doi.org/10.1177/00405175231163587.

(264) Bagherzadeh, R.; Gorji, M.; Latifi, M.; Payvandy, P.; Kong, L. X. Evolution of Moisture Management Behavior of High-Wicking 3D Warp Knitted Spacer Fabrics. *Fibers and Polymers* **2012**, *13* (4), 529–534. https://doi.org/10.1007/S12221-012-0529-6/METRICS.

(265) Kissa, E. Wetting and Wicking. *http://dx.doi.org/10.1177/004051759606601008* **1996**, *66* (10), 660–668. https://doi.org/10.1177/004051759606601008.

(266) Kejkar, V.; Dhore, R. Active Sportswear Fabrics. https://doi.org/10.31031/TTEFT.2019.05.000606.

(267) Sharabaty, T.; Biguenet, F.; Dupuis, D.; Viallier, P. Investigation on Moisture Transport through Polyester/Cotton Fabrics. *Indian J Fibre Text Res* **2008**.

(268) Duprat, C. Moisture in Textiles. *https://doi.org/10.1146/annurev-fluid-030121-034728* **2022**, *54*, 443–467. https://doi.org/10.1146/ANNUREV-FLUID-030121-034728.

(269) Das, B.; Das, A.; Kothari, V. K.; Fanguiero, R.; De Araújo, M. Effect of Fibre Diameter and Cross-Sectional Shape on Moisture Transmission through Fabrics. *Fibers and Polymers* **2008**, *9* (2), 225–231. https://doi.org/10.1007/S12221-008-0036-Y/METRICS.

(270) Varshney, R. K.; Kothari, V. K.; Dhamija, S. A Study on Thermophysiological Comfort Properties of Fabrics in Relation to Constituent Fibre Fineness and Cross-Sectional Shapes. *The Journal of The Textile Institute* **2010**, *101* (6), 495–505. https://doi.org/10.1080/00405000802542184.

(271) Das, B.; Das, A.; Kothari, V.; Fanguiero, R.; Araujo, M. D. Moisture Flow through Blended Fabrics – Effect of Hydrophilicity. *https://doi.org/10.1177/155892500900400405* **2009**, *4* (4), 20–28. https://doi.org/10.1177/155892500900400405.

(272) Onofrei, E.; Rocha, A. M.; Catarino, A. The Influence of Knitted Fabrics' Structure on the Thermal and Moisture Management Properties. *https://doi.org/10.1177/155892501100600403* **2011**, *6* (4), 10–22. https://doi.org/10.1177/155892501100600403.

(273) *Wool Properties*. http://sff.arts.ac.uk/Fibre%20Properties/woolproperties.html (accessed 2023-09-23).

(274) Naylor, G. The Wool Fibre and Its Applications.

(275) Rippon, J. 'Wool', in Encyclopedia of Polymer Science and Technology. **2003**.

(276) Rossi, R. M.; Stämpfli, R.; Psikuta, A.; Rechsteiner, I.; Brühwiler, P. A. Transplanar and In-Plane Wicking Effects in Sock Materials under Pressure. *http://dx.doi.org/10.1177/0040517511413317* **2011**, *81* (15), 1549–1558. https://doi.org/10.1177/0040517511413317.

(277) Wang, H.; Wang, H.; Jin, X.; Zhou, H.; Wang, H.; Wang, W.; Ruan, F.; Feng, Q.; Lin, T. Tuning In-Plane Wicking Properties of Hydrophilic Fibrous Membranes Using Hydrophobic Fibrous Cover Layers. *Adv Mater Interfaces* **2023**, *10* (1), 2200741. https://doi.org/10.1002/ADMI.202200741.

(278) Miao, M.; Xin, J. H. *Engineering of High-Performance Textiles*.

(279) Morton, W. E.; Hearle, J. W. S. Physical Properties of Textile Fibres (4th Edition).

(280) Mak, A. F. T.; Zhang, M.; Boone, D. A. State-of-the-Art Research in Lower-Limb Prosthetic Biomechanics-Socket Interface: A Review. *J Rehabil Res Dev 38* (2), 161–174.

(281) Hachisuka, K.; Matsushima, Y.; Ohmine, S.; Shitama, H.; Shinkoda, K. Moisture Permeability of the Total Surface Bearing Prosthetic Socket with a Silicone Liner: Is It Superior to the Patella-Tendon Bearing Prosthetic Socket? *J UOEH* **2001**, *23* (3), 225–232. https://doi.org/10.7888/JUOEH.23.225.

(282) Cagle, J. C.; Reinhall, P. G.; Hafner, B. J.; Sanders, J. E. Development of Standardized Material Testing Protocols for Prosthetic Liners. *J Biomech Eng* **2017**, *139* (4), 0450011. https://doi.org/10.1115/1.4035917.

(283) Lao, L.; Shou, D.; Wu, Y. S.; Fan, J. T. "Skin-like" Fabric for Personal Moisture Management. *Sci Adv* **2020**, *6* (14). https://doi.org/10.1126/SCIADV.AAZ0013/SUPPL_FILE/AAZ0013_SM.PDF.

(284) Klute, G. K.; Glaister, B. C.; Berge, J. S. Prosthetic Liners for Lower Limb Amputees: A Review of the Literature. *http://dx.doi.org/10.3109/03093641003645528* **2010**, *34* (2), 146–153. https://doi.org/10.3109/03093641003645528.

(285) Klute, G. K.; Rowe, G. I.; Mamishev, A. V.; Ledoux, W. R. The Thermal Conductivity of Prosthetic Sockets and Liners. *Prosthet Orthot Int* **2007**, *31* (3), 292–299.

(286) Seymour, R. Introduction to Prosthetics and Orthotics. *Prosthetics and Orthotics: Lower Limb and Spinal* **2002**, 3–35.

(287) Walter, D. *Perforated liner U.S. patent number 10,639,173, Aug 24, 2017*. https://uspto.report/patent/grant/10,639,173 (accessed 2023-08-02).

(288) Hansen, A.; Koehler-Mcnicholas, S.; Nickel, E.; Barrons, K.; Starker, F.; Mion, S.; Ferguson, J.; Fairhurst, S.; Ramasamy, E.; Koester, K.; Dearth, C.; Hendershot, B.; Pruziner, A.; Anderson, P.; Hassinger, L.; Laufer, D.; Schneider, U. *BREATHABLE RESIDUAL-LIMB SOCKET SYSTEM. US Patent Application Application #20210137707, May 13, 2021*. https://patents.justia.com/patent/20210137707 (accessed 2023-08-02).

(289) Wehmeyer, G.; Yabuki, T.; Monachon, C.; Wu, J.; Dames, C. Thermal Diodes, Regulators, and Switches: Physical Mechanisms and Potential Applications. https://doi.org/10.1063/1.5001072.

(290) Lee, S.; Hippalgaonkar, K.; Yang, F.; Hong, J.; Ko, C.; Suh, J.; Liu, K.; Wang, K.; Urban, J. J.; Zhang, X.; Dames, C.; Hartnoll, S. A.; Delaire, O.; Wu, J. Anomalously Low Electronic Thermal Conductivity in Metallic Vanadium Dioxide. *Science* **2017**, *355* (6323), 371–374. https://doi.org/10.1126/SCIENCE.AAG0410.

(291) Liu, H.; Shi, X.; Xu, F.; Zhang, L.; Zhang, W.; Chen, L.; Li, Q.; Uher, C.; Day, T.; Snyder Jeffrey, G. Copper Ion Liquid-like Thermoelectrics. *Nat Mater* **2012**, *11* (5), 422–425. https://doi.org/10.1038/NMAT3273.

(292) Kim, K.; Kaviany, M. Thermal Conductivity Switch: Optimal Semiconductor/Metal Melting Transition. *Phys Rev B* **2016**, *94* (15), 155203. https://doi.org/10.1103/PHYSREVB.94.155203/FIGURES/18/MEDIUM.

(293) Li, C.; Ma, Y.; Tian, Z. Thermal Switching of Thermoresponsive Polymer Aqueous Solutions. *ACS Macro Lett* **2018**, *7* (1), 53–58. https://doi.org/10.1021/ACSMACROLETT.7B00938/SUPPL_FILE/MZ7B00938_SI_001.PDF.

(294) Choy, C. L. Thermal Conductivity of Polymers. *Polymer (Guildf)* **1977**, *18* (10), 984–1004. https://doi.org/10.1016/0032-3861(77)90002-7.

(295) Choy, C. L.; Chen, F. C.; Luk, W. H. Thermal Conductivity of Oriented Crystalline Polymers. *Journal of Polymer Science: Polymer Physics Edition* **1980**, *18* (6), 1187–1207. https://doi.org/10.1002/POL.1980.180180603.

(296) Shanker, A.; Li, C.; Kim, G. H.; Gidley, D.; Pipe, K. P.; Kim, J. High Thermal Conductivity in Electrostatically Engineered Amorphous Polymers. *Sci Adv* **2017**, *3* (7). https://doi.org/10.1126/SCIADV.1700342/SUPPL_FILE/1700342_SM.PDF.

(297) Shulumba, N.; Hellman, O.; Minnich, A. J. Lattice Thermal Conductivity of Polyethylene Molecular Crystals from First-Principles Including Nuclear Quantum Effects. *Phys. Rev. Lett* **2017**, *119*, 185901. https://doi.org/10.1103/PhysRevLett.119.185901.

(298) Diaz, J. A.; Ye, Z.; Wu, X.; Moore, A. L.; Moon, R. J.; Martini, A.; Boday, D. J.; Youngblood, J. P. Thermal Conductivity in Nanostructured Films: From Single Cellulose Nanocrystals to Bulk Films. *Biomacromolecules* **2014**, *15* (11), 4096–4101. https://doi.org/10.1021/BM501131A/SUPPL_FILE/BM501131A_SI_001.PDF.

(299) Antlauf, M.; Andersson, O. Thermal Conductivity of Porous and Dense Networks of Cellulose Nanocrystals. *Macromolecules* **2022**, *55* (13), 5326–5331. https://doi.org/10.1021/ACS.MACROMOL.2C00153/ASSET/IMAGES/LARGE/MA2C00153_0007.JPEG.

(300) Uetani, K.; Hatori, K. Thermal Conductivity Analysis and Applications of Nanocellulose Materials. *Sci Technol Adv Mater* **2017**, *18* (1), 877–892. https://doi.org/10.1080/14686996.2017.1390692.

(301) Liu, J. C.; Martin, D. J.; Moon, R. J.; Youngblood, J. P. Enhanced Thermal Stability of Biomedical Thermoplastic Polyurethane with the Addition of Cellulose Nanocrystals. *J Appl Polym Sci* **2015**, *132* (22). https://doi.org/10.1002/APP.41970.

Chapter 2: Quantitative Determination of Metal Ion Adsorption on Cellulose Nanocrystals Surfaces

This chapter is presented as submitted to ACS Nano.

2.1 Abstract

Nanocellulose is a bio-based material that holds significant potential in the field of water purification. Of particular interest is its potential use as a key sorbent material for the removal of metal ions from solution. However, the structure of metal ions adsorbed onto cellulose surfaces is not well understood. The focus of this work is to determine quantitatively the three-dimensional distribution of metal ions of different valencies surrounding negatively charged carboxylate functionalized cellulose nanocrystals (CNC) using Anomalous Small Angle X-ray Scattering (ASAXS). These distributions can affect water and ionic permeability in these materials. The data show that increasing the carboxylate density on the surface of the CNCs from 740 mmol/kg to 1100 mmol/kg changed the nature of structure of the adsorbed ions from a monolayer into a multilayer structure. The monolayer was modeled as a Stern layer around the CNC nanoparticles, whereas the multilayer structure was modeled as a diffuse layer on top of the Stern layer around the nanoparticles. Within the Stern layer, the maximum ion density increases from 1680 mmol of Rb^+ per kg of CNC to 4350 mmol of Rb^+ per kg of CNC with the increase in the carboxylate density on the surface of the nanoparticles. Additionally, the data show that the CNCs can leverage multiple mechanisms, such as electrostatic attraction and the chaotropic effect, to adsorb ions of different valencies. By understanding the spatial organization of the adsorbed metal ions, the design of cellulose-based sorbents can be further optimized to improve uptake capacity and selectivity in separation applications.

2.2 Introduction

As the need for water in industrial processes, agriculture, and for personal consumption continues to increase and natural reservoirs are strained, more regions are becoming water-stressed such that the demand for water in these regions has (or soon will) exceeded the available water. Increased urbanization in these water-stressed regions coupled with industrial expansion increases the demand for these limited water sources.[1,2] Additionally, pollution from dyes[3], heavy metals, and pesticides[4] is a growing problem that threatens the supply of fresh water.[5,6] Dye effluents have been identified as the largest class of pollutants from industrial sources and are especially problematic as they pose health risks to humans, flora, and fauna.[3,6–8] In addition to dye contamination, heavy metal pollution is a growing ecological and public health concern.[9,10] Heavy metals can have deleterious effects even at extremely low concentrations, so effective removal methods are essential to producing safe, potable water.

This demand, coupled with the declining supply, heightens the need for potable water to be produced from underutilized resources, like contaminated fresh water and wastewater. For example, according to the US Environmental Protection Agency (EPA), only 7 to 8% of the thirty-two billion gallons of waste effluent produced each day are recycled.[11] To improve this, several technologies like membrane filtration, flocculation, and sorbents are used to generate potable water.[6] Of these methods, sorbents are commonly used to remove contaminants that are not easily degraded. Sorbents sequester chemicals in the water through adsorption and absorption processes, enabling the elimination of these contaminants when the sorbents are removed from solutions. Traditionally, activated carbons are commonly used as sorbents. However, their use can be expensive both from financial and energy standpoints, so attempts have been made to identify alternative sorbents.[3,6,12]

Natural biopolymers derived from low-cost, renewable bio-sources such as algae, plants, microbes, and animals represent promising foundations for sustainable alternatives.[6,13] In particular, polysaccharides and their derivatives have exhibited high removal efficiency for both inorganic contaminants like heavy metals and organic pollutants such as dyes via adsorption. As such various polysaccharides, including chitosan[7,10,14] and cellulose[15,16], have been utilized in water purification applications.[6] Cellulose is particularly promising as it is the most common biopolymer on the planet,[17] and can act as an abundant, low-cost adsorbent with a surface that can be engineered through facile chemical modification to enhance the sorption capacity and selectivity.[18,19] Nanocellulose are nanosized particles of cellulose that can be obtained directly from the biosource.[13,18,20–22] Cellulose nanocrystals (CNCs) are a class of nanocellulose that consists of high aspect ratio nanoparticles that can be isolated from many different biosources, like cotton, wood, or grasses such as *Miscanthus* x. *Giganteus* (*MxG*).[13,23,24] Various charged moieties, such as carboxylates, sulfates, and phosphates, have been introduced to the surface of CNCs. Studies have been conducted to evaluate the ability of these functionalized materials to remove inorganic contaminants such as Cr^{3+}, Pb^{2+}, and Cd^{2+} or charged organic dyes such as Methylene Blue and Crystal Violet.[18,25–39]

While these studies have shown that cellulose-based sorbents can effectively sequester various ionic contaminants, the spatial distribution of the resulting adsorbed species in and around the adsorbent has not been thoroughly investigated. The reason for this limited knowledgebase is that most characterization techniques do not reveal enough information about the differences in the arrangement of heavy metal ions relative to the crystalline cellulose sorbent. Previous studies have employed adsorption isotherms combined with data fitting models (i.e., the Langmuir model) to determine the adsorption mechanism.[25] Other studies have utilized spectroscopic techniques like

Fourier Transform Infrared (FTIR) spectroscopy and X-ray Photoelectron spectroscopy (XPS) to investigate the mechanism behind metal ion adsorption.[26] These studies provide a very localized interfacial bonding structure and found the adsorption mechanism to be a combination of complexation between the ions and the surface functional groups as well as ion-exchange.[26] However, these techniques lack information about the long range diffuse three-dimensional distribution of the ions around the charged cellulose nanoparticles.

Anomalous Small-angle X-ray Scattering (ASAXS) has been used to characterize a variety of charged nanomaterials systems including polyelectrolyte brushes,[40,41] DNAs,[42–45] and polyoxometalates[46] to quantitatively determine the distribution of ions surrounding them. A typical ASAXS measurement records the changes in the small-angle X-ray scattering (SAXS) intensity from a sample of interest as a function of energy very near and traversing the absorption edge of an element of interest (resonant element) in the sample. The elemental sensitivity in the scattering pattern comes from the changes in the scattering contrast of the resonant element near its absorption edges. After obtaining the energy-dependent scattering patterns it is possible to extract the scattering contribution of the resonant element. In addition, the energy-dependent scattering pattern can be directly analyzed via a physical model of the nanomaterial system.[47] The extraction method of scattering contributions from energy-dependent scattering patterns was first introduced by Stuhrmann[48–50] and, is hence, named the Stuhrmann method.[51] The extraction of the scattering components can be challenging on account of the weak scattering contribution from the resonant element and the presence of statistical fluctuations in the scattering patterns obtained experimentally. While this approach can be challenging, it does provide a direct way to examine the scattering contribution from the resonant element. Alternatively, if the size and morphology of the nanomaterial being investigated is known, e.g., from real space imaging techniques such as

electron microscopy or atomic force microscopy, then this information allows models of the distribution of ions surrounding the nanomaterial to be developed. Such models can then be used to either calculate the scattering contributions from the element of interest or calculate the energy-dependent scattering patterns.

Reported herein are studies of monovalent (Rb^+), divalent (Sr^{2+}), and trivalent (Y^{3+}) ions adsorbed onto carboxylate functionalized cellulose nanocrystals (CNC-COOH) using ASAXS to determine the structure of the adsorbed ions and gain insight into the mechanism behind their adsorption. As one of the goals of this work is to show the feasibility of ASAXS to determine the ion-distribution around CNCs and the role of electrostatic interactions, initial ASAXS experiments were carried out at the energies at which the absorption of the X-rays by the samples can be minimized, while at the same time maintaining a strong X-ray scattering signal. In this regard, Rb^+ with the K-edge X-ray absorption energy of 15.2 keV is a good initial choice of ion for these experiments. Sr^{2+} and Y^{3+} were selected as multivalent adsorption targets on account of their proximity to Rb^+ in the periodic table enabling the effect of valency on ion adsorption to be investigated while comparing ions of similar size and with similar X-ray absorption edges of 16.105 keV, and 17.038keV for Sr and Y, respectively.

2.3 Results and Discussion

2.3.1 Isolation and Functionalization of Cellulose Nanocrystals

CNCs were isolated from *Miscanthus* x. *Giganteus* (*MxG*) before being oxidized to yield the *MxG*-CNC-COOH following literature procedures.[13,52] In short, the *MxG* stalks undergo a series of steps, mechanical treatment, base washes, bleaching, and acid washes, in order to isolate the CNCs. (2,2,6,6-Tetramethylpiperidin-1-yl)oxyl (TEMPO)-mediated oxidation is then used to introduce carboxylic acid groups on the surface (Figure 2.1(a)). This oxidation method is

commonly used in the literature to introduce negative charges on the surfaces of CNCs, which also enables electrostatically-driven adsorption of cations to the carboxylate surface groups. The carboxylate density of the crystals was measured to be ca. 1100 mmol/kg via conductometric titration (Figure S2.1 and Table S2.1). In order to probe the effect of carboxylate density on ion adsorption, this TEMPO-mediated step was also carried out under different conditions with a lower ratio of TEMPO to NaOCl to synthesize a second batch of CNCs with a lower carboxylic acid density of ca. 740 mmol/kg. These two samples will be referred to as *MxG*-CNC-$COOH_{1100}$ and *MxG*-CNC-$COOH_{740}$ to differentiate the higher and lower surface density samples. The successful functionalization was confirmed by FTIR showing the peak that corresponds to the formation of the carboxylate's carbonyl stretch and TGA exhibiting the degradation and carbon yield associated with carboxylate functionalized CNCs (Figures S2.2 and S2.3, respectively). Both batches of *MxG*-CNC-COOHs maintained a crystallinity index of 0.78 and 0.71 for the *MxG*-CNC-$COOH_{1100}$ and the *MxG*-CNC-$COOH_{740}$ samples, respectively (determined by WAXS, Figure S2.4). The *MxG*-CNC-$COOH_{1100}$ crystals were measured by AFM (Figure 2.1(b)) and found to have an average length of 250 ± 170 nm (n = 700) and average height and width of 2.4 ± 0.6 nm and 13 ± 2.0 nm (n = 30), respectively. The *MxG*-CNC-$COOH_{740}$ crystals were found to have dimensions of 300 ± 120 nm by 3.5 ± 0.7 nm by 8.5 ± 1.9 nm when measured with the same AFM procedure (Figure S2.5). However, the width measurement is artificially larger than the real width of the CNC crystals on account of the tip broadening phenomenon (Figure S2.6). After accounting for this effect, the width of the CNCs is 3.5 ± 2.0 nm. These data are consistent with the literature values for *MxG*-CNCs.[13,24,52]

2.3.2 Parallelepiped Model of CNCs

The *MxG*-CNCs can be described as having a ribbon-like parallelepiped shape.[13] Thus, in order to extract metrical information from ASAXS data, a multilayered parallelepiped models, as shown in Figure 2.1(c) and Figure 2.1(d), were used to describe the *MxG*-CNC-COOH nanoparticles and the distribution of ions surrounding them in an aqueous environment. As per the model, the bare CNC is the core and the initial shell surrounding the core represents the Stern layer of adsorbed metal ions on the nanocrystal surfaces. The thickness of the Stern layer is defined as the ionic diameter of the appropriate metal ion.[53–55] A subsequent layer on top of the Stern layer is included in the model as a diffuse layer of ions surrounding the nanoparticle. Additional details about model are discussed in the Supporting Information, Section S2.1.

Simulation: To validate the parallelepiped model, the model was applied with the XModFit program[56] to the simulated energy-dependent X-ray scattering data (Figure S2.7) based on CNCs of with dimensions obtained from the AFM measurements (H=2.4nm, W=3.5nm, L=250.0nm), with metal ions surrounding them in an aqueous environment. The metal ions used for the simulation were Rb^+ ions with uniform density 0.3 gm/cm^3 adsorbed onto the CNC surfaces and 0.00855 gm/cm^3 (100mM) in the bulk aqueous phase. The thickness of the Stern layer is considered the ionic diameter of Rb^+ (0.332nm). The energies chosen to simulate the intensities are within 1keV of the Rb K-Edge (i.e., 14.2-15.2keV). In order to be able to simulate the energy-dependent SAXS data that resembles experimental data, statistical variances similar to those of the experimental data (shown in Figure 2.1(e)) were added to the simulated intensities. As the energy dependence is relatively weak, a point at Q=0.021Å^{-1} is taken from each simulated spectrum and plotted against energy (Figure S2.7) and the data clearly show the expected increase in intensity

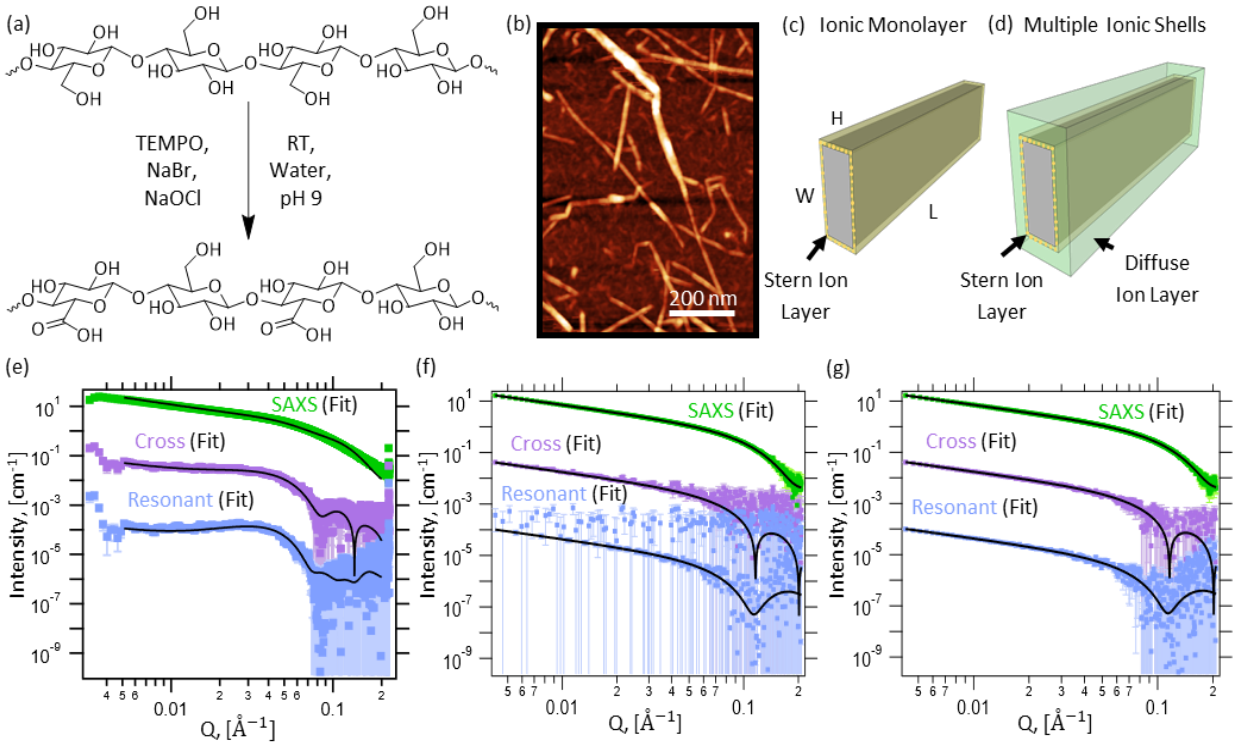

Figure 2.1. (a) Synthesis of carboxylic acid-functionalized CNCs (*MxG*-CNC-COOH$_X$), where x is the surface density of carboxylic acid groups in mmol/kg. (b) AFM Image of *MxG*-CNC-COOH$_{1100}$ on a mica substrate (c) Representation of a Stern layer of ions (yellow) adsorbed in a monolayer to the CNC core (grey). (d) Representation of a diffuse layer of ions associating with the Stern layer and CNC core. (e) ASAXS data from *MxG*-CNC-COOH$_{1100}$ in 50 mM RbCl solution with parallelepiped model fits. Scattering components with error bars obtained using Sturhmann method with (f) inequality and (g) equality constraints fit to simulated X-ray scattering data from the parallelepiped model of CNCs as seen in Figure S2.7. The corresponding scattering components simulated from the model are shown as solid black lines.

as scattering factor (f′) increases with incident X-ray energy moving away from the absorption edge of the metal ion.

The Stuhrmann method is applied to the energy-dependent simulated intensities to obtain different scattering components with both the inequality and equality constraints (Supplementary

Information Section S2.2). On account of the presence of statistical variance in the data, variances in the scattering components were also observed. It is important to note that the inequality constraint only provides a lower limit for the resonant term and is therefore not capable of providing a well-constrained estimate of weak 'resonant scattering' from metals ions, as evident from the large uncertainties shown in Figure 2.1(f) at low Q values in the absence of statistical variances. The equality constraint, on the other hand, provides constrained estimates of the resonant term for the ion distribution of the parallelepiped model as shown in Figure 2.1(g). While the equality constraint can provide a constrained estimate, it is to be used with caution as the minima of energy-dependent SAXS data might provide artifacts and should be verified with simulations similar to those presented here. Satisfied that the equality constraint does not produce artifacts and provides a better fit for the parallelepiped model when applied to the simulated data, the same equality constraint was applied to the experimental energy-dependent SAXS data to obtain the scattering components and subsequently the metrical information about the CNCs and the distribution of ions surrounding them.

The parallelepiped model was initially used to fit the scattering components obtained from the ASAXS data and in the process to determine the distribution of the adsorbed Rb^+ ions in the Stern layer around the *MxG*-CNC-COOH. The model was also used to refine the dimensions of the *MxG*-CNC-COOH nanoparticles in the samples starting with the anticipated dimensions from AFM data. The length of 250 nm was input as a constant to reduce the number of variables in the fitting. The heights of the crystals determined by AFM and ASAXS match within error. As mentioned previously, the width of the crystals will be overestimated in the AFM measurement on account of the tip-broadening phenomenon. However, taking the size of the AFM tip into account (Figure S2.6) the width calculated by the model agrees with the AFM measurements, within error. By

comparing the size of the crystals as determined by the model (H=2.8 ± 0.12 nm, W=4.2 ± 0.18 nm, L=250 nm) with the size of crystals as determined by AFM (H=2.4 ± 0.6 nm, W=3.5 ± 2.0 nm, L=250 ± 170 nm), the model can be validated as it generates accurate metrical data from the anomalous scattering components as shown in Figure 2.1(e).

2.3.3 Investigation of the Adsorption of the Rb^+ ions on the CNCs

With the validation of the parallelepiped model in hand the next step was to explore the metal ion adsorption on the CNCs. To this end the *MxG*-CNC-$COOH_{740}$ and *MxG*-CNC-$COOH_{1100}$ samples were soaked in 50 mM RbCl solutions which were then studied using ASAXS. Interestingly, the one-dimensional ASAXS data (Figure 2.2) shows a shift in the form factor for these two samples. This shift is most clearly seen in the resonant and cross terms as the terms for *MxG*-CNC-$COOH_{1100}$ exhibit higher intensities than the corresponding *MxG*-CNC-$COOH_{740}$ terms. Since the resonant term is correlated with Rb^+ for these experiments, the increase in the intensity of the resonant term is indicative of a larger amount of Rb^+ around the CNC in those samples. In order to extract metrical information about the adsorbed ions, several parameters such as the density of Rb^+ within each layer around the CNCs were varied in the parallelepiped model to generate the best fit. By fitting the parallelepiped model to the data, it was determined that a peak concentration

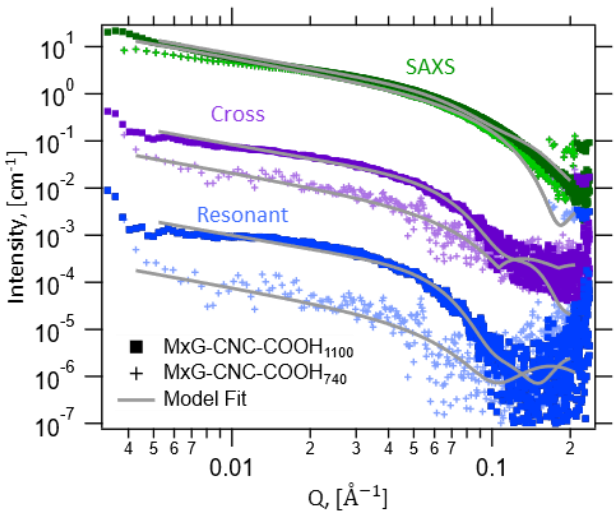

Figure 2.2. ASAXS data of *MxG*-CNC-COOH$_{740}$ and *MxG*-CNC-COOH$_{1100}$ soaked in 200 mM RbCl split into their respective SAXS, cross, and resonant terms with the parallelepiped model fits for each set of data shown in gray.

of Rb^+ ions, which is orders of magnitude larger than the bulk concentration, forms within 3.32 Angstroms of the *MxG*-CNC-COOH$_{740}$ surface and quickly returns to the bulk concentration beyond this distance. This result is indicative of the formation of a Stern layer, which has a thickness on the order of the ionic diameter of the adsorbed ion, around the nanoparticle (Figure 2.1(c)). Although the *MxG*-CNC-COOH$_{1100}$/RbCl samples also exhibited a peak concentration of Rb^+ ions within the same distance from the crystal surface, a single Rb^+ layer in the parallelepiped model was insufficient to fit the ASAXS data. Thus, the model was adjusted to include multiple Rb^+ shells around the CNC core (Figure 2.1(d)). This multilayer model fits the *MxG*-CNC-COOH$_{1100}$/RbCl data by adding a diffuse layer on top of the highly concentrated Stern layer. A diffuse layer around a Stern layer is a known phenomenon that is observed in charged colloids in accordance with the Gouy-Chapman and Grahame models for electrolyte adsorption.[55] The introduction of a diffuse layer for the MxG-CNC-COOH$_{1100}$/RbCl samples implies that the Rb^+ could not fill in the Stern layer in a manner that was able to balance the surface potential of the

charged CNCs. Since the Stern layer is composed of Rb^+ ions adsorbing to the surface as well as water molecules solvating both the ions and the surface, these solvent molecules limit the maximum capacity of the Stern layer. The combination of electrostatic interactions and hydrostatic repulsion leads to the formation of the diffuse layer.[55] In the case of the MxG-CNC-$COOH_{740}$/RbCl samples, the Rb^+ ions are able to occupy the Stern layer such that the surface potential is sufficiently neutralized without the formation of a diffuse layer.

After fitting the ASAXS data generated by the *MxG*-CNC-$COOH_{1100}$ and *MxG*-CNC-$COOH_{740}$/Rb^+ samples with the parallelepiped model (Figures S2.8 and S2.11), the adsorbed Rb^+ ion density was extracted from the model and compared to the surface charge density for each sample as determined by the conductometric titration (Figure S2.1). The *MxG*-CNC-$COOH_{1100}$ shows a maximum total Rb^+ ion adsorption in both the Stern and diffuse layers of 14700 ± 265 mmol of Rb^+ per kg of CNC with a maximum Rb^+ ion density in the Stern layer of 4350 ± 54 mmol of Rb^+ per kg of CNC. The *MxG*-CNC-$COOH_{740}$ exhibits a maximum Rb^+ ion adsorption of 1680 ± 51 mmol of Rb^+ per kg of CNC in the monolayer surrounding the CNC. Comparison of the Rb^+ ion density adsorbed on to *MxG*-CNC-$COOH_{1100}$ and *MxG*-CNC-$COOH_{740}$ (Figure 2.3) shows that the multilayer adsorption (Stern layer plus the surrounding diffuse layer) of the *MxG*-CNC-$COOH_{1100}$ results in significantly more ions surrounding these CNCs. In both the *MxG*-CNC-COOH samples the number of adsorbed cations is greater than the amount of negative charge on the surface of both *MxG*-CNC-COOH samples (horizontal dashed lines in Figure 2.3). This significant ion adsorption implies that the driving force behind this effect is more than the ionic electrostatic interactions between the metal ions and the carboxylates on the surface. Additional specific adsorption sites for the Rb^+ could be provided by the diols present along the cellulose chains - the hydroxyl groups on the C2 and C3 carbons of the cellulose repeat unit can associate

with the Rb^+ through ion-dipole interactions. The number of diols on the surface of the CNCs is approximately equal to the number of carboxylate groups on the surface and as such the presence of the diols effectively doubles the number of potential adsorption sites along the hydrophilic faces of the CNC surface to 2200 mmol/kg of CNC on the *MxG*-CNC-$COOH_{1100}$ samples. However, these potential adsorption sites are still less than the calculated amount of Rb^+ ions adsorbed to the CNCs. Therefore, additional Rb^+ ion adsorption sites are needed to account for the additional Rb^+ in the Stern layer. Adsorption to these other sites may be driven by the chaotropic effect. It has been shown that poorly solvated monovalent ions (chaotropic ions) like Rb^+ are capable of adsorbing onto oppositely charged hydrophobic particles through interactions between the ions and hydrophobic regions of the particles.[57] The poor solvation environment around the hydrophobic surface interacts favorably with the poorly solvated chaotropic ion leading to adsorption and entropic gain by releasing the solvent molecules around both the ion and the hydrophobic surface. As recent studies utilizing three-dimensional AFM corroborated by molecular dynamic simulations have shown that, certain cellulose crystal faces like the (200) crystal face exhibit regions void of cellulose-water hydrogen bonds indicating that these faces are hydrophobic.[58] Furthermore, CNCs have been shown to exhibit amphiphilicity since these nanoparticles can stabilize oil-water interfaces by acting as nano-sized surfactants.[59–62] As such the CNCs have hydrophobic regions which can provide additional adsorption site for chaotropic ions. The combination of both electrostatic and chaotropic adsorption sites for the Rb^+ ions enables a higher than expected concentration of Rb^+ to reside in the Stern layer.

The structure and adsorption process also depend on the concentration of metal ions in the initial solution. By varying the feed solution's concentration between 50 mM, 100 mM, 200 mM, and 400 mM, it was observed that the adsorbed Rb^+ in the Stern layer peaks at 1680 ± 51 mmol of Rb^+

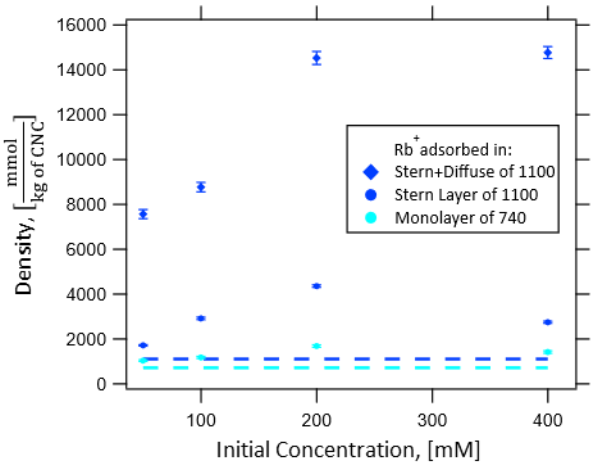

Figure 2.3. Comparison of the density of Rb^+ ions adsorbed on the *MxG*-CNC-$COOH_{740}$ to the density of Rb^+ ions on the *MxG*-CNC-$COOH_{1100}$ for various concentrations (50, 100, 200, and 400 mM RbCl) and to the surface density of carboxylates on both the *MxG*-CNC-$COOH_{740}$ and the *MxG*-CNC-$COOH_{1100}$ as represented by the horizontal dashed lines. The errorbars on the density values were obtained from fitting the ASAXS data with rectangular parallelepiped model with 68% of confidence interval.

per kg of CNC around an initial solution concentration of 200 mM RbCl for the *MxG*-CNC-$COOH_{740}$ samples (Figure 2.3). For the *MxG*-CNC-$COOH_{1100}$ samples, the total amount of adsorbed Rb^+ appears to reach a plateau from 200 to 400 mM RbCl with total adsorbed ion densities of 14500 ± 290 mmol of Rb^+ per kg of CNC 14700 ± 265 mmol of Rb^+ per kg of CNC, respectively (Figure 2.3). However, as the concentration of the initial solution increases, the Rb^+ ions appear to be less strongly associated with the *MxG*-CNC-COOH surface since the density of ions in the Stern layer decreases from 4350 ± 54 mmol of Rb^+ per kg of CNC to 2740 ± 43 mmol of Rb^+ per kg of CNC after 200 mM. This decline in density of ions in the Stern layer implies that at higher concentrations solute-solute and solute-solvent interactions begin to become more favorable than some of the solute-substrate interactions, which corresponds with the shortening of the Debye length as salt concentration increases.

2.3.4 Effect of Multivalent Ions

After investigating the adsorption of Rb^+ ions to the CNC surface, the adsorption of two multivalent ions, namely Sr^{2+} and Y^{3+}, to the CNCs was explored. Similar to the *MxG*-CNC-$COOH_{740}$/RbCl samples, a monolayer parallelepiped model as illustrated in Figure 2.1(b) fits the ASAXS data sufficiently well (see Figures S2.12-S2.13). These data indicate that the low surface charge density of the *MxG*-CNC-$COOH_{740}$ only supports the formation of an adsorbed Stern layer of these ions. As shown in Figure 2.4(a), for the *MxG*-CNC-$COOH_{740}$ samples, the adsorption isotherms exhibit a maximum in the adsorbed ion density of 1200 ± 51 mmol of Sr^{2+} per kg of CNC and 888 ± 26 mmol of Y^{3+} per kg of CNC for Sr^{2+} and Y^{3+}, respectively. Similarly, type *mx* adsorption isotherms with a maximum have been seen in other cellulose-based substrates when ion pairs are being adsorbed to the surface after initial cation exchange.[63–66] This maximum in the shape of the adsorption curve implies that as the bulk concentration increases the solute-solute interactions within the solution start to overcome the solute-substrate interactions.[63] It is likely, that as the concentration of salt in the solution increases, the driving force leading to the adsorption of ions and ion pairs decreases with the shortening of the Debye length and an electrical screening of the surface.[65,66] The maximum adsorbed ion density occurs at different initial ion concentrations for the *MxG*-CNC-$COOH_{740}$ samples, 200 mM, 200 mM, and 50 mM for Rb^+, Sr^{2+}, and Y^{3+}, respectively (Figure 2.4(a)). Unlike Rb^+, Sr^{2+} and Y^{3+} ions are not chaotropic but kosmotropic such that the hydration sheaths around the Sr^{2+} and Y^{3+} ions are more stable and as a result the chaotropic interaction with the hydrophobic regions of the CNCs is less favorable with such ions. Thus, the primary driving forces for Sr^{2+} and Y^{3+} adsorption appear to be electrostatic in nature with a combination of specific chemical interaction between the Sr^{2+} or Y^{3+} and the carboxylate and diol moieties on the surface as well as ion-ion correlations between the metal ions and

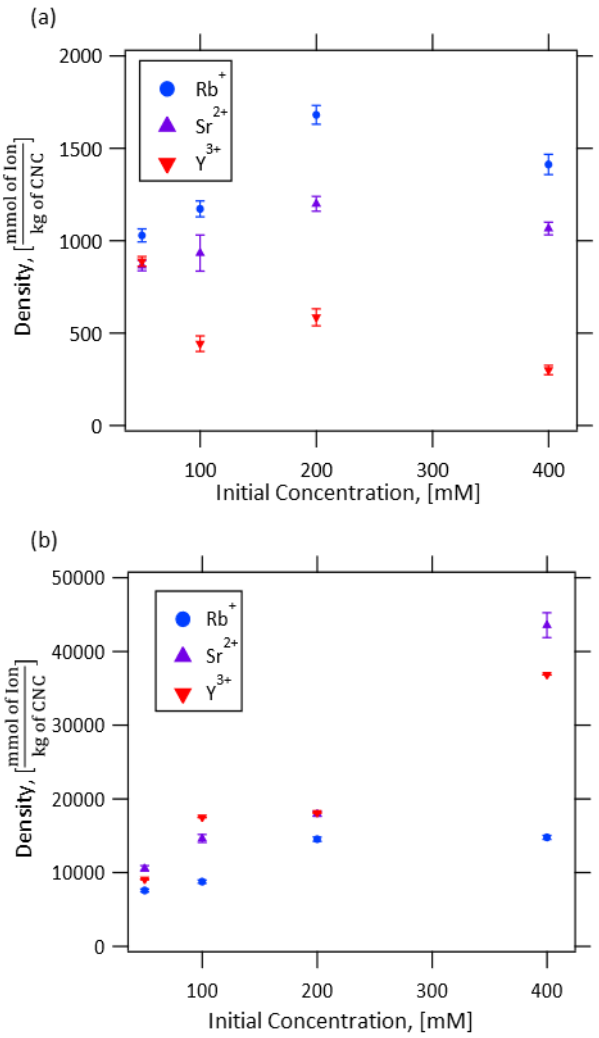

Figure 2.4. (a) The density of Rb^{+}, Sr^{2+}, and Y^{3+} adsorbed into the stern layer around the MxG-CNC-$COOH_{740}$ as the initial concentration of these ions increases (50, 100, 200, and 400 mM). (b) The total adsorbed ion density of Rb^{+}, Sr^{2+}, and Y^{3+} in both the stern and diffuse layers normalized by the mass of *MxG*-CNC-$COOH_{1100}$ in each sample as the initial ion concentration increases (50, 100, 200, and 400 mM). The errorbars on the density values were obtained from fitting the ASAXS data with rectangular parallelepiped model with 68% of confidence interval.

counterions. As observed in Figure 2.4(a), the Sr^{2+} exhibits a maximum adsorbed ion density at 200 mM initial concentration, whereas the Y^{3+} appears to saturate at 50 mM before decreasing as the initial concentration of the solution is increased. The shift in maximum adsorption density from

200 mM in the case of Sr^{2+} to 50 mM in the case of Y^{3+} is expected for the electrostatic adsorption of kosmotropic ions like Sr^{2+} and Y^{3+}. Since the Debye length scales with the ion valency, the increased salt concentration of the bulk solution will have a greater electrostatic effect on the more highly charged ions. Since the Y^{3+} ion is trivalent compared to the divalent Sr^{2+} ion the surface will likely be more effectively screened at lower concentrations of Y^{3+} than at equal concentrations of Sr^{2+}. The differences in the electrostatic screening of the surface may contribute to the Stern layer saturating at lower concentrations for Y^{3+} because the primary driving force is electrostatic in nature.

When the surface charge density on the CNCs is increased, the *MxG*-CNC-$COOH_{1100}$ samples adsorb more multivalent ions than the *MxG*-CNC-$COOH_{740}$ samples. As with the RbCl absorption data, a monolayer parallelepiped model is insufficient to fit these data. Therefore, a multilayer parallelepiped model illustrated in Figure 2.1(d) is used to fit the Sr^{2+} and Y^{3+} adsorption data for the *MxG*-CNC-$COOH_{1100}$ samples. The formation of both a Stern and diffuse layer of adsorbed ions is expected for kosmotropic ions like Sr^{2+} and Y^{3+}. As Figure 2.4(b) shows, the adsorbed ion densities of Sr^{2+} and Y^{3+} continue to increase as the initial concentrations increase showing that adsorption becomes easier as more ions are present and adsorb. This continued increase in adsorbed ions is seen in other kosmotropic ion adsorption isotherms as ion-ion correlations encourage more ions to fill the diffuse layer and potentially form additional layers as previous layers saturate.[63] Unlike the multivalent ions, the Rb^{+} isotherm plateaus at higher concentrations, indicative of saturation instead of the growth of additional adsorbed layers. This phenomenon could be caused by the limited amount of hydrophobic surface area on the sample such that once these regions are covered by Rb^{+} ions, the chaotropic driving force substantially weakens and the Stern and diffuse layers saturate. The nature of the adsorption at these higher concentrations

further supports the notion that the Sr^{2+} and Y^{3+} ions adsorbed through electrostatic driving forces while the Rb^{+} ions are adsorbed at least partially by different mechanisms.

2.4 Conclusions

A parallelepiped model was developed to analyze ASAXS data from parallelepiped-shaped nanoparticles like CNCs. This model was used in combination with ASAXS studies to give insights the nature of metal ion binding to CNCs. In particular, it was shown that the structure of ions adsorbed to *MxG*-CNC-COOH nanoparticles shifts as the carboxylate surface density is increased. In addition, the data shows that *MxG*-CNC-COOHs can leverage chaotropic, electrostatic, and complexation mechanisms to adsorb ions to their surfaces. The knowledge of these structures and mechanisms can help inform the design of improved cellulose-based sorbents for water purification applications. For example, understanding the dependence of the adsorbed ion distribution on initial concentration could improve efforts to optimize contaminant removal informing what contaminated sources could be ideal for purification with cellulose-based sorbents. This adsorbed molecular structure will likely vary between different contaminants. As such, future studies into the structure of other relevant water contaminants such as Hg, Cd, Pb, Cr, or As on cellulose nanocrystals may be of interest. Additional methods of improving the adsorptive capacity of these sorbents like polymer grafting may also be studied.

2.5 Materials and methods

2.5.1 Materials

Miscanthus x. *Giganteus* (*MxG*) pulp was provided by Aloterra Energy, LLC. Sodium hydroxide (NaOH), sodium hypochlorite (NaOCl), and acetic acid were purchased from Thermo Fisher Scientific. Sodium chlorite ($NaClO_2$), hydrochloric acid (HCl), 2,2,6,6-tetramethylpiperidine 1-oxyl (TEMPO), and sodium bromide (NaBr) were purchased from Millipore Sigma. Rubidium

chloride (RbCl), strontium chloride ($SrCl_2$), and yttrium chloride (YCl_3) were purchased from Sigma-Aldrich. All water used was deionized in-house and all chemicals were used as-received without further purification.

2.5.2 Cellulose Nanocrystal Isolation from Miscanthus X. Giganteus

Ground *MxG* stalks (266.6 g) were soaked in 4 L of 2 wt% sodium hydroxide solution at room temperature for 24 hrs. The stalks were then treated twice more with 4 L 2 wt.% sodium hydroxide solutions at 95°C for 24 hours each. After each treatment, the stalks were washed with deionized (DI) water until the permeate was neutral pH. The pulp was then suspended in 4 L of 2 wt.% sodium chlorite solution and 15 mL of glacial acetic acid and heated to 70°C for 2 hrs. After the reaction, the solution was vacuum filtered and washed with DI water until the solid was white with no other color. For these samples, the color of the *MxG* pulp remained white. To isolate CNCs, hydrolysis was carried out by suspending the bleached white pulp in 4L of 1M HCl. This slurry was then heated to 75°C and stirred for 15 hrs. The mixture was then cooled at room temperature before being vacuum filtered and rinsed with DI water until the permeate was neutral. The solids were then subjected to dialysis with DI water for 5 days with the external solution being replaced twice every day. The solutions were then freeze-dried to obtain the alcohol functionalized *MxG* CNCs (*MxG*-CNC-OH) as a white crystalline solid.

2.5.3 Synthesis of *MxG*-CNC-COOH from *MxG*-CNC-OH via TEMPO oxidation

In order to synthesize the *MxG*-CNC-$COOH_{1100}$ samples, TEMPO oxidation was conducted immediately after isolating the MxG-CNC-OH, without drying, following the previously published procedure with slight modifications.[13,52] The *MxG*-CNC-OH isolated from 250 g of dried *MxG* stalks were suspended in solution with 7.5 g of TEMPO, and 75 g of NaBr. 110 mL of

NaOCl was then added to this solution after which the pH was adjusted to 10.5 with 10 M NaOH. The pH was maintained between 10 and 11 for 3 hrs at which time the resulting *MxG*-CNC-$COOH_{1100}$ was centrifuged at 10,000 rpm and resuspended approximately 5 times in DI water to purify the sample. The nanoparticles were suspended in DI again before being freeze dried to yield a fluffy white powder of *MxG*-CNC-$COOH_{1100.}$

In order to synthesize the *MxG*-CNC-$COOH_{740}$ samples, 21.6 g of *MxG*-CNC-OH were dispersed into 1500 mL of DI water. Simultaneously, 1.687 g of TEMPO, 16.926 g of NaBr, and 138.109 g of NaOCl were dissolved into 500 mL of DI water. These two solutions were then mixed together and the pH was adjusted to 10 with NaOH and HCl. Once at pH 10, the reaction was allowed to proceed for 4.5 hrs with the pH being checked every half hour. The reaction was then quenched with 40 g of sodium chloride before being filtered and washed with DI water. The solid was redispersed in DI water and dialyzed for 5 days before being freeze-dried to produce *MxG*-CNC-$COOH_{740}$.

2.5.4 Conductometric Titration

The functional group density of the *MxG*-CNC-COOH samples was determined by conductometric titration. 75 mg of the *MxG*-CNC-COOH were dispersed into 150 mL of DI water using sonication. 15 µL of 12 M hydrochloric acid was added to 50 mL of the CNC dispersion to lower the solution's pH to 2-3. This suspension was then titrated with 0.01 M sodium hydroxide. In order to determine the charge density on the surface of the CNCs, the volume of 0.01 M sodium hydroxide used to titrate the weak acid functional groups in the conductometric titration was determined in Figure S2.1. The length of the initial trend line represents the volume of 0.01 M NaOH used to titrate the strong acid functional groups, while the plateau region corresponds to the

weak acid functional groups. From the volume of NaOH used to titrate these functional groups, the functional group density on the CNC surface can be determined by:

$$\textbf{\textit{Functional Group Density}} = \frac{\boldsymbol{CV_{NaOH}}}{\boldsymbol{M}}$$

Where C is the concentration of NaOH, V_{NaOH} is the volume of NaOH used to titrate the functional groups based on the difference between where the trendlines intersect, and M is the mass of CNCs in kg.

2.5.5 Thermogravimetric Analysis

The thermal stability of each CNC sample was measured through thermogravimetric analysis. For each sample, approximately 5 mg of the CNCs was heated from ambient temperature to 600 °C at a rate of 20 °C/min under a nitrogen atmosphere at a flow rate of 25 mL/min.

2.5.6 Degree of Crystallinity

Wide angle X-ray scattering (WAXS) conducted at the 12-ID-B beamline at the Advanced Photon Source at Argonne National Laboratory was used to determine the degree of crystallinity of the CNCs after hydrolysis and oxidation. The CNCs were packed tightly into a washer and held in place between two pieces of Kapton tape. The data was then processed using the SAXS GUI software at the beamline before being analyzed with the SAS Irena package in IGOR Pro 7. The crystallinity index of the samples was determined with the peak deconvolution method with a Gaussian fit.

2.5.7 Atomic Force Microscopy

Atomic force microscopy (AFM) was conducted on a Cipher ES Environmental AFM. Samples were prepared on a freshly-cleaved mica surface by first drop-casting poly(L-lysine), gently rinsing with DI water, then drop-casting the desired CNC sample suspended in DI water at 0.005

wt.%. The solution was allowed to sit for 3 minutes before once again gently rinsing with DI water before drying overnight. The samples were imaged in tapping mode with FS-1500 probes from Asylum Research and data was analyzed with Gwyddion software (Czech Metrology Institute).

2.5.8 Anomalous Small-Angle X-ray Scattering (ASAXS)

The *MxG*-CNC-COOH were vacuum cast onto PVDF membranes to form CNC nanopapers. PVDF was selected as the support membrane so that the nanopapers could be delaminated from the surface to create freestanding *MxG*-CNC-COOH films. In order to access the information about the distribution of cations, namely Rb^{+}, Sr^{2+}, and Y^{3+}, energy-dependent Small-angle X-ray Scattering (SAXS) or ASAXS measurements were performed on the chloride salt solution-soaked *MxG*-CNC-COOH samples. The ASAXS measurements were performed with X-rays of 20 energies within 1 keV below the K-absorption edges of Rb (15.2keV), Sr (16.105keV), and Y (17.038keV), respectively. The measurements were performed at the ASAXS facility of the NSF's ChemMatCARS, Sector-15 of Advanced Photon Source. The energy values were chosen in a way that the real part of the scattering factor (f′) of Rb, Sr, and Y could be equally spaced. For better understanding of the interaction of the cations with the *MxG*-CNC-COOH surfaces the ASAXS measurements were performed with increasing concentrations (50, 100, 200, 400mM) of the chloride salts of the cations. The samples in the form of thin films were loaded in Quartz capillary tubes of 1.5 mm outer diameter with 0.010mm wall thickness. Different samples were prepared by pouring salt solutions of different concentrations into the capillary tube to soak the films completely. ASAXS measurements were collected from the regions of the capillary tubes where the soaked films were present and from the regions with only solutions which will be considered as backgrounds. The salt solution scattering acts as a better background because it also takes care of the fluorescence background coming from the solution when the X-ray energies are closer to

the absorption edges. It is important that the changes in the intensity due to X-ray beam energy only comes from the changes in the scattering from the resonant element and not from the beam induced changes in the samples. Due to this reason, samples were tested for X-ray beam induced changes with varying lengths of exposure to the X-ray beam. These experiments established the maximum time of exposure for the ASAXS experiments to ensure that the samples were not damaged during the process. Apart from the samples and backgrounds, ASAXS data were also measured for an empty capillary tube, air, and glassy carbon for absolute scale normalization. Background subtraction and absolute scale normalization were done on the azimuthally averaged ASAXS data using software 'XAnoS' developed at NSF's ChemMatCARS.[67] Energy dependent azimuthally averaged data after background subtraction and absolute scale normalization were further processed to obtain SAXS-term ($\boldsymbol{I_S}$), Cross-term ($\boldsymbol{I_C}$), and Resonant-term ($\boldsymbol{I_R}$) as per Stuhrmann method as discussed in details in the Supplementary Information equations S1-S6.

2.5.9 Parallelepiped Model Development

Two different functions, 'Parallelepiped_Uniform' and Parallelepiped_Uniform_Edep', were created in the ASAXS category of the XModFit Software developed by ChemMatCARS[68] and available freely from Github[56] to simulate ASAXS scattering intensity from multilayered-parallelepiped structures. 'Parallelepiped_Uniform' calculates different scattering components ('SAXS-term', 'Cross-term', 'Resonant-term', and 'Total') from the above-mentioned multilayered-parallelepiped model. Whereas 'Parallelepiped_Uniform_Edep' calculates energy dependent total X-ray scattering from the multilayered-parallelepiped model. More details about the functions are available in the Supplementary Information, S1. This model can fit the data by varying several parameters. For these samples, the width and height of the inner core were varied while the length was held constant at the average length of the CNCs as determined by the AFM

measurements. Additionally, the concentration of adsorbed ions in the Stern were varied while the size of the Stern layer was held constant at the ionic diameter of the metal ion being measured by the ASAXS experiment. Additional layers beyond the Stern layer were also included with varying ion densities and lengths for each layer if they improved the model's ability to fit the data as they did for the case of the *MxG*-CNC-$COOH_{1100}$ samples.

2.6 Acknowledgements

This work was supported in part by National Science Foundation PIRE program under Grant No. NSF #1743475 and the NSF Center for Sustainable Polymers (CSP) (CHE-1901635) at the University of Minnesota. It made use of the shared facilities at the University of Chicago Materials Research Science and Engineering Center (MRSEC), supported by National Science Foundation (NSF) under award number DMR-2011854. Parts of this work were carried out at the Soft Matter Characterization Facility of the University of Chicago. NSF's ChemMatCARS, Sector 15 at the Advanced Photon Source (APS), Argonne National Laboratory (ANL) is supported by the Divisions of Chemistry (CHE) and Materials Research (DMR), National Science Foundation, under grant number NSF/CHE-1834750. This research used resources of the Advanced Photon Source, a U.S. Department of Energy (DOE) Office of Science user facility operated for the DOE Office of Science by Argonne National Laboratory under Contract No. DE-AC02-06CH11357. This work was supported as part of the Advanced Materials for Energy-Water Systems (AMEWS), an Energy Frontier Research Center funded by the U.S. Department of Energy, Office of Science, Basic Energy Sciences.

2.7 Supporting Information

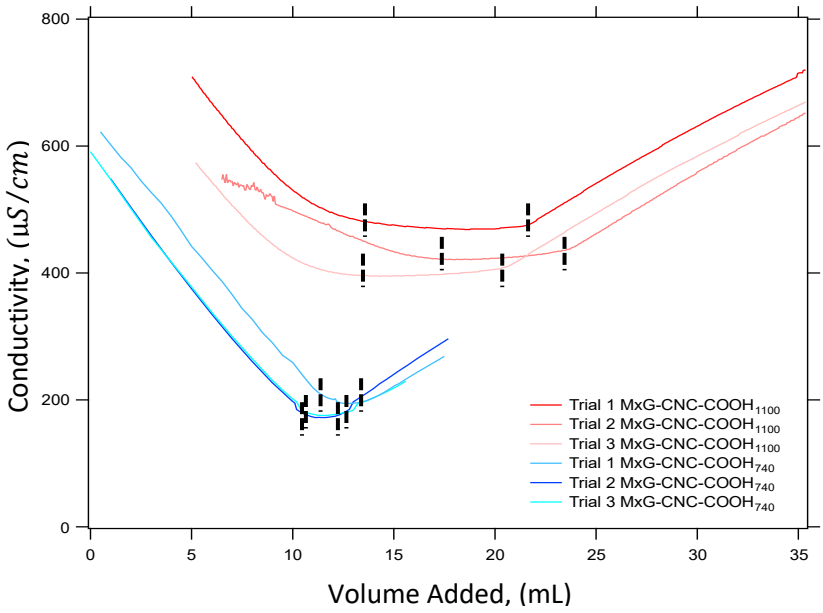

Figure S2.1. Plot of the Conductivity versus the volume of 0.01 M NaOH added to determine the amount of -COOH present on the MxG-CNC-COOH surfaces.[52] The amount of -COOH was determined by the length of the weak acid neutralization regime which corresponds to the plateaus in the curves as denoted by the black lines on each curve.

Table S2.1. Conductivity titration results used to measure the amount of -COOH on the surface of both MxG-CNC-COOH samples.

Samples	CNC Mass (mg)	Plateau Volume (mL)	-COOH Concentration ($^{mmol}/_{kg}$)	-COOH Density ($^{groups}/_{nm^2}$)
MxG-CNC-COOH$_{1100}$ 1	68	7.8	1147	1.20
MxG-CNC-COOH$_{1100}$ 2	48	5.9	1229	1.28
MxG-CNC-COOH$_{1100}$ 3	65	6.9	1062	1.11
Average			**1100 ± 100**	**1.2 ± 0.1**
MxG-CNC-COOH$_{740}$ 1	23.5	1.75	742	0.77
MxG-CNC-COOH$_{740}$ 2	25.33	1.73	683	0.71
MxG-CNC-COOH$_{740}$ 3	25.33	2.02	796	0.83
Average			**740 ± 56**	**0.77 ± 0.06**

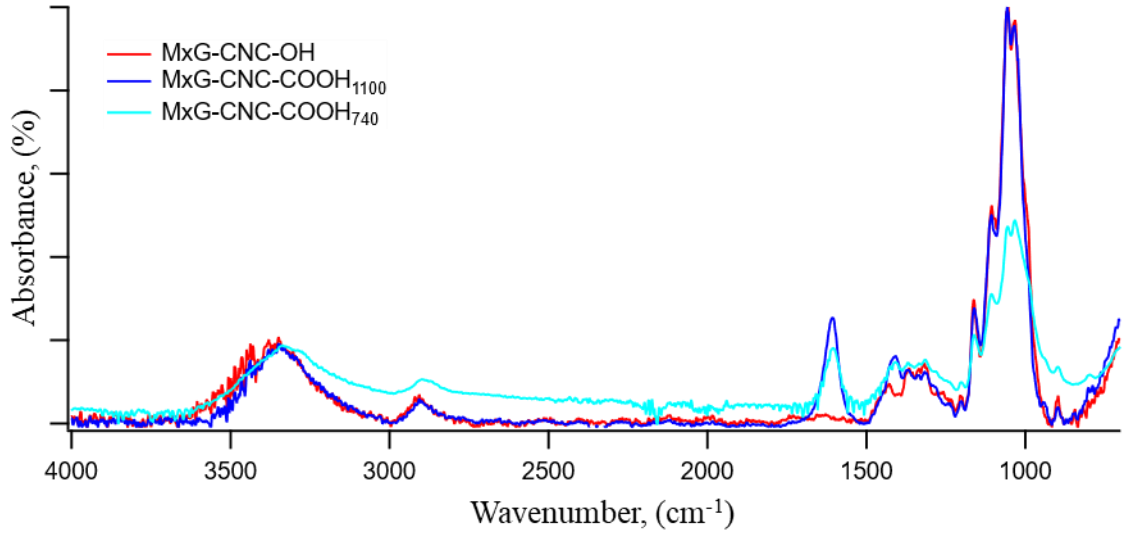

Figure S2.2. FTIR data showing the emergence of a peak that corresponds to a carbonyl stretch (@ 1600 cm^{-1}) that confirms the functionalization of MxG-CNC-OH into MxG-CNC-

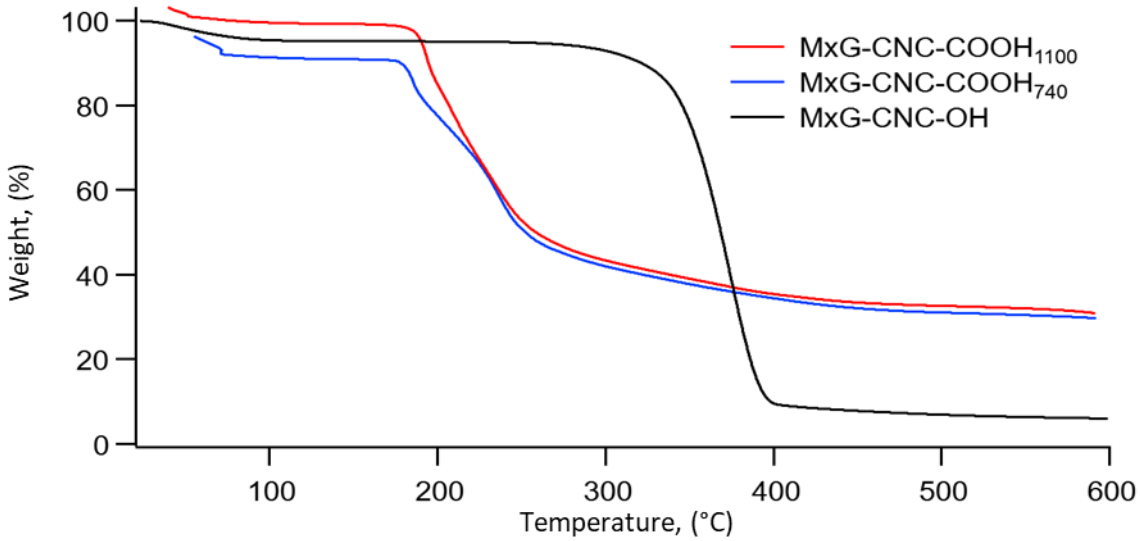

Figure S2.3. Hi-Res TGA curves for MxG-CNC-$COOH_{1100}$ (red), MxG-CNC-$COOH_{740}$ (blue), and MxG-CNC-OH (black) showing a shift in the degradation pattern and an increase in char yield after successful -COOH functionalization.

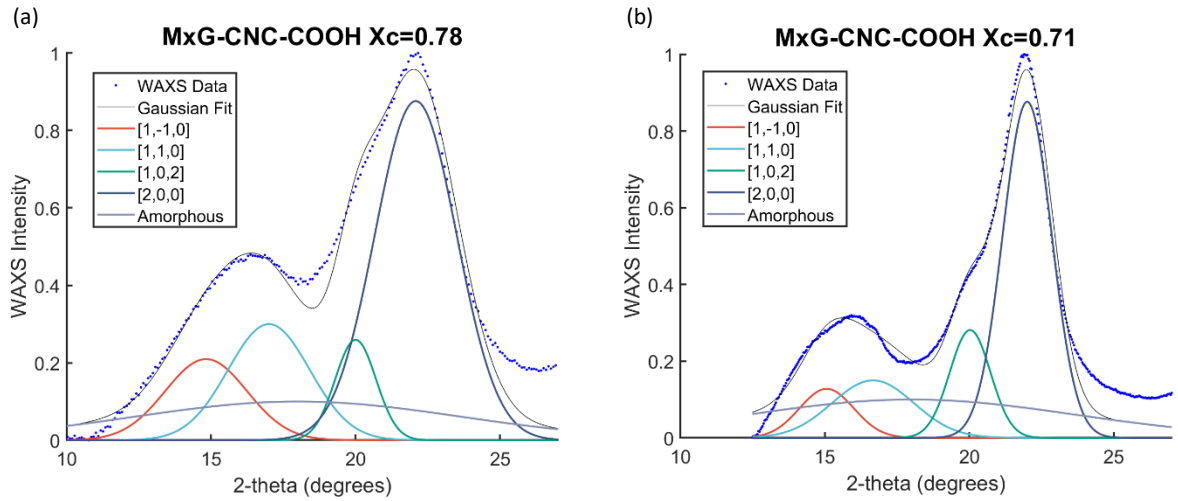

Figure S2.4. Wide angle X-ray scattering data (blue dots) plotted with Gaussian deconvolution peaks associated with each crystal plane to determine the crystallinity index of the MxG-CNC-COOH Samples.[52] a) MxG-CNC-$COOH_{1100}$ has a crystallinity index of 0.78. b) MxG-CNC-$COOH_{740}$ has a crystallinity index of 0.71.

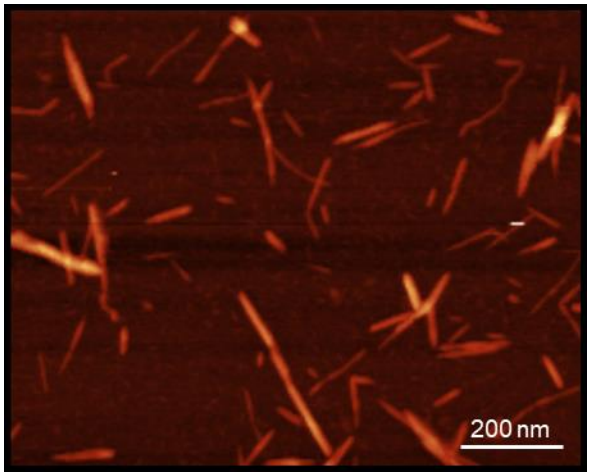

Figure S2.5. AFM Image of *MxG*-CNC-$COOH_{740}$ on a mica substrate

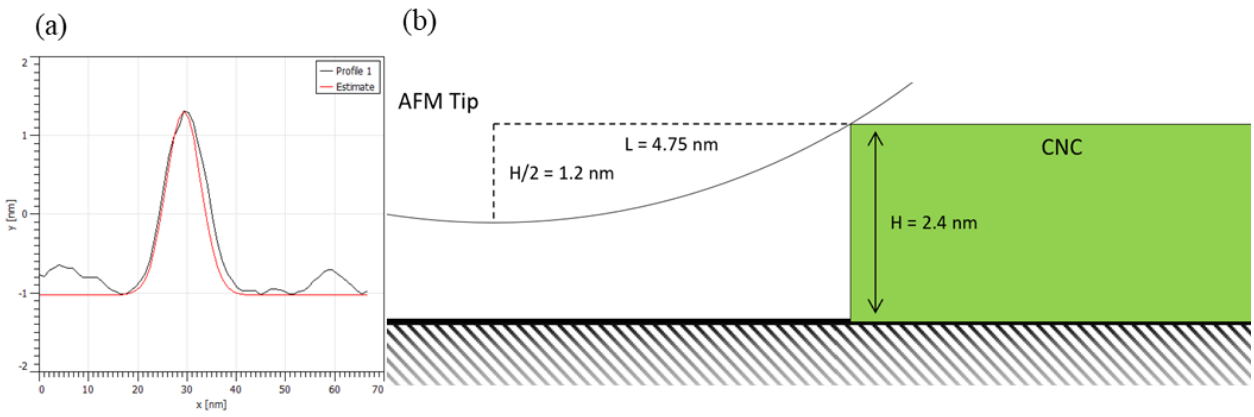

Figure S2.6. (a) Characteristic AFM height profile of a CNC (black) as well as the gaussian fit used to measure CNC width (red), and (b) schematic of AFM tip broadening as a result of the AFM tip radius (10 nm) being much larger than the CNC width (3.5 nm). This figure illustrates how the measured FWHM is considerably large than the actual CNC dimensions. Dimensions are scaled to match the AFM tip size and CNC height measured in this work.

CNC width measurements were done by fitting AFM height profiles with a Gaussian profile in the Gwyddion software (Figure S2.5(a)), then taking the full width at half of the peak maximum (FWHM) using the equation $FWHM = \sqrt{2\ln 2}\, b$, where b is a fit parameter output by Gwyddion. To correct for AFM tip broadening, the AFM tip radius and CNC height can be used to calculate the additional width contributed by tip curvature. With FS-1500 AFM tips from Asylum Research, the tip radius is 10 nm and the height of the CNCs measured via AFM is 2.4 nm. Using the trigonometry illustrated in Figure S2.5(b), the additional width at the half height on one side of the CNC can be calculated to be 4.75 nm using the equation $L = \sqrt{r^2 - d^2}$, where r is the tip radius (10 nm) d is the tip radius minus half the CNC height (8.8 nm) and L is the additional width. Subtracting $2L$ from the measured width of 13 nm results in a corrected CNC width of 3.5 nm.

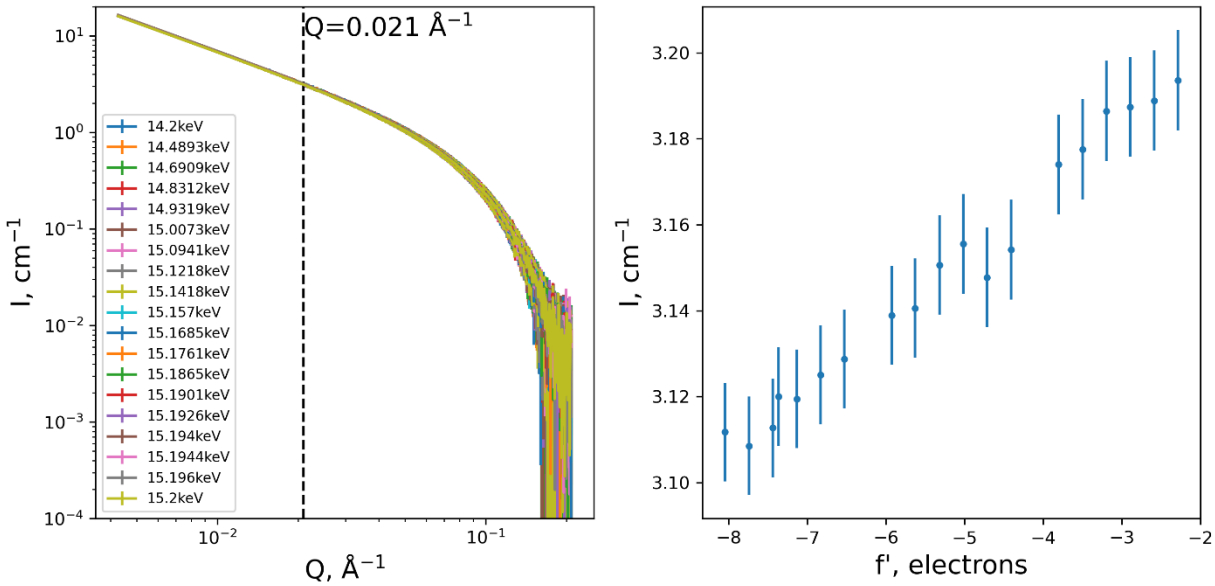

Figure S2.7. (a) Energy-dependent SAXS patterns simulated with CNCs of dimensions (H=2.4nm, W=3.5nm, L=250.0nm) with stern layer of Rb^+ ions of thickness 0.332 nm surrounding the nanocrystals (statistical error bars were estimated based on experimental data shown in Figure *2*.1(e)). (b) The energy dependence of SAXS intensity at Q=0.021, as shown with dashed black vertical line in (a).

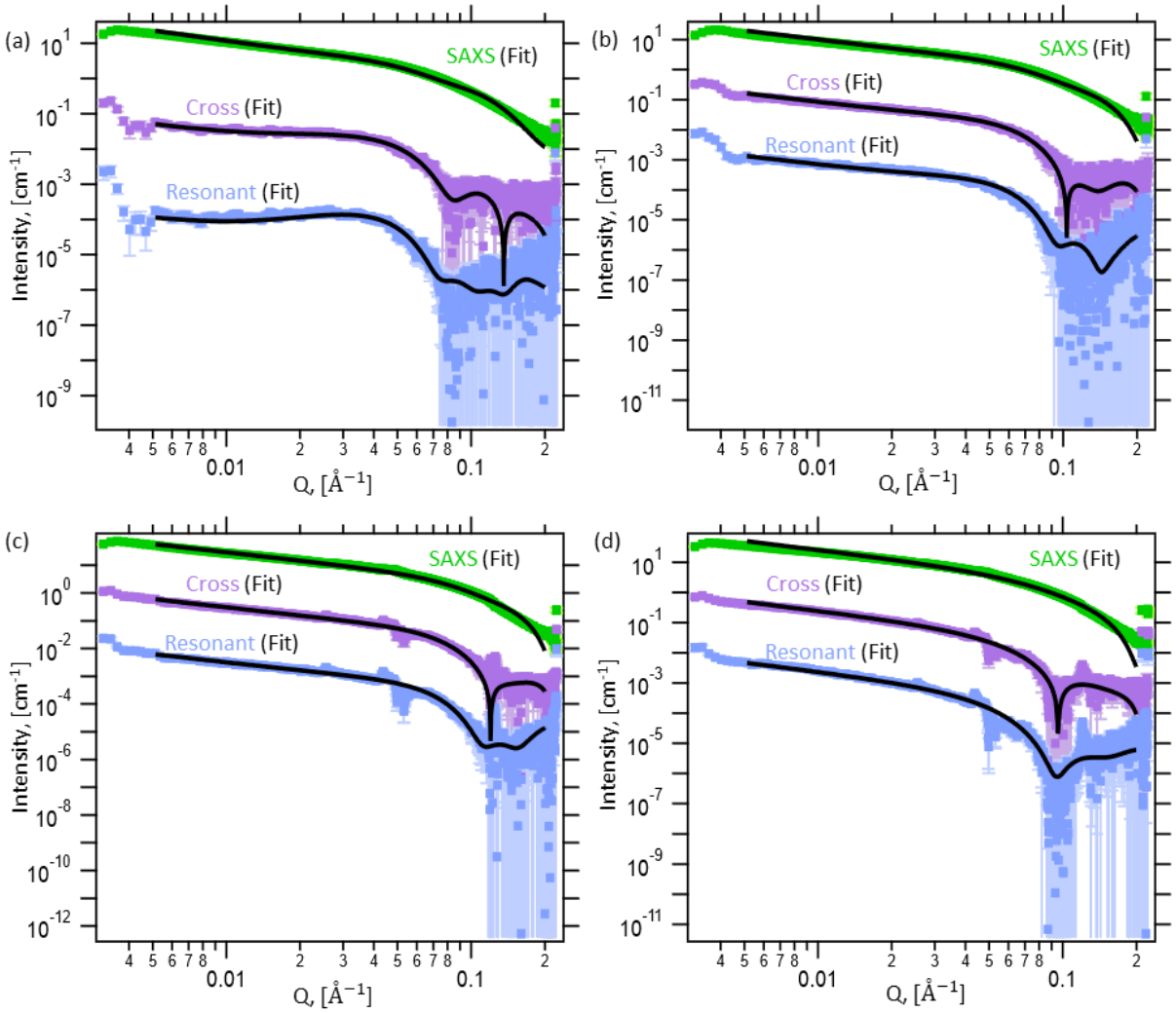

Figure S2.8. Data from MxG-CNC-COOH$_{1100}$ the ASAXS data with the parallelepiped fit. ASAXS data from MxG-CNC-COOH$_{1100}$ in (a) 50 mM RbCl solution, (b) 100 mM RbCl solution, (c) 200 mM RbCl solution, and (d) 400 mM RbCl solution

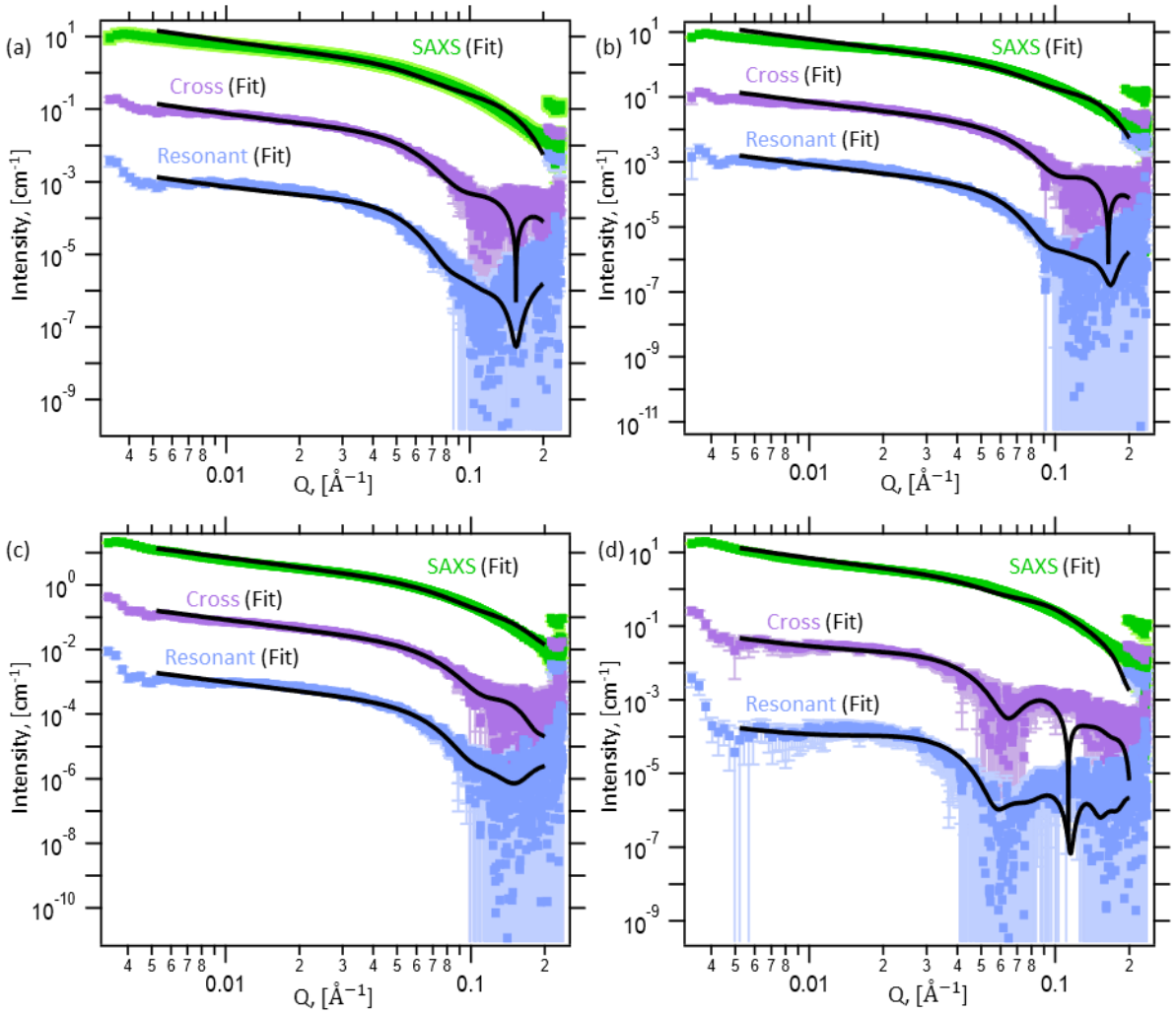

Figure S2.9. Data from MxG-CNC-COOH$_{1100}$ the ASAXS data with the parallelepiped fit. ASAXS data from MxG-CNC-COOH$_{1100}$ in (a) 50 mM $SrCl_2$ solution, (b) 100 mM $SrCl_2$ solution, (c) 200 mM $SrCl_2$ solution, and (d) 400 mM $SrCl_2$ solution

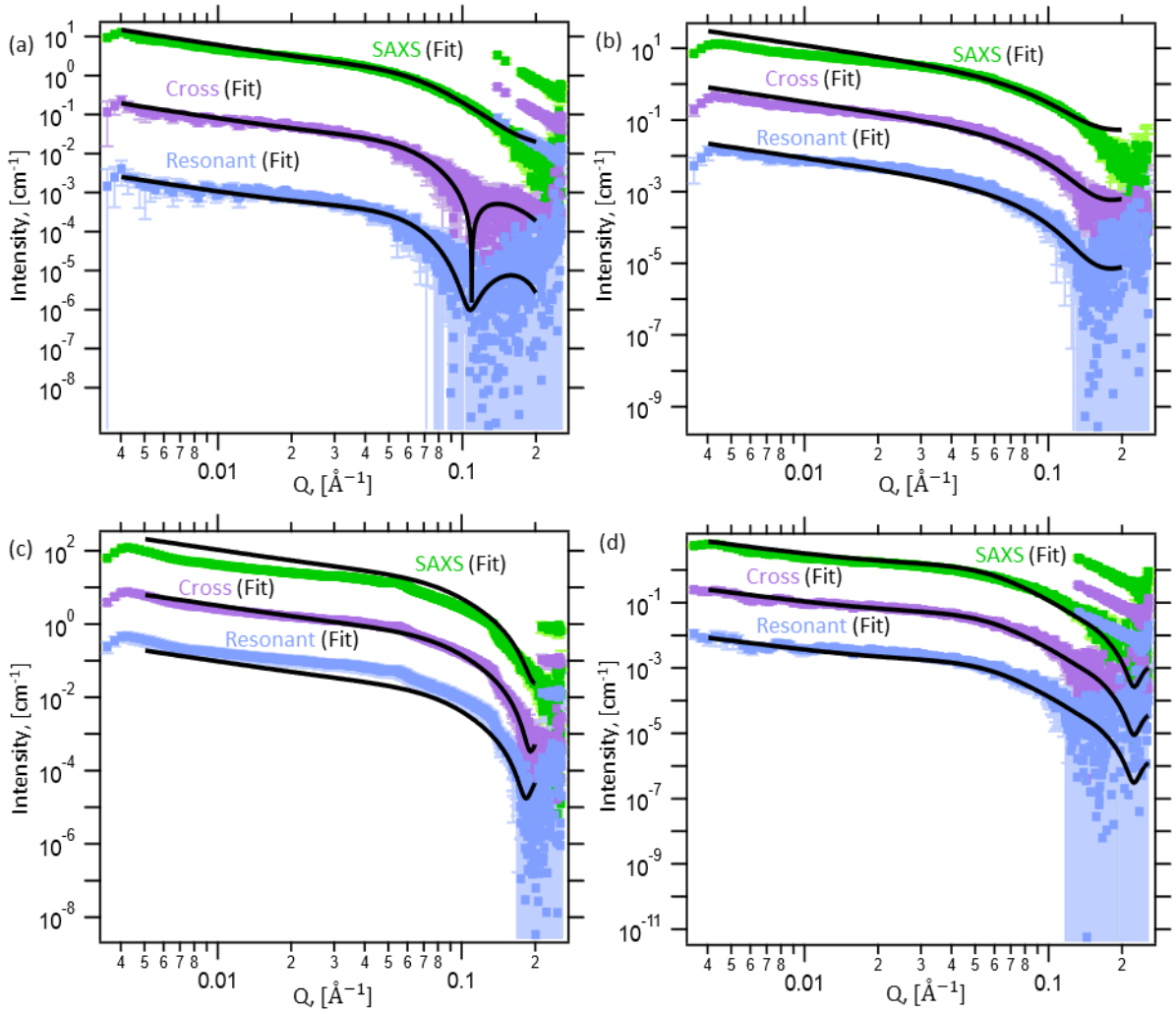

Figure S2.10. Data from MxG-CNC-COOH$_{1100}$ the ASAXS data with the parallelepiped fit. ASAXS data from MxG-CNC-COOH$_{1100}$ in (a) 50 mM YCl_3 solution, (b) 100 mM YCl_3 solution, (c) 200 mM YCl_3 solution, and (d) 400 mM YCl_3 solution

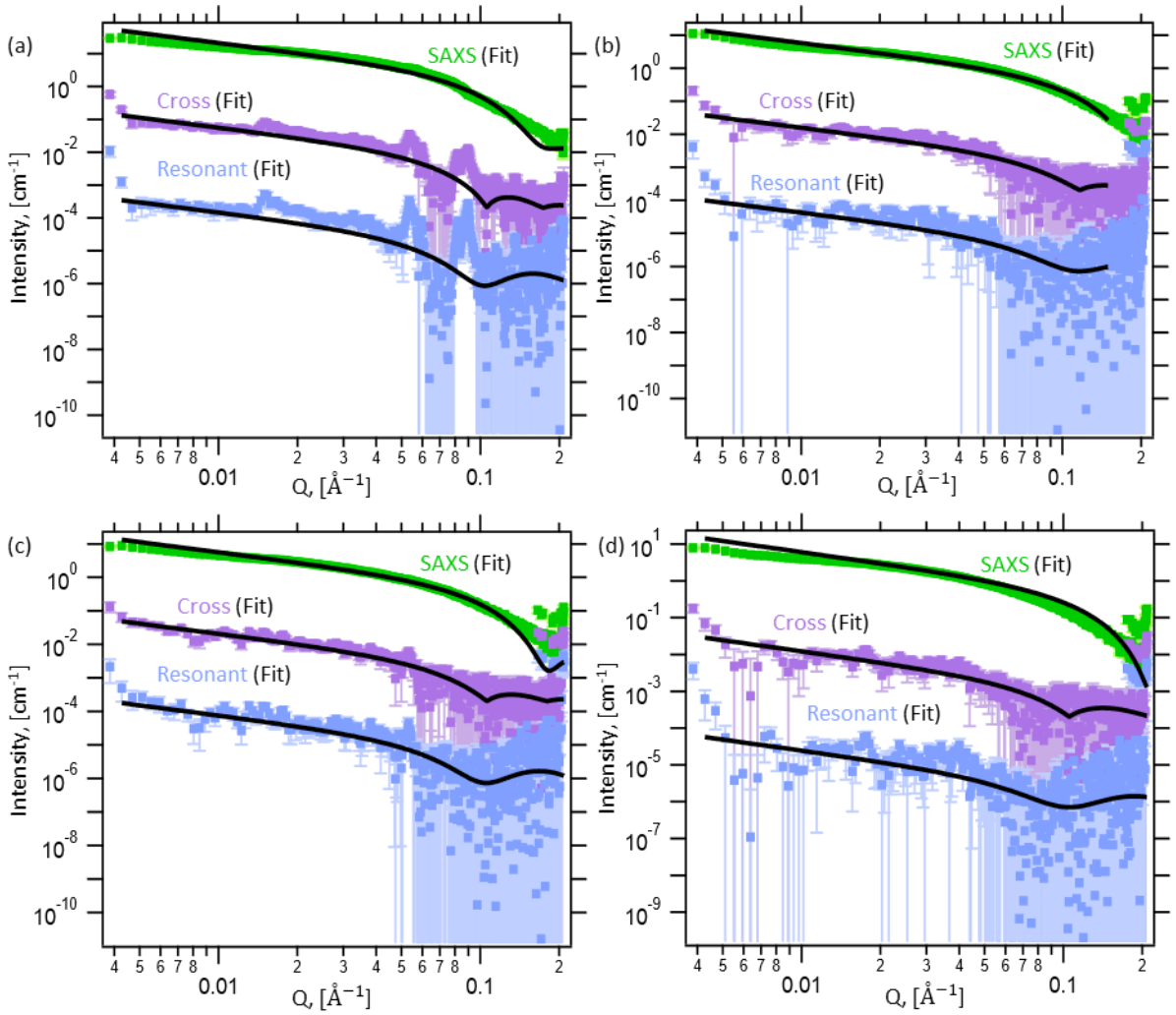

Figure S2.11. Data from MxG-CNC-COOH$_{740}$ the ASAXS data with the parallelepiped fit. ASAXS data from MxG-CNC-COOH$_{740}$ in (a) 50 mM RbCl solution, (b) 100 mM RbCl solution, (c) 200 mM RbCl solution, and (d) 400 mM RbCl solution

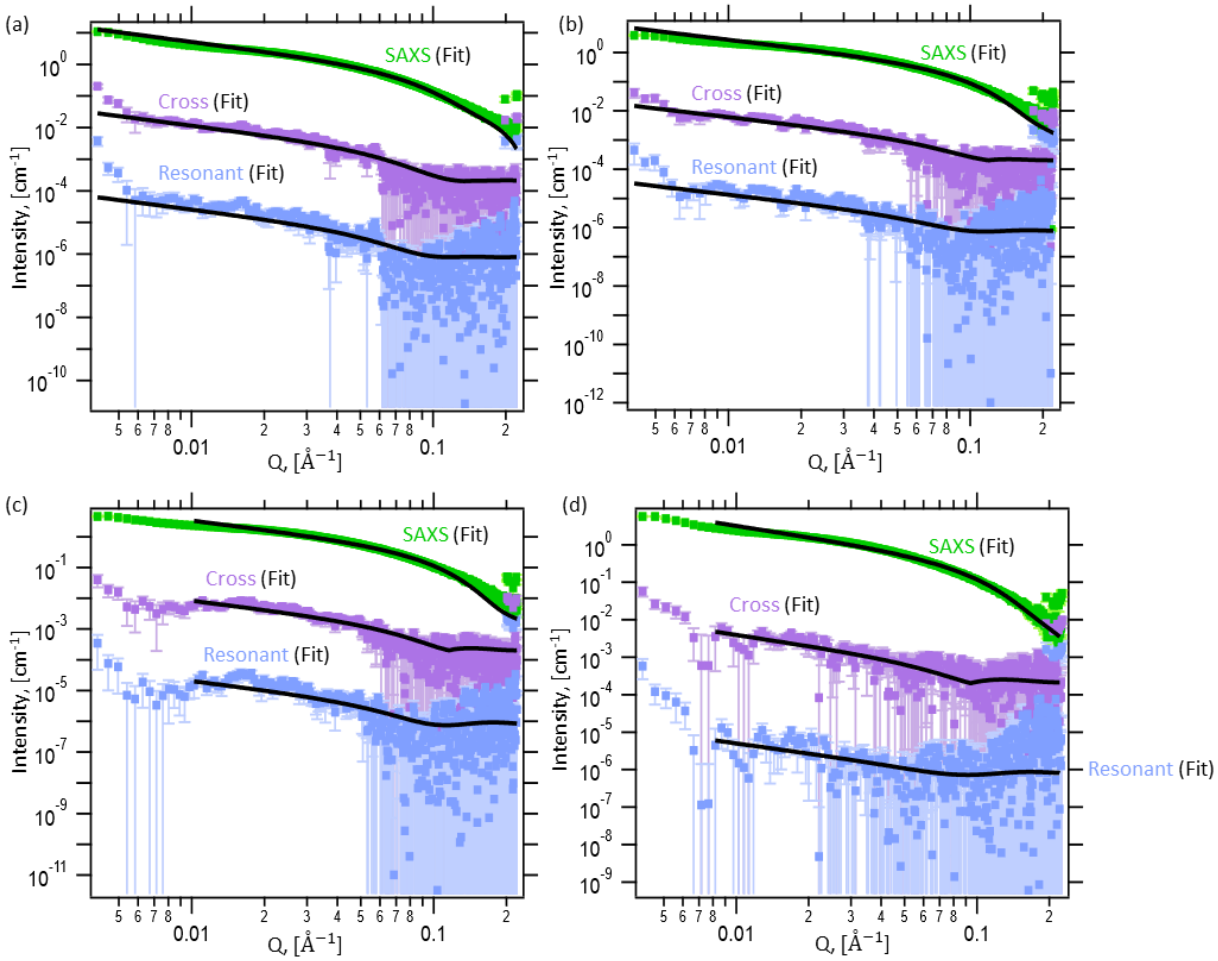

Figure S2.12. Data from MxG-CNC-COOH$_{740}$ the ASAXS data with the parallelepiped fit. ASAXS data from MxG-CNC-COOH$_{740}$ in (a) 50 mM $SrCl_2$ solution, (b) 100 mM $SrCl_2$ solution, (c) 200 mM $SrCl_2$ solution, and (d) 400 mM $SrCl_2$ solution

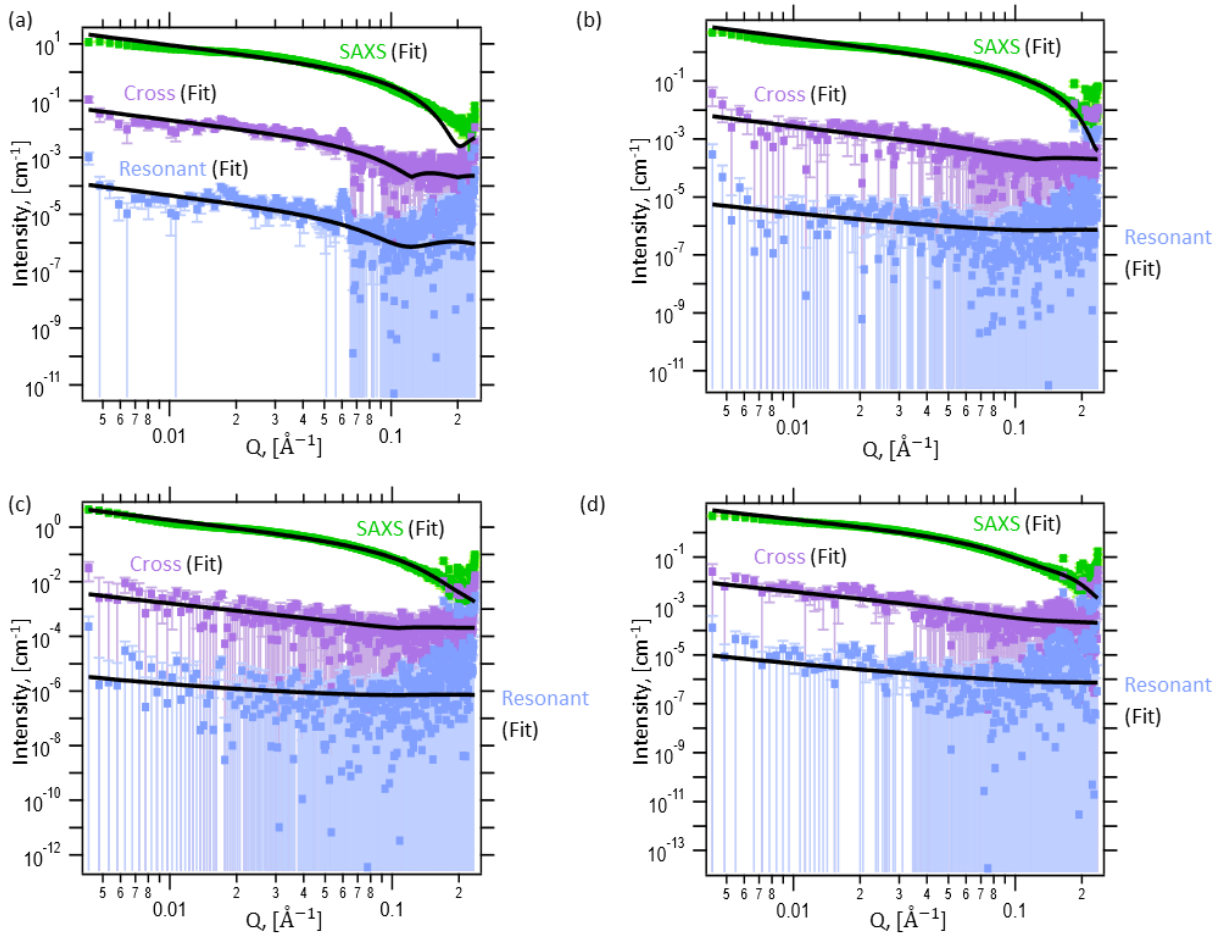

Figure S2.13. Data from MxG-CNC-COOH$_{740}$ the ASAXS data with the parallelepiped fit. ASAXS data from MxG-CNC-COOH$_{740}$ in (a) 50 mM YCl_3 solution, (b) 100 mM YCl_3 solution, (c) 200 mM YCl_3 solution, and (d) 400 mM YCl_3 solution

2.7.1 Section S2.1. Multilayered Parallelepiped Model and functions developed under XModFit

In order to model ion-distribution surrounding parallelepiped CNCs a Multilayered Parallelepiped Model is developed as shown in Figure 2.1(c) of the main text. The multilayered parallelopiped is defined by the core's linear dimensions ($L_o \times B_o \times H$) and the shells of different thicknesses (t_i) on top of the core. In the model heights of the shells are kept the same as the core whereas the shell thicknesses can be variable. For analyzing the ASAXS data obtained from CNCs in the present case we only used an one-shell model for the stern-layer and a two-shell model for the stern-layer

and diffuse layer on top of the CNCs. In general, the heights of the CNCs are much longer than the lengths and breadths and are not accessible in the q-range in the ASAXS data. Hence, for our analysis we kept the heights fixed with the values obtained from AFM. Assuming the CNCs are randomly oriented with respect to the X-Ray beam and randomly spatially distributed (Structure factor, $S(q) = 1$) the intensity from the CNCs can be the form factor of parallelepiped as:[69]

$$I(q) = \frac{N}{V}\left|\sum_{i=0}^{N_L} L_i B_i H(\rho_{e,i} - \rho_{e,i+1}) \int_0^{2\pi}\int_0^{\pi} \mathrm{sinc}^2 A_i \,\mathrm{sinc}^2 B_i \,\mathrm{sinc}^2 C \sin\phi \, d\phi d\psi\right|^2 \quad \text{S2.1}$$

Where $A_i = qL_i \sin\phi \cos\psi\,/2$, $B_i = qB_i \sin\phi \cos\psi\,/2$, and $C = qH\cos\phi\,/2$ with ϕ and ψ being the polar and azimuthal angles in spherical polar co-ordinates with X-axis being the direction of the beam. The layer corresponding to $i = 0$ represent the core with electron density, $\rho_{e,o}$, and dimensions, (L_o, B_o, H). Whereas, the layer coresponsing to the last shell with electron density, $\rho_{e,L}$, and dimensions, $(L_{N_L} = (L_0 + \sum_{j=1}^{J=NL} t_j),\ B_{N_L} = (B_0 + \sum_{j=1}^{J=NL} t_j),\ H)$, resepectively. $i = N_L$+1 represents the bulk medium with electron density, ρ_{es}, in which the parallelepiped is dispersed randomly. In order to incorporate polydispersity of the CNCs, equation S8 can be either integrated over 'Gaussian' or 'Log-Normal' distributions over the lateral core dimensions (L_0, B_0). The energy dependent intensity in equation S8 can be calculated using the energy-dependent electron densities of the multilayers of the parallelepiped caclulated from equation S2.1. Electron density of a layer is calculated from the elemental composition of the layer provided by the molecular formula and the mass density of the layer. All the calculations are implemented in the form of two functions 'Parallelepiped_Uniform' and 'Parallelepiped_Uniform_Edep' in the XModFit package developed by NSF's ChemMatCARS.[68] 'Parallelepiped_Uniform' calculates

the SAXS-term, the Cross-term, and the Anomalous-term from the model whereas 'Parallelepiped_Uniform_Edep' calculates energy dependent total SAXS intensity from the parallelepiped model. In the XModfit package the materials for the two functions are defined as 'Multiple fitting parameters' as:

1) If the material is in solid form with known elemental composition the material can be defned by its Chemical Formula (Example: Au, Ag, AgNO3..etc).
2) The moles of the resonant element in the molecular formula will be defined by the parameter 'Rmoles'.
3) If the material is defined as a solution where the material composition will be written in the format of 'Solute:Solvent' where both the 'Solute' and 'Solvent' material described by their respecitve chemical formulas with known elemental compositions (Example: AuCl3:H2O, NaCl:H2O etc)
4) If the resonant element of a material (R) is shared with another element (C), the material should be described as chemical formula as $A_{nA}B_{nB}C_{nC}*E_{nE}R$, where (A, B, E) are non-resonant elements with (nA, nB, nE) moles, respectively, and R is the resonant element with 'Rmoles' moles. The number of moles of 'C' in the chemical formula will be (nC-Rmoles).
5) The density of the 'solute' and 'solvent' are provided by parameters 'Density' and 'SolDensity' in the 'Multiple Fitting Parameters'. It is important to note here that if either solute or solvent contains a resonant element along with other non-resonant elements the 'Density' or 'SolDensity' represents only the density of non-resonant elements. The software will calculate the overall density of the material using 'Rmoles' of the resonant element. For example, for a solution of RbCl in H_2O the material should be described as RbCl:H2O, the 'Density' should be the density of the Cl and 'SolDensity' should be the density of H2O. If the material is described by a single element including the resonant element then the 'Density' should be the density of the element itself.

The simulation of SAXS-term, Cross-term, and Anomalous-term was calculated from the parallelepiped model of CNCs using 'Parallelepiped_Uniform' function in XModFit.[68] The core-dimensions used for the CNCs are L=40Å, B=28Å, and H=2500Å. The molecular formula used for the CNC is for the cellulose, $C_6H_{10}O_5$, with mass density of 1.5 gm/cm^3. A Stern layer of thickness same as twice the ionic-radius of Rb^+ (3.32 Å) with density of 0.3 gm/cm^3 is also considered for the simulation along with the bulk concentration of 100mM (0.00854 gm/cm^3) Rb^+.

The experimental ASAXS data were fitted using the same model with norm, L, B, and stern layer density as fitting parameters.

2.7.2 Section S2.2. ASAXS data reduction using Sturhmann method

The energy-dependent electron density contrast from a system with energies very close to the X-ray absorption of one of the element (termed as the resonant element) within the system can be written as[48,70–74]:

$$\rho_e(\vec{r}, E) = \rho_{eo}(\vec{r}) - \rho_{es} + v(\vec{r})(f'(E) + if"(E)) \qquad \text{S2.2}$$

Where $\rho_{eo}(\vec{r})$ is the energy-independent total electron density of the sample, and ρ_s is the electron density of solvent (in our case the solvent is water with $\rho_{es} = 0.334$ el/Å^3), whereas $v(\vec{r})$ is the number density of the resonant element only in the system. $(f'(E), f"(E))$ are the complex scattering factors of the resonant element.

Taking the fourier transform one can obtain the X-ray scattering as[48,70–74]:

$$\begin{aligned} I(\vec{q}, E) &= \frac{N}{V} r_e^2 |\int \rho_e(\vec{r}, E) e^{i\vec{q}.\vec{r}} \mathrm{d}\vec{r}|^2 \\ &= |\rho_{os}(\vec{q})|^2 + f'(E) Re[\rho_{os}(\vec{q})\rho_r^*(\vec{q}) + \rho_{os}^*(\vec{q})\rho_r(\vec{q})] \\ &\quad + \left(f'^2(E) + f"^2(E)\right)|\rho_r(\vec{q})|^2 \end{aligned} \qquad \text{S2.3}$$

Where, N/V is the number of scattering samples per unit volume, r_e is the classical electron radius, $\rho_{os}(\vec{q}) = \int (\rho_{eo}(\vec{r}) - \rho_{es}) e^{i\vec{q}.\vec{r}} \mathrm{d}\vec{r}$ and $\rho_r(\vec{q}) = \int v(\vec{r}) e^{i\vec{q}.\vec{r}} \mathrm{d}\vec{r}$ are complex numbers, Re denotes real part of the complex number. But for systems with centrosymmetric geometries like sphere, cylinder, ellipsoid, etc, these terms become real and isotropic in $\vec{q}$. Owing to that, the above equation can be further simplified into

$$I(q,E) = \frac{N}{V}[\rho_{os}^2(q) + 2f'(E)\rho_{os}(q)\rho_r(q) + \left(f'^2(E) + f''^2(E)\right)\rho_r^2(q)] \quad \text{S2.4}$$

The above equation holds good for monodisperse system of particles. In case of polydisperse system of particles the intensity needs to be averaged over the particle size distribution and equation S2.4 becomes

$$I(q,E) = \frac{N}{V}[\langle\rho_{os}^2(q)\rangle + 2f'(E)\langle\rho_{os}(q)\rho_r(q)\rangle + \left(f'^2(E) + f''^2(E)\right)\langle\rho_r^2\rangle] \quad \text{S2.5}$$

The first term in this equation is energy independent and can be termed as *SAXS-term* ($I_S = \frac{N}{V}\langle\rho_{os}^2(q)\rangle$). Whereas both the 2nd and 3rd terms have energy dependence. The 2nd term contains the *Cross-term* ($I_C = \frac{N}{V}\langle\rho_o(q)\rho_r(q)\rangle$) and has the contribution from the resonant element as well as all other atoms in the system. Whereas the 3rd term has the *Resonant-term* ($I_R = \frac{N}{V}\langle\rho_r^2(q)\rangle$) that only has a contribution from the resonant element. In general, just below the absorption edge of the resonant element the imaginary part of the scattering constant ($f''(E)$) of the resonant element does not change considerably. Hence, the above equation is basically a quadratic function of the real part of the scattering factor of the resonant element ($f'(E)$).

As per ASAXS experiments, we obtained the scattering intensity as a function of q and E, i.e. the left-hand side of eq. S2.5. In general, the complex scattering factors ($f'(E), f''(E)$) of the resonant element can be obtained from the online database of National Institute of Standards and Technology.[75] With the tabulated values for resonant element one can have a system of linear equations based on equation S2.4. By solving the linear equation one can obtain the values of I_S, I_C, and I_R, as mentioned here.[76]

The *Resonant-term* in the equation, in general, is a few orders of magnitude smaller than the other terms, and for most practical purposes the equation can be further approximated into:

$$I(q,E) \approx I_s + 2f'(E)I_C \qquad \text{S2.6}$$

As the cross term is essentially a product of SAXS and Resontant terms, the *Resonant-term* can also be approximated from the non-zero *Cross-term* directly as:

$$I_R(q) = \langle \rho_R^2(q) \rangle = I_C^2(q)/I_S(q) \qquad \text{S2.7}$$

Without any approximation the scattering terms (I_S, I_C, I_R) in Eq. S3 will have to satisfy a constraint using Cauchy-Schwarz inequality:

$$I_R(q) \geq I_C^2(q)/I_S(q) \qquad \text{S2.8}$$

This in-equality provides a minimum limit for I_R when I_S and I_C are known and is the reason for the equality in Equation S2.8 under approximation. We applied both the constraints in S2.7 and S2.8 on the energy-dependent simulated data from the parallelopiped model as discussed in the main text to obtain the scattering terms. The data reduction process is implemented in one of the packages 'XAnoS_Components' under the software suite 'XAnoS' developed at NSF's ChemMatCARS.[77] Due to the presence of statistical variances in the data and the very weak contribution of the resonant term in the energy-dependent data, we found the equality constraint to provide resonant terms with narrow error bars.

2.8 References

(1) Vörösmarty, C. J.; Green, P.; Salisbury, J.; Lammers, R. B. Global Water Resources: Vulnerability from Climate Change and Population Growth. *Science (1979)* **2000**, *289* (5477), 284–288. https://doi.org/DOI: 10.1126/science.289.5477.284.

(2) Vörösmarty, C. J.; McIntyre, P. B.; Gessner, M. O.; Dudgeon, D.; Prusevich, A.; Green, P.; Glidden, S.; Bunn, S. E.; Sullivan, C. A.; Liermann, C. R.; Davies, P. M. Global Threats to Human Water Security and River Biodiversity. *Nature 2010 467:7315* **2010**, *467* (7315), 555–561. https://doi.org/10.1038/nature09440.

(3) Crini, G. Non-Conventional Low-Cost Adsorbents for Dye Removal: A Review. *Bioresour Technol* **2006**, *97* (9), 1061–1085. https://doi.org/10.1016/J.BIORTECH.2005.05.001.

(4) Sahithya, K.; Das, D.; Das, N. Effective Removal of Dichlorvos from Aqueous Solution Using Biopolymer Modified MMT–CuO Composites: Equilibrium, Kinetic and Thermodynamic Studies. *J Mol Liq* **2015**, *211*, 821–830. https://doi.org/10.1016/J.MOLLIQ.2015.08.013.

(5) Keith, L. H.; Telliard, W. A. Priority Pollutants. I. A Perspective View. *Environ Sci Technol* **1979**, *13* (4), 416–423. https://doi.org/10.1021/ES60152A601/ASSET/ES60152A601.FP.PNG_V03.

(6) Nasrollahzadeh, M.; Sajjadi, M.; Iravani, S.; Varma, R. S. Starch, Cellulose, Pectin, Gum, Alginate, Chitin and Chitosan Derived (Nano)Materials for Sustainable Water Treatment: A Review. *Carbohydr Polym* **2021**, *251*, 116986. https://doi.org/10.1016/J.CARBPOL.2020.116986.

(7) Khan, S. B.; Ali, F.; Kamal, T.; Anwar, Y.; Asiri, A. M.; Seo, J. CuO Embedded Chitosan Spheres as Antibacterial Adsorbent for Dyes. *Int J Biol Macromol* **2016**, *88*, 113–119. https://doi.org/10.1016/J.IJBIOMAC.2016.03.026.

(8) Albukhari, S. M.; Ismail, M.; Akhtar, K.; Danish, E. Y. Catalytic Reduction of Nitrophenols and Dyes Using Silver Nanoparticles @ Cellulose Polymer Paper for the Resolution of Waste Water Treatment Challenges. *Colloids Surf A Physicochem Eng Asp* **2019**, *577*, 548–561. https://doi.org/10.1016/J.COLSURFA.2019.05.058.

(9) Sun, Y.; Zhou, G.; Xiong, X.; Guan, X.; Li, L.; Bao, H. Enhanced Arsenite Removal from Water by Ti(SO4)2 Coagulation. *Water Res* **2013**, *47* (13), 4340–4348. https://doi.org/10.1016/J.WATRES.2013.05.028.

(10) Elwakeel, K. Z.; Guibal, E. Arsenic(V) Sorption Using Chitosan/Cu(OH)2 and Chitosan/CuO Composite Sorbents. *Carbohydr Polym* **2015**, *134*, 190–204. https://doi.org/10.1016/J.CARBPOL.2015.07.012.

(11) Epa, U.; Supply, W.; Resources Division, W.; Smith, C. 2012 Guidelines for Water Reuse. **2004**.

(12) Crini, G.; Lichtfouse, E.; Wilson, L. D.; Morin-Crini, N. Conventional and Non-Conventional Adsorbents for Wastewater Treatment. *Environ Chem Lett* **2019**, *17* (1), 195–213. https://doi.org/10.1007/S10311-018-0786-8/.

(13) Cudjoe, E.; Hunsen, M.; Xue, Z.; Way, A. E.; Barrios, E.; Olson, R. A.; Hore, M. J. A.; Rowan, S. J. Miscanthus Giganteus: A Commercially Viable Sustainable Source of Cellulose Nanocrystals. *Carbohydr Polym* **2017**, *155*, 230–241. https://doi.org/10.1016/J.CARBPOL.2016.08.049.

(14) Mende, M.; Schwarz, D.; Steinbach, C.; Boldt, R.; Schwarz, S. The Influence of Salt Anions on Heavy Metal Ion Adsorption on the Example of Nickel. *Materials* **2018**, *11* (3). https://doi.org/10.3390/MA11030373.

(15) Mautner, A.; Lee, K. Y.; Tammelin, T.; Mathew, A. P.; Nedoma, A. J.; Li, K.; Bismarck, A. Cellulose Nanopapers as Tight Aqueous Ultra-Filtration Membranes. *React Funct Polym* **2015**, *86*, 209–214. https://doi.org/10.1016/j.reactfunctpolym.2014.09.014.

(16) Mautner, A.; Maples, H. A.; Sehaqui, H.; Zimmermann, T.; Perez de Larraya, U.; Mathew, A. P.; Lai, C. Y.; Li, K.; Bismarck, A. Nitrate Removal from Water Using a Nanopaper Ion-Exchanger. *Environ Sci (Camb)* **2016**, *2* (1), 117–124. https://doi.org/10.1039/C5EW00139K.

(17) Habibi, Y.; Lucia, L. A.; Rojas, O. J. Cellulose Nanocrystals: Chemistry, Self-Assembly, and Applications. *Chem Rev* **2010**, *110* (6), 3479–3500. https://doi.org/https://doi.org/10.1021/cr900339w.

(18) Voisin, H.; Bergström, L.; Liu, P.; Mathew, A. P. Nanocellulose-Based Materials for Water Purification. *Nanomaterials (Basel)* **2017**, *7* (3). https://doi.org/10.3390/nano7030057.

(19) Yu, X.; Tong, S.; Ge, M.; Wu, L.; Zuo, J.; Cao, C.; Song, W. Adsorption of Heavy Metal Ions from Aqueous Solution by Carboxylated Cellulose Nanocrystals. *Journal of Environmental Sciences* **2013**, *25* (5), 933–943. https://doi.org/10.1016/S1001-0742(12)60145-4.

(20) Dufresne, A. Nanocellulose: A New Ageless Bionanomaterial. *Materials Today* **2013**, *16* (6), 220–227. https://doi.org/10.1016/J.MATTOD.2013.06.004.

(21) Capron, I.; Rojas, O. J.; Bordes, R. Behavior of Nanocelluloses at Interfaces. *Current Opinion in Colloid and Interface Science*. 2017. https://doi.org/10.1016/j.cocis.2017.04.001.

(22) Klemm, D.; Cranston, E. D.; Fischer, D.; Gama, M.; Kedzior, S. A.; Kralisch, D.; Kramer, F.; Kondo, T.; Lindström, T.; Nietzsche, S.; Petzold-Welcke, K.; Rauchfuß, F. Nanocellulose as a Natural Source for Groundbreaking Applications in Materials Science: Today's State. *Materials Today*. 2018. https://doi.org/10.1016/j.mattod.2018.02.001.

(23) Yang, H.; Zhang, Y.; Kato, R.; Rowan, S. J. Preparation of Cellulose Nanofibers from Miscanthus x. Giganteus by Ammonium Persulfate Oxidation. *Carbohydr Polym* **2019**, *212*, 30–39. https://doi.org/10.1016/j.carbpol.2019.02.008.

(24) Weiss, A. M.; MacKe, N.; Zhang, Y.; Calvino, C.; Esser-Kahn, A. P.; Rowan, S. J. In Vitro and in Vivo Analyses of the Effects of Source, Length, and Charge on the Cytotoxicity and Immunocompatibility of Cellulose Nanocrystals. *ACS Biomater Sci Eng* **2021**, *7* (4), 1450–1461. https://doi.org/10.1021/acsbiomaterials.0c01618.

(25) Li, W.; Ju, B.; Zhang, S. A Green L-Cysteine Modified Cellulose Nanocrystals Biosorbent for Adsorption of Mercury Ions from Aqueous Solutions. *RSC Adv* **2019**, *9* (12), 6986–6994. https://doi.org/10.1039/c9ra00048h.

(26) Yu, X.; Tong, S.; Ge, M.; Wu, L.; Zuo, J.; Cao, C.; Song, W. Adsorption of Heavy Metal Ions from Aqueous Solution by Carboxylated Cellulose Nanocrystals. *J Environ Sci (China)* **2013**, *25* (5), 933–943. https://doi.org/10.1016/S1001-0742(12)60145-4.

(27) Liu, P.; Sehaqui, H.; Tingaut, P.; Wichser, A.; Oksman, K.; Mathew, A. P. Cellulose and Chitin Nanomaterials for Capturing Silver Ions (Ag+) from Water via Surface Adsorption. *Cellulose* **2014**, *21* (1), 449–461. https://doi.org/10.1007/s10570-013-0139-5.

(28) Sehaqui, H.; Perez de Larraya, U.; Tingaut, P.; Zimmermann, T. Humic Acid Adsorption onto Cationic Cellulose Nanofibers for Bioinspired Removal of Copper(Ii) and a Positively Charged Dye. *Soft Matter* **2015**, *11* (26), 5294–5300. https://doi.org/10.1039/C5SM00566C.

(29) Sheikhi, A.; Safari, S.; Yang, H.; Van De Ven, T. G. M. Copper Removal Using Electrosterically Stabilized Nanocrystalline Cellulose. *ACS Appl Mater Interfaces* **2015**, *7* (21), 11301–11308. https://doi.org/10.1021/ACSAMI.5B01619/SUPPL_FILE/AM5B01619_SI_001.ZIP.

(30) Saito, T.; Isogai, A. Ion-Exchange Behavior of Carboxylate Groups in Fibrous Cellulose Oxidized by the TEMPO-Mediated System. *Carbohydr Polym* **2005**, *61* (2), 183–190. https://doi.org/10.1016/J.CARBPOL.2005.04.009.

(31) Sehaqui, H.; de Larraya, U. P.; Liu, P.; Pfenninger, N.; Mathew, A. P.; Zimmermann, T.; Tingaut, P. Enhancing Adsorption of Heavy Metal Ions onto Biobased Nanofibers from Waste Pulp Residues for Application in Wastewater Treatment. *Cellulose* **2014**, *21* (4), 2831–2844. https://doi.org/10.1007/S10570-014-0310-7/FIGURES/9.

(32) Shen, W.; Chen, S.; Shi, S.; Li, X.; Zhang, X.; Hu, W.; Wang, H. Adsorption of Cu(II) and Pb(II) onto Diethylenetriamine-Bacterial Cellulose. *Carbohydr Polym* **2009**, *75* (1), 110–114. https://doi.org/10.1016/J.CARBPOL.2008.07.006.

(33) Kardam, A.; Raj, K. R.; Srivastava, S.; Srivastava, M. M. Nanocellulose Fibers for Biosorption of Cadmium, Nickel, and Lead Ions from Aqueous Solution. *Clean Technol Environ Policy* **2014**, *16* (2), 385–393. https://doi.org/10.1007/S10098-013-0634-2/TABLES/4.

(34) Pillai, S. S.; Deepa, B.; Abraham, E.; Girija, N.; Geetha, P.; Jacob, L.; Koshy, M. Biosorption of Cd(II) from Aqueous Solution Using Xanthated Nano Banana Cellulose: Equilibrium and Kinetic Studies. *Ecotoxicol Environ Saf* **2013**, *98*, 352–360. https://doi.org/10.1016/J.ECOENV.2013.09.003.

(35) Liu, P.; Borrell, P. F.; Božič, M.; Kokol, V.; Oksman, K.; Mathew, A. P. Nanocelluloses and Their Phosphorylated Derivatives for Selective Adsorption of Ag+, Cu2+ and Fe3+ from Industrial Effluents. *J Hazard Mater* **2015**, *294*, 177–185. https://doi.org/10.1016/J.JHAZMAT.2015.04.001.

(36) Ma, H.; Hsiao, B. S.; Chu, B. Ultrafine Cellulose Nanofibers as Efficient Adsorbents for Removal of UO22+ in Water. *ACS Macro Lett* **2012**, *1* (1), 213–216.

(37) Batmaz, R.; Mohammed, N.; Zaman, M.; Minhas, G.; Berry, R. M.; Tam, K. C. Cellulose Nanocrystals as Promising Adsorbents for the Removal of Cationic Dyes. *Cellulose* **2014**, *21* (3), 1655–1665. https://doi.org/10.1007/S10570-014-0168-8/FIGURES/4.

(38) Qiao, H.; Zhou, Y.; Yu, F.; Wang, E.; Min, Y.; Huang, Q.; Pang, L.; Ma, T. Effective Removal of Cationic Dyes Using Carboxylate-Functionalized Cellulose Nanocrystals. *Chemosphere* **2015**, *141*, 297–303. https://doi.org/10.1016/J.CHEMOSPHERE.2015.07.078.

(39) Timofei, S.; Schmidt, W.; Kurunczi, L.; Simon, Z. A Review of QSAR for Dye Affinity for Cellulose Fibres. *Dyes and Pigments* **2000**, *47* (1–2), 5–16. https://doi.org/10.1016/S0143-7208(00)00058-9.

(40) Dingenonts, N.; Patel, M.; Rosenfeldt, S.; Pontoni, D.; Narayanan, T.; Ballauff, M. Counterion Distribution around a Spherical Polyelectrolyte Brush Probed by Anomalous Small-Angle X-Ray Scattering. *Macromolecules* **2004**, *37* (21), 8152–8159. https://doi.org/10.1021/MA048828J.

(41) Patel, M.; Rosenfeldt, S.; Ballauff, M.; Dingenouts, N.; Pontoni, D.; Narayanan, T. Analysis of the Correlation of Counterions to Rod-like Macroions by Anomalous Small-Angle X-Ray Scattering. *Physical Chemistry Chemical Physics* **2004**, *6* (11), 2962–2967. https://doi.org/10.1039/B402155J.

(42) Das, R.; Mills, T. T.; Kwok, L. W.; Maskel, G. S.; Millett, I. S.; Doniach, S.; Finkelstein, K. D.; Herschlag, D.; Pollack, L. Counterion Distribution around DNA Probed by Solution X-Ray Scattering. *Phys Rev Lett* **2003**, *90* (18), 4. https://doi.org/10.1103/PHYSREVLETT.90.188103/FIGURES/1/THUMBNAIL.

(43) Pabit, S. A.; Finkelstein, K. D.; Pollack, L. Using Anomalous Small Angle X-Ray Scattering to Probe the Ion Atmosphere around Nucleic Acids. *Methods Enzymol* **2009**, *469*, 391–410. https://doi.org/10.1016/S0076-6879(09)69019-4.

(44) Pabit, S. A.; Meisburger, S. P.; Li, L.; Blose, J. M.; Jones, C. D.; Pollack, L. Counting Ions around DNA with Anomalous Small-Angle X-Ray Scattering. *J Am Chem Soc* **2010**, *132* (46), 16334–16336. https://doi.org/10.1021/JA107259Y/SUPPL_FILE/JA107259Y_SI_001.PDF.

(45) Pollack, L. SAXS Studies of Ion–Nucleic Acid Interactions. *https://doi.org/10.1146/annurev-biophys-042910-155349* **2011**, *40* (1), 225–242. https://doi.org/10.1146/ANNUREV-BIOPHYS-042910-155349.

(46) Chen, J.; Bera, M. K.; Li, H.; Yang, Y.; Sun, X.; Luo, J.; Baughman, J.; Liu, C.; Yao, X.; Chuang, S. S. C.; Liu, T. Accurate Determination of the Quantity and Spatial Distribution of Counterions around a Spherical Macroion. *Angewandte Chemie International Edition* **2021**, *60* (11), 5833–5837. https://doi.org/10.1002/ANIE.202013806.

(47) Sztucki, M.; di Cola, E.; Narayanan, T. Instrumental Developments for Anomalous Small-Angle X-Ray Scattering from Soft Matter Systems. *urn:issn:0021-8898* **2010**, *43* (6), 1479–1487. https://doi.org/10.1107/S002188981003298X.

(48) Stuhrmann, H. B. Anomalous Dispersion of Small-angle Scattering of Horse-spleen Ferritin at the Iron K Absorption Edge. *Acta Crystallographica Section A* **1980**, *36* (6), 996–1001. https://doi.org/10.1107/S0567739480002033.

(49) Stuhrmann, H. B. Anomalous Small Angle Scattering. *Q Rev Biophys* **1981**, *14* (3), 433–462. https://doi.org/10.1017/S0033583500002365.

(50) Stuhrmann, H. B.; Notbohm, H. Configuration of the Four Iron Atoms in Dissolved Human Hemoglobin as Studied by Anomalous Dispersion. *Proc Natl Acad Sci U S A* **1981**, *78* (10), 6216. https://doi.org/10.1073/PNAS.78.10.6216.

(51) Tatchev, D. Structure Analysis of Multiphase Systems by Anomalous Small-Angle X-Ray Scattering. *https://doi.org/10.1080/14786430802279760* **2008**, *88* (12), 1751–1772. https://doi.org/10.1080/14786430802279760.

(52) Macke, N.; Hemmingsen, C. M.; Rowan, S. J. The Effect of Polymer Grafting on the Mechanical Properties of PEG-Grafted Cellulose Nanocrystals in Poly(Lactic Acid). *Journal of Polymer Science* **2022**, *60* (24), 3318–3330. https://doi.org/10.1002/POL.20220127.

(53) Nagata, Y.; Mukamel, S. Electrical Double Layer Probed by Surface-Specific Vibrational Technique. *Chem* **2018**, *4* (7), 1484–1485. https://doi.org/10.1016/J.CHEMPR.2018.06.009.

(54) Kawaguchi, T.; Komanicky, V.; Rao, R.; -, al; Jarvey, N.; Henrique, F.; Gupta -, A. The Effect of Stern Layer Thickness on the Diffuse Capacitance for Size Asymmetric Electrolyte inside the Charged Spherical Cavities by Density Functional Theory. *J Electrochem Soc* **2022**, *169* (2), 020547. https://doi.org/10.1149/1945-7111/AC52FE.

(55) Brown, M. A.; Bossa, G. V.; May, S. Emergence of a Stern Layer from the Incorporation of Hydration Interactions into the Gouy-Chapman Model of the Electrical Double Layer. *Langmuir* **2015**, *31* (42), 11477–11483.

(56) *XModFit: X-ray Modeling and Fitting*. https://github.com/chemmatcars/XModFit (accessed 2023-02-21).

(57) Calero, C.; Faraudo, J.; Bastos-Gonz Alez, D. Interaction of Monovalent Ions with Hydrophobic and Hydrophilic Colloids: Charge Inversion and Ionic Specificity. *J. Am. Chem. Soc* **2011**, *133*, 15025–15035. https://doi.org/10.1021/ja204305b.

(58) Yurtsever, A.; Wang, P.-X.; Priante, F.; Jaques, Y. M.; Miyazawa, K.; MacLachlan, M. J.; Foster, A. S.; Fukuma, T. Molecular Insights on the Crystalline Cellulose-Water Interfaces via Three-Dimensional Atomic Force Microscopy. *Sci Adv* **2022**, *8* (41), 160. https://doi.org/10.1126/SCIADV.ABQ0160.

(59) Zhang, Y.; Yang, H.; Naren, N.; Rowan, S. J. Surfactant-Free Latex Nanocomposites Stabilized and Reinforced by Hydrophobically Functionalized Cellulose Nanocrystals. *ACS Appl Polym Mater* **2020**, *2* (6), 2291–2302. https://doi.org/10.1021/ACSAPM.0C00263/SUPPL_FILE/AP0C00263_SI_001.PDF.

(60) Malaspina, D. C.; Faraudo, J. Molecular Insight into the Wetting Behavior and Amphiphilic Character of Cellulose Nanocrystals. *Adv Colloid Interface Sci* **2019**, *267*, 15–25. https://doi.org/10.1016/J.CIS.2019.02.003.

(61) Gestranius, M.; Stenius, P.; Kontturi, E.; Sjöblom, J.; Tammelin, T. Phase Behaviour and Droplet Size of Oil-in-Water Pickering Emulsions Stabilised with Plant-Derived Nanocellulosic Materials. *Colloids Surf A Physicochem Eng Asp* **2017**, *519*, 60–70. https://doi.org/10.1016/J.COLSURFA.2016.04.025.

(62) Kalashnikova, I.; Bizot, H.; Cathala, B.; Capron, I. Modulation of Cellulose Nanocrystals Amphiphilic Properties to Stabilize Oil/Water Interface. *Biomacromolecules* **2012**, *13* (1), 267–275. https://doi.org/10.1021/BM201599J/SUPPL_FILE/BM201599J_SI_001.PDF.

(63) H Giles, B. C.; Macewan, T. H.; Nakhwa, S. N.; Smith, D. Solution Adsorption Isotherms, and Its Use in Diagnosis of Adsorption Mechanisms and in Measurement of Specific Surface Areas of Solids. **1960**, 279.

(64) Piccin, J. S.; Cadaval, T. R. S. A.; De Pinto, L. A. A.; Dotto, G. L. Adsorption Isotherms in Liquid Phase: Experimental, Modeling, and Interpretations. *Adsorption Processes for Water Treatment and Purification* **2017**, 19–51. https://doi.org/10.1007/978-3-319-58136-1_2/FIGURES/7.

(65) Sexsmith, F. H.; White, H. J. The Absorption of Cationic Surfactants by Cellulosic Materials: I. The Uptake of Cation and Anion by a Variety of Substrates. *J Colloid Sci* **1959**, *14* (6), 598–618. https://doi.org/10.1016/0095-8522(59)90026-1.

(66) Sexsmith, F. H.; White, H. J. The Absorption of Cationic Surfactants by Cellulosic Materials: III. A Theoretical Model for the Absorption Process and a Discussion of Maxima in Absorption Isotherms for Surfactants. *J Colloid Sci* **1959**, *14* (6), 630–639. https://doi.org/10.1016/0095-8522(59)90028-5.

(67) *X-ray Anomalous Scattering (XAnoS)*. https://github.com/nayanbera/XAnoS (accessed 2023-02-21).

(68) Bera, M. K.; Bu, W. XModFit: X-Ray Modeling and Fitting. **2022**. https://doi.org/10.5281/ZENODO.7047225.

(69) Mao, Y.; Liu, K.; Zhan, C.; Geng, L.; Chu, B.; Hsiao, B. S. Characterization of Nanocellulose Using Small-Angle Neutron, X-Ray, and Dynamic Light Scattering

Techniques. *Journal of Physical Chemistry B* **2017**, *121* (6), 1340–1351. https://doi.org/10.1021/ACS.JPCB.6B11425/SUPPL_FILE/JP6B11425_SI_001.PDF.

(70) Ballauff, M.; Jusufi, A. Anomalous Small-Angle X-Ray Scattering: Analyzing Correlations and Fluctuations in Polyelectrolytes. *Colloid Polym Sci* **2006**, *284* (11), 1303. https://doi.org/10.1007/S00396-006-1516-5.

(71) Tatchev, D. Structure Analysis of Multiphase Systems by Anomalous Small-Angle X-Ray Scattering. *https://doi.org/10.1080/14786430802279760* **2008**, *88* (12), 1751–1772. https://doi.org/10.1080/14786430802279760.

(72) Sztucki, M.; Di Cola, E.; Narayanan, T.; Sztucki, M.; Cola, E. Di; Narayanan, T. New Opportunities for Anomalous Small-Angle X-Ray Scattering to Characterize Charged Soft Matter Systems. *J Phys Conf Ser* **2011**, *272* (1), 012004. https://doi.org/10.1088/1742-6596/272/1/012004.

(73) Sztucki, M.; Di Cola, E.; Narayanan, T. Anomalous Small-Angle X-Ray Scattering from Charged Soft Matter. *The European Physical Journal Special Topics 2012 208:1* **2012**, *208* (1), 319–331. https://doi.org/10.1140/EPJST/E2012-01627-X.

(74) Wieland, D. C. F.; Schroer, M. A.; Gruzinov, A. Y.; Blanchet, C. E.; Jeffries, C. M.; Svergun, D. I. ASAXS Measurements on Ferritin and Apoferritin at the BioSAXS Beamline P12 (PETRA III, DESY). *J Appl Crystallogr* **2021**, *54* (Pt 3), 830–838. https://doi.org/10.1107/S1600576721003034.

(75) Phys Lett, A.; Chantler, C. T. Detailed Tabulation of Atomic Form Factors, Photoelectric Absorption and Scattering Cross Section, and Mass Attenuation Coefficients in the Vicinity of Absorption Edges in the Soft X-Ray (Z=30–36, Z=60–89, E=0.1 KeV–10 KeV), Addressing Convergence Issues of Earlier Work. *J Phys Chem Ref Data* **2000**, *29* (4), 597–1056. https://doi.org/10.1063/1.1321055.

(76) Sztucki, M.; Di Cola, E.; Narayanan, T. Instrumental Developments for Anomalous Small-Angle X-Ray Scattering from Soft Matter Systems. *urn:issn:0021-8898* **2010**, *43* (6), 1479–1487. https://doi.org/10.1107/S002188981003298X.

(77) Bera, M. K. XAnoS: X-Ray Anomalous Scattering. *Zonedo*. 2023.

Chapter 3: Enhanced Membrane Based Separation through the Design of Polymer Grafted Cellulose Nanocrystal One-Component Nanocomposite Membranes

3.1 Abstract

Membrane filtration is an important industrial purification process used to access clean, potable water. The fabrication of the membranes used in these purification applications often involves expensive and energy intensive processes which have a large negative impact on the environment. Sustainable alternatives with high water flux and strong rejection performance are needed to purify water. The focus of this work was to investigate the use of polymer grafted cellulose nanocrystals (CNCs) in membrane applications. The impact of the polymer grafting density and polymer conformation was investigated and showed that by increasing the grafting density of PEG such that it adopted a semi-dilute polymer brush conformation, the water flux through the membranes could be increased from 3.5 L hr^{-1} m^{-2} to 2900 L hr^{-1} m^{-2} for CNC membranes without and with grafted PEG, respectively. These membranes also exhibited rejection performances with molecular weight cut-offs between 62 kDa and 100 kDa for all polymer grafted samples, consistent with the ultrafiltration regime. Thus, the design of these one-component composite materials can enhance the water permeability of ultrafiltration membranes while maintaining effective selectivity.

3.2 Introduction

As the global demand for water from industrial processes, agriculture, and personal consumption increases, natural reservoirs are becoming progressively more strained. The regions that rely on these strained reservoirs are in turn becoming water-stressed, such that their demand for water has, or soon will, exceed the availability of the resource. The stress on these limited clean water resources is heightened by increased urbanization, coupled with industrial expansion across these water-stressed regions.[1,2] As the supply of clean water is decreasing, there is a significant increase

in the need for potable water to be produced from underutilized sources, like contaminated fresh water and wastewater. Based on reports from the US Environmental Protection Agency (EPA), only 7 to 8% of the thirty-two billion gallons of waste effluent produced each day are recycled.[3] To help address these issues, several technologies like membrane filtration,[4–10] flocculation,[11–13] and sorbents[14–16] are used to generate potable water.

One of the most common methods of water purification is membrane filtration, as it typically exhibits a sufficiently high separation efficiency to provide high quality water with low chemical sludge effluent.[4] Membrane filtration is a process that separates molecules of different sizes and characteristics through the use of a pressure differential to drive separation through a specific membrane. One class of membranes, namely porous films, rely on size exclusion, which depends on the membrane's microstructure, or adsorption, and can target specific solutes based on the surface chemistry of the membrane to separate contaminants from water.[4,10,17–20] Filtration membranes are classified into different regimes based on their pore sizes, i.e. microfiltration (5 to 0.1 μm), ultrafiltration (0.1 to 0.01 μm), nanofiltration (0.01 to 0.001 μm), or reverse osmosis membranes (0.001 to 0.0001 μm or nonporous).[4,21] These pore sizes in turn determine the types of contaminants that each membrane can remove. For example, ultrafiltration membranes are suitable for the removal of bio-based contaminants such as viruses or proteins from water.[4,21,22] However, there are several challenges that must be resolved in order for membrane filtration technology to fully meet the growing demand for potable water. Some of these challenges include improved water permeability, membrane stability, environmental impact, fouling, and water solute selectivity.[4,23,24]

Typical materials used for ultrafiltration membranes include inorganic ceramics,[25–27] as well as organic polymers like polyacrylonitrile (PAN),[28,29] polysulfone amides (PSA),[4]

polysulfone (PSU),[30] polyether sulfone (PES),[31] and polyvinylidene fluoride (PVDF).[4,10,17,22,32,33] Many of these membrane materials are produced using chemicals from petroleum-based sources, often requiring a significant number of organic solvents and small molecule components to manufacture functional membranes.[34,35]

Natural biopolymers derived from low-cost, renewable bio-sources such as algae, plants, and microbes represent promising foundations for sustainable membrane alternatives that are petroleum-free and can be fabricated and modified in aqueous solutions instead of organic solvents.[16,36] In particular, various polysaccharides including chitosan[37–42] and cellulose[18,43–53] have been utilized in water purification applications.[16] Cellulose is a particularly promising material, as it is the most common biopolymer on the planet with a surface that can be engineered through facile chemical modification to introduce functional moieties.[54–56] In fact cellulose derivatives, such a cellulose acetate,[50,57–60] are commonly used as membrane materials. However, they are chemically modified and fabricated into membranes using processes that requires large amounts of organic solvents and produces a significant amount of waste.[43,61–63] Nanocelluloses, such as cellulose nanofiber (CNFs) and cellulose nanocrystals (CNCs), have also recently received some attention as membranes materials. CNCs are highly crystalline, rod-like nanoparticles that can be isolated from a variety of different bio-sources, like cotton, wood, or fast-growing grasses such as *Miscanthus* x. *Giganteus* (*MxG*).[36,64–67] CNCs make promising candidates for membrane applications on account of their mechanical strength, chemical stability, and hydrophilic surface chemistry. Their high mechanical strength is a potential advantage if the material needs to withstand the high-pressure conditions required for ultrafiltration as well as nanofiltration,[68,69] while their inherent hydrophilicity is an advantage to reduce the fouling of the membrane surface.[70]

Nanocellulose can be used to enhance the water permeability and anti-fouling properties of membranes by blending them into the polymer matrix and using that two-component nanocomposite as a barrier layer.[71] Additional studies have investigated the potential of nanocellulose as the sole component of the membrane barrier layer. Many of these membranes were designed to be affinity membranes focusing on the removal of charged contaminants like metal ions or organic dyes from solution via adsorption.[23,41,54,72,73] However, Mautner *et al.* has shown that size exclusion based ultrafiltration membranes can be fabricated from nanocellulose without being blended with a polymer.[53] While these membranes exhibited flowrates comparable to commercially available membranes, the barrier layers were prone to point defects that could compromise the selectivity of the membranes. Additionally, the pore sizes were shown to be dependent on the dimensions of the nanocellulose used in the fabrication of the membrane with larger diameter nanoparticles leading to larger pore sizes;[53] therefore, the selectivity of these nanocellulose barrier layers is limited and these materials cannot be easily tuned to target specific contaminants.

Thus, the goal of this work is to explore if grafting polymers to the CNCs can be used to tailor their behavior in membrane applications. Polymer-grafted CNCs can be processed directly into what has been termed a one-component nanocomposite (OCNs) film.[74–76] The covalently linked nature of these materials prevents phase separation between the nanofiller and the polymer and as such allows access to a wider range of polymer to nanofiller ratios than traditional two-component composites.[76] Prior work on OCNs of polymer grafted CNCs has shown that such materials exhibit

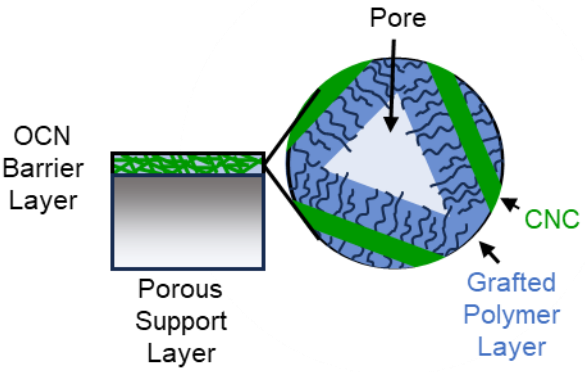

Figure 3.1. Schematic illustration of polymer grafted CNC membranes. The anisotropic thin-film composite membranes are composed of a one-component nanocomposite barrier layer on top of a porous membrane support structure. The OCN barrier layer is composed of distinct polymer grafted CNCs with pores in between the outer edges of their tethered polymer regions.

enhanced toughness and, in some cases, enhanced ion transport over equivalent two-component composites.[76–78] Thus, it was of interest to see how functionalization of the nanocellulose with a polymer impacted the behavior of the resulting OCN membranes. As such, reported herein is the exploration of poly(ethylene glycol) (PEG) grafted CNCs as the OCN barrier layer for ultrafiltration membranes (Figure 3.1). A specific focus of this work is to explore how polymer graft molecular weight and density impacts the properties of these membranes.

3.3 Results and Discussion

3.3.1 Isolation and Functionalization of Cellulose Nanocrystals

CNCs were isolated from *Miscanthus x. Giganteus* (*MxG*) and oxidized to form MxG-CNC-COOH according to established literature procedures.[36,79] The *MxG* stalks undergo mechanical processing, base washes, and acid washes to isolate the CNCs. Carboxylate groups are then introduced to the surface of the CNCs through (2,2,6,6-tetramethylpiperidin-1-yl)oxyl (TEMPO)-mediated oxidation in aqueous dispersions (Figure 3.2(a)). These carboxylate groups serve to

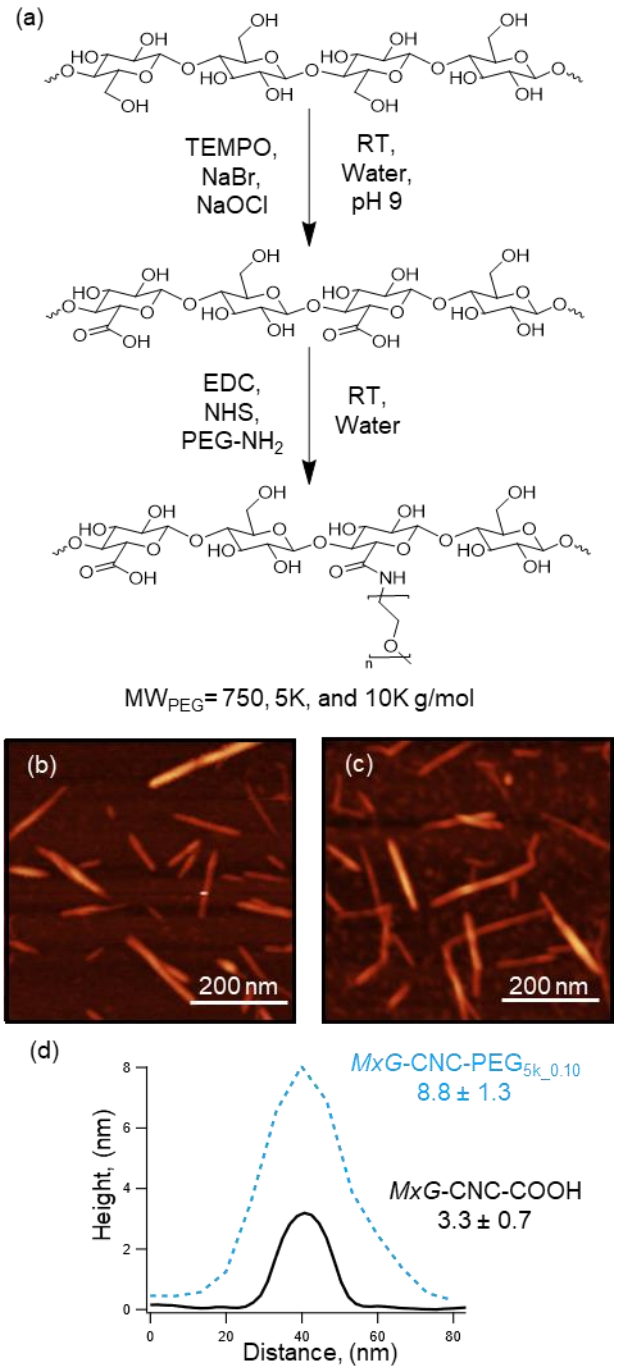

Figure 3.4. (a) Synthesis of carboxylic acid functionalized CNCs (*MxG*-CNC-COOH) followed by the subsequent grafting reaction to attach PEG-NH_2 to the CNCs, (b) AFM height image of *MxG*-CNC-COOH, (c) AFM height image of *MxG*-CNC-g-$PEG_{5k\_0.10}$ ($PEG_{5k\_0.10}$ refers to 5000 g mol^{-1} grafted using EDC/NHS at a grafting density of 0.10 chains per nm^2), and (d) AFM height profile comparison between *MxG*-CNC-COOH and *MxG*-CNC-g-$PEG_{5k\_0.10}$

improve the dispersion of the CNCs in solution as the electrostatic repulsion mitigates CNC

aggregation, while also providing a reactive moiety for further functionalization. The density of carboxylates on the CNC surface was determined (via a conductivity titration) to be ca. 1000 mmol/kg, which is equivalent to ca. 1.14 carboxylate groups per nm^2 (Figure S3.1). The *MxG*-CNC-COOH exhibited a crystallinity index of 0.85 as measured by wide angle X-ray scattering (Figure S3.2) and the dimensions of the crystals (determined by AFM) had an average length of 300 ± 120 nm, a width of 8.5 ± 2 nm, and a height of 3.3 ± 0.7 nm (Figure 3.2(b)).

Amine-terminated methoxy poly(ethylene glycol) (PEG-NH_2) of various molecular weights, 750 g mol^{-1}, 5k g mol^{-1}, and 10k g mol^{-1}, was grafted to the *MxG*-CNC-COOH (Figure 3.2(a)) using 1-ethyl-3-(3-dimethylaminopropyl) carbodiimide (EDC) and N-hydroxysuccinimide (NHS) as coupling agents in deionized water following literature procedures.[79,80] The resulting polymer grafted CNCs (termed *MxG*-CNC-*g*-PEG_x, where x is represents the M.Wt. of the PEG graft in g/mol, 750, 5k, or 10k) exhibit an increase in height from 3.3 ± 0.7 nm to 8.8 ± 1.3 nm after grafting for *MxG*-CNC-*g*-PEG_{5k}, which is consistent with successful covalent attachment of the PEG-NH_2 to the CNC surface (Figure 3.2(c) and 3.2(d)).[76,79] *MxG*-CNC-*g*-PEG_{10k} also exhibits an increase in height to 5.0 ± 0.2 nm, however, the *MxG*-CNC-*g*-PEG_{750} shows only a slight change in height (4.2 ± 0.5 nm) relative to the height of the ungrafted *MxG*-CNC-COOH (Figure S3.3).

To determine the amount of PEG grafted to the CNCs high-resolution thermogravimetric analysis (Hi-Res TGA) was used. The degradation of the *MxG*-CNC-g-PEG samples exhibit three degradation events as observed in the Hi-Res TGA data (a-c in Figure 3.3 and Figure S3.4). Based on the TGA of the MxG-CNC-COOH and the PEG-NH_2 the lower temperature degradation events (a and b) are associated with cellulose degradation, while the higher temperature degradation event (c) corresponds to PEG degradation. To estimate the weight fraction of PEG in these samples, a peak deconvolution method with a Lorenztian fit was used to determine the contribution of each

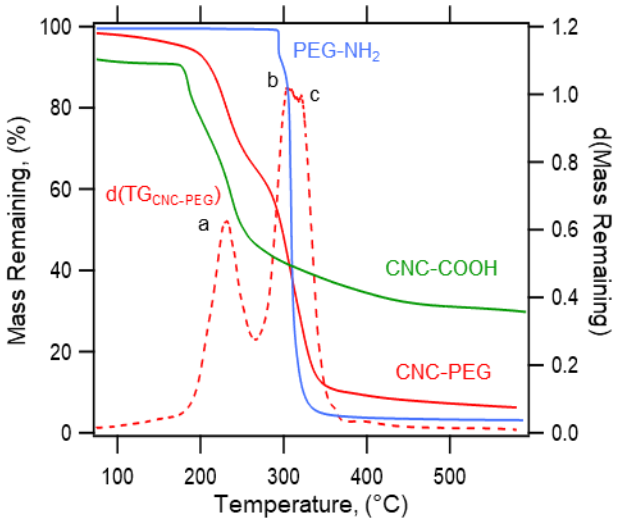

Figure 3.5. Hi-Res TGA curves of *MxG*-CNC-COOH (green), PEG-NH_2 (blue), and *MxG*-CNC-*g*-$PEG_{5k\_0.10}$ (solid red). The derivative of *MxG*-CNC-*g*-$PEG_{5k\_0.10}$ is presented to highlight the degradation events corresponding to cellulose (labeled a and b) and PEG degradation (labeled c). component to the peaks of the dTG curve (Figure S3.5). The area under these fits were integrated to estimate PEG weight fractions, which ranged from 8 to 32 wt.% (Table 3.1) depending on the sample, which corresponds to volume fractions from 10 to 38% PEG (Table 3.1, Section S3.1).

Table 3.1. Polymer content and grafting density for *MxG*-CNC-*g*-PEG samples with various molecular weights of grafted PEG

Sample	Grafted Polymer (wt%)	Polymer Volume Fraction (%)	Grafting Density (Chains/nm^2)
MxG-CNC-*g*-PEG_{750}	14	18	0.25
MxG-CNC-*g*-$PEG_{5k\_0.02}$	8	10	0.02
MxG-CNC-*g*-$PEG_{5k\_0.05}$	17	21	0.05
MxG-CNC-*g*-$PEG_{5k\_0.07}$	24	30	0.07
MxG-CNC-*g*-$PEG_{5k\_0.10}$	31	37	0.10
MxG-CNC-*g*-PEG_{10k}	32	38	0.05

The weight fractions were used to calculate the grafting density of each sample, which ranges from 0.02 to 0.25 chains per nm^2 (Table 3.1, SI Section S3.2).[79]

It has been shown in the polymer brush literature on planar surfaces that molecular weight and grafting density each play a role in the nature of the polymer conformation of the grafted brush. In order to explore if the grafted polymer conformation plays a role in the resulting properties of the PEG grafted CNC membranes, in addition to varying the molecular weight of the grafted PEG, the *MxG*-CNC-*g*-PEG_{5k} material was prepared at different grafting densities. The initially synthesized *MxG*-CNC-g-PEG_{5k} has a grafting density of 0.10 chains/nm^2. To access samples with different grafting densities, the same grafting procedure was performed with varying equivalents of PEG-NH_2 from 0.5 eq. to 2 eq. The different *MxG*-CNC-g-PEG_{5k} samples were then purified with dialysis until amine-sensing Kaiser tests confirmed the absence of unreacted PEG-NH_2.[81] The resulting samples are labeled *MxG*-CNC-*g*-$PEG_{5k\_y,}$ where the y indicates their relative grafting densities in chains/nm^2, 0.02, 0.05, 0.07, and 0.10, (Table 3.1). As one might expect the height of the grafted CNCs as obtained by AFM decreases with grafting density going from 8.8 ± 1.3 nm, 5.5 ± 0.5 nm, 4.3 ± 0.1 nm to 3.7 ± 0.2 nm for the *MxG*-CNC-$COOH_{5k\_y}$ where y=0.1, 0.07, 0.05 and 0.02, respectively. The lower grafting density sample *MxG*-CNC-$COOH_{5k\_0.02}$ has a height of that is statistically equivalent to the height of *MxG*-CNC-COOH (Figure S3.3).

The tethered polymer conformations can be divided into three regimes, namely the mushroom regime, the concentrated brush regime (CPB), and the semi-dilute brush regime (SDPB).[76,82–85] The radius of gyration (R_g) and the grafting density of the tethered polymer largely influence which conformation will be adopted by the grafted polymer.[75] The mushroom regime is defined by the phase space in which the tethered polymers are spread across the surface such that adjacent chains do no interact with each other.[76,79] As such, the boundary of mushroom regime is the point at which

each polymer chain's conformation would be influenced by its neighbors for a given molecular weight. As grafting density is increased to the point that neighboring chains are at a distance less than R_g from each other, the polymers adopt a SDPB conformation.[86] In this regime, the polymers extend away from the nanoparticle surface and deviate from the loose coil conformation seen in the mushroom regime. As chains are packed more densely on the nanoparticle surface, the polymers enter the CPB regime, where they elongate to form a stiffer polymer layer. For polymer grafted nanoparticles that exhibit a CPB, the polymer chains with sufficiently high molecular weights may transition from a CPB to a SDPB regime at some radial distance away from the particle's surface on account of the innate curvature of the nanoparticle causing [86] the volume to increase in accordance with predictions by Daoud−Cotton models applied to nanoparticles.[76,87–89]

With the grafting densities calculated and the molecular weights known, it was possible to determine the nature of the grafted polymer conformations by plotting the grafting density and molecular weight of the grafted PEG onto a tethered polymer phase diagram (Figure 3.4). The transition between the mushroom and brush regimes (the red line in Figure 3.4) was defined by taking the inverse of the area of a circle defined by the R_g of the grafted polymer that would be projected onto the surface.[76,79,85] The concentrated brush to semi-dilute brush transition (the teal line in Figure 3.4) was calculated based on work by Hansoge et al. using their model of polybutadiene, which exhibits a similar persistence length to PEG.[79,90] Based on this phase diagram, *MxG*-CNC-*g*-PEG_{750}, *MxG*-CNC-*g*-$PEG_{5k\_0.02}$, and *MxG*-CNC-*g*-$PEG_{5k\_0.05}$ each appear

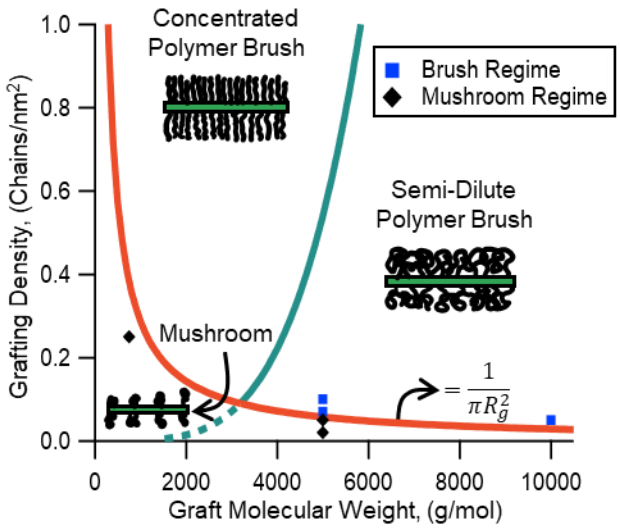

Figure 3.4. Polymer conformation phase space with synthesized *MxG*-CNC-*g*-PEG samples plotted. The concentrated polymer brush to semi-dilute polymer brush transition (teal line) is modeled based off polybutadiene.[90] The mushroom to brush transition (red line) is estimated based on the grafting density at which circles defined by the R_g of the polymer would start to overlap.

to fall in the mushroom regime, while *MxG*-CNC-*g*-PEG$_{5k_0.07}$, *MxG*-CNC-*g*-PEG$_{5k_0.10}$, and *MxG*-CNC-*g*-PEG$_{10k}$ have moved more into the semi-dilute polymer brush regime.

3.3.2 One-Component Nanocomposite Membranes

Membranes were prepared by vacuum casting the different *MxG*-CNC-*g*-PEG samples onto cellulose filter paper, with the *MxG*-CNC-*g*-PEG acting as the barrier layer and the cellulose filter paper providing additional support. As a control, *MxG*-CNC-COOH membrane samples were prepared using the same process. The morphologies of these membranes were characterized by scanning electron microscopy (SEM), which shows that the CNC nanoparticles appear to form porous, fibrous networks with individualized particles or bundles of nanoparticles visible in the

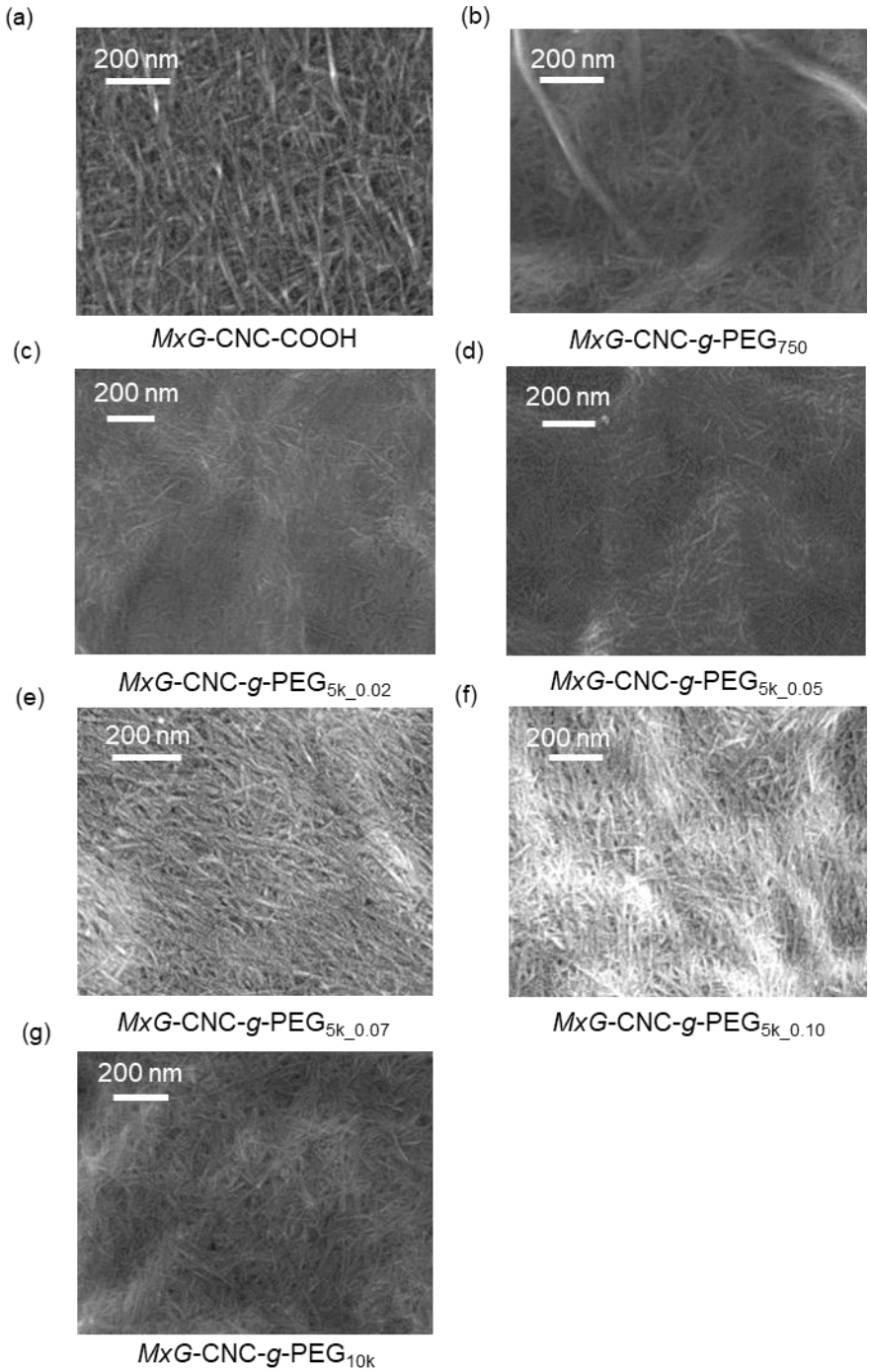

Figure 3.5. SEM images of *MxG*-CNC-COOH and *MxG*-CNC-*g*-PEG membrane surfaces with PEG of different molecule weights and grafting densities. (a) *MxG*-CNC-COOH, (b) *MxG*-CNC-*g*-PEG_{750}, (c) *MxG*-CNC-*g*-$PEG_{5k\_0.02}$, (d) *MxG*-CNC-*g*-$PEG_{5k\_0.05}$, (e) *MxG*-CNC-*g*-$PEG_{5k\_0.07}$, (f) *MxG*-CNC-*g*-$PEG_{5k\_0.10}$, (g) *MxG*-CNC-*g*-PEG_{10k}

images for *MxG*-CNC based membranes instead of a dense, solid polymer film (Figure 3.5). These membranes were tested in a dead-end filtration configuration to determine the flux of deionized

water passing through the films under two bars of pressure. The *MxG*-CNC-COOH film exhibits a water flux of 3.50 ± 0.10 ($\frac{L}{hr\ m^2}$) (Figure 3.6(a)). The samples in which the graft PEG is predicated to be in the mushroom regime, namely *MxG*-CNC-*g*-PEG_{750} (3.27 ± 0.71 ($\frac{L}{hr\ m^2}$)), *MxG*-CNC-*g*-$PEG_{5k\_0.02}$ (3.99 ± 0.41 ($\frac{L}{hr\ m^2}$)), and *MxG*-CNC-*g*-$PEG_{5k\_0.05}$ 3.76 ± 0.06 ($\frac{L}{hr\ m^2}$)), show no statistical improvement in the flux when compared to the *MxG*-CNC-COOH membranes (Figure 3.6(a) and 3.6(b)). This data also shows the polymer volume fraction in these samples, which ranges from 10% for *MxG*-CNC-*g*-$PEG_{5k\_0.02}$ to 21% for *MxG*-CNC-*g*-$PEG_{5k\_0.05}$, has little-to-no effect on the flux through the membranes.

However, the story appears different as the tethered polymer conformation transitions into the semi-dilute polymer brush regime. There is a significant increase in the water flux to 6.30 ± 0.05 ($\frac{L}{hr\ m^2}$), 250 ± 5.14 ($\frac{L}{hr\ m^2}$) , and 2900 ± 290 ($\frac{L}{hr\ m^2}$) for the *MxG*-CNC-*g*-PEG_{10k}, the *MxG*-CNC-*g*-$PEG_{5k\_0.07}$, and the *MxG*-CNC-*g*-$PEG_{5k\_0.10}$ samples, respectively (Figure 3.6(a) and 3.6(c)). It is worthy of note that the flux of 2900 ($\frac{L}{hr\ m^2}$) for *MxG*-CNC-*g*-$PEG_{5k\_0.10}$ is significantly higher than the flux of 6.30 ($\frac{L}{hr\ m^2}$) for *MxG*-CNC-*g*-PEG_{10k} even though these two samples have similar volume fractions of 37% and 38%, respectively, suggesting that the volume fraction of PEG in these composites is not the only driver of the water flux through these materials.

Additional control experiments were conducted with blends of *MxG*-CNC-COOH and PEG-NH_2 to evaluate the role of covalent attachment between the PEG and the CNC nanoparticles. As might be expected these tests showed an increase in water flux after each additional test (not

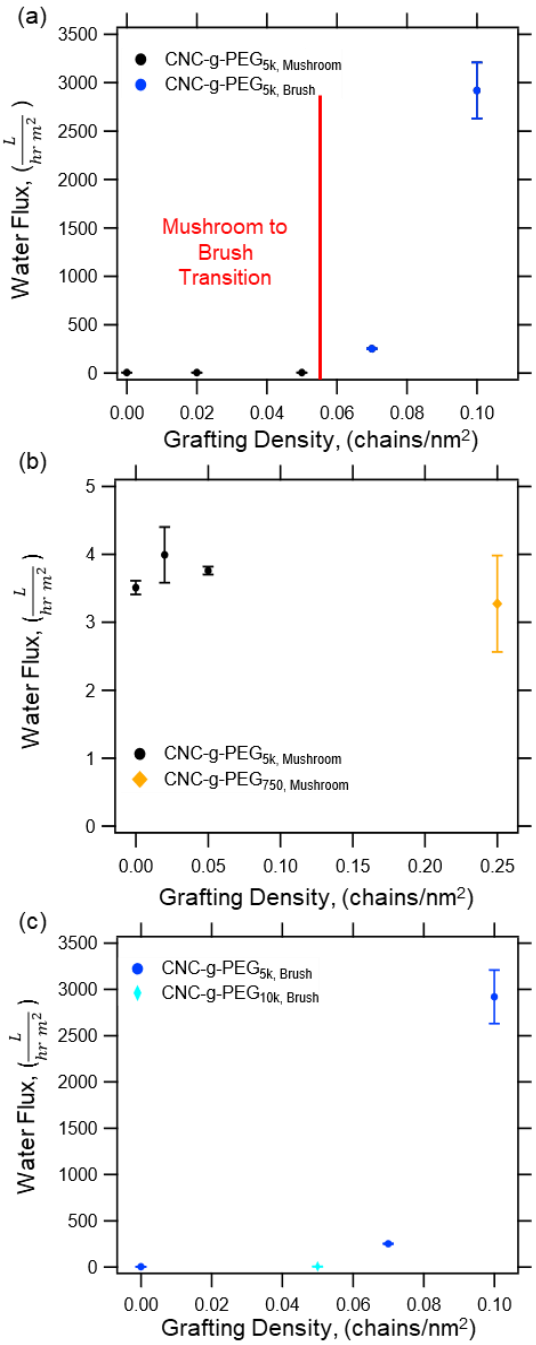

Figure 3.6. (a) Water flux for the *MxG*-CNC-*g*-PEG$_{5k_y}$ samples as grafting density is increased from the mushroom regime (black circles) to the semi-dilute polymer brush regime (blue circles) with the transition point denoted with a solid red line. (b) Water flux of all mushroom regime samples as grafting density increases. (c) Water flux of all semi-dilute polymer brush samples as grafting density increases.

observed in the *MxG*-CNC-*g*-PEG-based membranes) as the free PEG was washed through the film (Figure S3.6).

In addition to measuring the deionized water flux through these composite membranes, rejection performance of each membrane was evaluated by determining the molecular weight cut-off (MWCO) of each sample. The MWCO is defined as the molecular weight at which 90% of a tested solute is rejected and kept in the retentate and 10% of the solute with that particular molecular weight passing into the permeate.[4,53,91] For these studies, aqueous solutions of PEG polymers with molecular weights ranging from 10 kDa to 100 kDa with concentrations of 5 mg per mL were used as the solute to test the rejection performance of each membrane. The selectivity of the membranes was estimated by interpolating between the rejection percentages for PEG solutes with molecular weights of 35 kDa and 100 kDa for each sample (Figure 3.7(a)). The selectivity of the membranes with mushroom regime samples was shown to be 62 kDa for *MxG*-CNC-*g*-PEG_{750}, 100 kDa for *MxG*-CNC-*g*-$PEG_{5k\_0.02}$ and 97 kDa for *MxG*-CNC-*g*-$PEG_{5k\_0.05}$. The selectivity of the membranes fabricated from the brush regime samples was determined to be 65 kDa for *MxG*-CNC-*g*-$PEG_{5k\_0.07}$, 82 kDa for *MxG*-CNC-*g*-$PEG_{5k\_0.10}$, and 85 kDa for *MxG*-CNC-*g*-PEG_{10k}. Each of these membranes exhibited a reduction in the MWCO relative to the MWCO of the *MxG*-CNC-COOH samples, which was > 100 kDa (the rejection percentage for 100 kDa solutes was below 90% so an exact MWCO could not be determined). The MWCO is maintained within the low end of the ultrafiltration regime, namely between 1 kDa and 1000 kDa for all samples (Figure 3.7(b)).[4] The selectivity appears to be not significantly impacted by either the amount or the grafting density of the bound PEG polymer. The tethered polymer morphology also does not seem to change the selectivity of the membranes. This consistency may be expected for the samples in the mushroom conformation based on the previously observed flux trends for these materials. However, this result

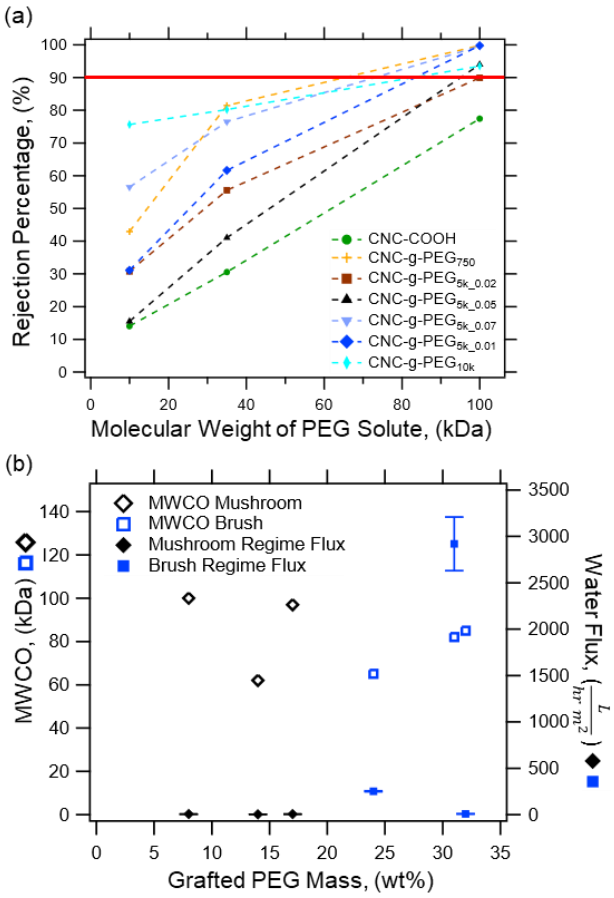

Figure 3.7. (a) The rejection of PEG is shown for MxG-CNC-COOH (green circles), MxG-CNC-g-PEG750 (orange plus symbols), MxG-CNC-g-PEG5k_0.02 (brown squares), MxG-CNC-g-PEG5k_0.05 (black up triangles), MxG-CNC-g-PEG5k_0.07 (periwinkle down triangles), MxG-CNC-g-PEG5k_0.10 (blue diamonds), and MxG-CNC-g-PEG10k (cyan thin rhomboids). The MWCO is the point at which 90% of the solute is rejected (red line). (b) The molecular weight cutoff (open diamonds for the mushroom regime samples and open squares for the brush regime samples) of MxG-CNC-COOH and MxG-CNC-g-PEG membranes and the water flux of the membranes with membrane regime samples denoted with black diamonds and the semi-dilute brush regime samples denoted with blue squares as a function of the amount of grafted polymer.

is perhaps a little surprising for the semi-dilute polymer brush regime samples since the water flux through these materials is drastically higher when compared to other samples, while the MWCO

remains similar to the other grafted CNCs (Figure 3.7).

Even though steps such as washes and stirring were taken to mitigate fouling on the membranes, the potential for fouling normalizing the selectivity was also evaluated. In order to test for the presence of a fouling layer, the membranes used in the MWCO experiments were inverted and DI water was driven through the membranes at 2 bar. The permeates of these tests were collected and examined via light scattering, which showed no signal in the light scattering detector indicating that the foulants were not present at a detectable concentration in the permeate. These experiments indicate that the films were either not severely fouled or that the foulants are more strongly adsorbed to the membrane such that the pressurized water is unable to remove the fouling layer. To further explore the possibility of fouling additional MWCO experiments were conducted under conditions that enhance the likelihood of fouling, namely without the stirring or washing used in the prior experiments. These experiments were conducted on both *MxG*-CNC-*g*-PEG_{750} and *MxG*-CNC-*g*-$PEG_{5k\_0.07}$ such that a mushroom conformation sample and a brush conformation sample could be tested. Under such conditions that encourage fouling, the MWCO of the films was calculated as 40 kDa for *MxG*-CNC-*g*-PEG_{750} and 54 kDa *MxG*-CNC-*g*-$PEG_{5k\_0.07}$ (Figure S3.7), which is a reduction from 62 kDa and 65 kDa, respectively, that was obtained under conditions used to minimize fouling. Such reduction in MWCO when washing and stirring is not used is indicative of increased fouling as the foulants restrict the pores and reduce the size of the solutes that can pass through the membrane.[92] This data suggests that the stirring and washing steps carried out in the initial studies appear to, at least partially, mitigate the fouling of the membrane.

Based on literature precedent, MWCO data is commonly used to estimate pore size in ultrafiltration membranes using measured relationships between the MWCO and known pore size.[4] According to these comparisons, the MWCO data indicate that the pore sizes within these materials

remain on the order of a few nanometers.[4] This pore size measured by MWCO likely correlates to the space between the polymer-grafted CNCs (labeled as "Pore" in Figure 3.1). The presence of these pores is consistent with the SEM images, which show that the *MxG*-CNC-*g*-PEG nanoparticles remain distinct from one another with spaces in between their cylindrical forms for each sample (Figure 3.5). Based on these flux data, the polymer brush on the samples appears to increase the rate of water transport through the membranes while maintaining similar pore sizes. As such, the structure of the membranes was evaluated with helium pycnometry to determine the density of these membranes as the polymer conformation shifted (Figure S3.8). These data show that the introduction of PEG to the surface of the CNCs leads to a reduction in the density of the samples from 1.71 ± 0.0004 g/(cm^3) for *MxG*-CNC-COOH to 1.61 ± 0.0002 g/(cm^3) for *MxG*-CNC-*g*-PEG$_{750}$ (Figure S8), which is in the mushroom regime. Within the CNC-g-PEG$_{5k}$ series the density of the mushroom regime samples remains relatively constant at 1.62 ± 0.0002 g/(cm^3) and 1.61 ± 0.0003 g/(cm^3) for *MxG*-CNC-*g*-PEG$_{5k_0.02}$ and *MxG*-CNC-*g*-PEG$_{5k_0.05}$, respectively. However, there is a decrease in density as the grafted PEG transitions into more into the brush regime with values of 1.58 ± 0.0003 g/(cm^3) for *MxG*-CNC-*g*-PEG$_{5k_0.07}$, 1.44 ± 0.0003 g/(cm^3) for *MxG*-CNC-*g*-PEG$_{5k_0.10}$, and 1.53 ± 0.0004 g/(cm^3) for *MxG*-CNC-*g*-PEG$_{10k}$. The introduction of PEG brushes to the surface of the CNCs appears to shift how the nanoparticles pack together as the membrane is formed such that the structure is less dense. These less dense samples correlate with the increased water flux.

Thus, the PEG brush appears to reduce the density of the membrane providing more space for water to pass through. However, since the MWCO remains relatively constant, the average pore size does not appear to be changing significantly, so the introduction of the polymer brush may lead to an increase in the number of pores or potentially a reduction in tortuosity that leads to an

increase in water permeability. It is also possible that the increase in flux for the brush regime *MxG*-CNC-*g*-PEG samples is aided, in part, by the PEG brushes increasing the water permeability of the membranes. For these brush samples, which are on the boundary of the mushroom to semi-dilute brush regimes, the PEG brush on the surface of the nanoparticle presumably remains water permeable, thus potentially increasing the effective radius of the pores to water,[93–96] increasing the water flux. While the PEG brush on the surface of the nanoparticle should remain water permeable, the brush may sterically hinder transport of macromolecules through the membrane.[93–95] This would then result in the water permeable volume of the membrane being larger than the effective pore size for macromolecules.

Irrespective of the exact mechanism, it is worth noting that for the materials in the CPB/SDPB regime, the flux increases with increasing grafting density. For these CPB/SDPB samples, higher grafting densities will lead to a larger fraction of CPB before the tethered polymer transitions to the SDPB phase. Based on the model from Hansoge et. al (Figure 3.4), the CPD/SDPB samples have CPB regime fractions of 27.5%, 60.0%, and 65.5% for *MxG*-CNC-*g*-PEG_{10k}, *MxG*-CNC-*g*-$PEG_{5k\_0.07}$, and *MxG*-CNC-*g*-$PEG_{5k\_0.10}$, respectively. As the flux through these samples is *MxG*-CNC-*g*-PEG_{10k} < *MxG*-CNC-*g*-$PEG_{5k\_0.07}$ < *MxG*-CNC-*g*-$PEG_{5k\_0.10}$, this data suggests that the CPB regime may be more favorable to water transport than the SDPB.

3.4 Conclusions

A series of PEG grafted *MxG*-CNCs have been synthesized and membranes consisting of one-component nanocomposite barrier layers on top of cellulose-based support layers prepared. The water flux and selectivity of these composite MxG-CNC-g-PEG membranes were evaluated by stirred cell flux test and MWCO measurements. In particular, it was shown that the water flux through the membranes could be increased by orders of magnitude from 3.5 ($\frac{L}{hr\ m^2}$) to 2900

($\frac{L}{hr\ m^2}$), while maintaining a MWCO under 100 kDa, through the addition of grafted PEG at a high enough grafting density such that the polymer graft adopted a CPB/SDB polymer conformation. This system of polymer-grafted CNCs appears (at least to some extent) to be able to decouple the traditional tradeoff between flux and selectivity. This system can also be synthesized and fabricated entirely in aqueous solutions removing the need for large volumes of organic solvents used to fabricate commercially available ultrafiltration membranes. This methodology could provide a modular platform for the design of higher-efficiency polymer grafted CNC membranes that are capable of selective removal or recovery of target contaminants by modifying the grafted polymers to include specialized functional groups. In addition to different polymer chemistries, studies of alternative grafting materials like phosphate binding proteins for the selective recovery of dissolved solids may also be of interest.

3.5 Materials and Methods

3.5.1 Materials

Miscanthus x. *Giganteus* (*MxG*) pulp was provided by Aloterra Energy, LLC. Sodium hydroxide (NaOH), sodium hypochlorite (NaOCl), acetic acid, dimethylformamide (DMF) potassium cyanide (KCN), ninhydrin, butanol, and phenol were purchased from Thermo Fisher Scientific. Sodium chlorite ($NaClO_2$), hydrochloric acid (HCl), 2,2,6,6-tetramethylpiperidine 1-oxyl (TEMPO), sodium bromide (NaBr), and N-hydroxysuccinimide (NHS) were purchased from Millipore Sigma. 1-Ethyl-3-(3-dimethylaminopropyl) carbodiimide (EDC) was purchased from Combi-Blocks. Amine-terminated methoxy poly(ethylene glycol) (PEG-NH2) of various molecular weights (750, 5k, 10k g mol−1) were purchased from CreativePEGWorks. All water used was deionized in-house and all chemicals were used as-received without further purification.
Cellulose Nanocrystal Isolation from *Miscanthus x. Giganteus*

3.5.1 Preparation of the MxG-CNC-COOH

Ground *MxG* stalks (266.6 g) were soaked in 4 L of 2 wt% sodium hydroxide solution at room temperature for 24 hrs. The stalks were then treated twice more with 4 L 2 wt.% sodium hydroxide solutions at 95°C for 24 hours each. After each treatment, the stalks were washed with deionized (DI) water until the permeate was neutral pH. The pulp was then suspended in 4 L of 2 wt.% sodium chlorite solution and 15 mL of glacial acetic acid and heated to 70°C for 2 hrs. After the reaction, the solution was vacuum filtered and washed with DI water until the solid was white with no other color. To isolate the CNCs, hydrolysis was carried out by suspending the bleached white pulp in 4L of 1M HCl. This slurry was then heated to 75°C and stirred for 15 hrs. The mixture was then cooled at room temperature before being vacuum filtered and rinsed with DI water until the permeate was neutral. The solids were then subjected to dialysis with DI water for 5 days with the external solution being replaced twice every day. The solutions were freeze-dried to obtain the alcohol functionalized *MxG* CNCs (*MxG*-CNC-OH) as a white crystalline solid.

3.5.3 Synthesis of *MxG*-CNC-COOH from *MxG*-CNC-OH via TEMPO oxidation

In order to synthesize the *MxG*-CNC-COOH samples, TEMPO oxidation was conducted following the previously published procedure with slight modifications.[36,79] 21.6 g of *MxG*-CNC-OH were dispersed into 1500 mL of DI water. Simultaneously, 1.7 g of TEMPO, 16.9 g of NaBr, and 138 g of NaOCl were dissolved into 500 mL of DI water. These two solutions were then mixed together and the pH was adjusted to 10 with NaOH and HCl. Once at pH 10, the reaction was allowed to proceed for 4.5 hrs with the pH being checked every half hour. The reaction was then quenched with 40 g of sodium chloride before being filtered and washed with DI water. The solid was redispersed in DI water and dialyzed for 5 days before being freeze-dried to produce *MxG*-CNC-COOH.

3.5.4 Grafting PEG-NH_2 to *MxG*-CNC-*g*-PEG

MxG-CNC-COOH were suspended in DI water at 10 mg mL^{-1} using a sonic bath to promote dispersion. Relative to the carboxylate content determined by conductivity titration, PEG-NH_2 (1 eq.) of the desired molecular weight was added to the CNC suspension and allowed to dissolve. EDC (3 eq.) was added and stirred for 15 min before adding NHS (3 eq.). The reaction proceeded overnight before centrifuging and resuspending in DI water. This new CNC suspension was dialyzed in dialysis tubing with a 10k MWCO to remove any remaining EDC, NHS, and free polymer. The *MxG*-CNC-*g*-PEG suspension was dialyzed until a Kaiser test for primary amines confirmed that the free polymer had been removed. To perform the Kaiser test, three separate solutions were prepared for the testing process: (A) KCN (0.65 mg) was dissolved in DI water (1 ml) then added to pyridine (49 ml), (B) ninhydrin (1 g) was dissolved in butanol (20 ml), and (C) phenol (40 g) was dissolved in butanol (20 ml). To conduct a test, sample solution (1 ml) was placed in a vial on a hot plate at 100°C. Two drops of each solution were added and allowed to react, shaking occasionally. The color of the test solution was then compared to a control solution that had no primary amines. Once the test sample did exhibit a color change the *MxG*-CNC-*g*-PEG suspension was deemed to no longer contain a significant amount of free polymer. After purification, the resulting *MxG*-CNC-*g*-PEGs were suspended in water and freeze dried to obtain a fluffy white powder. To access samples with various grafting density, this process was repeated with varying amounts of PEG-NH_3 (0.5 eq., 1.5 eq., and 2 eq. for *MxG*-CNC-*g*-$PEG_{5k\_0.02}$, *MxG*-CNC-*g*-$PEG_{5k\_0.07}$, and *MxG*-CNC-*g*-$PEG_{5k\_0.10}$, respectively).

3.5.5 Preparation of MxG-CNC-g-PEG Membranes

To prepare *MxG*-CNC-*g*-PEG membranes, 100 mg of each sample was suspending in deionized water at a concentration of 1 mg mL^{-1}. These suspensions were then vacuum filtered

onto cellulose filter paper with an average pore size of 0.2 μm. The filtrate was then collected and passed through the membrane twice more to ensure that any CNCs that passed through the filter were collected. The membranes were then dried under ambient conditions overnight.

3.5.6 Conductivity Titration

The functional group density of the *MxG*-CNC-COOH samples was determined by conductometric titration. 75 mg of the *MxG*-CNC-COOH were dispersed into 150 mL of DI water using sonication. 15 μL of 12 M hydrochloric acid was added to 50 mL of the CNC dispersion to lower the solution's pH to 2-3. This suspension was then titrated with 0.01 M sodium hydroxide. In order to determine the charge density on the surface of the CNCs, the volume of 0.01 M sodium hydroxide used to titrate the weak acid functional groups in the conductometric titration was determined in Figure S3.1. The length of the initial trend line represents the volume of 0.01 M NaOH used to titrate the strong acid functional groups, while the plateau region corresponds to the weak acid functional groups. From the volume of NaOH used to titrate these functional groups, the functional group density on the CNC surface can be determined by:

$$Functional\ Group\ Density = \frac{CV_{NaOH}}{M}$$

Where C is the concentration of NaOH, V_{NaOH} is the volume of NaOH used to titrate the functional groups based on the difference between where the trendlines intersect, and M is the mass of CNCs in kg.

3.5.7 Degree of Crystallinity

Wide angle X-ray scattering (WAXS) conducted at the 12-ID-B beamline at the Advanced Photon Source at Argonne National Laboratory was used to determine the degree of crystallinity of the CNCs after hydrolysis and oxidation. The CNCs were packed tightly into a washer and held

in place between two pieces of Kapton tape. The data was then processed using the SAXS GUI software at the beamline before being analyzed with the SAS Irena package in IGOR Pro 7. The crystallinity index of the samples was determined with the peak deconvolution method with a Gaussian fit.

3.5.8 Thermogravimetric Analysis

The total amount of PEG in the *MxG*-CNC-*g*-PEG samples was measured using high resolution thermogravimetric analysis (Hi-Res TGA). The Hi-Res TGA procedure slows the heating rate when a mass loss event is detected so that the distinction between degradation events for cellulose degradation and PEG degradation can be improved. For these samples, procedure was conducted with the default settings (sensitivity = 1, amplitude 5 °C, period 200 s, ramp = 5 °C min−1 to 600°C, resolution = 6) in platinum pans. Taking the derivative of the mass loss curve and fitting with multipeak fitting software, the area under the peak associated with PEG degradation can be measured to determine the weight fraction of PEG relative to CNC. Based on this analysis, a polymer grafting density can be obtained. The calculations for these conversions can be found in the Supporting Information.

3.5.9 Atomic Force Microscopy

Atomic force microscopy (AFM) was conducted on a Cipher ES Environmental AFM. Samples were prepared on a freshly-cleaved mica surface by first drop-casting poly(L-lysine), gently rinsing with DI water, then drop-casting the desired CNC sample suspended in DI water at 0.005 wt.%. The solution was allowed to sit for 3 minutes before once again gently rinsing with DI water before drying overnight. The samples were imaged in tapping mode with FS-1500 probes from Asylum Research and data was analyzed with Gwyddion software (Czech Metrology Institute).

3.5.10 Scanning Electron Microscopy

SEM images of the cast films were taken with a Carl Zeiss Merlin high-resolution Field Emission Scanning Electron Microscope (FE-SEM). The SEM was operated under the In-Lens mode with an acceleration voltage of 1.0 kV with a working distance of 2−3 mm. The samples were placed on copper tape stuck onto stubs, and sputter-coated with with a thin layer (~4 nm) of Pt/Pd alloy using a Cressington 108 Auto Sputter Coater to reduce electron beam charging and improve the image quality.

3.5.11 Dead-end Filtration Flux Tests

To prepare samples for flux measurements, 25 mm disks were punched out of each *MxG*-CNC-*g*-PEG film. These membrane samples were then placed at the base of an Amicon Stirred Cell, which was then filled with 10 mL of DI water. The stirred cell was connected to a nitrogen tank and pressurized to 2 bar. The permeate was collected in a beaker on a mass balance that was connected to computer so that the mass flowrate through each membrane could be measured over time.

3.5.12 Molecular Weight Cut-Off Measurements

To determine the rejection performance of each membrane, the same experimental set up from the flux tests was used except the DI water was replaced with polymer solutions. These polymer solutions were prepared by dissolving PEG with molecular weights of 10 kDa, 35 kDa, and 100 kDa into DI water at a concentration of 5 mg mL^{-1}. These solutions were then flowed through each membrane, and the permeates were collected. In order to mitigate fouling, the solution was stirred for the duration of the test, and the membranes were washed between trials. Two mL of each permeate was then freeze dried before being resuspended in 2 mL of DMF. The

concentration of these solutions was then determined by RI detection in a DMF gel permeation chromatography instrument.

3.5.13 Helium Pycnometer Density Measurements

The volume of each *MxG*-CNC membrane was measured with an Anton-Paar Ultrapyc 5000. In order to calculate density, each sample was weighed before being placed in the sample chamber of the pycnometer. Each sample was placed into the microcell with filler metal spheres to reduce the void space of the cell and increase the accuracy of the measurements. The cell was pressurized to 18 psi with helium at 25 °C for each test. Each measurement was repeated 8 times.

3.6 Acknowledgements

This work was supported in part by National Science Foundation PIRE program under Grant No. NSF #1743475, the NSF Center for Sustainable Polymers (CSP) (CHE-1901635) at the University of Minnesota and by the Advanced Materials for Energy-Water Systems (AMEWS), an Energy Frontier Research Center funded by the U.S. Department of Energy, Office of Science, Basic Energy Sciences. It made use of the shared facilities at the University of Chicago Materials Research Science and Engineering Center (MRSEC), supported by National Science Foundation (NSF) under award number DMR-2011854. Parts of this work were carried out at the Soft Matter Characterization Facility of the University of Chicago. This research used resources of the Advanced Photon Source, a U.S. Department of Energy (DOE) Office of Science user facility operated for the DOE Office of Science by Argonne National Laboratory under Contract No. DE-AC02-06CH11357.

3.7 Supporting Information

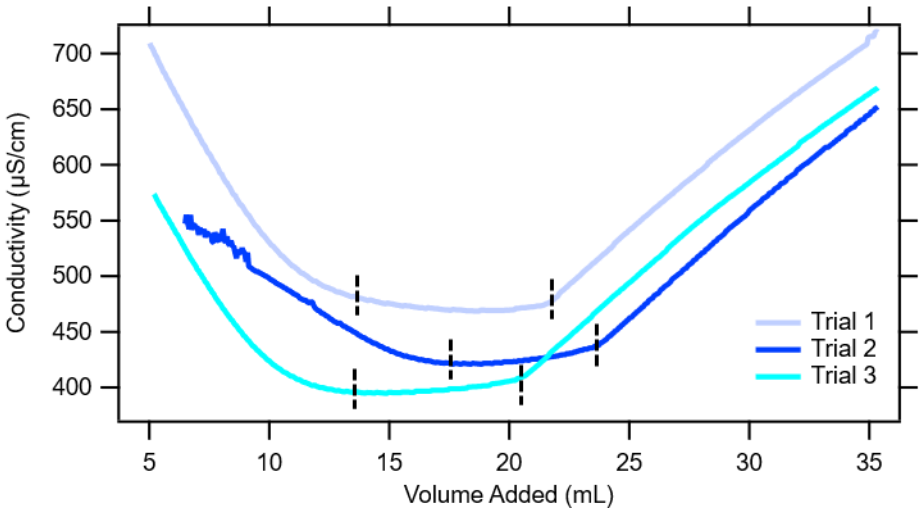

Figure S3.1. Plot of the conductivity versus the volume of 0.01 M NaOH added to determine the amount of -COOH present on the *MxG*-CNC-COOH surfaces. The amount of -COOH was determined by the length of the weak acid neutralization regime which corresponds to the plateaus in the curves as denoted by the black lines on each curve.

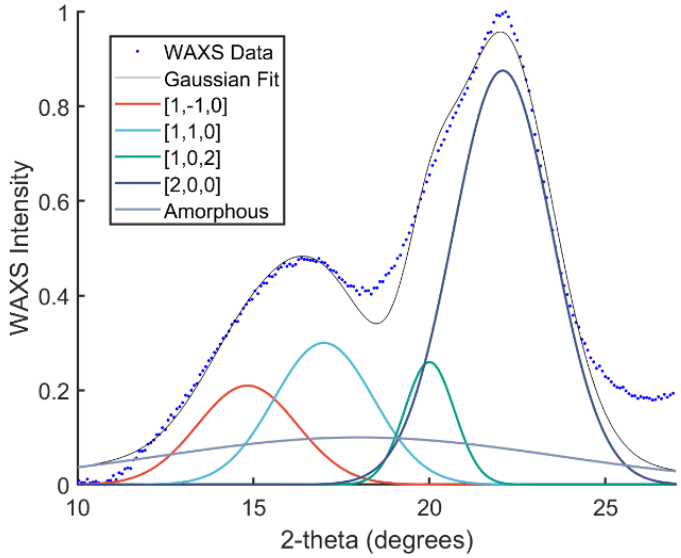

Figure S3.2. Wide angle X-ray scattering data (blue dots) plotted with Gaussian deconvolution peaks associated with each crystal plane to determine the crystallinity index of the *MxG*-CNC-COOH Samples.[79]

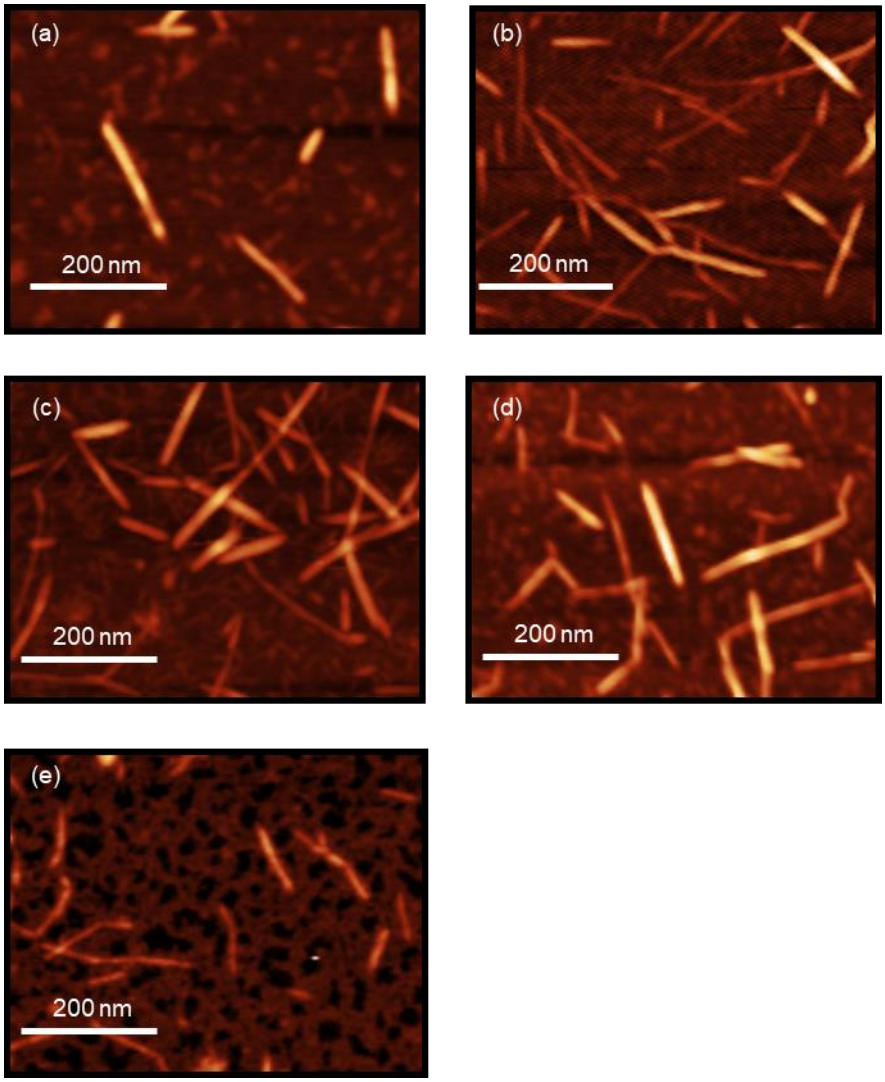

Figure S3.3. AFM height images of *MxG*-CNC-g-PEG (a) 750, (b) 5k_0.02, (c) 5k_0.05, (d) 5k_0.07, (e) 10k (750, 5k, and 10k refer to the molecular weights in g mol^{-1} of the PEG grafted using EDC/NHS and the labels xx_y refer to the molecular weight of the grafted polymer and the grafting density in chains per nm^2)

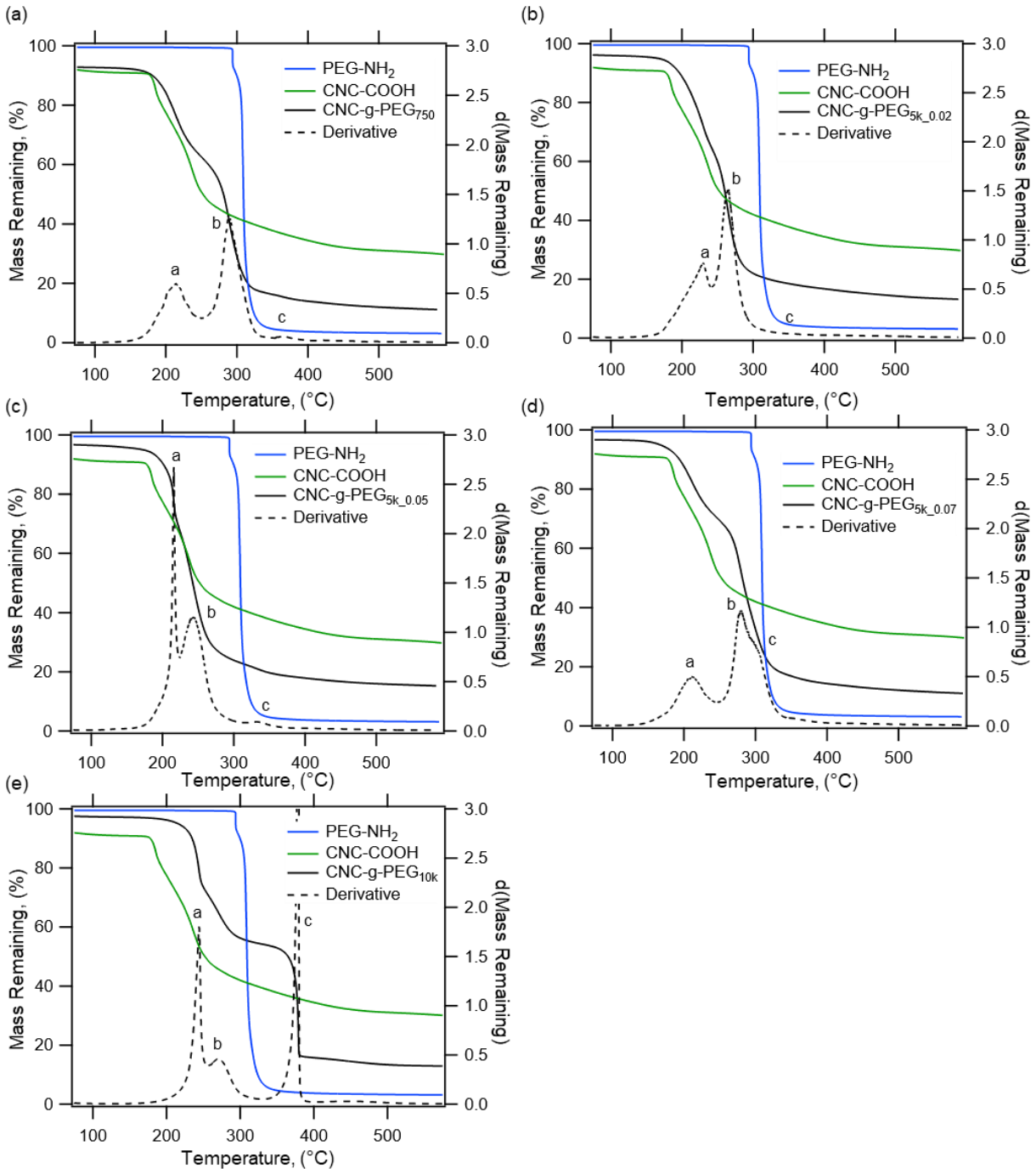

Figure S3.4. Hi-Res TGA (see the experimental section of the manuscript for details) decomposition curves of *MxG*-CNC-*g*-PEG samples (solid black line) with (a) 750, (b) 5k_0.02, (c) 5k_0.05, (d) 5k_0.07, (e) 10k g mol-1 and the associated derivatives (dashed line) with the decomposition of PEG amine (blue line) and *MxG*-CNC-COOH (green line). The peaks in the derivative have been labeled as a and b for *MxG*-CNC-COOH degradation and c for the PEG degradation event.

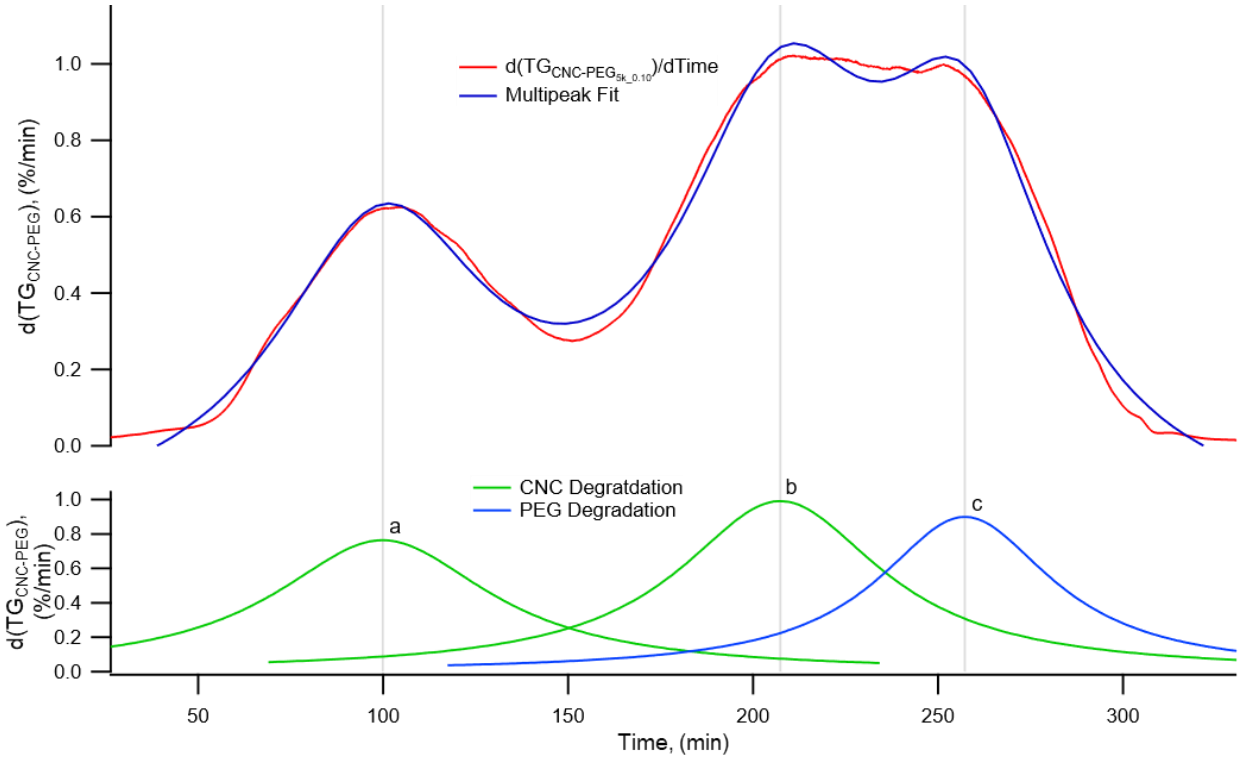

Figure S3.5. Example of multipeak fitting of the Hi-Res TGA data for *MxG*-CNC-*g*-PEG$_{5k_0.10}$. The derivative of the mass loss with respect to time is plotted over the time of the experiment. The derivative is fit with Lorenztian curves for each of the three degradation events with peaks a and b (green curves) being assigned to the degradation of the cellulose in the CNC and peak c (blue curve) being associated with PEG degradation.

In order to determine the weight fraction of PEG in the polymer grafted CNC samples, the data was fit with Lorenztian curves using the multipeak fitting software in Igor Pro 7. To fit the data using this method, the mass loss data was plotted with time instead of temperature as the temperature data is a multivalued data set with multiple mass values for some of the temperatures and the time-based data is a single valued data set, which is necessary for the multipeak fitting function. Additionally, visualizing the data with time assists with increasing the separation between the cellulose degradation and the PEG degradation. Once the data was fit, the area under the curve of each degradation event was calculated to determine the mass loss associated with cellulose and PEG degradation.

3.7.1 Supplemental Section S3.1: Volume Fraction Calculations[77,98]

To calculate the volume fraction of polymer in the *MxG*-CNC-*g*-PEG samples, the following equation is used in accordance with literature precedent:

$$VolFrac_{Polymer} = \frac{{\Phi_{polymer}}/{\rho_{polymer}}}{{\Phi_{polymer}}/{\rho_{polymer}} + {\Phi_{CNC}}/{\rho_{CNC}}}$$

where $\Phi_{polymer}$ and Φ_{CNC} are the weight fractions as determine by thermogravimetric analysis of the polymer and the CNC, respectively. are the densities of the polymer and CNC, respectively. A value of 1.125 g/cm^3 was used for $\rho_{polymer}$ based on the supplier's specifications, and a value of 1.5 g/cm^3 was used for ρ_{CNC} based on literature.[99,100]

3.7.2 Supplement Section S3.2: Grafting Density Calculations[79,101,102]

In order to simply the calculations, the CNCs are assumed to be 100% crystalline with a crystal unit cell size of 1.038 nm by 0.820 nm by 0.778 nm.[101] The CNC dimensions are 300 nm by 8.5 nm by 3.3 nm based on the AFM images of *MxG*-CNC-COOH. From these assumptions, 8304 unit cells can be tiled across the surface of the CNC assuming that the largest unit cell face is being tiled.

$$\frac{2 * (300 * 8.5 + 300 * 3.3 + 8.5 * 3.3)\frac{nm^2}{crystal}}{1.038 * 0.820\frac{nm^2}{unit\ cell}} = 8304\frac{unit\ cells}{crystal}$$

Since each unit cell has one exposed primary hydroxyl group (-OH) and the other primary -OH is buried within the crystal, it can be calculated that there are 1.16 primary -OH groups per nm^2 on the CNC surface.

$$\frac{8304\frac{unit\ cells}{crystal}}{2 * (300 * 8.5 + 300 * 3.3 + 8.5 * 3.3)\frac{nm^2}{crystal}} * 1\frac{-OH\ group}{unit\ cell} = 1.16\frac{-OH\ groups}{nm^2}$$

Based on the density of cellulose being 1.6 g cm^{-3},[102] the mass of a single crystal is 1.3 *10^{-20} kg, so there a 7.4*10^{19} crystals per kg of CNC.

$$1600\frac{kg}{m^3} * (300 * 8.5 * 3.3) * (10^{-9})^3 \frac{m^3}{crystal} = 1.3 * 10^{-20}\frac{kg}{crystal} = 7.4 * 10^{19}\frac{crystals}{kg}$$

Combining this information with the number of primary -OH groups per nm^2 calculated earlier, the number of primary -OH groups per kg of CNCs can be calculated as 6.14*10^{23} or based on Avogadro's number 1020 mmol of primary -OH groups per kg of CNC.

$$8304\frac{unit\ cells}{crystal} * 7.4 * 10^{19}\frac{crystals}{kg} = 6.14 * 10^{23}\frac{-OH\ groups}{kg} = 1020\ \frac{mmol}{kg}$$

Therefore to convert between surface density (groups per nm^2) and molar density (mmol per kg), the following conversion factor was used (note this conversion only applies to the specific CNC crystal dimensions assumed for these calculations):

$$1020\ \frac{mmol}{kg} = 1.16\frac{-OH\ groups}{nm^2}$$

These numbers represent the theoretical maximum grafting density if all accessible primary hydroxyl groups could be converted to carboxylate groups during TEMPO oxidation and that then all of those carboxylate groups react to bind PEG-NH_2 to the surface of the CNCs.

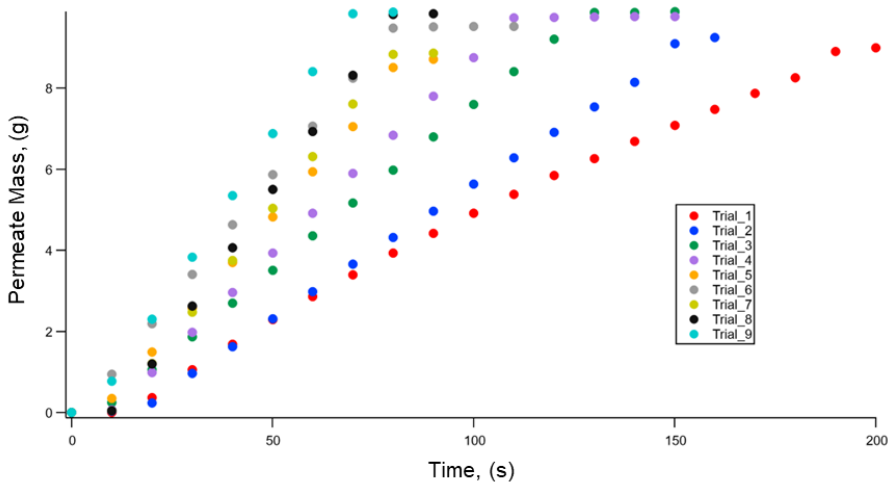

Figure S3.6. Permeate mass collected after passing through an *MxG*-CNC-COOH PEG-NH_2 blend membrane over time with nine trials illustrating an increase in mass flowrate (slope) with each subsequent trial.

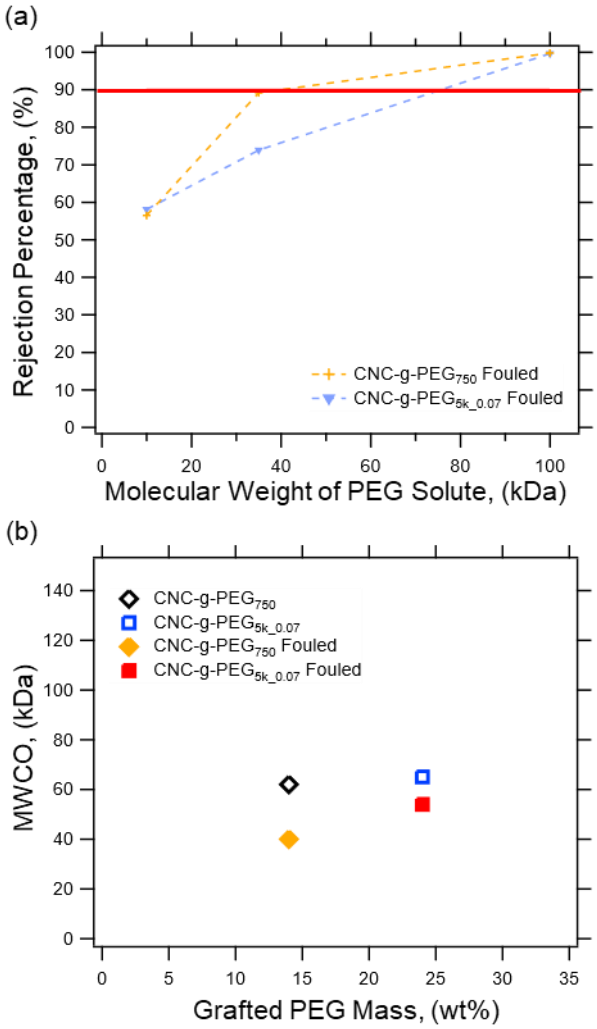

Figure S3.7. (a) The rejection of PEG is shown for *MxG*-CNC-*g*-PEG$_{750}$ (orange plus symbols) and *MxG*-CNC-*g*-PEG$_{5k_0.07}$ (periwinkle down triangles). The MWCO is the point at which 90% of the solute is rejected (red line). (b) The molecular weight cutoff with fouling mitigation (open diamonds for the mushroom regime samples and open squares for the brush regime samples) of *MxG*-CNC-*g*-PEG membranes and MWCO for *MxG*-CNC-*g*-PEG membranes without fouling mitigation precautions (orange diamond for mushroom regime sample and red square for brush regime sample) as a function of the amount of grafted polymer.

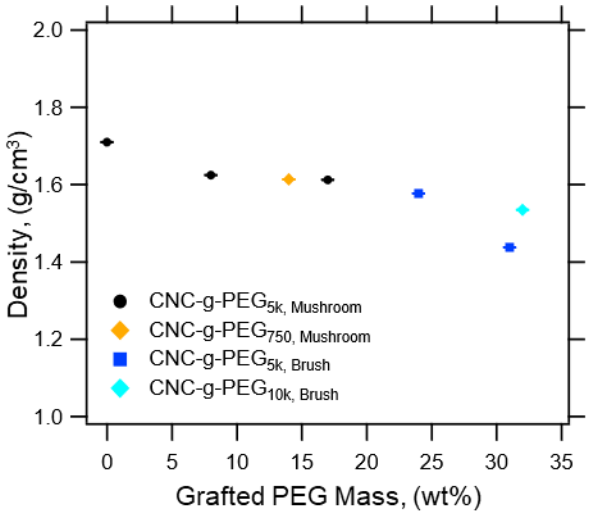

Figure S3.8. True density of *MxG*-CNC-COOH and *MxG*-CNC-*g*-PEG membranes as measured by helium pycnometry with error bars calculated as the standard error with an n of 8.

3.8 References

(1) Vörösmarty, C. J.; Green, P.; Salisbury, J.; Lammers, R. B. Global Water Resources: Vulnerability from Climate Change and Population Growth. *Science (1979)* **2000**, *289* (5477), 284–288. https://doi.org/DOI: 10.1126/science.289.5477.284.

(2) Vörösmarty, C. J.; McIntyre, P. B.; Gessner, M. O.; Dudgeon, D.; Prusevich, A.; Green, P.; Glidden, S.; Bunn, S. E.; Sullivan, C. A.; Liermann, C. R.; Davies, P. M. Global Threats to Human Water Security and River Biodiversity. *Nature 2010 467:7315* **2010**, *467* (7315), 555–561. https://doi.org/10.1038/nature09440.

(3) Epa, U.; Supply, W.; Resources Division, W.; Smith, C. 2012 Guidelines for Water Reuse. **2004**.

(4) Lee, A.; Elam, J. W.; Darling, S. B. Membrane Materials for Water Purification: Design, Development, and Application. *Environ Sci (Camb)* **2016**, *2* (1), 17–42. https://doi.org/10.1039/C5EW00159E.

(5) Hilal, N.; Al-Zoubi, H.; Darwish, N. A.; Mohamma, A. W.; Abu Arabi, M. A Comprehensive Review of Nanofiltration Membranes:Treatment, Pretreatment, Modelling, and Atomic Force Microscopy. *Desalination* **2004**, *170* (3), 281–308. https://doi.org/10.1016/j.desal.2004.01.007.

(6) Klein, E. Affinity Membranes: A 10-Year Review. *J Memb Sci* **2000**, *179* (1–2), 1–27. https://doi.org/10.1016/S0376-7388(00)00514-7.

(7) Geise, G. M.; Lee, H.-S.; Miller, D. J.; Freeman, B. D.; McGrath, J. E.; Paul, D. R. Water Purification by Membranes: The Role of Polymer Science. *J Polym Sci B Polym Phys* **2010**, *48* (15), 1685–1718. https://doi.org/10.1002/polb.22037.

(8) Goosen, M. F. A.; Sablani, S. S.; Al-Hinai, H.; Al-Obeidani, S.; Al-Belushi, R.; Jackson, D. Fouling of Reverse Osmosis and Ultrafiltration Membranes: A Critical Review. *Sep Sci Technol* **2005**, *39* (10), 2261–2297. https://doi.org/10.1081/SS-120039343.

(9) Lau, W. J.; Gray, S.; Matsuura, T.; Emadzadeh, D.; Paul Chen, J.; Ismail, A. F. A Review on Polyamide Thin Film Nanocomposite (TFN) Membranes: History, Applications, Challenges and Approaches. *Water Res* **2015**, *80*, 306–324. https://doi.org/10.1016/J.WATRES.2015.04.037.

(10) Baker, R. W. *Membrane Technology and Applications*; John Wiley & Sons, Ltd: Chichester, UK, 2012. https://doi.org/10.1002/9781118359686.

(11) Fu, F.; Wang, Q. Removal of Heavy Metal Ions from Wastewaters: A Review. *J Environ Manage* **2011**, *92* (3), 407–418. https://doi.org/10.1016/J.JENVMAN.2010.11.011.

(12) Liu, T.; Ding, E.; Xue, F. Polyacrylamide and Poly(N,N-Dimethylacrylamide) Grafted Cellulose Nanocrystals as Efficient Flocculants for Kaolin Suspension. *Int J Biol Macromol* **2017**, *103*, 1107–1112. https://doi.org/10.1016/J.IJBIOMAC.2017.05.098.

(13) Verma, A. K.; Dash, R. R.; Bhunia, P. A Review on Chemical Coagulation/Flocculation Technologies for Removal of Colour from Textile Wastewaters. *J Environ Manage* **2012**, *93* (1), 154–168. https://doi.org/10.1016/J.JENVMAN.2011.09.012.

(14) Crini, G. Non-Conventional Low-Cost Adsorbents for Dye Removal: A Review. *Bioresour Technol* **2006**, *97* (9), 1061–1085. https://doi.org/10.1016/J.BIORTECH.2005.05.001.

(15) Crini, G.; Lichtfouse, E.; Wilson, L. D.; Morin-Crini, N. Conventional and Non-Conventional Adsorbents for Wastewater Treatment. *Environ Chem Lett* **2019**, *17* (1), 195–213. https://doi.org/10.1007/S10311-018-0786-8/.

(16) Nasrollahzadeh, M.; Sajjadi, M.; Iravani, S.; Varma, R. S. Starch, Cellulose, Pectin, Gum, Alginate, Chitin and Chitosan Derived (Nano)Materials for Sustainable Water Treatment: A Review. *Carbohydr Polym* **2021**, *251*, 116986. https://doi.org/10.1016/J.CARBPOL.2020.116986.

(17) Ulbricht, M. Advanced Functional Polymer Membranes. *Polymer (Guildf)* **2006**, *47* (7), 2217–2262. https://doi.org/10.1016/J.POLYMER.2006.01.084.

(18) Carpenter, A. W.; de Lannoy, C.-F.; Wiesner, M. R. Cellulose Nanomaterials in Water Treatment Technologies. *Environ Sci Technol* **2015**, *49* (9), 5277–5287. https://doi.org/10.1021/es506351r.

(19) Van der Bruggen, B. Microfiltration, Ultrafiltration, Nanofiltration, Reverse Osmosis, and Forward Osmosis. *Fundamental Modelling of Membrane Systems* **2018**, 25–70. https://doi.org/10.1016/B978-0-12-813483-2.00002-2.

(20) Wang, J.; Zhu, J.; Zhang, Y.; Liu, J.; Van der Bruggen, B. Nanoscale Tailor-Made Membranes for Precise and Rapid Molecular Sieve Separation. *Nanoscale* **2017**, *9* (9), 2942–2957. https://doi.org/10.1039/C6NR08417F.

(21) Jonsson, G. Molecular Weight Cut-off Curves for Ultrafiltration Membranes of Varying Pore Sizes. *Desalination* **1985**, *53* (1–3), 3–10. https://doi.org/10.1016/0011-9164(85)85048-7.

(22) Pellegrin, M.-L.; Aguinaldo, J.; Arabi, S.; Sadler, M. E.; Min, K.; Liu, M.; Salamon, C.; Greiner, A. D.; Diamond, J.; McCandless, R.; Owerdieck, C.; Wert, J.; Padhye, L. P. Membrane Processes. *Water Environment Research* **2013**, *85* (10), 1092–1175. https://doi.org/10.2175/106143013X13698672321940.

(23) Ma, H.; Burger, C.; Hsiao, B. S.; Chu, B. Highly Permeable Polymer Membranes Containing Directed Channels for Water Purification. *ACS Macro Lett* **2012**, *1* (6), 723–726. https://doi.org/10.1021/mz300163h.

(24) Werber, J. R.; Deshmukh, A.; Elimelech, M. The Critical Need for Increased Selectivity, Not Increased Water Permeability, for Desalination Membranes. *Environ Sci Technol Lett* **2016**, *3* (4), 112–120. https://doi.org/10.1021/acs.estlett.6b00050.

(25) DeFriend, K. A.; Wiesner, M. R.; Barron, A. R. Alumina and Aluminate Ultrafiltration Membranes Derived from Alumina Nanoparticles. *J Memb Sci* **2003**, *224* (1–2), 11–28. https://doi.org/10.1016/S0376-7388(03)00344-2.

(26) Mohmood, I.; Lopes, C. B.; Lopes, I.; Ahmad, I.; Duarte, A. C.; Pereira, E. Nanoscale Materials and Their Use in Water Contaminants Removal—a Review. *Environmental Science and Pollution Research 2013 20:3* **2013**, *20* (3), 1239–1260. https://doi.org/10.1007/S11356-012-1415-X.

(27) Kumar, S.; Ahlawat, W.; Bhanjana, G.; Heydarifard, S.; Nazhad, M. M.; Dilbaghi, N. Nanotechnology-Based Water Treatment Strategies. *J Nanosci Nanotechnol* **2014**, *14* (2), 1838–1858. https://doi.org/10.1166/JNN.2014.9050.

(28) Lohokare, H. R.; Muthu, M. R.; Agarwal, G. P.; Kharul, U. K. Effective Arsenic Removal Using Polyacrylonitrile-Based Ultrafiltration (UF) Membrane. *J Memb Sci* **2008**, *320* (1–2), 159–166. https://doi.org/10.1016/J.MEMSCI.2008.03.068.

(29) Kim, I. C.; Yun, H. G.; Lee, K. H. Preparation of Asymmetric Polyacrylonitrile Membrane with Small Pore Size by Phase Inversion and Post-Treatment Process. *J Memb Sci* **2002**, *199* (1), 75–84. https://doi.org/10.1016/S0376-7388(01)00680-9.

(30) Saljoughi, E.; Mousavi, S. M. Preparation and Characterization of Novel Polysulfone Nanofiltration Membranes for Removal of Cadmium from Contaminated Water. *Sep Purif Technol* **2012**, *90*, 22–30. https://doi.org/10.1016/J.SEPPUR.2012.02.008.

(31) Ahmad, A. L.; Abdulkarim, A. A.; Ooi, B. S.; Ismail, S. Recent Development in Additives Modifications of Polyethersulfone Membrane for Flux Enhancement. *Chemical Engineering Journal* **2013**, *223*, 246–267. https://doi.org/10.1016/J.CEJ.2013.02.130.

(32) Yuliwati, E.; Ismail, A. F. Effect of Additives Concentration on the Surface Properties and Performance of PVDF Ultrafiltration Membranes for Refinery Produced Wastewater Treatment. *Desalination* **2011**, *273* (1), 226–234. https://doi.org/10.1016/J.DESAL.2010.11.023.

(33) Liu, F.; Hashim, N. A.; Liu, Y.; Abed, M. R. M.; Li, K. Progress in the Production and Modification of PVDF Membranes. *J Memb Sci* **2011**, *375* (1–2), 1–27. https://doi.org/10.1016/J.MEMSCI.2011.03.014.

(34) Lee, K. P.; Arnot, T. C.; Mattia, D. A Review of Reverse Osmosis Membrane Materials for Desalination—Development to Date and Future Potential. *J Memb Sci* **2011**, *370* (1–2), 1–22. https://doi.org/10.1016/J.MEMSCI.2010.12.036.

(35) Soroko, I.; Bhole, Y.; Livingston, A. G. Green Chemistry Environmentally Friendly Route for the Preparation of Solvent Resistant Polyimide Nanofiltration Membranes. **2011**. https://doi.org/10.1039/c0gc00155d.

(36) Cudjoe, E.; Hunsen, M.; Xue, Z.; Way, A. E.; Barrios, E.; Olson, R. A.; Hore, M. J. A.; Rowan, S. J. Miscanthus Giganteus: A Commercially Viable Sustainable Source of Cellulose Nanocrystals. *Carbohydr Polym* **2017**, *155*, 230–241. https://doi.org/10.1016/J.CARBPOL.2016.08.049.

(37) Mende, M.; Schwarz, D.; Steinbach, C.; Boldt, R.; Schwarz, S. The Influence of Salt Anions on Heavy Metal Ion Adsorption on the Example of Nickel. *Materials* **2018**, *11* (3). https://doi.org/10.3390/MA11030373.

(38) Elwakeel, K. Z.; Guibal, E. Arsenic(V) Sorption Using Chitosan/Cu(OH)2 and Chitosan/CuO Composite Sorbents. *Carbohydr Polym* **2015**, *134*, 190–204. https://doi.org/10.1016/J.CARBPOL.2015.07.012.

(39) Khan, S. B.; Ali, F.; Kamal, T.; Anwar, Y.; Asiri, A. M.; Seo, J. CuO Embedded Chitosan Spheres as Antibacterial Adsorbent for Dyes. *Int J Biol Macromol* **2016**, *88*, 113–119. https://doi.org/10.1016/J.IJBIOMAC.2016.03.026.

(40) Liu, J.; Chen, X.; Shao, Z.; Zhou, P. Preparation and Characterization of Chitosan/Cu(II) Affinity Membrane for Urea Adsorption. *J Appl Polym Sci* **2003**, *90*, 1108–1112.

(41) Karim, Z.; Mathew, A. P.; Grahn, M.; Mouzon, J.; Oksman, K. Nanoporous Membranes with Cellulose Nanocrystals as Functional Entity in Chitosan: Removal of Dyes from Water. *Carbohydr Polym* **2014**, *112*, 668–676. https://doi.org/10.1016/J.CARBPOL.2014.06.048.

(42) Thakur, V. K.; Voicu, S. I. Recent Advances in Cellulose and Chitosan Based Membranes for Water Purification: A Concise Review. *Carbohydr Polym* **2016**, *146*, 148–165. https://doi.org/10.1016/J.CARBPOL.2016.03.030.

(43) Mautner, A.; Lee, K. Y.; Tammelin, T.; Mathew, A. P.; Nedoma, A. J.; Li, K.; Bismarck, A. Cellulose Nanopapers as Tight Aqueous Ultra-Filtration Membranes. *React Funct Polym* **2015**, *86*, 209–214. https://doi.org/10.1016/j.reactfunctpolym.2014.09.014.

(44) Mautner, A.; Maples, H. A.; Sehaqui, H.; Zimmermann, T.; Perez de Larraya, U.; Mathew, A. P.; Lai, C. Y.; Li, K.; Bismarck, A. Nitrate Removal from Water Using a Nanopaper Ion-Exchanger. *Environ Sci (Camb)* **2016**, *2* (1), 117–124. https://doi.org/10.1039/C5EW00139K.

(45) Hokkanen, S.; Bhatnagar, A.; Sillanpää, M. A Review on Modification Methods to Cellulose-Based Adsorbents to Improve Adsorption Capacity. *Water Research*. 2016. https://doi.org/10.1016/j.watres.2016.01.008.

(46) Liu, L.; Gao, Z. Y.; Su, X. P.; Chen, X.; Jiang, L.; Yao, J. M. Adsorption Removal of Dyes from Single and Binary Solutions Using a Cellulose-Based Bioadsorbent. *ACS Sustain Chem Eng* **2015**, *3* (3), 432–442. https://doi.org/10.1021/sc500848m.

(47) O'Connell, D. W.; Birkinshaw, C.; O'Dwyer, T. F. Heavy Metal Adsorbents Prepared from the Modification of Cellulose: A Review. *Bioresour Technol* **2008**, *99* (15), 6709–6724. https://doi.org/10.1016/J.BIORTECH.2008.01.036.

(48) Pillai, S. S.; Deepa, B.; Abraham, E.; Girija, N.; Geetha, P.; Jacob, L.; Koshy, M. Biosorption of Cd(II) from Aqueous Solution Using Xanthated Nano Banana Cellulose: Equilibrium and Kinetic Studies. *Ecotoxicol Environ Saf* **2013**, *98*, 352–360. https://doi.org/10.1016/J.ECOENV.2013.09.003.

(49) Liu, Y.; Li, L.; Pan, N.; Wang, Y.; Ren, X.; Xie, Z.; Buschle-Diller, G.; Huang, T.-S. Antibacterial Cellulose Acetate Films Incorporated with *N* -Halamine-Modified Nano-Crystalline Cellulose Particles. *Polym Adv Technol* **2017**, *28* (4), 463–469. https://doi.org/10.1002/pat.3906.

(50) Lv, J.; Zhang, G.; Zhang, H.; Yang, F. Exploration of Permeability and Antifouling Performance on Modified Cellulose Acetate Ultrafiltration Membrane with Cellulose Nanocrystals. *Carbohydr Polym* **2017**, *174*, 190–199. https://doi.org/10.1016/J.CARBPOL.2017.06.064.

(51) Jin, L.; Li, W.; Xu, Q.; Sun, Q. Amino-Functionalized Nanocrystalline Cellulose as an Adsorbent for Anionic Dyes. *Cellulose* **2015**, *22* (4). https://doi.org/10.1007/s10570-015-0649-4.

(52) Kamtsikakis, A.; McBride, S.; Zoppe, J. O.; Weder, C. Cellulose Nanofiber Nanocomposite Pervaporation Membranes for Ethanol Recovery. *ACS Appl Nano Mater* **2021**, *4* (1), 568–579. https://doi.org/10.1021/ACSANM.0C02881.

(53) Mautner, A.; Lee, K.-Y.; Tammelin, T.; Mathew, A. P.; Nedoma, A. J.; Li, K.; Bismarck, A. Cellulose Nanopapers as Tight Aqueous Ultra-Filtration Membranes. *React Funct Polym* **2015**, *86*, 209–214. https://doi.org/10.1016/j.reactfunctpolym.2014.09.014.

(54) Voisin, H.; Bergström, L.; Liu, P.; Mathew, A. P. Nanocellulose-Based Materials for Water Purification. *Nanomaterials (Basel)* **2017**, *7* (3). https://doi.org/10.3390/nano7030057.

(55) Yu, X.; Tong, S.; Ge, M.; Wu, L.; Zuo, J.; Cao, C.; Song, W. Adsorption of Heavy Metal Ions from Aqueous Solution by Carboxylated Cellulose Nanocrystals. *Journal of*

Environmental Sciences **2013**, *25* (5), 933–943. https://doi.org/10.1016/S1001-0742(12)60145-4.

(56) Habibi, Y.; Lucia, L. A.; Rojas, O. J. Cellulose Nanocrystals: Chemistry, Self-Assembly, and Applications. *Chem Rev* **2010**, *110* (6), 3479–3500. https://doi.org/https://doi.org/10.1021/cr900339w.

(57) Qin, J. J.; Li, Y.; Lee, L. S.; Lee, H. Cellulose Acetate Hollow Fiber Ultrafiltration Membranes Made from CA/PVP 360 K/NMP/Water. *J Memb Sci* **2003**, *218* (1–2), 173–183. https://doi.org/10.1016/S0376-7388(03)00170-4.

(58) Shibutani, T.; Kitaura, T.; Ohmukai, Y.; Maruyama, T.; Nakatsuka, S.; Watabe, T.; Matsuyama, H. Membrane Fouling Properties of Hollow Fiber Membranes Prepared from Cellulose Acetate Derivatives. *J Memb Sci* **2011**, *376* (1–2), 102–109. https://doi.org/10.1016/J.MEMSCI.2011.04.006.

(59) Soyekwo, F.; Zhang, Q. G.; Deng, C.; Gong, Y.; Zhu, A. M.; Liu, Q. L. Highly Permeable Cellulose Acetate Nanofibrous Composite Membranes by Freeze-Extraction. *J Memb Sci* **2014**, *454*, 339–345. https://doi.org/10.1016/J.MEMSCI.2013.12.014.

(60) Goetz, L. A.; Jalvo, B.; Rosal, R.; Mathew, A. P. Superhydrophilic Anti-Fouling Electrospun Cellulose Acetate Membranes Coated with Chitin Nanocrystals for Water Filtration. *J Memb Sci* **2016**, *510*, 238–248. https://doi.org/10.1016/J.MEMSCI.2016.02.069.

(61) Mungray, A. A.; Murthy, Z. V. P. Comparative Performance Study of Four Nanofiltration Membranes in the Separation of Mercury and Chromium. *Ionics (Kiel)* **2012**, *18* (8), 811–816. https://doi.org/10.1007/s11581-012-0743-7.

(62) Henmi, M.; Nakatsuji, K.; Ichikawa, T.; Tomioka, H.; Sakamoto, T.; Yoshio, M.; Kato, T. Self-Organized Liquid-Crystalline Nanostructured Membranes for Water Treatment: Selective Permeation of Ions. *Advanced Materials* **2012**, *24* (17), 2238–2241. https://doi.org/10.1002/adma.201200108.

(63) Wolfs, J.; Meier, M. A. R. A More Sustainable Synthesis Approach for Cellulose Acetate Using the DBU/CO2 Switchable Solvent System. *Green Chemistry* **2021**, *23*, 4410. https://doi.org/10.1039/d1gc01508g.

(64) Yang, H.; Zhang, Y.; Kato, R.; Rowan, S. J. Preparation of Cellulose Nanofibers from Miscanthus x. Giganteus by Ammonium Persulfate Oxidation. *Carbohydr Polym* **2019**, *212*, 30–39. https://doi.org/10.1016/j.carbpol.2019.02.008.

(65) Weiss, A. M.; Macke, N.; Zhang, Y.; Calvino, C.; Esser-Kahn, A. P.; Rowan, S. J. In Vitro and in Vivo Analyses of the Effects of Source, Length, and Charge on the Cytotoxicity and Immunocompatibility of Cellulose Nanocrystals. *ACS Biomater Sci Eng* **2021**, *7* (4), 1450–1461. https://doi.org/10.1021/acsbiomaterials.0c01618.

(66) Eichhorn, S. J.; Etale, A.; Wang, J.; Berglund, L. A.; Li, Y.; Cai, Y.; Chen, C.; Cranston, E. D.; Johns, M. A.; Fang, Z.; Li, G.; Hu, L.; Khandelwal, M.; Lee, K. Y.; Oksman, K.;

Pinitsoontorn, S.; Quero, F.; Sebastian, A.; Titirici, M. M.; Xu, Z.; Vignolini, S.; Frka-Petesic, B. Current International Research into Cellulose as a Functional Nanomaterial for Advanced Applications. *Journal of Materials Science 2022 57:10* **2022**, *57* (10), 5697–5767. https://doi.org/10.1007/S10853-022-06903-8.

(67) Mariano, M.; El Kissi, N.; Dufresne, A. Cellulose Nanocrystals and Related Nanocomposites: Review of Some Properties and Challenges. *J Polym Sci B Polym Phys* **2014**, *52* (12), 791–806. https://doi.org/10.1002/polb.23490.

(68) Tashiro, K.; Kobayashi, M. Theoretical Evaluation of Three-Dimensional Elastic Constants of Native and Regenerated Celluloses: Role of Hydrogen Bonds. *Polymer (Guildf)* **1991**, *32* (8), 1516–1526. https://doi.org/10.1016/0032-3861(91)90435-L.

(69) Adriana Šturcová, †; Geoffrey R. Davies, ‡ and; Stephen J. Eichhorn*, †. Elastic Modulus and Stress-Transfer Properties of Tunicate Cellulose Whiskers. **2005**. https://doi.org/10.1021/BM049291K.

(70) Mansouri, J.; Harrisson, S.; Chen, V. Strategies for Controlling Biofouling in Membrane Filtration Systems: Challenges and Opportunities. *J Mater Chem* **2010**, *20* (22), 4567. https://doi.org/10.1039/b926440j.

(71) Ma, H.; Yoon, K.; Rong, L.; Shokralla, M.; Kopot, A.; Wang, X.; Fang, D.; Hsiao, B. S.; Chu, B. Thin-Film Nanofibrous Composite Ultrafiltration Membranes Based on Polyvinyl Alcohol Barrier Layer Containing Directional Water Channels. *Ind Eng Chem Res* **2010**, *49* (23), 11978–11984. https://doi.org/10.1021/ie100545k.

(72) Ma, H.; Burger, C.; Hsiao, B. S.; Chu, B. Nanofibrous Microfiltration Membrane Based on Cellulose Nanowhiskers. https://doi.org/10.1021/bm201421g.

(73) Ma, H.; Burger, C.; Hsiao, B. S.; Chu, B. Ultrafine Polysaccharide Nanofibrous Membranes for Water Purification. **2011**. https://doi.org/10.1021/bm1013316.

(74) Hore, M. J. A.; Korley, L. S. T. J.; Kumar, S. K. Polymer-Grafted Nanoparticles. *J Appl Phys* **2020**, *128* (3), 30401. https://doi.org/10.1063/5.0019326/1025564.

(75) Fernandes, N. J.; Koerner, H.; Giannelis, E. P.; Vaia, R. A. Hairy Nanoparticle Assemblies as One-Component Functional Polymer Nanocomposites: Opportunities and Challenges. *MRS Commun* **2013**, *3* (1), 13–29. https://doi.org/10.1557/MRC.2013.9/METRICS.

(76) Lettow, J. H.; Yang, H.; Nealey, P. F.; Rowan, S. J. Effect of Graft Molecular Weight and Density on the Mechanical Properties of Polystyrene-Grafted Cellulose Nanocrystal Films. *Macromolecules* **2021**, *54* (22), 10594–10604. https://doi.org/10.1021/ACS.MACROMOL.1C01886.

(77) Lettow, J. H.; Kaplan, R. Y.; Nealey, P. F.; Rowan, S. J. Enhanced Ion Conductivity through Hydrated, Polyelectrolyte-Grafted Cellulose Nanocrystal Films. *Macromolecules* **2021**, *54* (14), 6925–6936. https://doi.org/10.1021/ACS.MACROMOL.1C01155.

(78) Kato, R.; Lettow, J. H.; Patel, S. N.; Rowan, S. J. Ion-Conducting Thermoresponsive Films Based on Polymer-Grafted Cellulose Nanocrystals. *ACS Appl Mater Interfaces* **2020**, *12* (48), 54083–54093. https://doi.org/10.1021/acsami.0c16059.

(79) Macke, N.; Hemmingsen, C. M.; Rowan, S. J. The Effect of Polymer Grafting on the Mechanical Properties of PEG-Grafted Cellulose Nanocrystals in Poly(Lactic Acid). *Journal of Polymer Science* **2022**, *60* (24), 3318–3330. https://doi.org/10.1002/POL.20220127.

(80) Araki, J.; Wada, M.; Kuga, S. Steric Stabilization of a Cellulose Microcrystal Suspension by Poly(Ethylene Glycol) Grafting. *Langmuir* **2001**, *17* (1), 21–27. https://doi.org/10.1021/la001070m.

(81) Kaiser, E.; Colescott, R. L.; Bossinger, C. D.; Cook, P. I. Color Test for Detection of Free Terminal Amino Groups in the Solid-Phase Synthesis of Peptides. *Anal Biochem* **1970**, *34* (2), 595–598. https://doi.org/10.1016/0003-2697(70)90146-6.

(82) Halperin, A.; Tirrell, M.; Lodge, T. P. Tethered Chains in Polymer Microstructures. *Advances in Polymer Science* **1991**, *100*, 30–71. https://doi.org/10.1007/BFB0051635/.

(83) Dan, N.; Tirrell, M. Polymers Tethered to Curved Interfaces. A Self-Consistent-Field Analysis. *Macromolecules* **1992**, *25* (11), 2890–2895. https://doi.org/10.1021/MA00037A016/.

(84) Jiao, Y.; Tibbits, A.; Gillman, A.; Hsiao, M. S.; Buskohl, P.; Drummy, L. F.; Vaia, R. A. Deformation Behavior of Polystyrene-Grafted Nanoparticle Assemblies with Low Grafting Density. *Macromolecules* **2018**, *51* (18), 7257–7265. https://doi.org/https://doi.org/10.1021/acs.macromol.8b01524.

(85) Lenart, W. R.; Hore, M. J. A. Structure–Property Relationships of Polymer-Grafted Nanospheres for Designing Advanced Nanocomposites. *Nano-Structures & Nano-Objects* **2018**, *16*, 428–440. https://doi.org/10.1016/J.NANOSO.2017.11.005.

(86) Fischer, S.; Salcher, A.; Kornowski, A.; Weller, H.; Förster, S. Completely Miscible Nanocomposites. *Angewandte Chemie International Edition* **2011**, *50* (34), 7811–7814. https://doi.org/10.1002/ANIE.201006746.

(87) Ohno, K.; Morinaga, T.; Takeno, S.; Tsujii, Y.; Fukuda, T. Suspensions of Silica Particles Grafted with Concentrated Polymer Brush: Effects of Graft Chain Length on Brush Layer Thickness and Colloidal Crystallization. *Macromolecules* **2007**, *40* (25), 9143–9150. https://doi.org/10.1021/ma071770z.

(88) Morinaga, T.; Honma, S.; Ishizuka, T.; Kamijo, T.; Sato, T.; Tsujii, Y. Synthesis of Monodisperse Silica Particles Grafted with Concentrated Ionic Liquid-Type Polymer Brushes by Surface-Initiated Atom Transfer Radical Polymerization for Use as a Solid State Polymer Electrolyte. *Polymers (Basel)* **2016**, *8* (4). https://doi.org/10.3390/POLYM8040146.

(89) Ohno, K.; Morinaga, T.; Koh, K.; Tsujii, Y.; Fukuda, T. Synthesis of Monodisperse Silica Particles Coated with Well-Defined, High-Density Polymer Brushes by Surface-Initiated Atom Transfer Radical Polymerization. *Macromolecules* **2005**, *38* (6), 2137–2142. https://doi.org/10.1021/MA048011Q.

(90) Hansoge, N. K.; Keten, S. Effect of Polymer Chemistry on Chain Conformations in Hairy Nanoparticle Assemblies. *ACS Macro Lett* **2019**, *8* (10), 1209–1215. https://doi.org/10.1021/acsmacrolett.9b00526.

(91) See Toh, Y. H.; Loh, X. X.; Li, K.; Bismarck, A.; Livingston, A. G. In Search of a Standard Method for the Characterisation of Organic Solvent Nanofiltration Membranes. *J Memb Sci* **2007**, *291* (1–2), 120–125. https://doi.org/10.1016/J.MEMSCI.2006.12.053.

(92) Novellani, M.; Santini, R.; Tadrist, L. Experimental Study of the Porosity of Loose Stacks of Stiff Cylindrical Fibres: Influence of the Aspect Ratio of Fibres. *European Physical Journal B* **2000**, *13* (3), 571–578. https://doi.org/10.1007/S100510050069/.

(93) Wenli Zhang. Experimental and Computational Analysis of Random Cylinder Packings with Applications. *LSU Doctoral Dissertations* **2006**, 163.

(94) Drobek, T.; Spencer, N. D.; Heuberger, M. Compressing PEG Brushes. *Macromolecules* **2005**, *38* (12), 5254–5259. https://doi.org/10.1021/MA0504217.

(95) Shi, L.; Zhang, J.; Zhao, M.; Tang, S.; Cheng, X.; Zhang, W.; Li, W.; Liu, X.; Peng, H.; Wang, Q. Effects of Polyethylene Glycol on the Surface of Nanoparticles for Targeted Drug Delivery. *Nanoscale* **2021**, *13* (24), 10748–10764. https://doi.org/10.1039/D1NR02065J.

(96) Liu, M.; Yu, C.; Dong, Z.; Jiang, P.; Lü, Z.; Yu, S.; Gao, C. Improved Separation Performance and Durability of Polyamide Reverse Osmosis Membrane in Tertiary Treatment of Textile Effluent through Grafting Monomethoxy-Poly(Ethylene Glycol) Brushes. *Sep Purif Technol* **2019**, *209*, 443–451. https://doi.org/10.1016/J.SEPPUR.2018.07.072.

(97) Rajendran, S. R. C. K.; Mason, B.; Doucette, A. A. Review of Membrane Separation Models and Technologies: Processing Complex Food-Based Biomolecular Fractions. *Food Bioproc Tech* **2021**, *14* (3), 415–428. https://doi.org/10.1007/S11947-020-02559-X/.

(98) Sharon, D.; Bennington, P.; Dolejsi, M.; Webb, M. A.; Dong, B. X.; De Pablo, J. J.; Nealey, P. F.; Patel, S. N. Intrinsic Ion Transport Properties of Block Copolymer Electrolytes. *ACS Nano* **2020**, *14* (7), 8902–8914. https://doi.org/10.1021/ACSNANO.0C03713.

(99) Eichhorn, S. J.; Dufresne, A.; Aranguren, M.; Marcovich, N. E.; Capadona, J. R.; Rowan, S. J.; Weder, C.; Thielemans, W.; Roman, M.; Renneckar, S.; Gindl, W.; Veigel, S.; Keckes, J.; Yano, H.; Abe, K.; Nogi, M.; Nakagaito, A. N.; Mangalam, A.; Simonsen, J.; Benight, A. S.; Bismarck, A.; Berglund, L. A.; Peijs, T. Review: Current International Research into Cellulose Nanofibres and Nanocomposites. *J Mater Sci* **2010**, *45* (1), 1–33. https://doi.org/10.1007/S10853-009-3874-0.

(100) *HO-PEG-NH2 - Creative PEGWorks | PEG Products Leader*. https://creativepegworks.com/group/ho-peg-nh2 (accessed 2023-09-26).

(101) Elazzouzi-Hafraoui, S.; Nishiyama, Y.; Putaux, J. L.; Heux, L.; Dubreuil, F.; Rochas, C. The Shape and Size Distribution of Crystalline Nanoparticles Prepared by Acid Hydrolysis of Native Cellulose. *Biomacromolecules* **2008**, *9* (1), 57–65. https://doi.org/10.1021/BM700769P/SUPPL_FILE/BM700769P-FILE003.PDF.

(102) Moon, R. J.; Martini, A.; Nairn, J.; Simonsen, J.; Youngblood, J. Cellulose Nanomaterials Review: Structure, Properties and Nanocomposites. *Chem Soc Rev* **2011**, *40* (7), 3941–3994. https://doi.org/10.1039/C0CS00108B.

Chapter 4: Bioinspired Moisture Wicking Rubber Composites of Hydrophobic Polymeric Latexes and Cellulose Nanocrystals

4.1 Abstract

Wicking materials leverage capillary action to draw water into the material. They are typically composed of woven synthetic fabrics that excel at mitigating potential negative outcomes from moisture accumulation. However, these woven fabrics have a limited mechanical property range and, as such, are not suitable for applications that require substantial mechanical robustness. Reported here are studies aimed at accessing moisture wicking rubbery films by the incorporation of cellulose nanocrystals (CNCs) into a hydrophobic latex matrix. This design is inspired by treated wool fibers, which exhibit excellent wicking properties aided by a hydrophobic cuticle coated by a hydrophilic exterior layer. The hydrophobic cuticle mitigates water absorption while the hydrophilic protein sheath provides a wetting surface for the water to wick. Using a latex templating approach, CNC:polydimethylsiloxane (PDMS) composites were prepared with the ability to wick water through the composite film, in contrast to the water impermeable, hydrophobic PDMS. The data show that the rate of water transport through the film increases with CNC loadings until about 5wt% where CNC aggregation/phase separation disrupts both the mechanical strength and water transport properties of the material. The combination of a hydrophobic latex rubber with hydrophilic CNC architecture opens the door to water wicking rubbery composite materials.

4.2 Introduction

Moisture management is the ability of a garment to transport moisture away from one side of the material to the opposite surface.[1] The moisture management performance of fabrics is dictated by the mechanisms of wetting, wicking, and water vapor transmission.[2–6] Wicking is the spontaneous transfer of liquid through a material by capillary action.[4,5] These water transport

properties of the fabric are influenced by the composition of the fibers, the structure of the fibers, and the chemical treatment of the fabric.[1,4–16] For example, as reported by Das *et al.*, the hydrophilicity of the fabric has a significant impact on the water transport properties of the material.[15] They showed that by blending polyester fibers with hydrophilic viscose fibers, the hydrophilicity of the fabric could be varied and found that as the number of hydrophilic fibers in the fabric increased, the absorbency and water vapor permeability of the fabric also increased; however, at higher levels of blended hydrophilic fibers in the garment had an adverse effect of the wicking rate through the fabric material.[15] While wicking requires enough hydrophilic character for the liquid to wet the fiber surface and allow the fluid to imbibe into the material, too much hydrophilicity can reduce the rate of wicking by causing the water to adhere to the fiber surface instead of transporting through the pores.[4–6] As such, it is important to find the right hydrophobic/hydrophilic ratio to promote higher wicking rates.[15]

Certain natural fibers have been used to impact a fabric's water management capabilities. The versatility, softness, and comfort of cotton fibers have made it a main stay in garment technology and encouraged its use in a wide variety of applications.[4] However, cotton's high absorbency and tendency to retain water mean that cotton fibers exhibit poor wicking characeristics.[10] Wool is another natural fiber that is commonly used in fabrics. Natural wool exhibits excellent breathability, i.e., water vapor transport properties, and water repellant qualities. Unlike cotton fibers wool fibers are not homogenous structures. In addition to the keratin (a primary component of the core of a wool fiber) the outer layers of wool fibers are composed of a hydrophobic cuticle covered by a hydrophilic protein layer which in turn is coated by a waxy hydrophobic exterior coating, called lanolin, that makes the untreated wool fibers water repelling.[17] However, wool can be treated through scouring, chlorination, or plasma treatment to remove the waxy outer coating

around the wool fiber, which transforms the surface of the fiber from a hydrophobic layer to a hydrophilic protein sheath.[18,19] Treated wool is an ideal wicking fabric, as the hydrophobic cuticle of the fiber minimizes absorption of water, while the hydrophilic protein sheath around the fiber enables rapid water transport between fibers as a result of capillary action.[18–23]

In addition to natural fibers, several synthetic polymers have been used to create fibers for fabric manufacturing. While many trademarked formulations and specifically structured fibers are employed in textile manufacturing, the most common synthetic polymers tend to be polyester, polypropylene, and nylon.[10] Many of these polymers are commonly used in wicking applications because of their low moisture absorption and hydrophobic nature, leading to desirable wicking properties once treated or blended with hydrophilic components.[4]

While fibrous moisture management fabrics that promote sweat wicking away from the skin are well-known and commercially available, these materials lack other properties needed in a number of applications. For example, prothesis liners commonly use materials like silicone and polyurethane elastomers that provide mechanical protection that moisture wicking fabrics lack.[24] However, these materials trap moisture in the socket as their low water permeability prevents moisture from evaporating.[25] Thus, while moisture management along the residual limb is an essential consideration for the comfort, performance, and health of prosthesis wearers, the current industry standards for prothesis liners provide no such accommodation.[24–29] The moisture build-up in the liner is not only uncomfortable for the patient, but can also lead to skin breakdown as the moisture softens the skin. In addition, moisture build up can result in a poor fit for the prosthesis, which can result in severe consequences such as slippage, skin irritation and skin lesions.[25,26,29,30] The resulting wounds can become especially problematic as the moist environment provides an ideal breeding ground for bacteria that can lead to infection of the patient.

Investigations into wicking through dense polymer films with robust mechanical properties are of interest in this field. Some groups have developed breathable polymeric materials that allow wicking and water vapor transport.[31,32] These methods for creating breathable elastomers involve introducing perforations along the material through which moisture can escape. While these breathable perforations improve moisture management, they can compromise the mechanical properties and durability of the material, which result in mechanical failure if the stresses applied to the perforated polymer film are inadequately dissipated.[30]

Inspired by the structure of wool, namely a hydrophilic surface coating a hydrophobic fiber, it was hypothesized that it might be possible to use hydrophobic latex particles that are coated with a hydrophilic nanofiller to access nonwoven, nonfibrous polymeric materials that exhibit the ability to wick water (Figure 4.1). Building on this design, it is proposed that hydrophobic silicone latex-based composites with percolating high aspect ratio hydrophilic nanofillers would result in a material with hydrophilic channels that enable water transport through the silicone-base material (Figure 4.1(b)). Latex materials are commonly used to access durable, flexible materials for applications in textile coatings, sealants, and several other applications.[33] Latexes can be obtained from emulsion polymerizations and are usually prepared using a small molecule surfactant. It has been shown that cellulose nanocrystals (CNCs) can stabilize latex particles and be incorporated into latex polymer films to reinforce their mechanical properties.[34–42] CNCs are high aspect ratio nanoparticles that can be isolated from cellulose[43–45] and in addition to providing mechanical reinforcement to polymeric materials,[46–50] studies have also shown that nanocellulose can enhance

the pressure driven water flux of polymer-based membranes.[51–54] As such, CNCs were chosen as the hydrophilic nanofiller chosen for this study.

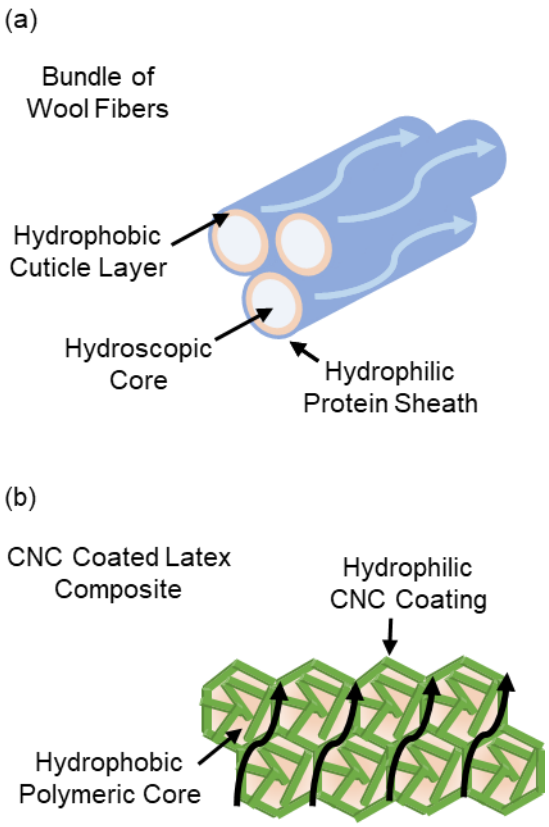

Figure 4.1. Simplified schematics of (a) a bundle of treated wool fibers and the structural components of wool that enable water wicking across the material and (b) latex particles coated in CNCs to mimic the structure of wool fibers and enable wicking across the material.

4.3 Results

4.3.1 Synthesis of Materials

To synthesize a PDMS-based latex material, silanol terminated PDMS oligomers and tetraethyl orthosilicate (TEOS) crosslinkers were dispersed into an aqueous sodium dodecyl sulfate (SDS) solution. By ultrasonicating this suspension, a surfactant-stabilized emulsion was formed between the hydrophobic oligomers and the aqueous solution. The transition from a transparent, colorless layered solution to an opaque white dispersion upon ultrasonication indicated the successful

formation of the emulsion. The oligomers and TEOS were then crosslinked by reducing the pH to 2 with 1M HCL (Figure 4.2). The resulting latex particles exhibited an average radius of 136 nm as determined by dynamic light scattering (Figure S4.1).

CNCs were isolated from *Miscanthus x. Giganteus* (*MxG*) following established literature procedures.[43,50] In short, *MxG* stalks were broken down through mechanical treatment followed by a series of base washes, bleaching, and acid treatment to isolate the hydroxyl functionalized *MxG*-derived CNCs (MxG-CNC-OH). To improve their dispersibility in water these *MxG*-CNC-OH were then modified via (2,2,6,6-tetramethylpiperidin-1-yl)oxyl (TEMPO)-mediated oxidation to introduce carboxylates moieties to the surface, yielding carboxylate functionalized *MxG*-derived CNCs (*MxG*-CNC-COOH). The surface density of carboxylate groups was determined to be 1100 mmol/kg by conductometric titrations (Figure S4.2).[50] Fourier transform infrared spectroscopy was used to confirm the presence of carboxylate groups on the surface based on the peak corresponding to the stretch of the carbonyl in the carboxylate group (Figure S4.3).[50] The crystallinity index of the samples was calculated to be 0.78 from wide angle X-ray scattering (Figure S4.4) and the dimensions of the crystals were measured as 2.4 ± 0.6 by 3.5 ± 2.0 by 250 ± 170 nm via atomic force microscopy (Figure S4.5).[50]

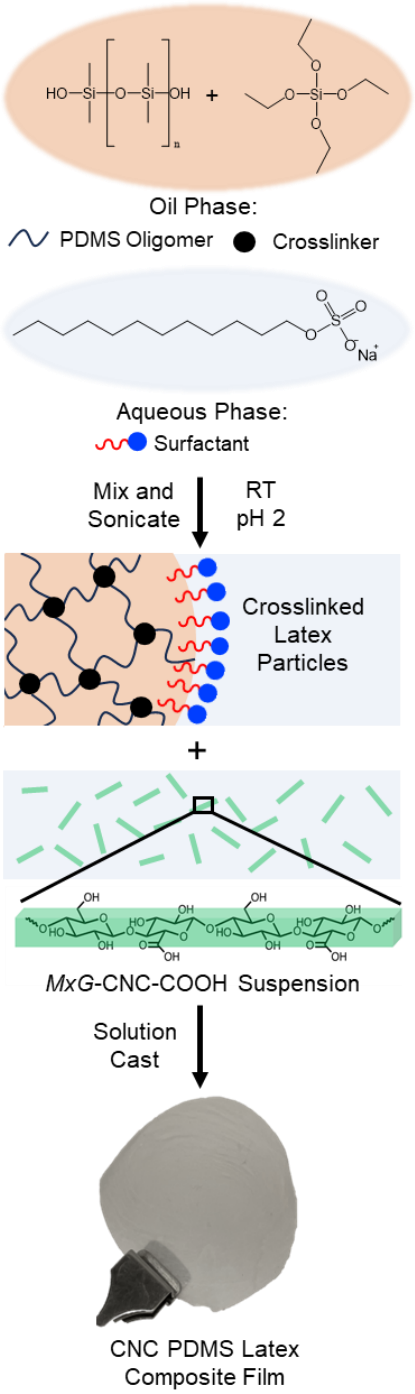

Figure 4.2. An oil phase of PDMS oligomers and TEOS crosslinker combine with an aqueous phase consisting of SDS surfactants to form an emulsion that is crosslinked into PDMS latex particles. The latex particle suspension is mixed with a suspension of MxG-CNC-COOH before the CNC latex particle mixture is solution-cast to form a solid composite film.

Aqueous dispersions with concentrations of 5 mg of *MxG*-CNC-COOH per mL of water were added to the latex emulsions (Figure 4.2). While the amount of latex emulsion remained constant for each sample, varying amounts of *MxG*-CNC-COOH were added to the emulsions. These mixtures were then solution-cast to form solid CNC:PDMS latex composite films (**CPL$_x$**; where x is the weight% CNC loading) with *MxG*-CNC-COOH loadings from 1 to 5 wt% (Figure 4.2). In addition, a film was made with no added CNCs (**CPL$_0$**) as a control. Composite films with higher CNC loadings were attempted. However, at these higher loadings, the films exhibited heterogeneity/phase separation and lacked mechanical robustness.

4.3.2 Optical microscope evidence of wicking

CPL$_{0\text{-}5}$ were then tested for their ability to transport water. Since PDMS is less dense than water, the films can float on the surface of an aqueous solution.[55] Interestingly after 20 minutes of floating on DI water, water droplets could be observed on the surface of the **CPL$_{1\text{-}5}$** films with the naked eye, consistent with the films being able to wick water, while no water droplets are observed with the film prepared with no CNCs (**CPL$_0$**). To investigate this phenomenon further, samples of the **CPL** films were floated on a small water bath in an optical microscope so that the droplet formation could be observed at higher magnifications (Figure S4.6). The films were positioned in such a way that the side of the container prevented any drifting for the duration of the observation period. Thus, videos of the droplet formation and growth could be recorded while consistently focusing in the same area of the film as shown for **CPL$_1$** in Figure 4.3 and the supplemental information videos. At t_0 the surface was relatively smooth without well-defined droplets (Figure 4.3(a)). Initially, there was no visible change on the surface of the films. However, as the films began wicking water, the distance from the objective lens to the surface of the film changed. The focus was regularly adjusted to compensate for the shifts in the position of the surface to keep the

surface within the depth of field of the objective lens. By 5 minutes, microscopic droplets could be observed forming on the surface for all films shown in Figure 4.3(b). Over time, the size of these droplets increased, (Figures 4.3(c) and 4.3(d)) eventually merging as the waterfronts of the droplets encountered neighboring droplets. In each of the videos, droplets can be observed forming on the surface and growing overtime (Videos S4.1-S4.3). Repeating the same process with the **CPL$_0$** confirms that this material exhibits no wicking behavior, illustrating the importance of the *MxG*-CNC-COOH for enabling the water transport.

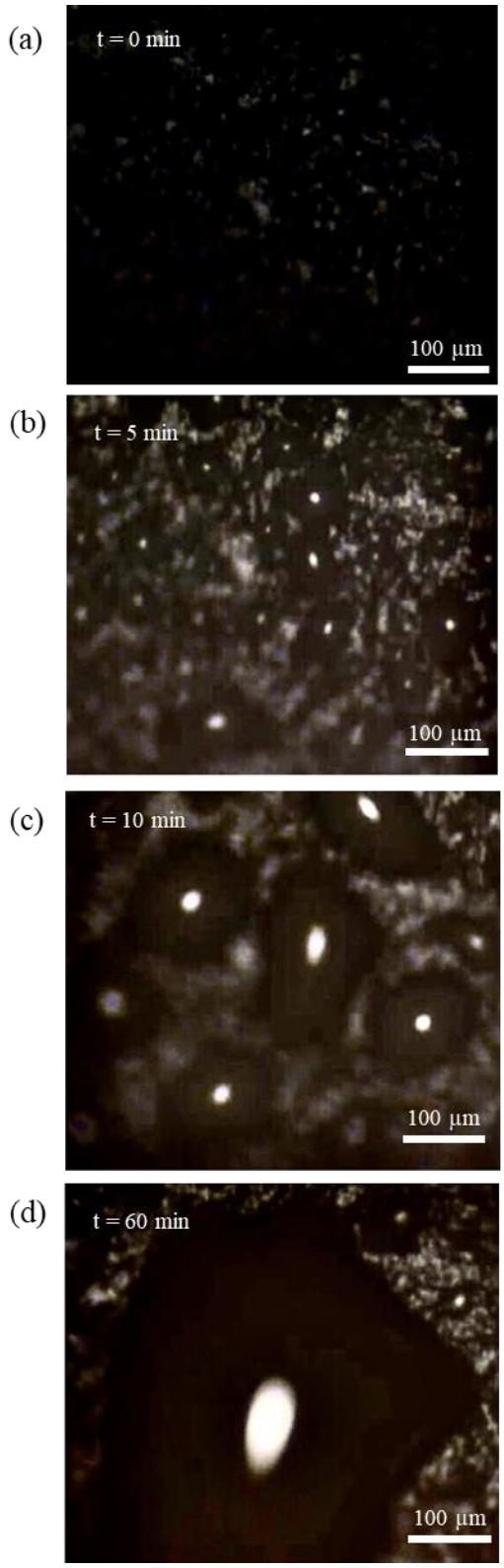

Figure 4.3. Optical microscope images illustrating water droplet formation on the 1wt% MxG-CNC-COOH PDMS latex surface at time points: (a) 0 min, (b) 5 min, (c) 10 min, and (d) 60 min.

4.3.3 Quantitative Assessment of Composite Wicking Phenomenon

The wicking behavior of the latex composite films was quantified through inverted permeation cup tests. **CPL$_{0\text{-}5}$** were used to seal DI water into permeation cups. The rate at which the mass within the cup decreased was recorded over time. Since the water can only leave the cup through the films, this rate of mass loss corresponds to the rate that water transports through the latex films. As Figure 4.4 shows, **CPL$_0$** acts as an impermeable barrier with no water loss from the cup. Per the Young-Laplace equation, the capillary pressure will be negative with a hydrophobic water contact angle, and thus, capillary pressure will not drive water transport across the hydrophobic film.[56] Incorporation of *MxG*-CNC-COOHs within the latex films (**CPL$_{1\text{-}5}$**) results in wicking being observed at all CNC loadings. The rate of wicking is dependent on the amount of CNCs in the composite. **CPL$_1$** shows a wicking rate of 1.8 ($\frac{g}{m^2 hr}$) which increases to a peak wicking rate of 39.55 ($\frac{g}{m^2 hr}$) for **CPL$_4$**. Interestingly, if the CNC loading is further increased there is a detrimental effect on the wicking rate, which decreases to 6.93 ($\frac{g}{m^2 hr}$) at **CPL$_5$**. It is proposed that once the CNCs are introduced, they can provide a hydrophilic pathway with sufficient capillary pressure to drive water transport across the **CPL** composite films. Increasing the CNC

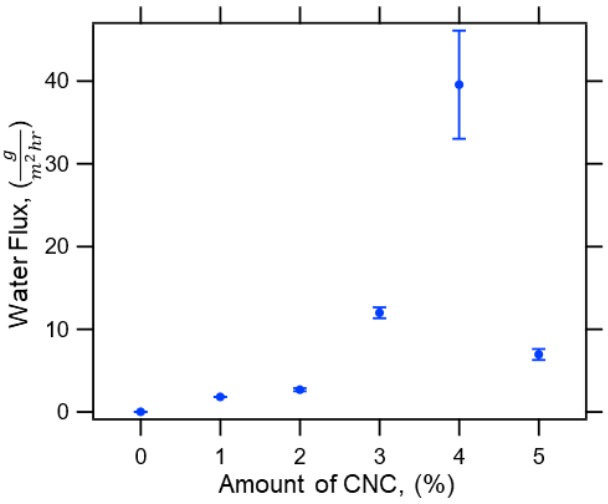

Figure 4.4. The rate of water transport through the CNC PDMS latex films (determined by inverted permeation cup tests) as a function of their CNC loadings as. The error bars on the flux values were obtained by calculating the standard error of the flux values for the replicates of the experiment as each sample was tested in triplicate.

loading in the composite materials appears to increase the capillary action across the films until a threshold is reached between 4 and 5 wt% CNC loading, where the water flux drops. Given the fact that it was hard to make mechanically robust composites with CNC content >5 wt.% it is possible that this decrease in flux at 5 wt.% may be indicative of aggregation/phase separation of the CNCs disrupting the water channels (*vide infra*).

In addition to the wicking characteristics of the **CPL** films, the absorbency of the materials was measured through water uptake experiments (Table S4.1). As expected, **CPL$_0$** does not swell in water, but after soaking in DI water for 2 hours, the CNC containing films saturate with water, exhibiting water uptakes of 11.0 ± 6.1 wt% for **CPL$_1$**, 12.6 ± 2.7 wt% for **CPL$_2$**, 10.3 ± 6.3 wt% for **CPL$_3$,** and 17.3 ± 3.2 wt% for **CPL$_4$** showing no statistical changes between the four films. However, **CPL$_5$** exhibits a significant increase in water uptake up to 70.6 ± 10.6 wt%. The increase in uptake at 5 wt% CNC loading also coincides with a significant decrease in wicking rate of the **CPL** films (Figure 4.4). This is consistent with the prior work by, for example Das et. al,[15] that

has shown that a large increase in the hydrophilic component of a wicking material can lead to both an increase in absorbency and a decrease in wicking rate.

When looking toward potential applications of such wicking films, it is important to understand their mechanical properties. Initially, tensile testing was carried out on each film to determine the impact the addition of the CNCs have on the mechanical properties of these films. Since these materials can uptake and wick water, the films were tested under both dry and wet conditions (Figure 4.5(a) and 4.5(b), respectively). As the CNCs are hydroscopic, the CNC containing **CPL** films uptake a small amount (ca. 0.5-3wt%) of water under ambient conditions (Figure S4.7 and Table S4.2). In this ambient (dry) state, all the **CPL$_{0\text{-}5}$** films are mechanically robust enough to undergo tensile testing. As might be expected, the mechanical properties of these films did significantly change with the addition of CNCs (Figure 4.5(c)).[39,48,57,58] For example, the Young's modulus of the **CPL** films increases with CNC content up to **CPL$_4$**, with Young's moduli of 0.50 ± 0.17 kPa (**CPL$_0$**), 0.64 ± 0.14 kPa (**CPL$_1$**), 1.74 ± 75 kPa (**CPL$_2$**), 7.27 ± 3.56 kPa (**CPL$_3$**), and 844 ± 156 kPa (**CPL$_4$**). Interestingly, as was the case for the water flux, the Young's

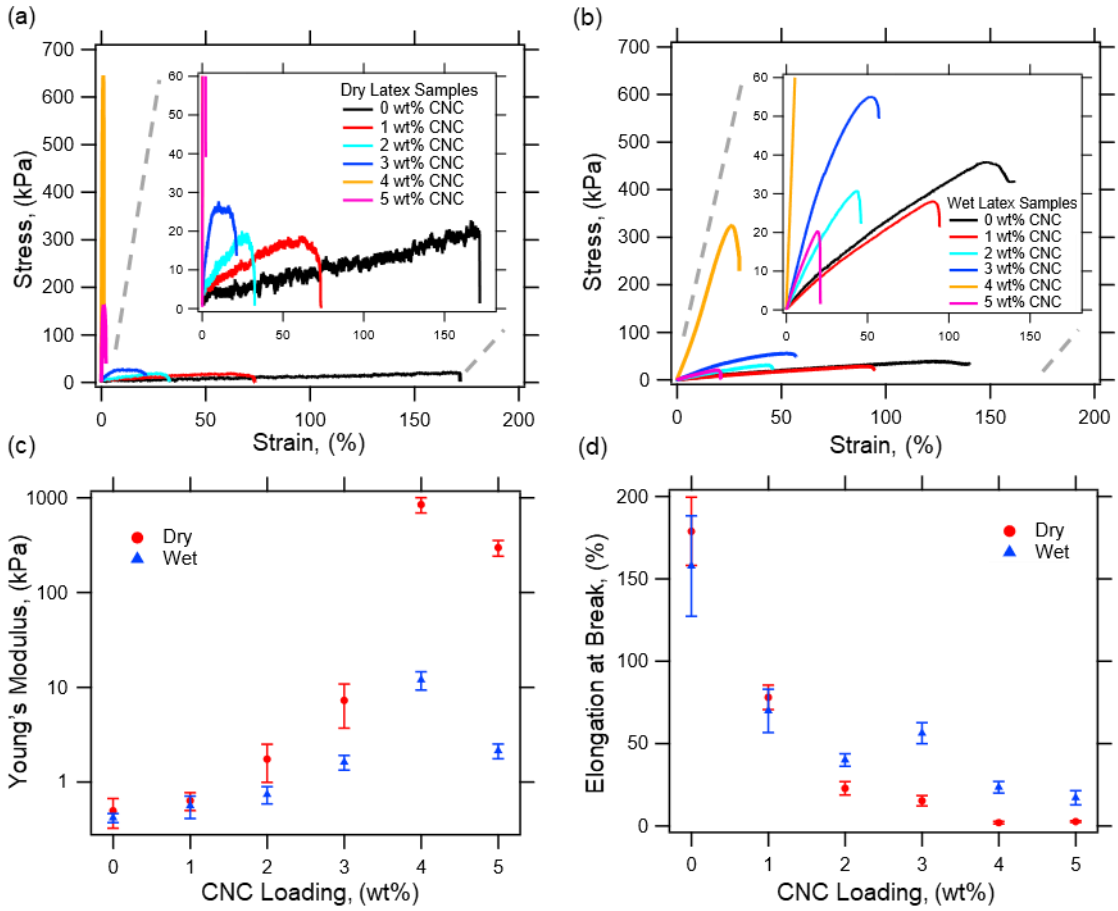

Figure 4.5. (a) Stress Strain curves for **CPL$_{0\text{-}5}$** under dry ambient conditions (b) Stress Strain curves for **CPL$_{0\text{-}5}$** under wet conditions submerged in DI water (c) Young's moduli of **CPL$_{0\text{-}5}$** for both dry (red circles) and wet (blue triangles) conditions (d) Elongation at break as CNC loading is increased from 0 wt% to 5 wt% under dry (red circles) and wet (blue triangles) conditions

modulus decreases to 298 ± 56 kPa once the CNC loading reaches 5 wt%, which again could be caused by some degree of CNC aggregation.[39]

The latex films were then allowed to uptake DI water for at least 2 hours after which no changes in the water uptake of the **CPL** films were observed (Table S4.1). These wet materials were then fully submerged in DI water and their tensile properties determined (Figure 4.5(b)). **CPL$_0$** and **CPL$_1$** exhibited wet Young's moduli of 0.418 ± 0.05 kPa and 0.56 ± 0.15 kPa, respectively, showing no significant differences between the dry and wet states (Figure 4.5(c)). However, at

higher loadings of CNCs, swelling with water did have an impact in the material properties of the **CPL** materials. For example, decreases in their Young's moduli are observed with values of 0.74 ± 0.15 kPa for **CPL$_2$**, 1.61 ± 0.28 kPa for **CPL$_3$**, 11.9 ± 2.59 kPa for **CPL$_4$**, and 2.13 ± 0.38 kPa for **CPL$_5$**. These changes in moduli are consistent with findings from prior work showing that water can act as a chemical regulator for CNC reinforced composites.[58–60]

As might be expected in addition to Young's modulus the elongation at break of these films is also significantly impacted. The **CPL$_0$** exhibits an elongation at break of 143.5 ± 17.5% in the dry state. As CNCs are added to the composite, the elongation at break in the dry state decreases, 78.0 ± 7.4% for **CPL$_1$**, 22.7 ± 4.0 % for **CPL$_2$**, 15.2 ± 3.1 % for **CPL$_3$**, 2.0 ± 0.8 % for **CPL$_4$**, and 2.6 ± 0.5 % for **CPL$_5$**. Upon the addition of water to the films, the elongation at break does not change significantly for **CPL$_0$** or **CPL$_1$** with values of 157.7 ± 30.5 % and 67.7 ± 13.1 %, respectively. However, for the materials with the higher CNC loadings the elongation at break increases (relative to the dry state) to 39.9 ± 3.8 % for **CPL$_2$**, 56.2 ± 6.4 % for **CPL$_3$**, 23.4 ± 3.6 % for **CPL$_4$**, and 17.1 ± 4.3 % for **CPL$_5$**. This data is consistent with the formation of a rigid reinforcing percolating CNC network at the higher loading that causes the films to become more brittle.[48,50,58,61] Introducing water results in the disruption of the hydrogen bonded CNC network which results in a drop in modulus and an increase in the elongation at break of the films.[58]

To further explore the mechanical properties of these composites shear rheology experiments were undertaken. **CPL$_0$** exhibits a storage modulus on the order of 10,000 Pa (Figure 4.6(a)) and a loss modulus on the order of 1000 Pa (Figure 4.6(b)). Upon the addition of CNCs to the latex structure, there does not appear to be any significant changes in the storage moduli until the CNC loading reaches 3 wt%. The increase in their storage and loss moduli with CNC content continues up to a loading of 4 wt.% CNC.[34,41,48,57,62,63] However, as before the shear rheology shows a drop

in the mechanical properties at **CPL$_5$** which would be consistent with CNC aggregation/phase separation.[39] CNCs are known to phase separate/aggregate at higher concentrations in composites, which can cause disruptions in the network of CNCs leading to a decrease in the moduli of the material.[49,64–66]

To further understand these trends, the storage and loss moduli for each sample were plotted in a frequency dependent manner using a Cole-Cole plot (Figure 4.6(c)). While Cole-Cole plots were originally developed for dielectric spectroscopy, analogous plots comparing G' and G" have been used in the literature to identify changes in the microstructure caused by the introduction of fillers to polymeric materials.[67–70] In those studies, it is proposed that shifts in the curves on the Cole-Cole plot are indicative of changes in the microstructure of the composite caused by the interactions between the filler and the polymer matrix or other components of the material. **CPL$_{0\text{-}5}$** exhibit multiple different curves in the Cole-Cole plot (Figure 4.6(c)). Each of these curves imply that **CPL$_{0\text{-}5}$** transition through different microstructures as the CNC loading is increased. Comparison of the **CPL$_0$** and **CPL$_1$** curves shows that addition of 1 wt% CNC to the material results in a noticeable lowering of the slope from 2.71 to 1.83 and the position of the G' G" curve (Figure 4.6(c)). At 1 wt% loading, the CNCs appear to cause a shift in the structure (Figure 4.6(c) and S4.8) of the composite, which is corroborated by the wicking data as **CPL$_1$** can wick water

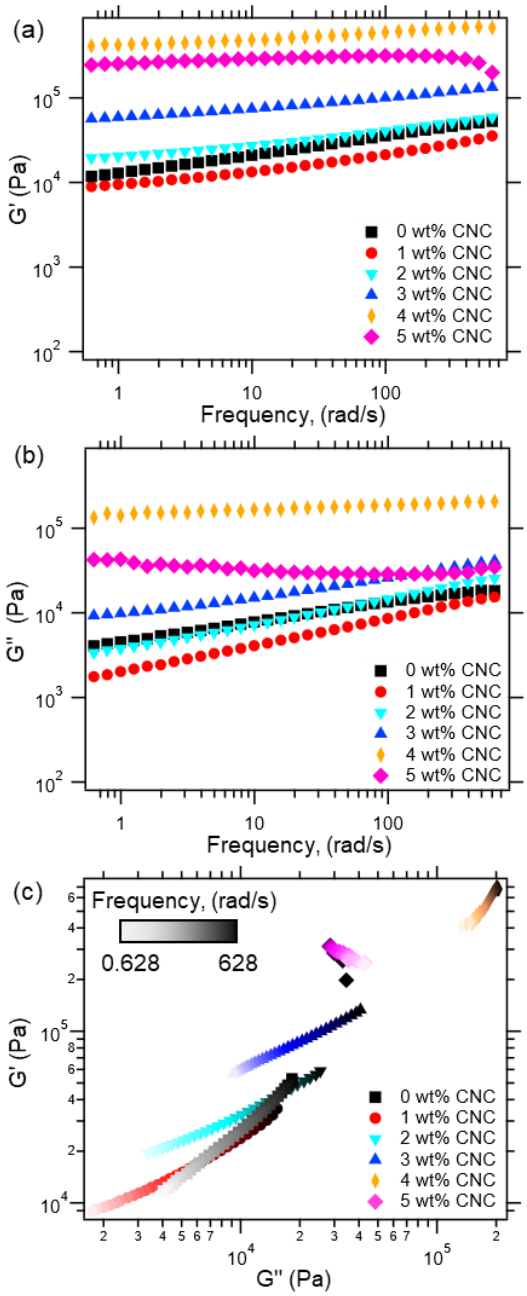

Figure 4.6. (a) Storage modulus (G') for CNC PDMS latex composites with increasing CNC loading from 0 to 5 wt% at 20°C as a function of frequency (b) Loss modulus (G") of CNC PDMS latex composites as CNC loading increases from 0 to 5 wt% at 20°C as a function of frequency (c) Determination of shifts in the storage modulus (G') versus the loss modulus (G") as CNC loadings increase in CNC PDMS latex composites. The frequency dependence of G' and G" are represented by the gradient in color for each sample.

while **CPL$_0$** cannot. With **CPL$_2$**, the G' G" curve shifts upwards while maintaining a similar slope

(1.77). This increase in storage modulus for a given loss modulus is indicative of a reinforcement effect from the filler.[67,69] As more CNCs are added to the composite in **CPL$_3$** and **CPL$_4$**, the additional filler further reinforces the composite and thus increases the storage modulus for each loss modulus. As the CNC loading is increased from 4 to 5 wt%, another significant shift in the Cole-Cole curve is observed as G' and G" decrease, and the 5 wt% curve exhibits a negative slope of -4.92. This decrease in the storage and loss moduli also coincides with the decrease in Young's modulus from the tensile testing (Figure 4.5) and is likely indicative of CNC aggregation disrupting the CNC network. The disruption of the CNC network by aggregation could lead to the decrease in water transport seen in Figure 4.4, since there would be fewer continuous channels from one surface of the film to the opposite side.

4.4 Exploration of Potential Applications

Once the wicking capabilities of these materials were established and the mechanical properties characterized, the latex composite films' viability for applications as a component in prosthesis liners was tested. The current generation of prosthesis liners commonly use materials such as silicone and polyurethane elastomers that provide mechanical protection,[24] but these materials trap moisture in the socket as their low water permeability prevents moisture from evaporating.[25] Thus while moisture management along the residual limb is an essential consideration for the comfort, performance, and health of prosthesis wearers, the current industry standards for prothesis liners provide no such accomodation.[24–29] The moisture build-up in the liner is not only uncomfortable for the patient, but can also lead to skin breakdown as the moisture softens the skin. In addition, moisture build up can result in a poor fit for the prosthesis, which can result in severe consequences such as slippage, skin irritation and skin lesions.[25,26,29,30] The

resulting wounds can become especially problematic as the moist environment provides an ideal breeding ground for bacteria that lead to infection of the patient.

In order to develop a sweat wicking prosthesis liner, a multilayer device was designed such that a sweat wicking layer would be in contact with the skin and a second absorbent layer would be on top of the sweat wicking layer to contain the sweat as it was removed from the socket of the prosthesis device. **CPL$_2$** was selected as the sweat wicking layer for these tests as its rheological properties closely align with **CPL$_0$** while still exhibiting wicking enhancement. Since **CPL$_2$** has similar mechanical properties to **CPL$_0$**, the portion of the device in contact with the patient should feel similar to a traditional silicone prosthesis liner and provide a good level of comfort for the patient. For the absorbent layer of the device, a highly porous polymer foam synthesized by polymerizing a high internal phase emulsion (poly(HIPE)) consisting of a styrene, 2-ethylhexyl acrylate (2-EHA) as monomers in the organic phase and calcium chloride in the aqueous phase was selected.[71–73] After polymerization the system is dried to create a highly porous structure. The styrene, 2-EHA copolymer exhibits soft, elastic mechanical properties, while the calcium chloride that is left in the pores after the system dries enables an osmotic gradient to drive water absorption into the pores of the poly(HIPE).[73] In order to fabricate a bilayer prototype, the absorbent poly(HIPE) layer was synthesized first. Once an emulsion was formed with the monomer containing organic phase and the salt containing aqueous phase of the HIPE, the mixture was spread into a layer at the base of a wide glass dish and sealed. The HIPE was then polymerized into a poly(HIPE) and dried. The **CPL$_2$** material was then synthesized with the same procedure as before except it was cast on top of the dry poly(HIPE) instead of being cast in a Teflon dish. Once

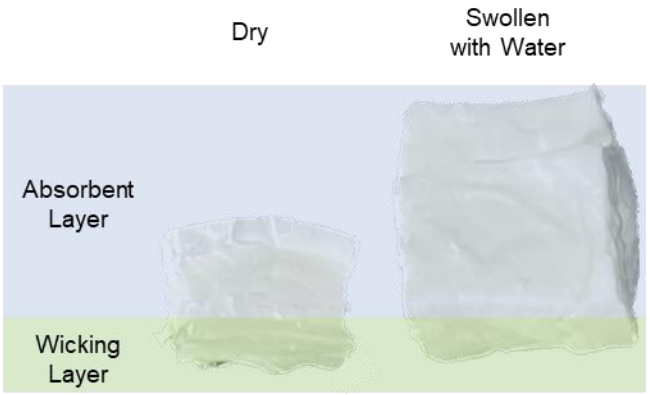

Figure 4.7. Wicking bilayer prosthesis liner prototype before and after wicking and absorbing DI water for 24 hrs. The wicking layer at the bottom of the material has been highlighted in green and the absorbent layer has been highlighted in blue.

dry, the uptake capabilities of the device were measured (Figure 4.7 and Table S3). The sample was able to wick water at a rate of 0.29 mg per min and absorbed a total of 420 mg of water over 24 hours, which is an uptake percentage of 52 wt% when compared to the initial weight of the sample. When an artificial sweat solution was used, the uptake rate increased to 0.69 mg per min, and the device was able to absorb a total of 990 mg of liquid over 24 hours corresponding to an uptake percentage of 170 wt% when compared to the initial weight of the sample. This bilayer prototype demonstrates the capability of these materials to effectively remove water or sweat from the wicking side of the device and then contain that liquid in the absorbent layer.

4.5 Conclusions

A latex templating approach was used to create CNC:PDMS latex composites with a continuous network of water channels that enable water wicking throughout an otherwise hydrophobic matrix. The rate of water transport can be increased by increasing the CNC loading until a critical threshold, where the CNCs begin to aggregate and disrupt the structure of the films, is reached. These materials also soften yet maintain mechanical integrity when exposed to water.

This technique could enable the design and fabrication of a suite of composite materials that allow water wicking in applications where robust materials are needed. As demonstrated, these composite materials can act as a base material to wick water into water absorbing foams demonstrating one potential use of these wicking rubbers in a water management system. Future studies into the range of polymers that can be used as the base of this method and the effects of different CNC functionalities that improve the transport properties could be of interest.

4.6 Materials and Methods

4.6.1 Materials

Miscanthus x. *Giganteus* (*MxG*) pulp was provided by Aloterra Energy, LLC. Sodium hydroxide (NaOH), sodium hypochlorite (NaOCl), and acetic acid (CH_3COOH) were purchased from Thermo Fisher Scientific. Sodium chlorite ($NaClO_2$), hydrochloric acid (HCl), 2,2,6,6-tetramethylpiperidine 1-oxyl (TEMPO), and sodium bromide (NaBr) were purchased from Millipore Sigma. Tetraethyl orthosilicate was purchased from Acros Organics. Sodium dodecyl sulfate and hydroxy terminated polydimethylsiloxane were purchased from Sigma-Aldrich. All water used was deionized in-house and all chemicals were used as-received without further purification.

4.6.2 Cellulose Nanocrystal Isolation from Miscanthus X. Giganteus

Cellulose nanocrystals were isolated from Miscanthus X. Giganteus following established procedures from previous studies.[43,50]

4.6.3 Synthesis of *MxG*-CNC-COOH from *MxG*-CNC-OH via TEMPO oxidation

In order to synthesize the *MxG*-CNC-COOH samples, TEMPO oxidation was conducted immediately after isolating the MxG-CNC-OH, without drying, following the previously published procedure.[43,50]

4.6.4 Latex Formation

In order to create a PDMS latex film, a process was adapted from the literature, where an oil in water emulsion was crosslinked to form a PDMS latex.[40,42,74] First, 0.03 g of SDS was dissolved in 7 g of DI water to form the aqueous phase. To this solution, 3 g of silanol terminated PDMS oligomer is added as well as 65 μL of TEOS. This biphasic mixture is then sonicated with a probe sonicator for 2 minutes at 20% amplitude to form an emulsion. Once the emulsion is formed, the pH of the mixture is lowered with 1 M HCl to a pH of 2 while stirring the solution. After 24 hours, the solution is neutralized with NaOH to quench the crosslinking reaction.

4.6.5 Film Casting

CNCs were dispersed into DI water at a concentration of 5 mg/mL in solution. This CNC dispersion was then mixed with the latex suspension such that the final concentration of CNCs in the dry films would range between 1 wt% and 5 wt% of the final CNC PDMS composite film. The mixtures of CNCs and PDMS latex were shaken for at least 10 minutes to ensure thorough mixing before being cast into poly(tetrafluoroethylene) dishes. The suspension was allowed to dry at room temperature in a fume hood for 3 days before the solid CNC PDMS latex film was removed from the dish.

4.6.6 Dynamic Light Scattering

Following literature procedures, the PDMS latex suspensions were analyzed with dynamic light scattering (DLS) to assess the size of the cross-linked PDMS particles.[40] 10 μL of the suspension was diluted into 2 mL of DI water and measured with a Wyatt Möbiuζ Dynamic and electrophoretic light scattering instrument.

4.6.7 Optical Microscopy of Wicking Phenomenon

Optical microscopy video was taken with a Leica DM2700P optical microscope using a 10x objective under reflection mode. First, a polystyrene Petri dish was filled with 5 mL deionized water. A 1 cm^2 sample of composite film was gently placed on top of the water surface, taking care to ensure only the bottom surface of the film was in contact with the water. The Petri dish cover was placed on top to prevent evaporation, and video was recorded for 60 minutes.

4.6.8 Inverted Cup Wicking Experiments

In order to perform quantitative assessments of the wicking properties of the CNC PDMS latex composite films, inverted cup wicking experiments were conducted. Permeation cups were filled with 7.5 mL of DI water. A sample of the latex films was then placed over the top of the cup and the percolation cup was sealed. The percolation cup was then inverted and placed on a mass balance connected to a computer so that the change in mass of the percolation cup could be monitored. The mass of the cups was monitored until the cup was empty or for 24 hours.

4.6.9 Thermogravimetric Analysis (TGA)

The moisture content of each sample was measured through thermogravimetric analysis. For each sample, approximately 10 mg of the composite was heated from ambient temperature to

115 °C at a rate of 20 °C/min under a nitrogen atmosphere at a flow rate of 25 mL/min. Once the temperature reached 115 °C, the temperature was maintained for 120 mins.

4.6.10 Scanning Electron Microscopy (SEM)

The films were frozen in liquid nitrogen before being fractured to expose the cross-sectional areas. SEM was conducted on the exposed cross-sectional areas with Carl Zeiss Merlin high-resolution Field Emission Scanning Electron Microscope (FE-SEM). The SEM was operated under the In-Lens mode with an accelerating voltage of 10 kV and a working distance of ~5-7 mm. The samples were placed on copper tape stuck onto stubs and sputter-coated with a thin layer (~4 nm) of Pt/Pd alloy to improve electron conductivity.

4.6.11 Tensile Testing

Tensile testing was performed on each film using a Zwick-Roell zwickiLine Z0.5 materials testing instrument with a submersion chamber. 5 mm wide strips were cut from each **CPL** film and strained at room temperature at a rate of 1 mm per min until break. For the wet tensile experiments, the submersion chamber was filled with DI water and each strip was allowed to swell until saturation before measurements began. Each film was tested in triplicate.

4.6.12 Rheology

Shear rheology was performed on each film using a TA Instruments Discovery HR-30 shear rheometer. In order to conduct these experiments, a 7/8 in. hammer punch was used to cut out circular pieces of each film. These samples were then placed on the probe with a 20 mm parallel plate geometry. An amplitude sweep was then run for each sample at room 20 °C before a frequency sweep would be run on the material as well.

4.6.13 Bilayer Prosthesis Liner Prototype Fabrication

In order to synthesize the absorbent layer, an emulsion polymerization was used to create a poly(HIPE) following established literature procedures with some slight modifications.[73] The organic phase of the emulsion consisted of 4:1 ratio of 2-EHA to styrene with 1.8:1 ratio of styrene to divinylbenzene as a crosslinker. The aqueous phase was made up of DI water, calcium chloride solution, and potassium persulfate as an initiator. The salt and initiator were dissolved to concentrations of 2.2 wt% and 0.22 wt%, respectively. The emulsion was also stabilized by 2.2 wt% of Span 80. The aqueous and organic phases were kept to a ratio of 10 to 1 by mass. The aqueous phase was then added to the organic phase in a drop-wise fashion while the mixture was stirred at a rate of 300 rpm. The emulsion was then poured into a glass dish and heated to 65 °C for 48 hours to form the poly(HIPE). The water was then removed from the poly(HIPE) by placing the material under vacuum for 48 additional hours. Once the poly(HIPE) absorbent layer was synthesized, a latex dispersion with 2 wt% CNC was cast onto the poly(HIPE) surface and allowed to dry for 3 days.

4.6.14 Uptake Measurement

To test the uptake capabilities of the bilayer device, small cubical samples were cut from the larger material. The samples were placed on a wire mesh such that the wicking layer was in contact with a large reservoir of DI water. The samples were monitored for 24 hours to ensure that contact between the wicking layer and the water was maintained and the weight of the sample was measured before and after wicking. Additionally, a synthetic sweat was made to test the uptake capacity when dissolved solid are present in the solution as well. The synthetic sweat solution was composed of 20 g of NaCl per L, 17.5 g NH_4Cl per L, 5 g acetic acid per L, and 15 g lactic acid per L. The uptake experiments were then repeated with this artificial sweat solution.

4.7 Acknowledgements

This work was supported in part by the National Institute of Health and the Department of Veterans Affairs. It made use of the shared facilities at the University of Chicago Materials Research Science and Engineering Center (MRSEC), supported by National Science Foundation (NSF) under award number DMR-2011854. Parts of this work were carried out at the Soft Matter Characterization Facility of the University of Chicago. This work was supported as part of the Advanced Materials for Energy-Water Systems (AMEWS), an Energy Frontier Research Center funded by the U.S. Department of Energy, Office of Science, Basic Energy Sciences.

4.8 Supporting Information

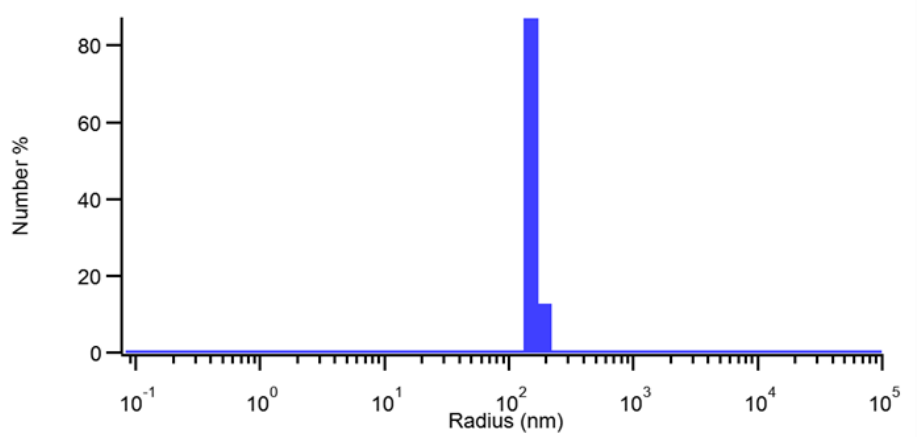

Figure S4.1. Plot of the number percentage of polydimethylsiloxane (PDMS) latex particles over their hydrodynamic radii as measured by dynamic light scattering.

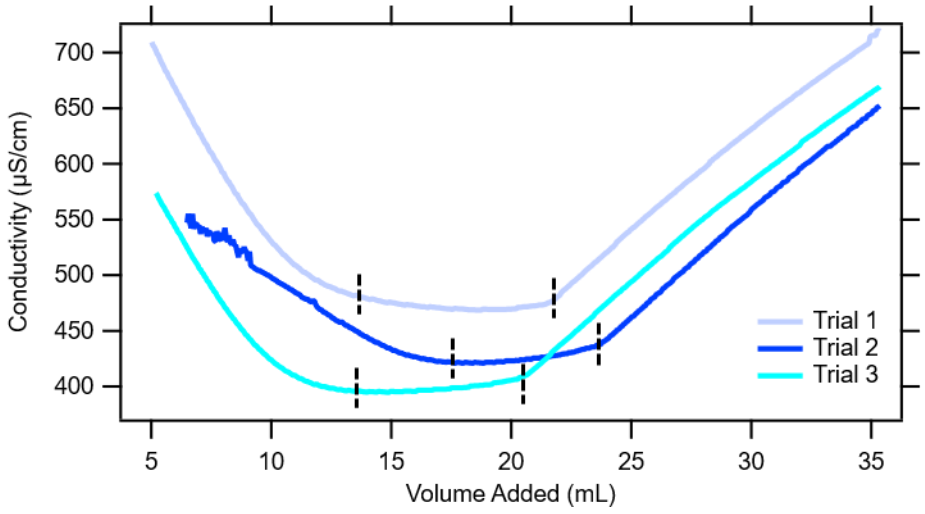

Figure S4.2. Plot of the conductivity versus the volume of 0.01 M NaOH added to determine the amount of -COOH present on the *MxG*-CNC-COOH surfaces.[50] The amount of -COOH was determined by the length of the weak acid neutralization regime which corresponds to the plateaus in the curves as denoted by the black lines on each curve. The -COOH density for each trial was calculated as 1147, 1229, and 1062 mmol/kg for trials 1, 2, and 3 respectively.

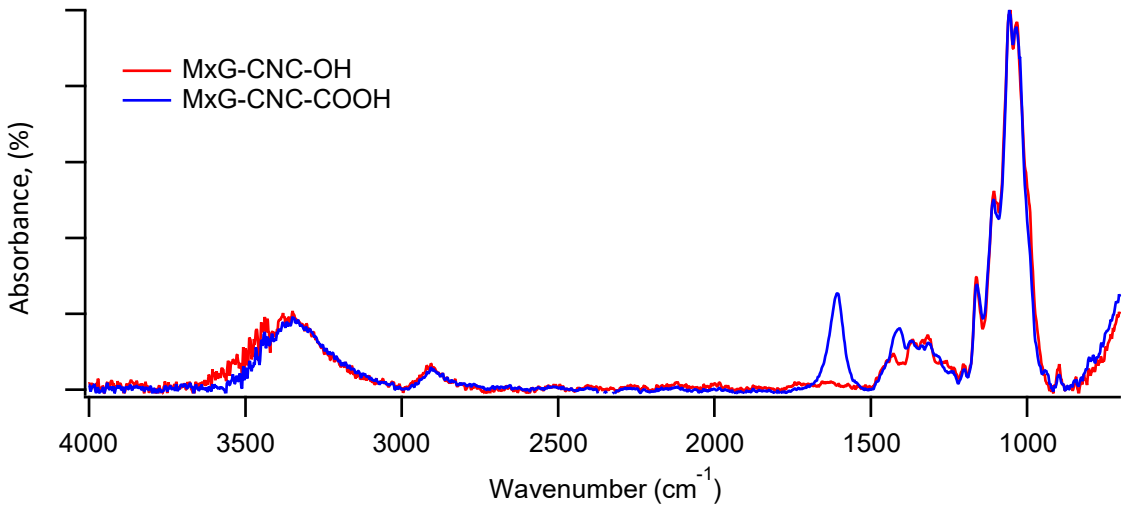

Figure S4.3. FTIR data showing the emergence of a peak that corresponds to a carbonyl stretch at 1600 cm^{-1} that confirms the functionalization of *MxG*-CNC-OH into *MxG*-CNC-COOH

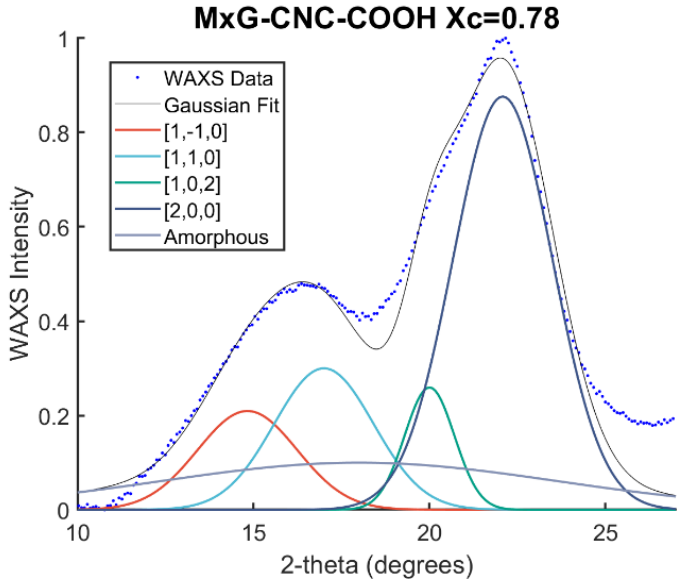

Figure S4.4. Wide angle X-ray scattering data (blue dots) plotted with Gaussian deconvolution peaks associated with each crystal plane to determine the crystallinity index of the *MxG*-CNC-COOH Samples.[50]

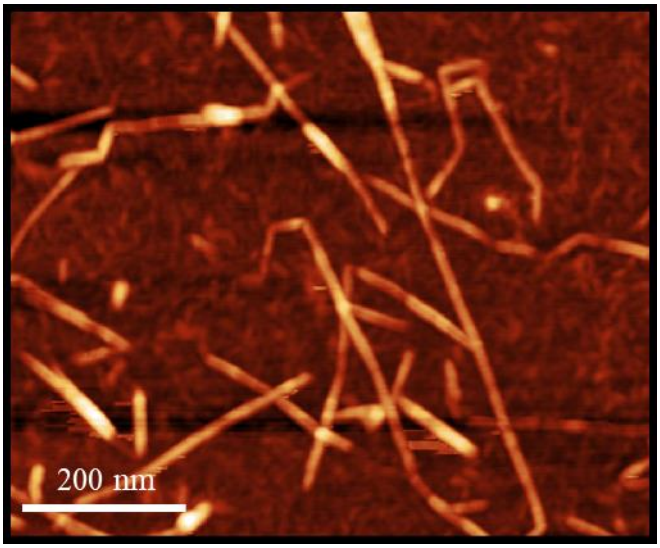

Figure S4.5. AFM image of *MxG*-CNC-COOH on a mica substrate

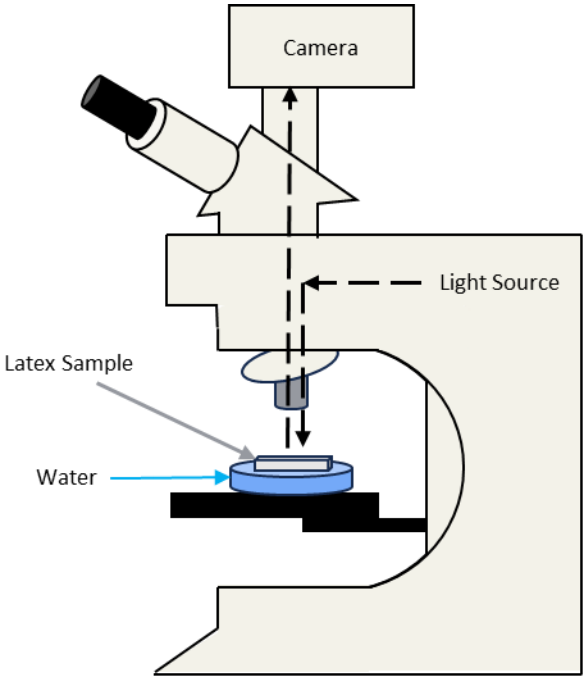

Figure S4.6. Diagram illustrates the experimental setup for recording optical microscopy videos of the latex films wicking water. The latex sample floats on top of a water solution where light from the illuminator reflects off the sample's surface before being recorded by the camera.

Table S4.1. Water uptake for CNC:PDMS latex composites (**CPL_x**) after 2 and 24 hours

Samples	Water Uptake at 2 hours (wt%)	Water Uptake at 24 hours (wt%)
CPL_0	0.0 ± 0.0	4.0 ± 4.0
CPL_1	11.0 ± 6.1	16.1 ± 4.5
CPL_2	12.6 ± 2.7	13.0 ± 3.5
CPL_3	10.3 ± 6.3	12.5 ± 2.1
CPL_4	17.3 ± 3.2	15.0 ± 2.7
CPL_5	70.6 ± 10.6	68.6 ± 6.9

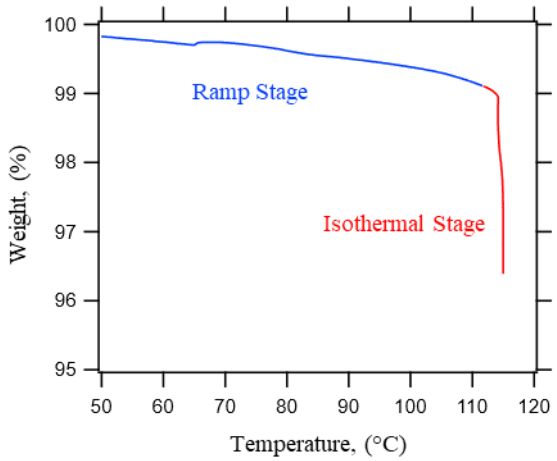

Figure S4.7. Representative TGA of **CPL_1** to show the moisture content within the film under ambient conditions equivalent to rheology tests. The temperature of the material was increased until it reached 115°C (Ramp stage in blue) and then the temperature was held at 115°C to evaporate the water in the film.

Table S4.2. Moisture content for CNC:PDMS latex composites (**CPL_x**) under ambient conditions as measured by TGA

Samples	Moisture Content (wt%)
CPL_0	0.51
CPL_1	3.62
CPL_2	0.43
CPL_3	0.66
CPL_4	0.75
CPL_5	0.89

Table S4.3. Uptake characteristics of bilayer prototype device in water and artificial sweat

Swelling Agent	Mass Uptake (%)	Mass Uptake (mg)	Rate of Mass Uptake (mg/min)
Water	52	420	0.29
Artificial Sweat	170	990	0.69

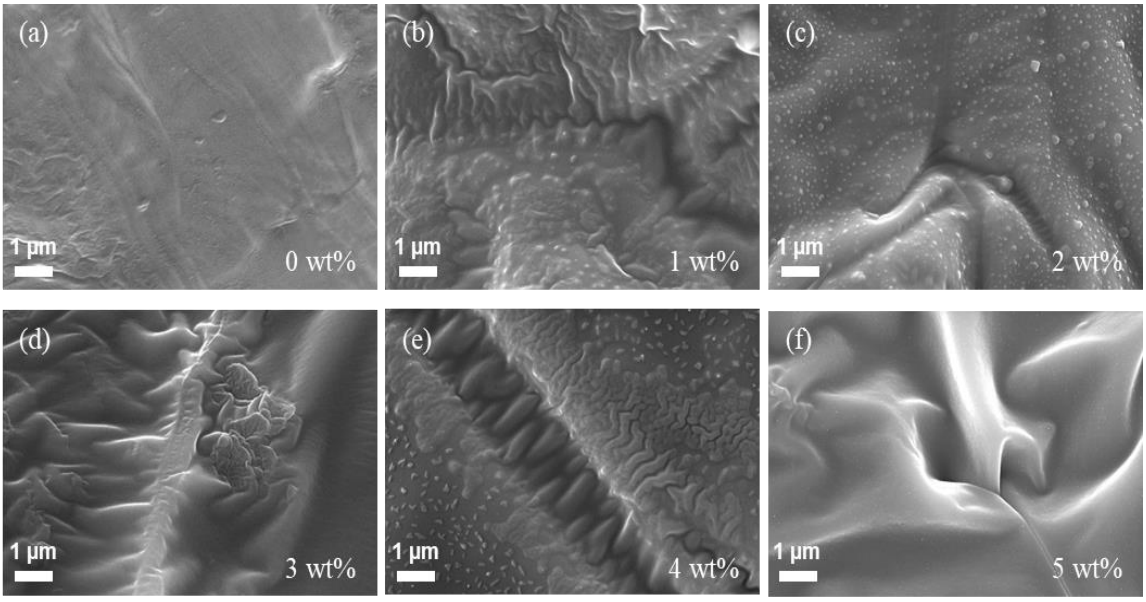

Figure S4.8. Cross-sectional SEM images of CNC PDMS latex composites with increasing CNC loadings of (a) 0 wt%, (b) 1 wt%, (c) 2 wt%, (d) 3 wt%, (e) 4 wt%, and (f) 5 wt%.

4.9 References

(1) Yilma, K. T.; Limeneh, D. Y. Review on Moisture Management Finish: Mechanism and Evaluation. *Journal of Natural Fibers* **2022**, *19* (14), 8628–8636. https://doi.org/10.1080/15440478.2021.1966566.

(2) Carroll, G. T.; Turro, N. J.; Mammana, A.; Koberstein, J. T. Photochemical Immobilization of Polymers on a Surface: Controlling Film Thickness and Wettability. *Photochem Photobiol* **2017**, *93* (5), 1165–1169. https://doi.org/10.1111/PHP.12751.

(3) El-Ghazali, S.; Khatri, M.; Kobayashi, S.; Kim, I. S. An Overview of Medical Textile Materials. *Medical Textiles from Natural Resources* **2022**, 3–42. https://doi.org/10.1016/B978-0-323-90479-7.00026-9.

(4) Mallick, P.; De, S. S.; Mallick, P.; De, S. S. Absorbency and Wicking Behaviour of Natural Fibre-Based Yarn and Fabric. *Natural Fiber* **2022**. https://doi.org/10.5772/INTECHOPEN.102584.

(5) Azeem, M.; Boughattas, A.; Wiener, J.; Havelka, A. Mechanism of Liquid Water Transport in Fabrics; A Review. *Vlakna a Textil* **2017**, *24* (4), 58–65.

(6) Adler, M. M.; Walsh, W. K. Mechanisms of Transient Moisture Transport Between Fabrics. *http://dx.doi.org/10.1177/004051758405400510* **1984**, *54* (5), 334–343. https://doi.org/10.1177/004051758405400510.

(7) Song, L. F.; Tao, Y.; Cheung, T. W.; Li, L. A Design-Driven Creation of an Innovative and Environment-Friendly Nature-Based Yarn with Moisture Wicking and Fast-Drying Effect. *https://doi.org/10.1177/00405175231163587* **2023**. https://doi.org/10.1177/00405175231163587.

(8) Bagherzadeh, R.; Gorji, M.; Latifi, M.; Payvandy, P.; Kong, L. X. Evolution of Moisture Management Behavior of High-Wicking 3D Warp Knitted Spacer Fabrics. *Fibers and Polymers* **2012**, *13* (4), 529–534. https://doi.org/10.1007/S12221-012-0529-6/METRICS.

(9) Kissa, E. Wetting and Wicking. *http://dx.doi.org/10.1177/004051759606601008* **1996**, *66* (10), 660–668. https://doi.org/10.1177/004051759606601008.

(10) Kejkar, V.; Dhore, R. Active Sportswear Fabrics. https://doi.org/10.31031/TTEFT.2019.05.000606.

(11) Sharabaty, T.; Biguenet, F.; Dupuis, D.; Viallier, P. Investigation on Moisture Transport through Polyester/Cotton Fabrics. *Indian J Fibre Text Res* **2008**.

(12) Duprat, C. Moisture in Textiles. *https://doi.org/10.1146/annurev-fluid-030121-034728* **2022**, *54*, 443–467. https://doi.org/10.1146/ANNUREV-FLUID-030121-034728.

(13) Das, B.; Das, A.; Kothari, V. K.; Fanguiero, R.; De Araújo, M. Effect of Fibre Diameter and Cross-Sectional Shape on Moisture Transmission through Fabrics. *Fibers and Polymers* **2008**, *9* (2), 225–231. https://doi.org/10.1007/S12221-008-0036-Y/METRICS.

(14) Varshney, R. K.; Kothari, V. K.; Dhamija, S. A Study on Thermophysiological Comfort Properties of Fabrics in Relation to Constituent Fibre Fineness and Cross-Sectional Shapes. *The Journal of The Textile Institute* **2010**, *101* (6), 495–505. https://doi.org/10.1080/00405000802542184.

(15) Das, B.; Das, A.; Kothari, V.; Fanguiero, R.; Araujo, M. D. Moisture Flow through Blended Fabrics – Effect of Hydrophilicity. *https://doi.org/10.1177/15589250090040405* **2009**, *4* (4), 20–28. https://doi.org/10.1177/155892500900400405.

(16) Onofrei, E.; Rocha, A. M.; Catarino, A. The Influence of Knitted Fabrics' Structure on the Thermal and Moisture Management Properties. *https://doi.org/10.1177/155892501100600403* **2011**, *6* (4), 10–22. https://doi.org/10.1177/155892501100600403.

(17) *Wool Properties*. http://sff.arts.ac.uk/Fibre%20Properties/woolproperties.html (accessed 2023-09-23).

(18) Naylor, G. The Wool Fibre and Its Applications.

(19) Rippon, J. 'Wool', in Encyclopedia of Polymer Science and Technology. **2003**.

(20) Rossi, R. M.; Stämpfli, R.; Psikuta, A.; Rechsteiner, I.; Brühwiler, P. A. Transplanar and In-Plane Wicking Effects in Sock Materials under Pressure. *http://dx.doi.org/10.1177/0040517511413317* **2011**, *81* (15), 1549–1558. https://doi.org/10.1177/0040517511413317.

(21) Wang, H.; Wang, H.; Jin, X.; Zhou, H.; Wang, H.; Wang, W.; Ruan, F.; Feng, Q.; Lin, T. Tuning In-Plane Wicking Properties of Hydrophilic Fibrous Membranes Using Hydrophobic Fibrous Cover Layers. *Adv Mater Interfaces* **2023**, *10* (1), 2200741. https://doi.org/10.1002/ADMI.202200741.

(22) Miao, M.; Xin, J. H. *Engineering of High-Performance Textiles*.

(23) Morton, W. E.; Hearle, J. W. S. Physical Properties of Textile Fibres (4th Edition).

(24) Mak, A. F. T.; Zhang, M.; Boone, D. A. State-of-the-Art Research in Lower-Limb Prosthetic Biomechanics-Socket Interface: A Review. *J Rehabil Res Dev 38* (2), 161–174.

(25) Hachisuka, K.; Matsushima, Y.; Ohmine, S.; Shitama, H.; Shinkoda, K. Moisture Permeability of the Total Surface Bearing Prosthetic Socket with a Silicone Liner: Is It Superior to the Patella-Tendon Bearing Prosthetic Socket? *J UOEH* **2001**, *23* (3), 225–232. https://doi.org/10.7888/JUOEH.23.225.

(26) Cagle, J. C.; Reinhall, P. G.; Hafner, B. J.; Sanders, J. E. Development of Standardized Material Testing Protocols for Prosthetic Liners. *J Biomech Eng* **2017**, *139* (4), 0450011. https://doi.org/10.1115/1.4035917.

(27) Lao, L.; Shou, D.; Wu, Y. S.; Fan, J. T. "Skin-like" Fabric for Personal Moisture Management. *Sci Adv* **2020**, *6* (14). https://doi.org/10.1126/SCIADV.AAZ0013/SUPPL_FILE/AAZ0013_SM.PDF.

(28) Klute, G. K.; Glaister, B. C.; Berge, J. S. Prosthetic Liners for Lower Limb Amputees: A Review of the Literature. *http://dx.doi.org/10.3109/03093641003645528* **2010**, *34* (2), 146–153. https://doi.org/10.3109/03093641003645528.

(29) Klute, G. K.; Rowe, G. I.; Mamishev, A. V.; Ledoux, W. R. The Thermal Conductivity of Prosthetic Sockets and Liners. *Prosthet Orthot Int* **2007**, *31* (3), 292–299.

(30) Seymour, R. Introduction to Prosthetics and Orthotics. *Prosthetics and Orthotics: Lower Limb and Spinal* **2002**, 3–35.

(31) Walter, D. *Perforated liner U.S. patent number 10,639,173, Aug 24, 2017*. https://uspto.report/patent/grant/10,639,173 (accessed 2023-08-02).

(32) Hansen, A.; Koehler-Mcnicholas, S.; Nickel, E.; Barrons, K.; Starker, F.; Mion, S.; Ferguson, J.; Fairhurst, S.; Ramasamy, E.; Koester, K.; Dearth, C.; Hendershot, B.; Pruziner, A.; Anderson, P.; Hassinger, L.; Laufer, D.; Schneider, U. *BREATHABLE RESIDUAL-LIMB SOCKET SYSTEM. US Patent Application Application #20210137707, May 13, 2021*. https://patents.justia.com/patent/20210137707 (accessed 2023-08-02).

(33) DeFusco, A. J.; Sehgal, K. C.; Bassett, D. R. Overview of Uses of Polymer Latexes. *Polymeric Dispersions: Principles and Applications* **1997**, 379–396. https://doi.org/10.1007/978-94-011-5512-0_25.

(34) Gabriel, V. A.; Tousignant, M. N.; Wilson, S. M. W.; Faure, M. D. M.; Cranston, E. D.; Cunningham, M. F.; Lessard, B. H.; Dubé, M. A. Improving Latex-Based Pressure-Sensitive Adhesive Properties Using Carboxylated Cellulose Nanocrystals. *Macromol React Eng* **2022**, *16* (3), 2100051. https://doi.org/10.1002/MREN.202100051.

(35) Kiriakou, M. V.; Pakdel, A. S.; Berry, R. M.; Hoare, T.; Dubé, M. A.; Cranston, E. D. Incorporation of Polymer-Grafted Cellulose Nanocrystals into Latex-Based Pressure-Sensitive Adhesives. *ACS Materials Au* **2022**, *2* (2), 176–189.

(36) Gabriel, V. A.; Cranston, E. D.; Dubé, M. A. Pushing the Limits with Cellulose Nanocrystal Loadings in Latex-Based Pressure-Sensitive Adhesive Nanocomposites. *Macromol React Eng* **2020**, *14* (6). https://doi.org/10.1002/MREN.202000027.

(37) Kedzior, S. A.; Dubé, M. A.; Cranston, E. D. Cellulose Nanocrystals and Methyl Cellulose as Costabilizers for Nanocomposite Latexes with Double Morphology. *ACS Sustain Chem Eng* **2017**, *5* (11), 10509–10517.

(38) Banjar, M. F.; Yahaya, A. N. A.; Khalil, N. A.; Al-Dulaimi, A. A.; Singh, M.; Zulkifli, M. Mechanical Properties and Conductivity of Polyaniline-Cellulose-Latex Hybrid. *Mater Today Proc* **2023**, *74*, 489–491. https://doi.org/10.1016/J.MATPR.2022.11.475.

(39) Limousin, E.; Rafaniello, I.; Schäfer, T.; Ballard, N.; Asua, J. M. Linking Film Structure and Mechanical Properties in Nanocomposite Films Formed from Dispersions of Cellulose Nanocrystals and Acrylic Latexes. *Langmuir* **2020**, *36* (8), 2052–2062. https://doi.org/10.1021/ACS.LANGMUIR.9B03861/SUPPL_FILE/LA9B03861_SI_001.PDF.

(40) Zhang, Y.; Yang, H.; Naren, N.; Rowan, S. J. Surfactant-Free Latex Nanocomposites Stabilized and Reinforced by Hydrophobically Functionalized Cellulose Nanocrystals. *ACS Appl Polym Mater* **2020**, *2* (6), 2291–2302. https://doi.org/10.1021/ACSAPM.0C00263/SUPPL_FILE/AP0C00263_SI_001.PDF.

(41) Rui, W.; Sun, Y.; Tian, Y.; Li, X.; Han, J. Poly(Dopamine)-Modified Microcrystalline Cellulose,a Green Reinforcing Filler for Natural Rubber Latex with High Performance. *https://doi.org/10.1080/09276440.2022.2116074* **2022**, *30* (4), 361–375. https://doi.org/10.1080/09276440.2022.2116074.

(42) Zhang, Y.; Karimkhani, V.; Makowski, B. T.; Samaranayake, G.; Rowan, S. J. Nanoemulsions and Nanolatexes Stabilized by Hydrophobically Functionalized Cellulose Nanocrystals. *Macromolecules* **2017**, *50* (16), 6032–6042. https://doi.org/10.1021/acs.macromol.7b00982.

(43) Cudjoe, E.; Hunsen, M.; Xue, Z.; Way, A. E.; Barrios, E.; Olson, R. A.; Hore, M. J. A.; Rowan, S. J. Miscanthus Giganteus: A Commercially Viable Sustainable Source of

Cellulose Nanocrystals. *Carbohydr Polym* **2017**, *155*, 230–241. https://doi.org/10.1016/J.CARBPOL.2016.08.049.

(44) Isogai, A.; Saito, T.; Fukuzumi, H. TEMPO-Oxidized Cellulose Nanofibers. *Nanoscale* **2011**, *3* (1), 71–85. https://doi.org/10.1039/c0nr00583e.

(45) Yang, H.; Zhang, Y.; Kato, R.; Rowan, S. J. Preparation of Cellulose Nanofibers from Miscanthus x. Giganteus by Ammonium Persulfate Oxidation. *Carbohydr Polym* **2019**, *212*. https://doi.org/10.1016/j.carbpol.2019.02.008.

(46) Favier, V.; Chanzy, H.; Cavaillé, J. Y. Polymer Nanocomposites Reinforced by Cellulose Whiskers. *Macromolecules* **1995**, *28* (18), 6365–6367. https://doi.org/10.1021/MA00122A053.

(47) Favier, V.; Cavaille, J. Y.; Canova, G. R.; Shrivastava, S. C. Mechanical Percolation in Cellulose Whisker Nanocomposites. *Polym Eng Sci* **1997**, *37* (10), 1732–1739. https://doi.org/10.1002/pen.11821.

(48) Cudjoe, E.; Advisor, D.; Rowan, S. J.; Rowan, S.; Korley, L. CELLULOSE NANOCRYSTALS AND RELATED POLYMER NANOCOMPOSITES. **2017**.

(49) Jantachum, P.; Khumpaitool, B.; Utara, S. Effect of Silane Coupling Agent and Cellulose Nanocrystals Loading on the Properties of Acrylonitrile Butadiene Rubber/Natural Rubber Nanocomposites. *Ind Crops Prod* **2023**, *195*, 116407. https://doi.org/10.1016/J.INDCROP.2023.116407.

(50) Macke, N.; Hemmingsen, C. M.; Rowan, S. J. The Effect of Polymer Grafting on the Mechanical Properties of PEG-Grafted Cellulose Nanocrystals in Poly(Lactic Acid). *Journal of Polymer Science* **2022**, *60* (24), 3318–3330. https://doi.org/10.1002/POL.20220127.

(51) Ma, H.; Burger, C.; Hsiao, B. S.; Chu, B. Ultrafine Polysaccharide Nanofibrous Membranes for Water Purification. **2011**. https://doi.org/10.1021/bm1013316.

(52) Kamtsikakis, A.; McBride, S.; Zoppe, J. O.; Weder, C. Cellulose Nanofiber Nanocomposite Pervaporation Membranes for Ethanol Recovery. *ACS Appl Nano Mater* **2021**, *4* (1), 568–579. https://doi.org/10.1021/ACSANM.0C02881.

(53) Ma, H.; Burger, C.; Hsiao, B. S.; Chu, B. Nanofibrous Microfiltration Membrane Based on Cellulose Nanowhiskers. https://doi.org/10.1021/bm201421g.

(54) Ma, H.; Burger, C.; Hsiao, B. S.; Chu, B. Highly Permeable Polymer Membranes Containing Directed Channels for Water Purification. *ACS Macro Lett* **2012**, *1* (6), 723–726. https://doi.org/10.1021/mz300163h.

(55) Cai, L. H.; Kodger, T. E.; Guerra, R. E.; Pegoraro, A. F.; Rubinstein, M.; Weitz, D. A. Soft Polydimethylsiloxane Elastomers from Architecture-Driven Entanglement Free Design. *Adv Mater* **2015**, *27* (35), 5132. https://doi.org/10.1002/ADMA.201502771.

(56) Welty, J. R. Fundamentals of Momentum, Heat and Mass Transfer. 758.

(57) Cudjoe, E.; Khani, S.; Way, A. E.; Hore, M. J. A.; Maia, J.; Rowan, S. J. Biomimetic Reversible Heat-Stiffening Polymer Nanocomposites. *ACS Cent Sci* **2017**, *3* (8), 886–894. https://doi.org/10.1021/ACSCENTSCI.7B00215.

(58) Capadona, J. R.; Shanmuganathan, K.; Tyler, D. J.; Rowan, S. J.; Weder, C. Stimuli-Responsive Polymer Nanocomposites Inspired by the Sea Cucumber Dermis. *Science (1979)* **2008**, *319* (5868), 1370–1374. https://doi.org/10.1126/science.1153307.

(59) Shanmuganathan, K.; Capadona, J. R.; Rowan, S. J.; Weder, C. Stimuli-Responsive Mechanically Adaptive Polymer Nanocomposites. *ACS Appl Mater Interfaces* **2010**, *2* (1), 165–174. https://doi.org/10.1021/am9006337.

(60) Shanmuganathan, K.; Capadona, J. R.; Rowan, S. J.; Weder, C. Bio-Inspired Mechanically-Adaptive Nanocomposites Derived from Cotton Cellulose Whiskers. **2010**, *20* (1), 180–186. https://doi.org/10.1039/b916130a.

(61) Capadona, J. R.; Shanmuganathan, K.; Trittschuh, S.; Seidel, S.; Rowan, S. J.; Weder, C. Polymer Nanocomposites with Nanowhiskers Isolated from Microcrystalline Cellulose. *Biomacromolecules* **2009**, *10* (4), 712–716. https://doi.org/10.1021/bm8010903.

(62) Chung, S.; Park, S.-A.; Park, S. B.; Kwak, H.; Oh, D. X.; Hwang, D. S.; Jeon, H.; Koo, J. M.; Park, J. Biobased Super Engineering Plastic Nanocomposite of Cellulose Nanofibers and Isosorbide. *Polym Degrad Stab* **2023**, *215*, 110445. https://doi.org/10.1016/J.POLYMDEGRADSTAB.2023.110445.

(63) Zhu, S.; Sun, H.; Lu, Y.; Wang, S.; Yue, Y.; Xu, X.; Mei, C.; Xiao, H.; Fu, Q.; Han, J. Inherently Conductive Poly(Dimethylsiloxane) Elastomers Synergistically Mediated by Nanocellulose/Carbon Nanotube Nanohybrids toward Highly Sensitive, Stretchable, and Durable Strain Sensors. *ACS Appl Mater Interfaces* **2021**, *13* (49), 59142–59153.

(64) Xu, X.; Liu, F.; Jiang, L.; Zhu, J. Y.; Haagenson, D.; Wiesenborn, D. P. Cellulose Nanocrystals vs. Cellulose Nanofibrils: A Comparative Study on Their Microstructures and Effects as Polymer Reinforcing Agents. *ACS Appl Mater Interfaces* **2013**, *5* (8), 2999–3009.

(65) Balachandrakurup, V.; Gopalakrishnan, J. Enhanced Performance of Cellulose Nanofibre Reinforced Styrene Butadiene Rubber Nanocomposites Modified with Epoxidised Natural Rubber. *Ind Crops Prod* **2022**, *183*, 114935. https://doi.org/10.1016/J.INDCROP.2022.114935.

(66) Yuan, H. ; Li, P. ; Wang, X. ; Zhao, H. ; Sun, J.; Yuan, H.; Li, P.; Wang, X.; Zhao, H.; Sun, J. Rod-like Cellulose Regenerated by Bottom-Up Assembly in Natural Rubber Latex and Its Reinforcement. *International Journal of Molecular Sciences 2023, Vol. 24, Page 6457* **2023**, *24* (7), 6457. https://doi.org/10.3390/IJMS24076457.

(67) Gupta, A.; Simmons, W.; Schueneman, G. T.; Hylton, D.; Mintz, E. A. Rheological and Thermo-Mechanical Properties of Poly(Lactic Acid)/Lignin-Coated Cellulose Nanocrystal Composites. *ACS Sustain Chem Eng* **2017**, *5* (2), 1711–1720.

(68) Gupta, A.; Choudhary, V. Rheologic and Mechanical Properties of Multiwalled Carbon Nanotubes-Reinforced Poly(Trimethylene Terephthalate) Composites. *J Mater Sci* **2013**, *48* (9), 3347–3356. https://doi.org/10.1007/S10853-012-7025-7/FIGURES/11.

(69) Pötschke, P.; Fornes, T. D.; Paul, D. R. Rheological Behavior of Multiwalled Carbon Nanotube/Polycarbonate Composites. *Polymer (Guildf)* **2002**, *43* (11), 3247–3255. https://doi.org/10.1016/S0032-3861(02)00151-9.

(70) Cole, K. S.; Cole, R. H. Dispersion and Absorption in Dielectrics I. Alternating Current Characteristics. *J Chem Phys* **1941**, *9* (4), 341–351. https://doi.org/10.1063/1.1750906.

(71) Foudazi, R.; Zhao, B.; Gokun, P.; Manas-Zloczower, I.; Rowan, S. J.; Feke, D. L. The Effect of Shear on the Evolution of Morphology in High Internal Phase Emulsions Used as Templates for Structural and Functional Polymer Foams. **2020**. https://doi.org/10.1021/acsapm.0c00003.

(72) Foudazi, R.; Gokun, P.; Feke, D. L.; Rowan, S. J.; Manas-Zloczower, I. Chemorheology of Poly(High Internal Phase Emulsions). *Macromolecules* **2013**, *46* (13), 5393–5396. https://doi.org/10.1021/ma401157b.

(73) Mahadik, D. B.; Jung, H. N. R.; Han, W.; Cho, H. H.; Park, H. H. Flexible, Elastic, and Superhydrophobic Silica-Polymer Composite Aerogels by High Internal Phase Emulsion Process. *Compos Sci Technol* **2017**, *147*, 45–51. https://doi.org/10.1016/j.compscitech.2017.04.036.

(74) Dai, Q.; Zhang, Z.; Wang, F.; Liu, J. *Preparation and Properties of Polydimethylsiloxane/Polyacrylate Composite Latex Initiated by 60 Co-Ray Irradiation*; 2003. https://onlinelibrary.wiley.com/doi/pdf/10.1002/app.11890 (accessed 2019-05-19).

Chapter 5: Stretching-Induced Thermal Conductivity Change in Shape-Memory Polymer Composites

Adapted from (*ASME. J. Heat Transfer*. August 2020; 142(8): 081401.)

5.1 Abstract

Active thermal materials like thermal diodes, regulators, and switches have the potential to revolutionize thermal management, creating an opportunity for significant energy savings. We present results on a proposed thermal switching composite that changes its thermal conductivity based on applied strain. The composite is constructed of highly-crystalline, high aspect ratio cellulose nanocrystal (CNC) nanorods embedded in a shape-memory polymer matrix. The properties of the matrix allow for changes to the mechanical state to be indefinitely retained and also for the state to be reversed; this work is the first step in demonstrating that the thermal state exhibits similar reversibility. Measurements of the neat matrix polymer show a factor of three increase in thermal conductivity with applied strain up 100% and abrupt decrease beyond this strain level. A two-fold increase in the thermal conductivity is achieved for the proof-of-concept composite at 100% strain. By comparing the measured results to a Maxwell mixing model, the primary drivers of the thermal conductivity change are traced to changes in crystallinity of the matrix and CNC alignment.

5.2 Introduction

Active control of thermal transport has the potential to revolutionize thermal management in fields as diverse as electronics, building materials, and textiles. Whereas current design practice relies predominantly on passive thermal elements such as thermal resistance (e.g. insulation) or capacitance (thermal mass), active thermal elements would open new control approaches that could lead to increased energy efficiency and performance. A recent review summarized emerging implementations of active thermal components including thermal diodes, regulators, and switches.[1] Thermal diodes allow heat to pass in only one direction. Thermal regulators attempt to maintain a fixed temperature by varying conductance between two states. Thermal switches permit or restrict heat flow based on the state of the switch. A thermal switch is characterized by the ratio of the thermal conductivity between the 'on' and 'off' states. Conduction-based thermal switches rely on changes in thermal conductivity to regulate heat flow through a material and utilize mechanisms such as phase transitions to accomplish this heat flow control. Representative implementations of this approach have made use of metal-insulator transitions,[2] solid-solid transitions,[3] solid-liquid transition,[4] and miscibility limits in aqueous polymer solutions.[5]

The focus of this paper is on the preparation and study of a thermal switch based on a polymer composite comprised of fibers embedded in a shape-memory matrix.[6] The hypothesis is that the random alignment of fibers would represent the lower thermal conductivity state, the 'off' position. The composite may be switched to the 'on' state through the application of a stimulus (e.g. mechanical, electrical, magnetic) that leads to fiber alignment. The use of a shape memory matrix allows for the "on" state to be temporarily fixed after the stimulus is removed until the addition of a second stimulus results in recovery of the original shape potentially allowing the original thermoconducting "off" state to be accessed again.

Cellulose nanocrystals (CNCs) were chosen as the filler for the composite.[7–9] CNCs are rod-like highly-crystalline bioderived organic nanoparticles that can be obtained from natural cellulose sources such as cotton, wood, and tunicates. The specific CNCs used in the present study are derived from tunicates with a typical aspect ratio of 80.[10] On account of their high crystallinity, CNCs have been shown to exhibit a relatively high thermal conductivity (1-6 W/mK) for an organic material and their addition into a polymer matrix is expected to enhance the thermal conductivity of the material.[11,12] Further, CNCs have been shown to disperse well in thermoplastic polyurethanes.[13] Higher thermal conductivity fibers (like carbon nanofibers) are prone to agglomeration that can lead to non-uniform composites during processing when mixed into typical polymers. Thus, for these initial proof-of-concept composites, the use of CNCs simplified composite preparation while providing the necessary thermal conductivity enhancement mechanism.

Past studies of semicrystalline polymers have shown that the thermal conductivity is influenced by temperature, polymer chain alignment, and the degree of crystallinity in the polymer.[14,15] High thermal conductivity values have been measured for ultra-drawn polyethylene; these high values have been attributed to polymer chain alignment and the elimination of material defects as a result of stretching the polymer.[16] These reported values of thermal conductivity approach the theoretical limit of defect-free polyethylene.[17] The focus of the current study is material performance around room temperature so the primary drivers of thermal conductivity are expected to be polymer chain and CNC alignment and the overall degree of crystallinity in the composites.

The versatile properties of thermoplastic polyurethanes (TPUs) make them a good choice for the matrix of the composite. The specific TPU used in the present study is Texin 270, an aromatic polyester-based thermoplastic polyurethane from Covestro. This TPU was of interest here as it is

a semicrystalline material that consists of hard crystalline domains (melting point, T_m ca. 220°C) and soft amorphous/semicrystalline domains with a lower melting point (T_m ca. 110°C). The hard domain stores the permanent shape of the material, while the crystallization of the soft phase allows the material to "fix" its shape upon stretching. Thus, in this material it should be possible to use mechanical strain to both pull the CNC fibers into alignment and fix the shape. Heating above the soft-domain melting point in the absence of a stimulus allows the material to return to its permanent (disordered) shape.

5.3 Methods

5.3.1 Shape-Memory Polymer and Composite Synthesis

Tunicate-derived CNCs were prepared according to documented procedures.[18,19] Briefly, the tunicate mantle was base washed three times and bleached once. The tunicate CNCs were isolated via hydrochloric acid hydrolysis and then carboxylic acid functionalized by TEMPO oxidation. Functionalization inhibits clumping of CNCs in solution and improves dispersion. The resulting tunicate CNC-COOHs had a charge density of 980 mmol/kg. The length and width of the tunicate CNC-COOHs were determined by atomic force microscopy (AFM) measurements to be 1794 ± 375 nm and 18± 2 nm, respectively. A representative AFM image of the isolated tunicate CNC-COOHs is shown in Figure 5.1. The image gives a sense of the spatial distribution of the fibers and the branching structure of their arrangement.

The polymer films and polymer composites were made through solution casting. First, Texin 270 was dissolved in DMF at a concentration of 80 mg/mL. For composites, tunicate CNC-COOHs were dispersed in DMF at a concentration of 5 mg/mL and this solution was blended with the Texin solution to achieve the desired CNC-COOH loading. The resulting mixture was sonicated for 4 hours before casting. Casting was done in Teflon dishes within a vacuum oven at 40°C for 1

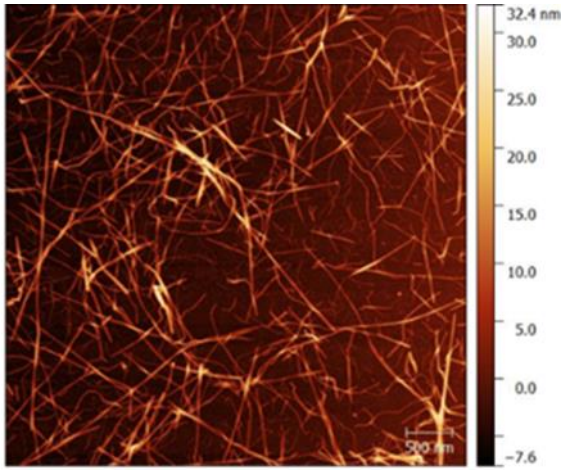

Figure 5.1. Atomic force microscope (AFM) image of tunicate CNC-COOHs

day followed by an additional 4 days at 60°C in the oven to maximize removal of DMF. Ultimately, pure TPU films and composites with 5%, 10%, 18% and 25% weight percent of tunicate CNC-COOH were made. Using this method, the resulting typical film thickness was approximately 100 microns. The cast disks then were cut into strips 12.7 mm x ~40 mm for stretching and thermal characterization.

5.3.2 Composite Straining

With the intent of impacting the thermal conductivity of the material, both polymer and polymer composite films were stretched up to 400% of their original length using a Zwick tensile instrument. In order to achieve high strains, it was necessary to heat the films to 120°C (which is above the first melting temperature of Texin 270, 107°C) for 30 minutes prior to and for the duration of stretching to melt the soft domains of the polymer to allow for strains as large as 400%. After straining, the strips were held in the clamps at the extended position until the chamber cooled to room temperature. Evidence suggested that heating led to some amount of annealing of the as-cast sample, reducing some of the residual stress in the material. Mechanical failure was observed at relatively low strain for unheated samples. For the composites, the CNC-COOH loading was observed to impact the maximum strain at failure. For example, low loading levels (< 5% CNC-

COOH mass percentage) increased the maximum allowable strain. CNC loading above 5% led to a reduction of the maximum allowable strain relative to the pure polymer. A fixed strain rate of 50% per minute was used for all film stretching. This strain rate was selected to minimize the degree of induced residual stress in the material during stretching.

5.3.3 Thermal Characterization

The thermal conductivity of these films was measured using a dual-mode heat flow meter technique shown schematically in Figure 5.2.[20] In this method, the sample is bonded to two strips of a material of known thermal conductivity. Copper shim stock (50.8 μm thick, 12.7 mm wide) was used as the reference material in these tests. The complete test specimen is mounted between two clamps with the sample and portions of reference material suspended between the clamps. Resistive heaters are pressed to the reference material held in one of the clamps and a heat sink is attached at the other clamp. This arrangement forces heat through the reference material and sample in a one-dimensional manner. To conduct a test, heat is applied until steady-state conditions are achieved. The temperature profile along the length of the specimen is measured using an infrared thermometer (Raytek RAYGPRCF) mounted to a motor-driven linear stage (Newmark Systems Inc MS-2-24). All experimental elements are housed within a vacuum chamber. Experiments are run at vacuum to minimize the influence of convection on the results; radiation losses are minimized in regions that are not thermally scanned.

A representative experimental temperature trace is shown at the top of Figure 5.2 (blue dots). The temperature variation in the reference region is nearly straight with low slope; the behavior in the sample region is marked by higher curvature due to the comparatively low thermal conductivity relative to the reference region. There is a sharp temperature change between the reference and sample regions as a result of thermal interface resistance; this interface region is omitted from the

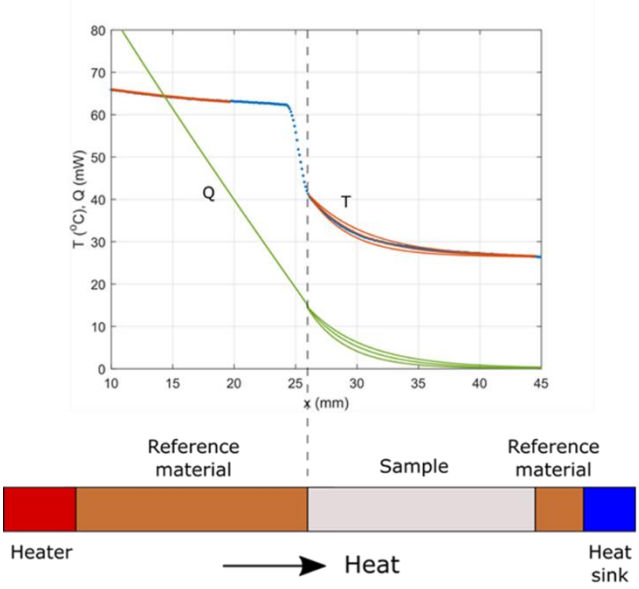

Figure 5.2. Representative data fit (above) and sample configuration (below). Blue points show IR sensor data; temperature profile curve fits (solid red) and heat flow (solid green) based on a one-dimensional heat transfer model accounting for radiation. The central curve is the best fit; curves above and below represent a value of thermal conductivity 20% above and below the best fit.

curve fit. To obtain the thermal conductivity of the sample, a theoretical curve obtained from a one-dimensional thermal model is fit to the experimental data. The model includes both conduction through the sample and radiation from the sample surface. The theoretical curve is shown in Figure 5.2 as solid red lines. There are separate fits in the reference and sample regions. The reference region fit determines the heat input; the fit in the sample region provides the sample thermal conductivity. Both fits minimize the error between the data and the model by varying the quantity to be found (heat input and thermal conductivity, respectively). Figure 5.2 shows the fit of minimum error as well curves that correspond to values of thermal conductivity ±20% from the best-fit value. In the sample region, both the thermal conductivity and emissivity of the sample are varied to minimize the error of the nonlinear fit.

Inputs to the model include the sample and reference material geometry and the reference material thermal conductivity and emissivity. Thickness was measured with a micrometer. Samples were measured before and after straining to account for thickness reduction due to stretching. The reference material thermal conductivity and emissivity were fixed across all tests. The emissivity of the reference material was determined though a preliminary test on the reference strip without a sample attached.

5.3.4 X-Ray Characterization and Analysis

The crystallinity of these films was determined through wide angle X-ray scattering at the Advanced Photon Source beamline 12-ID-B at Argonne National Lab. Strips from the same initial disks were strained and processed so that these measurements match the thermal conductivity measurements. Strips were mounted perpendicular to the beam and directly onto the sample holder without anything between the film and the beam. Each sample was exposed 9 times for 0.1 seconds for each exposure. The scattering data was compiled into one-dimensional functions of intensity and scattering vector (Q) via software at the beamline. The data was further processed and analyzed with the Irena package in IGOR Pro 7.[21–24] Crystallinity of the samples was determined with the peak deconvolution method with a Gaussian fit.[25] An example of this calculation can be found in the Supplemental Information section.

5.4 Results

Thermal conductivity results for the neat T270 polymer strained up to 400% are shown in Figure 5.3. The thermal conductivity was measured for all samples in the direction of straining; for four samples, the thermal conductivity also was measured perpendicular to the strain direction. These

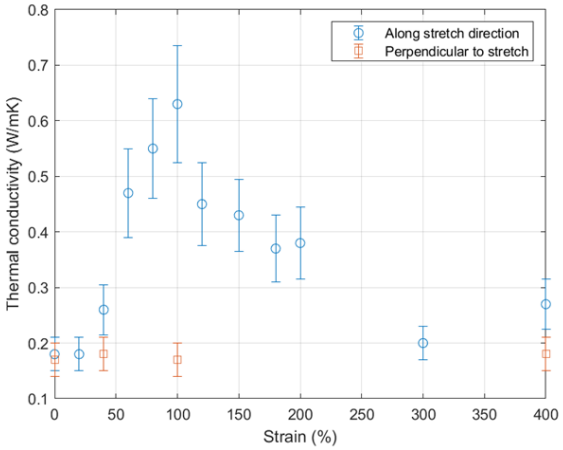

Figure 5.3. Thermal conductivity of T270 as a function of strain. Results shown for thermal conductivity both in the direction of stretched as well as perpendicular to the stretch direction.

perpendicular measurements were made on the same samples that were tested along the strain direction, but rotated 90 degrees and reassembled with the reference materials. As shown in Figure 5.3, the unstrained samples (0% strain) exhibit similar thermal conductivity values (< 0.2 W/m-K) in both measurement directions. This is expected as the polymer casting procedure does not impose any constraints on in-plane polymer alignment; polymer chains are expected to be randomly oriented in an isotropic manner. Once the samples have been strained, the thermal conductivity along the strain direction of the shape-memory polymer increases with strain up to 100% and then falls at higher strain levels, returning close to the unstrained thermal conductivity value. The material shows a peak thermal conductivity of 0.63 ± 0.11 W/mK at 100% strain. Crystalline alignment and polymer chain alignment in the soft phase are two possible explanations for the increase in thermal conductivity with strain below 100%. Thermal conductivity has been shown to increase with crystallinity and chain alignment for relatively simple polymers such as polyethylene.[14] While Texin 270 is also known to exhibit strain-induced crystallization,[26] it is important to note that these films where heated above the melting temperature of the strain induced crystals before being strained and as such the difference in conductivity is presumably not related

to an enhanced degree of crystallinity after straining (*vide infra*). It is worthy of note that the perpendicular thermal conductivities remain relatively constant (0.18 ± 0.06 W/m-K) with strain. Therefore, this anisotropy suggests that polymer chain alignment is likely the more significant driver of thermal conductivity increase in these polymer films. Stretching pulls the polymer chains into alignment with the draw direction and thermal conductivity is expected to be much higher along polymer chains than across different chains. Consequently, as strain is increased, the thermal conductivity along the strain direction increases as chain alignment increases. Perpendicular to the draw direction, the thermal conductivity is expected to decrease based on previous studies on polyethylene.[14] The decrease in thermal conductivity along the strain direction beyond 100% strain is likely the result of damage to the morphology of the TPU. While there is no observable damage in the films at the macroscale, at sufficient strain levels, it is conceivable that the hard segments of the polymer will begin to break.[27] The breaking of crystalline regions in either hard or soft segments increases the number of thermal interfaces in the material, decreasing the thermal conductivity. The thermal conductivity in the perpendicular direction remains largely unchanged at all straining conditions even though greater alignment is expected to decrease the thermal conductivity perpendicular to straining. As such the observed flat trend in the perpendicular thermal conductivity suggests that the unstrained thermal conductivity is very close to the value of thermal conductivity across polymer chains. This would be the case if the thermal conductivity was dominated by the thermal interfaces between polymer chains in both configurations. Since crystallinity would also influence the thermal conductivity, it was important to explore its potential impact next.

X-ray scattering studies were conducted at the Advanced Photon Source beamline 12-ID-B at Argonne National Lab to understand the degree of the crystallinity of the polymer at different

levels of strain (at temperature 120°C). As shown in Figure 5.4, the measured crystallinity of TPU was relatively insensitive to strain over the examined range with a mean value of approximately 45%, this is consistent with the idea that there is no significant amount of strain-induced crystallization. There does appear to be a slight decrease in crystallinity above 200% suggesting some disruption to the crystallinity in either the soft or hard phase although from the data it is difficult to say how significant this is.

Similar to the approach of Choy,[14] the Maxwell model can be used to describe the observed trends in thermal conductivity data shown in Figure 5.5. The particular form of these equations (Equations 1-3) account for effects of crystallinity and polymer chain alignment on the thermal conductivity. Here, crystallinity is described by the volume fraction crystallinity (X) and polymer chain orientation is characterized by an average angle (θ) between the primary axis of the polymer chains and the direction of straining. Alignment can also be quantified in terms of the crystalline orientation function (f_c) as given by Equation 3. The relationship between f_c and strain (or draw ratio) can be found through x-ray scattering studies, but it has been documented that the relationship between f_c and strain is similar for most polymers;[28] therefore, a representative mapping based on Choy is used here.[14] Equations 5.1, 5.2 and 5.3 below provide predictions for the thermal conductivity of the film along the direction of stretching ($K_{\parallel}$) and perpendicular to it ($K_{\perp}$), respectively, in terms of the properties of the crystalline regions of the polymer such that:

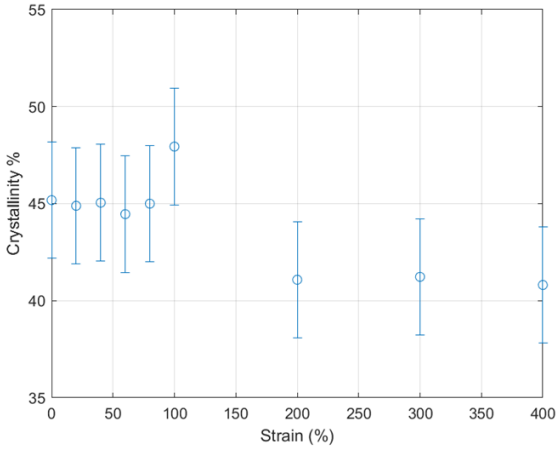

Figure 5.4. TPU crystallinity derived from wide angle x-ray scattering measurements

$$\frac{K_{\parallel}-K_0}{K_{\parallel}+2K_0} = X\left[\frac{k_{\perp}-1}{k_{\perp}+2}\times\langle\sin^2\theta\rangle + \frac{k_{\parallel}-1}{k_{\parallel}+2}\times\langle\cos^2\theta\rangle\right] \quad (5.1)$$

$$\frac{K_{\perp}-K_0}{K_{\perp}+2K_0} = X\left[\frac{k_{\perp}-1}{k_{\perp}+2}\times\frac{1+\langle\cos^2\theta\rangle}{2} + \frac{k_{\parallel}-1}{k_{\parallel}+2}\times\frac{1}{2}\langle\sin^2\theta\rangle\right] \quad (5.2)$$

$$f_c = \frac{1}{2}[3\langle\cos^2\theta\rangle - 1] \quad (5.3)$$

where $k_{\parallel}$ is the thermal conductivity along the polymer chains in the crystalline region relative to the amorphous thermal conductivity; and $k_{\perp}$ is the thermal conductivity across polymer chains, also relative to the amorphous value. The model curves are fit to the thermal conductivity data measured along the strain axis. All data is plotted relative to the isotropic (unstrained) thermal conductivity K_0. Based on the crystallinity measurements Figure 5.4, X is assumed to be constant across this range of straining. The best fit is found at a $k_{\parallel}$ value of 100 and a $k_{\perp}$ value of 0.05 with a crystallinity value of 75%. Fit agreement is better for the data obtained in the direction of straining (up to 100% strain). However, model predictions underestimate the thermal conductivity

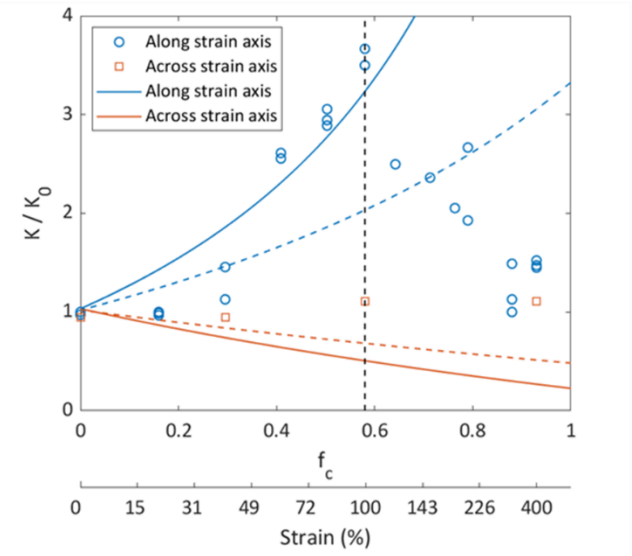

Figure 5.5. Normalized thermal conductivity of annealed TPU as a function of the crystalline orientation function, f_c and strain. Thermal conductivity measurements were made both along the direction of straining and perpendicular to it. Maxwell model fit to the data measured along the strain direction and plotted for both directions. Solid lines represent the best fit and use a crystallinity value of 75%, dashed lines are based on a crystallinity of 45%.

perpendicular to the strain direction. Further, the model predicts continued increase in the strain-direction thermal conductivity at strains greater than 100%. The model has no mechanism to account for disruption to the crystalline phase of the polymer so it is incapable of matching the behavior observed for strains greater than 100% for thermal conductivity along the strain axis. The model continues to predict enhanced alignment in the polymer and the associated increase in thermal conductivity.

The impact to thermal conductivity of adding tunicate cellulose nanocrystals to the polymer is shown in Figure 5.6 for strained and unstrained conditions. The thermal conductivity results were all measured in the direction of applied strain. For these samples, the focus is on investigating the individual contributions of CNC-COOH concentration and strain on the thermal conductivity

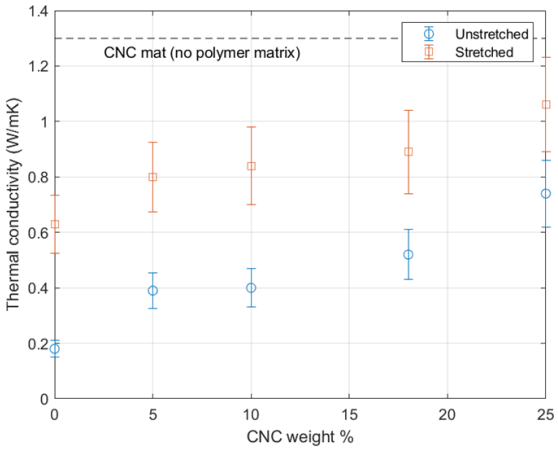

Figure 5.6. Thermal conductivity of tunicate CNC-T270 composites as a function of CNC-COOH concentration for both stretched and unstretched composite samples. For stretched samples, thermal conductivity is measured along the direction of stretching.

and anisotropy was not considered. Preliminary measurements of neat CNC-COOH mats (no polymer matrix) exhibited a thermal conductivity of 1.3 W/mK; previous work compared CNC polymer composite measurements to an effective medium model to infer a thermal conductivity 7.3 W/mK for individual CNC fibers.[29] Therefore, as expected, the addition of these relatively high thermal conductivity and highly crystalline nanorods leads to a consistent increase in the overall unstrained composite's thermal conductivity; the thermal conductivity continues to increase as a greater fraction of CNC-COOHs is added.[30] Stretching also leads to an increase in the thermal conductivity across all CNC-COOH loading amounts as evidenced by the difference between the stretched and unstretched data point in Figure 5.6. A fixed strain of 100% was applied to all stretched samples. The thermal conductivity enhancement is as large as 3X at the lower CNC-COOH loading levels and slightly less for the composites with the most nanocrystals. The addition of the CNC-COOHs and the application of strain drive the two mechanisms –overall composite crystallinity and alignment– predicted to lead to a thermal conductivity increase in these polymer composites. Given their inherent crystallinity, CNC-COOHs likely push the effective crystallinity

of the composite higher.[18] The crystallinity of the composite, measured by wide angle x-ray scattering, is shown in Figure 5.7. The solid line in Figure 5.7 shows the expected increase in crystallinity due to averaging the crystallinity of the two constituents of the composite. As expected, the presence of CNC-COOHs in the polymer leads to higher observed crystallinity (up to a CNC-COOH weight percentage of 18%) for both the stretched and unstretched composites. For the unstretched samples, crystallinity increases by 10% as the CNC-COOH mass percentage is increased from 0 to 18%. At a CNC weight percentage of 18%, the increase in composite crystallinity was larger than would be expected solely due to the addition of the more crystalline CNCs. At the highest CNC-COOH loading there is an anomalous and unexpected drop in crystallinity. This reduction in crystallinity is in spite of the continued increase in thermal conductivity seen in Figure 5.6. These opposing trends at the highest CNC loading suggest that the CNCs and their alignment are a stronger driver of thermal conductivity than crystallinity of the matrix. Stretching led to higher crystallinity for all samples at a given CNC-COOH loading. Interestingly, strain appears to have a compounding effect on the crystallinity when the CNC-COOHs are present. This observation is in contrast to the neat polymer for which strain at high temperatures had a minimal impact on crystallinity (see Figure 5.4). One possibility is that the CNC-COOHs in the composite serve as nucleation sites for crystallization that enhance the overall crystallinity relative to the neat polymer. However, at high CNC-COOH loadings, the CNC-COOH network may disrupt the formation of other crystals within the polymer matrix.

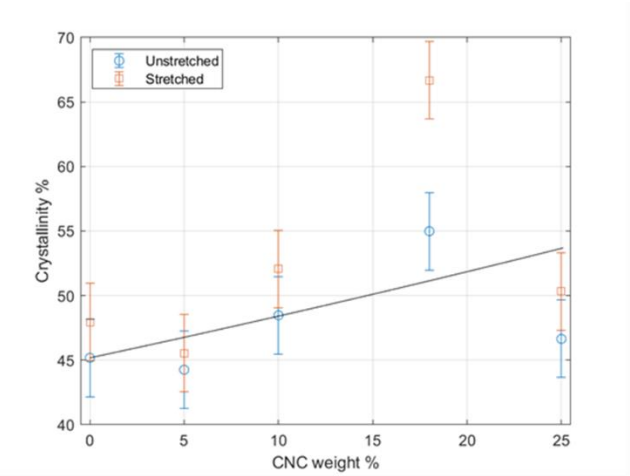

Figure 5.7. Crystallinity measured with wide angle x-ray scattering for both stretched and unstretched TPU-CNC-COOH composites. Solid line shows the expected increase in crystallinity due to the addition of CNC fibers based on crystallinity averaging between the two materials.

Further evidence of crystallinity changes and CNC-COOH alignment are provided by visual appearance changes (Figure 5.8) and Raman spectroscopy measurements (Figure 5.9).

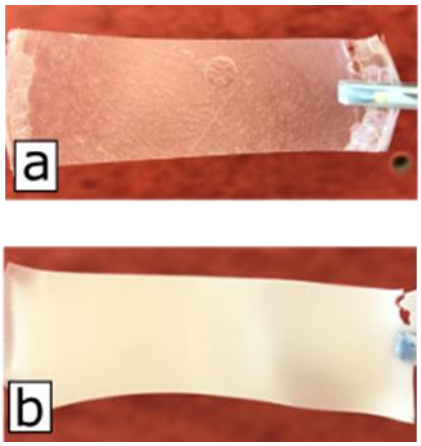

Figure 5.8. (a) Unstrained composite film with 10% tunicate-CNC-COOH, and (b) film was stretched to 100% of original length

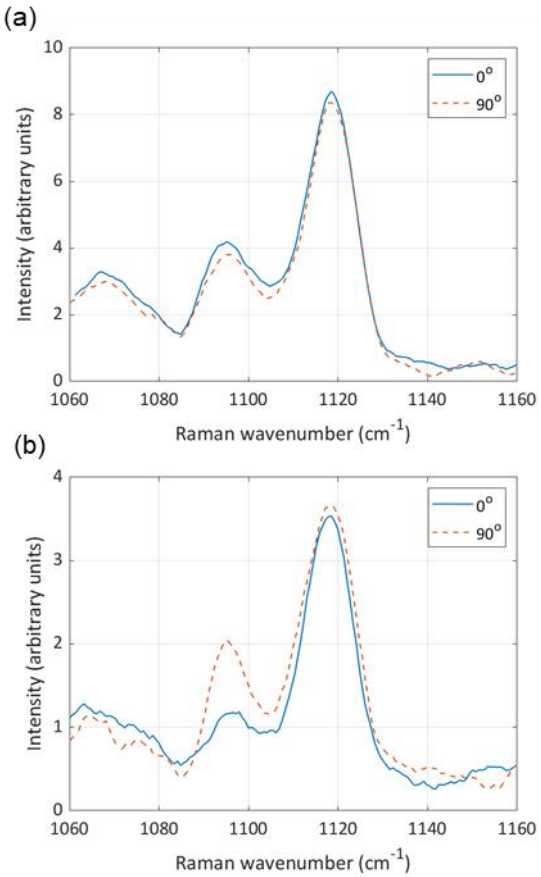

Figure 5.9. (a) Raman spectra of an unstrained 10% tunicate-CNC-COOH composite film at 0 and 90 degree of rotation angle, and (b) Raman spectra of a 10% tunicate-CNC composite film upon application of strain at 0 and 90 degree of rotation angle.

Figure 5.8 shows a composite film with 10% tunicate CNC-COOH both before and after stretching

to 100% of its original length. The unstretched film (Figure 5.8(a)) is mostly transparent. Upon stretching (Figure 5.8(b)), the material becomes an opaque white consistent with increased crystallization of the polymer matrix. This crystallinity is not caused by a strain induced crystallization mechanism since the samples are straining above the melting temperature for these crystals. These crystals are likely formed through a heterogeneous nucleation mechanism around the CNC filler when the samples are cooled below the melting temperature. Polymers typically become opaque at higher crystallinity due to the increased number of boundaries in or size of the crystalline region more effectively scattering light.[31] Figure 5.9 compares the Raman spectra for a similar 10% CNC-COOH composite film both before and after stretching. Tunicate CNCs have a well-defined Raman peak at 1095 cm^{-1}, which is associated with the C-O ring stretching along the chain axis of cellulose molecule.[32] For the unstretched film, the intensity of this peak does not change when rotating the film by 90°, suggesting that the CNCs are isotropically presented in the polymer matrix. After straining the composite, the intensity of Raman peak at 1095 cm^{-1} shows a marked difference when measured at rotation angles of 0° and 90°. The change in the peak at 1095 cm^{-1} suggests some degree of alignment of the CNC fiber; they are no longer isotropically presented in the matrix after stretching. For the composite, stretching both aligns the chains of the polymer matrix (as seen for the neat polymer) and also pulls the nanocrystals into alignment with the draw direction.

5.5 Conclusions

With the intent of creating a material whose thermal conductivity was responsive to an external stimulus, a composite was formed with tunicate-based cellulose nanocrystals embedded in thermoplastic polyurethane matrix. TPU exhibits shape-memory characteristics on account of its multiphase structure. These characteristics allow for composite to retain strain-induced

microstructural changes even after the strain is removed. Initial studies were conducted on the neat TPU polymer. The impact of strain on measured thermal conductivity was investigated. A fit of the thermal conductivity data to a Maxwell model suggested that polymer chain alignment on straining was the dominate cause of thermal conductivity increase. For the neat polymer, the increasing trend in thermal conductivity only held to 100%. Beyond 100% strain the thermal conductivity decreased, likely due to breakage of the crystalline hard segments within the polymer. Composites were formed from TPU and varying amounts of tunicate-derived cellulose nanocrystals. The highest thermal conductivity (1.06 ± 0.17 W/mK) was measured for a CNC-COOH loading of 25% (by weight) and an imposed strain of 150%. This value is over five times the value of the unstrained polymer matrix and 85% of the value for a mat made of pure CNC-COOHs. Thermal conductivity increase with strain in the composites was attributed to both alignment (polymer chain and CNC) and increased crystallization. Comparing the thermal conductivity at 150% strain to the unstrained value at this CNC-COOH loading gives a switching ratio of 1.4. This shows that the highest thermal conductivity configuration does not necessarily give the highest switching ratio (as the unstrained thermal conductivity is also higher). Both the 5% and 10% CNC composites have switching ratios in excess of 2 (and favorable mechanical properties) making them better potential thermal switch candidates. Studies of the reversibility of the observed thermal switching are ongoing. Future work will examine the cyclic performance of these materials and attempt to increase the switching ratio through the use of higher thermal conductivity fibers. The thermal conductivity and switching ratio will be documented over multiple strain-relaxation cycles with an intent in quantifying hysteresis.

5.6 Acknowledgements

SAXS and WAXS data was collected at the X-ray Science Division beamline 12-ID-B at the Advanced Photon Source, Argonne National Laboratory with the assistance of Dr. Byeongdu Lee and Dr. Xiaobing Zuo. Parts of this work were carried out at the Soft Matter Characterization Facility of the University of Chicago.

5.7 Funding

This material is based upon work supported by the National Science Foundation (NSF) under Grant No. 1605354. This research used resources of the Advanced Photon Source, a U.S. Department of Energy (DOE) Office of Science User Facility operated for the DOE Office of Science by Argonne National Laboratory under Contract No. DE-AC02-06CH11357.

5.8 Supplemental Information

The two-dimensional scattering pattern was averaged along azimuthal angle to obtain a one-dimensional plot of intensity as a function of scattering vector (Q). As shown in Figure 5.10, the individualized crystalline peaks in the x-ray scattering data were deconvoluted and fitted with Gaussian functions to determine the crystalline contribution to the intensity. Functions in the Irena tool package were used to calculate the area under the curve of the data and the crystalline peaks.[25] The crystallinity percentage was then calculated using Equation 4.

$$\% \text{ Crystallinity} = \frac{\text{Area from Crystal Peak}}{\text{Total Area}} \qquad (4)$$

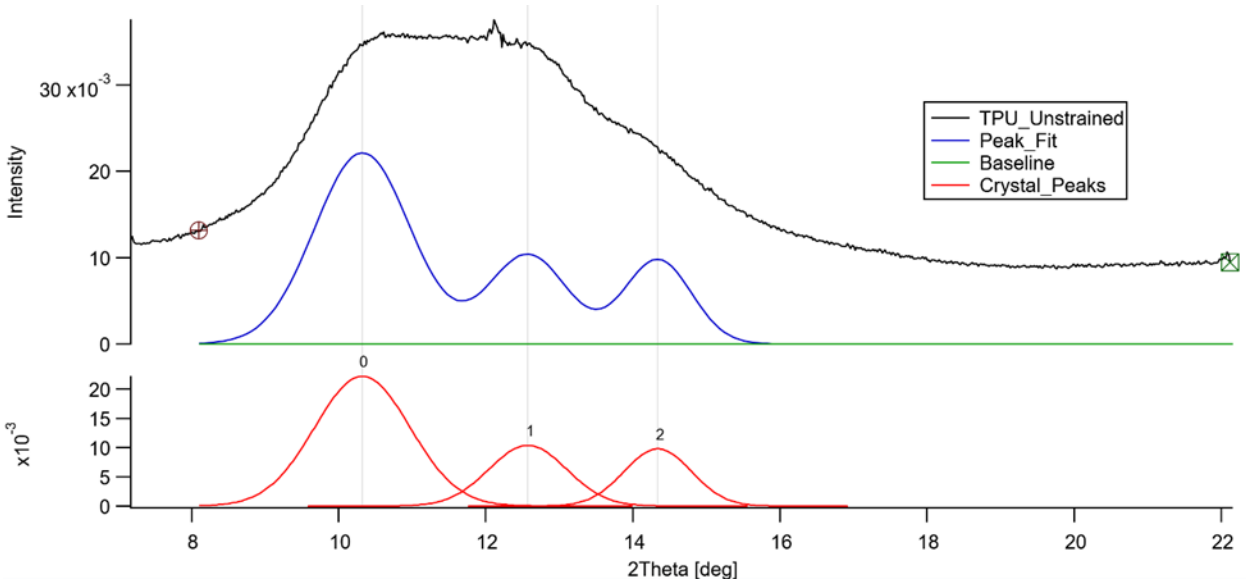

Figure 5.10. WAXS Data for the unstrained neat TPU sample as shown by the black curve. The blue curve denotes the crystalline portion of the data as identified by the multiple peak fitting tool. Red peaks in the bottom graph represent the deconvoluted Gaussian curves for each crystal peak.

5.9 Nomenclature

T_m	melting temperature
X	volume fraction crystallinity
θ	average angle between the primary axis of the polymer chains and the direction of straining
f_c	crystalline orientation function
$K_{\parallel}$	effective film thermal conductivity along the direction of straining
$K_{\perp}$	effective film thermal conductivity perpendicular to the direction of straining
$k_{\parallel}$	thermal conductivity along polymer chains in the crystalline region relative to the amorphous thermal conductivity
$k_{\perp}$	thermal conductivity across polymer chains in the crystalline region relative to the amorphous thermal conductivity
K_0	isotropic (unstrained) thermal conductivity

5.10 References

(1) Wehmeyer, G.; Yabuki, T.; Monachon, C.; Wu, J.; Dames, C. Thermal Diodes, Regulators, and Switches: Physical Mechanisms and Potential Applications. *Appl Phys Rev* **2017**, *4* (4), 41304. https://doi.org/10.1063/1.5001072/14574739/041304_1_ACCEPTED_MANUSCRIPT.PDF.

(2) Lee, S.; Hippalgaonkar, K.; Yang, F.; Hong, J.; Ko, C.; Suh, J.; Liu, K.; Wang, K.; Urban, J. J.; Zhang, X.; Dames, C.; Hartnoll, S. A.; Delaire, O.; Wu, J. Anomalously Low Electronic Thermal Conductivity in Metallic Vanadium Dioxide. *Science (1979)* **2021**, *355* (6323), 371–374. https://doi.org/10.1126/SCIENCE.AAG0410/SUPPL_FILE/LEE.SM.PDF.

(3) Liu, H.; Shi, X.; Xu, F.; Zhang, L.; Zhang, W.; Chen, L.; Li, Q.; Uher, C.; Day, T.; Snyder Jeffrey, G. Copper Ion Liquid-like Thermoelectrics. *Nature Materials 2012 11:5* **2012**, *11* (5), 422–425. https://doi.org/10.1038/nmat3273.

(4) Kim, K.; Kaviany, M. Thermal Conductivity Switch: Optimal Semiconductor/Metal Melting Transition. *Phys Rev B* **2016**, *94* (15), 155203. https://doi.org/10.1103/PHYSREVB.94.155203/FIGURES/18/MEDIUM.

(5) Li, C.; Ma, Y.; Tian, Z. Thermal Switching of Thermoresponsive Polymer Aqueous Solutions. *ACS Macro Lett* **2018**, *7* (1), 53–58. https://doi.org/10.1021/ACSMACROLETT.7B00938/SUPPL_FILE/MZ7B00938_SI_001.PDF.

(6) Lendlein, A.; Kelch, S. Shape-Memory Polymers. *Angewandte Chemie* **2002**. https://doi.org/10.1002/0471238961.1908011612051404.A01.

(7) Habibi, Y.; Lucia, L. A.; Rojas, O. J. Cellulose Nanocrystals: Chemistry, Self-Assembly, and Applications. *Chem Rev* **2010**, *110* (6), 3479–3500. https://doi.org/10.1021/CR900339W/ASSET/CR900339W.FP.PNG_V03.

(8) Eichhorn, S. J.; Dufresne, A.; Aranguren, M.; Marcovich, N. E.; Capadona, J. R.; Rowan, S. J.; Weder, C.; Thielemans, W.; Roman, M.; Renneckar, S.; Gindl, W.; Veigel, S.; Keckes, J.; Yano, H.; Abe, K.; Nogi, M.; Nakagaito, A. N.; Mangalam, A.; Simonsen, J.; Benight, A. S.; Bismarck, A.; Berglund, L. A.; Peijs, T. Review: Current International Research into Cellulose Nanofibres and Nanocomposites. *Journal of Materials Science 2009 45:1* **2010**, *45* (1), 1–33. https://doi.org/10.1007/S10853-009-3874-0.

(9) Xie, S.; Zhang, X.; Walcott, M. P.; Lin, H. Applications of Cellulose Nanocrystals: A Review. *Engineered Science* **2018**, *2*, 4–16. https://doi.org/10.30919/ES.1803302.

(10) Rusli, R.; Shanmuganathan, K.; Rowan, S. J.; Weder, C.; Eichhorn, S. J. Stress Transfer in Cellulose Nanowhisker Composites - Influence of Whisker Aspect Ratio and Surface Charge. *Biomacromolecules* **2011**, *12* (4), 1363–1369. https://doi.org/10.1021/BM200141X/ASSET/IMAGES/MEDIUM/BM-2011-00141X_0007.GIF.

(11) Diaz, J. A.; Ye, Z.; Wu, X.; Moore, A. L.; Moon, R. J.; Martini, A.; Boday, D. J.; Youngblood, J. P. Thermal Conductivity in Nanostructured Films: From Single Cellulose

Nanocrystals to Bulk Films. *Biomacromolecules* **2014**, *15* (11), 4096–4101. https://doi.org/10.1021/BM501131A/SUPPL_FILE/BM501131A_SI_001.PDF.

(12) Uetani, K.; Hatori, K. Thermal Conductivity Analysis and Applications of Nanocellulose Materials. *Sci Technol Adv Mater* **2017**, *18* (1), 877–892. https://doi.org/10.1080/14686996.2017.1390692.

(13) Liu, J. C.; Martin, D. J.; Moon, R. J.; Youngblood, J. P. Enhanced Thermal Stability of Biomedical Thermoplastic Polyurethane with the Addition of Cellulose Nanocrystals. *J Appl Polym Sci* **2015**, *132* (22). https://doi.org/10.1002/APP.41970.

(14) Choy, C. L. Thermal Conductivity of Polymers. *Polymer (Guildf)* **1977**, *18* (10), 984–1004. https://doi.org/10.1016/0032-3861(77)90002-7.

(15) Choy, C. L.; Chen, F. C.; Luk, W. H. Thermal Conductivity of Oriented Crystalline Polymers. *Journal of Polymer Science: Polymer Physics Edition* **1980**, *18* (6), 1187–1207. https://doi.org/10.1002/POL.1980.180180603.

(16) Shen, S.; Henry, A.; Tong, J.; Zheng, R.; Chen, G. Polyethylene Nanofibres with Very High Thermal Conductivities. *Nature Nanotechnology 2010 5:4* **2010**, *5* (4), 251–255. https://doi.org/10.1038/nnano.2010.27.

(17) Shulumba, N.; Hellman, O.; Minnich, A. J. Lattice Thermal Conductivity of Polyethylene Molecular Crystals from First-Principles Including Nuclear Quantum Effects. *Phys Rev Lett* **2017**, *119* (18), 185901. https://doi.org/10.1103/PHYSREVLETT.119.185901/FIGURES/4/MEDIUM.

(18) Cudjoe, E.; Hunsen, M.; Xue, Z.; Way, A. E.; Barrios, E.; Olson, R. A.; Hore, M. J. A.; Rowan, S. J. Miscanthus Giganteus: A Commercially Viable Sustainable Source of Cellulose Nanocrystals. *Carbohydr Polym* **2017**, *155*, 230–241. https://doi.org/10.1016/J.CARBPOL.2016.08.049.

(19) Dagnon, K. L.; Way, A. E.; Carson, S. O.; Silva, J.; Maia, J.; Rowan, S. J. Controlling the Rate of Water-Induced Switching in Mechanically Dynamic Cellulose Nanocrystal Composites. *Macromolecules* **2013**, *46* (20), 8203–8212. https://doi.org/10.1021/MA4008187/SUPPL_FILE/MA4008187_SI_001.PDF.

(20) Mahanta, N. K.; Abramson, A. R. The Dual-Mode Heat Flow Meter Technique: A Versatile Method for Characterizing Thermal Conductivity. *Int J Heat Mass Transf* **2010**, *53* (23–24), 5581–5586. https://doi.org/10.1016/J.IJHEATMASSTRANSFER.2010.05.063.

(21) Ilavsky, J.; Jemian, P. R. Irena: Tool Suite for Modeling and Analysis of Small-Angle Scattering. *urn:issn:0021-8898* **2009**, *42* (2), 347–353. https://doi.org/10.1107/S0021889809002222.

(22) Zhang, F.; Ilavsky, J.; Long, G. G.; Quintana, J. P. G.; Allen, A. J.; Jemian, P. R. Glassy Carbon as an Absolute Intensity Calibration Standard for Small-Angle Scattering. *Metall Mater Trans A Phys Metall Mater Sci* **2010**, *41* (5), 1151–1158. https://doi.org/10.1007/S11661-009-9950-X/FIGURES/8.

(23) Nelson, A.; IUCr. Co-Refinement of Multiple-Contrast Neutron/X-Ray Reflectivity Data Using MOTOFIT. *urn:issn:0021-8898* **2006**, *39* (2), 273–276. https://doi.org/10.1107/S0021889806005073.

(24) Beaucage, G.; IUCr. Approximations Leading to a Unified Exponential/Power-Law Approach to Small-Angle Scattering. *urn:issn:0021-8898* **1995**, *28* (6), 717–728. https://doi.org/10.1107/S0021889895005292.

(25) Park, S.; Baker, J. O.; Himmel, M. E.; Parilla, P. A.; Johnson, D. K. Cellulose Crystallinity Index: Measurement Techniques and Their Impact on Interpreting Cellulase Performance. *Biotechnol Biofuels* **2010**, *3* (1), 1–10. https://doi.org/10.1186/1754-6834-3-10/TABLES/2.

(26) Kojio, K.; Nakamura, S.; Furukawa, M. Effect of Side Methyl Groups of Polymer Glycol on Elongation-Induced Crystallization Behavior of Polyurethane Elastomers. *Polymer (Guildf)* **2004**, *45* (24), 8147–8152. https://doi.org/10.1016/J.POLYMER.2004.09.061.

(27) Qi, H. J.; Boyce, M. C. Stress–Strain Behavior of Thermoplastic Polyurethanes. *Mechanics of Materials* **2005**, *37* (8), 817–839. https://doi.org/10.1016/J.MECHMAT.2004.08.001.

(28) Pietralla, M. The Function of Twinning during the Deformation of Partially Crystalline Polymers. *Colloid and Polymer Science Kolloid Zeitschrift & Zeitschrift für Polymere* **1976**, *254* (3), 249–257. https://doi.org/10.1007/BF01384023/METRICS.

(29) Berkowitz, K. M. Characterization and Analysis of Shape Memory Polymer Composites With Cellulose Nanocrystal Fillers. Case Western Reserve University 2014.

(30) Shimazaki, Y.; Miyazaki, Y.; Takezawa, Y.; Nogi, M.; Abe, K.; Ifuku, S.; Yano, H. Excellent Thermal Conductivity of Transparent Cellulose Nanofiber/Epoxy Resin Nanocomposites. *Biomacromolecules* **2007**, *8* (9), 2976–2978. https://doi.org/10.1021/BM7004998/ASSET/IMAGES/BM7004998.SOCIAL.JPEG_V03.

(31) Peacock, A. J.; Calhoun, A. Polymer Science: Properties and Application. *Polymer Science: Properties and Application* **2006**, 1–398. https://doi.org/10.3139/9783446433434/ASSET/13ED315E-3713-D315-B371-ED315EB3713E/9783446433434.COVER.JPG.

(32) Rusli, R.; Shanmuganathan, K.; Rowan, S. J.; Weder, C.; Elchhorn, S. J. Stress-Transfer in Anisotropic and Environmentally Adaptive Cellulose Whisker Nanocomposites. *Biomacromolecules* **2010**, *11* (3), 762–768. https://doi.org/10.1021/BM1001203/SUPPL_FILE/BM1001203_SI_001.PDF.